NASA Contractor Report 175097

242 P.

IN-11623

The Evolution and Growth of Al_2O_3 Scales on β-NiAl

(NASA-CR-175097) THE EVOLUTION AND GROWTH OF Al2O3 SCALES ON BETA-NiAl Ph.D. Thesis. Final Report (Case Western Reserve Univ.) 242 p HC A11/MF A01 CSCL 11F
N86-27444
Unclas
G3/26 43233

CH486724

Joseph K. Doychak
Case Western Reserve University
Cleveland, Ohio

May 1986

Prepared for
Lewis Research Center
Under Grant NAG 3-498

National Aeronautics and
Space Administration

Table of Contents

Page

Introduction 1

Materials and Procedures 11

Results and Discussion 16

I. Transient Oxidation Stage 16

A. Oxidation at 800°C 22
1. Oxidation for times of 10.0 hours or less 27
2. Oxidation for times greater than 10.0 hours 46
a. Growth rates 46
i. (001) single crystal 49
ii. (011) single crystal 50
iii. Polycrystalline 53
iv. Discussion 56
b. Microstructure 64
B. 1100°C Oxidation 70
1. Growth rates 72
2. Microstructure 74
a. (001) single crystal 74
b. Polycrystal 96
3. Summary 100
C. Concluding remarks on the transient oxidation of β-NiAl 101

II. The Transformation to α-Al_2O_3 107

A. Review of previous studies 107
1. Thermodynamics of the $\gamma \rightarrow \alpha$ transformation 108
2. Kinetics of the $\gamma \rightarrow \alpha$ transformation 111
3. Crystallography and mechanisms of the $\gamma \rightarrow \alpha$ transformation 113
B. Results on the $\gamma \rightarrow \alpha$ transformation in oxide scales 121
1. Morphology of the transformation products 122
2. Crystallography of the $\gamma \rightarrow \alpha$ transformation 126
3. Porosity in transformed α-Al_2O_3 133
4. Surface smoothing of transformed scales 139

III. Mature Oxidation Stage 146

A. Growth rates 149
B. Scale Morphology 151
C. Discussion 171
1. Morphology 171
2. Growth mechanisms 176

VI. The Evolution of α-Al_2O_3 Scale Morphology on Alumina-forming Alloys 189
A. Oxidation of β-NiAl 190
1. Single crystal studies 190
2. Polycrystal studies 192
B. Oxidation of other alumina-forming alloy systems 203

Conclusions 208

References 211

Appendix A. Wagner Theory of Oxidation 218

Appendix B. Cahn 1000 Electrobalance System 224

Appendix C. In-situ Observations of Transient Al_2O_3 Scale Transformations 229

Appendix D. Morphological Changes due to Surface Diffusion 236

Introduction

Environmental degradation of high temperature metallic alloys has been and continues to be a serious problem in many applications. The most common forms of attack which reduce the lifetime of components are oxidation, hot corrosion and erosion. Resistance to these detrimental environments requires a protective coating covering exposed surfaces. This coating serves to resist fast oxidation, decrease metal loss and act as a barrier to corrosion products and erosion mechanisms. Stable oxide coatings are utilized for these purposes. Therefore the formation of a continuous, slow-growing, adherent oxide scale is necessary to protect against environmental degradation.

The oxide systems most often utilized for high temperature applications are Al_2O_3, SiO_2 and Cr_2O_3.[1] The Ellingham diagram in Figure 1 shows that these oxides are thermodynamically more stable than iron, nickel or cobalt oxides from which the metals constitute the majority of high temperature alloys. The plot of parabolic growth rate versus temperature in Figure 2 indicates that Al_2O_3, SiO_2 and Cr_2O_3 grow much more slowly than other constitutive oxides. Al_2O_3 is the most stable and slowest growing oxide of the three mentioned. Cr_2O_3 scales are generally utilized at lower temperatures where alloy stability is maintained and

ORIGINAL PAGE IS
OF POOR QUALITY

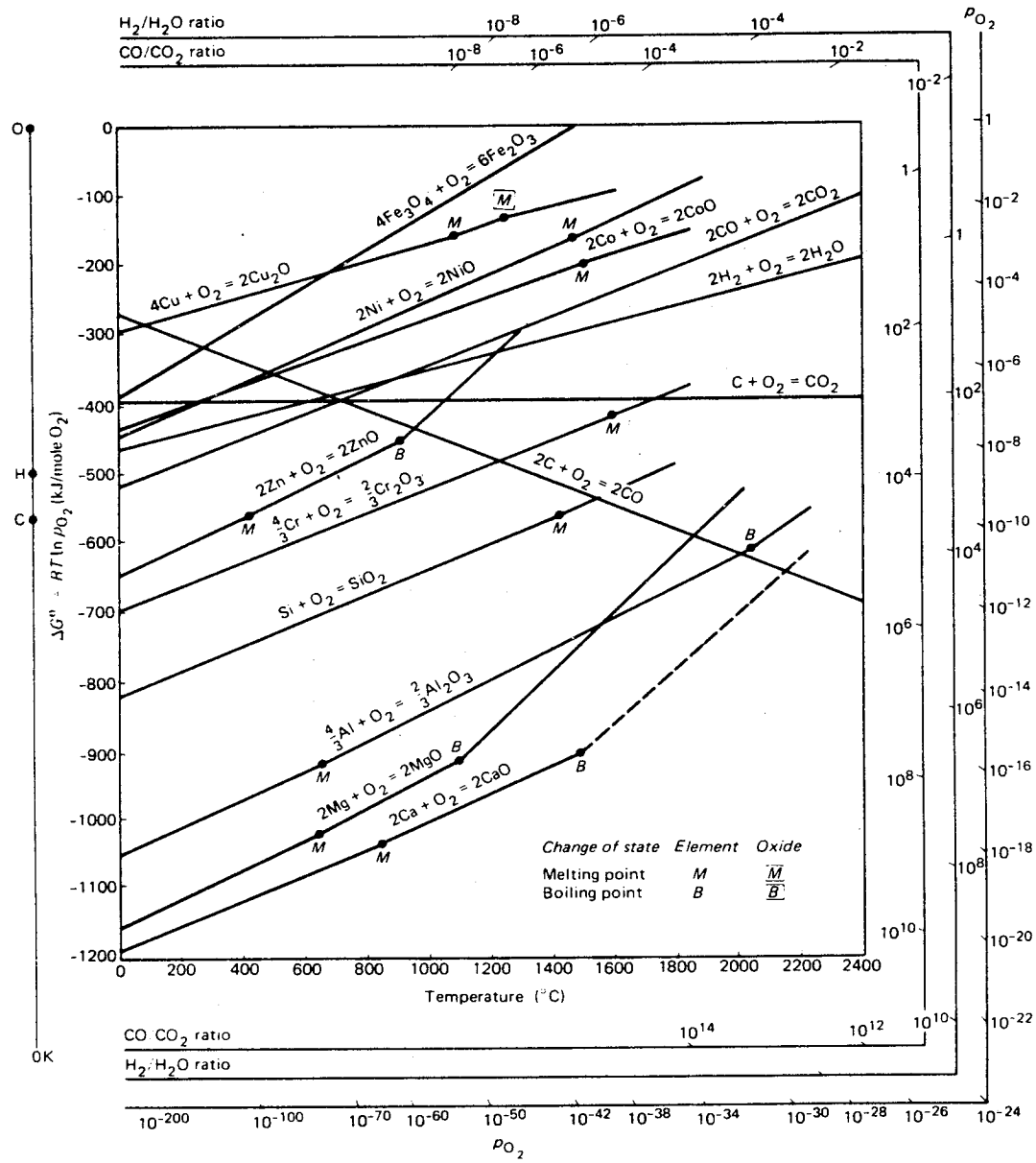

Figure 1

An Ellingham diagram of standard free energies of formation as a function of temperature.(Ref. 1).

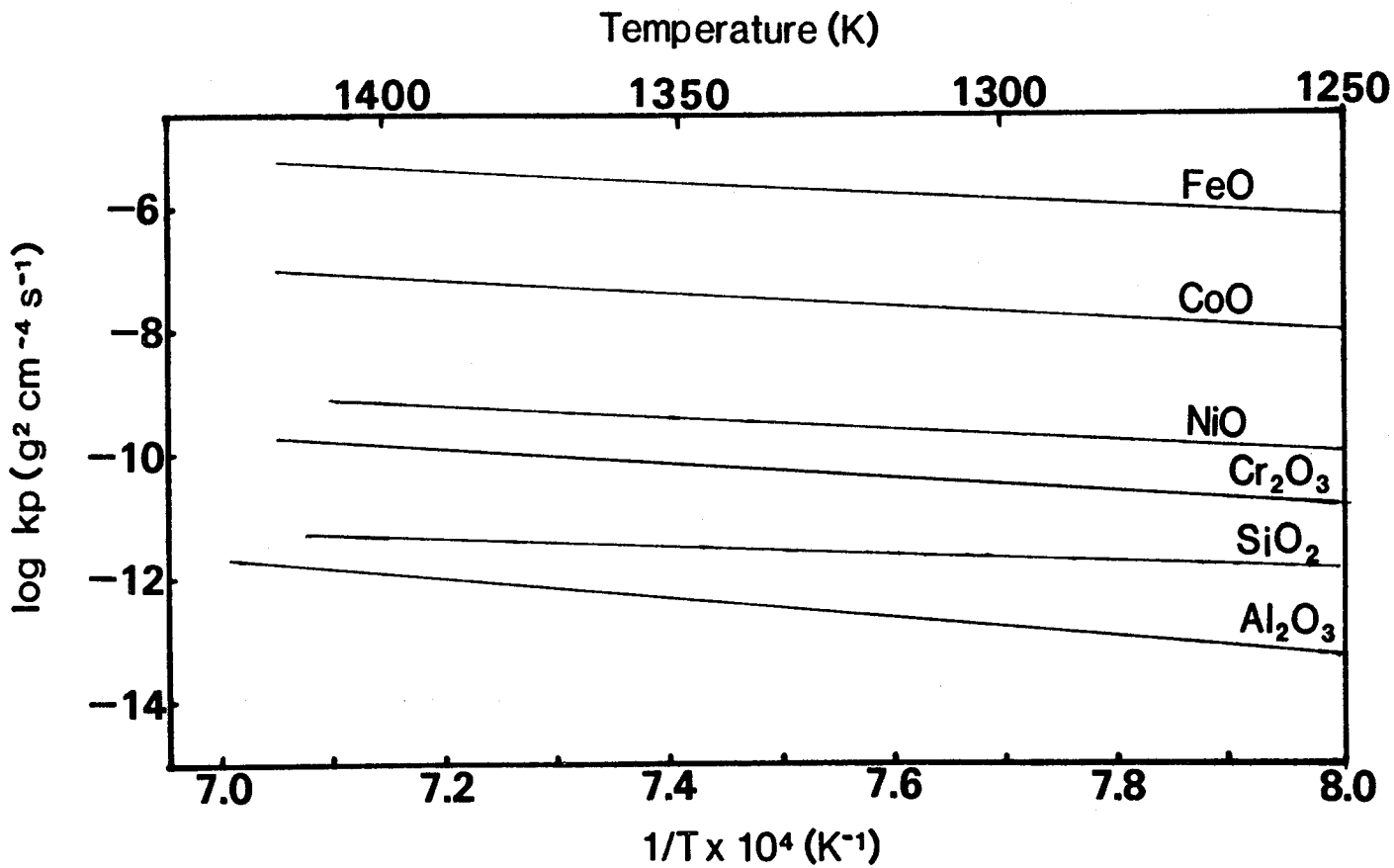

Figure 2

Parabolic growth rate, k_p, as a function of temperature for various high temperature oxide scales. (Ref. 1).

formation of the volatile CrO_3 phase is supressed.[2]

Because of their superior properties, Al_2O_3 scales are most desirable for high temperature applications. Sufficient aluminum to form and maintain a complete scale is usually incorporated as an essential part of alloy development. In these cases, an Al_2O_3 healing layer may not form during initial stages but will eventually form under a layer of other constitutive oxides. In cases where the aluminum content in the alloy is insufficient to properly maintain a scale, a metallic coating containing a high aluminum concentration is applied to the alloy surface. The coatings are generally Ni-base and may contain chromium for improved chemical compatability with the underlying alloy.[3] The most frequently used coating alloys are a multiphase $\gamma/\gamma' + \beta$ Ni-Cr-Al alloy and single phase β-NiAl. The chromium containing alloys form many oxide phases prior to Al_2O_3. The β-NiAl alloys on the other hand are especially conducive to fast formation and persistence of Al_2O_3.

Besides being an effective oxidation resistant coating alloy, β-NiAl is presently being considered as a structural material. The unique properties of aluminide intermetallics warrant their study as an effective high temperature structural alloy. However, markedly decreased ductility and processing difficulties keep these intermetallics from currently being marketable as structural materials.

β-NiAl is therefore important fundamentally as an Al_2O_3

former and practically as an oxidation resistant material. Its excellent oxidation resistance is a result of the Al_2O_3 scale that forms under most environmental conditions. The characteristics of the Al_2O_3 scales on β-NiAl are similar in many ways to those on other alumina-forming alloys. The main features of the scales are high thermodynamic stability, slow thickening rates and good oxide adherence when full advantage is taken of the "rare-earth" effect.[4] The mechanisms for each of these features will be explained briefly in light of the pertinent literature.

Pettit has provided the conditions necessary for formation of an Al_2O_3 layer as part of the scale.[5] If his result is combined with the kinetic treatment of Kear et al.,[6] the following description of the formation process of a healing layer on β-NiAl and other alumina-forming alloys is obtained. When the alloy is exposed to the oxidizing environment at temperature, all constituitive oxides nucleate and grow until a complete scale of oxide is formed. The oxides are usually cubic and are of the form AO and AB_2O_4 spinel(A=Ni,Co,Fe; B=Al,Cr). Chattopadhay and Wood have shown that the Al_2O_3 scale at this stage consists of γ-Al_2O_3.[7] Other metastable forms of Al_2O_3 based on a spinel structure may also be present. Because of its higher thermodymanic stability, Al_2O_3 forms as a complete healing layer adjacent to the metal. Once a complete layer of Al_2O_3 forms, scale growth usually involves only thickening of the Al_2O_3 layer.

Once phase boundary reactions are no longer rate controlling,

growth of the oxide scale is controlled by diffusion through the layer. According to the Wagner theory of oxidation, the growth kinetics should follow a parabolic growth equation because diffusion of mobile species is rate controlling.[8] Self-diffusion coefficients often have been determined by measuring the concentration gradient of an isotope of the desired species. Oxygen and aluminum self-diffusion coefficients in Al_2O_3 have been measured using bulk alumina and alumina scales as materials for study. Diffusion occurs by movement of defects, such as vacancies, within a material. In the case of polycrystalline oxide scales, grain boundaries and possibly dislocations act as short-circuit paths for diffusion. The defect mobility in these areas greatly exceeds the mobility of intrinsic or extrinsic point defects within the lattice. A number of tracer studies have been performed indicating that Al_2O_3 scales grow predominantly by inward oxygen grain boundary diffusion.[9-11] Aluminum outward grain boundary diffusion has also been concluded to occur in a limited number of cases.[12,13] Outward aluminum diffusion is believed to play a major role in oxide adherence as well.[14]

The phenomenon of oxide adherence on high temperature alloys has been a major area of study over the past few decades.[15] The problem arises from compressive stresses that are developed when an oxidized metal is cooled. The thermal expansion of the oxide is much smaller than that of the metal. Therefore, the oxide cannot contract as much as the metal when the temperature is

decreased. Often, the compressive stresses exceed the bond strength between the metal and oxide resulting in buckling of the oxide. Spallation occurs when the yield strength of the oxide has been exceeded for the given stress state. The first discovery of improved oxide adherence occurred when rare-earth elements were added to Cr_2O_3-forming heater alloys.[16] Since then, the mechanisms of adherence and the means to improve it have been sought. Similar findings have been found for both Cr_2O_3 and Al_2O_3 scales indicating that some commonalities exist between the two systems. For both systems, optimum amounts of rare-earth or other oxygen active elemental additions have been found to improve oxide adherence. Oxide dispersions have also been found to be effective.[17] In some cases, dopant additions have been found to effect growth mechanisms and rates.[18,19] The ways in which the oxide adherence is improved have been explained in a number of proposed theories of which all have been applied to the Al_2O_3 system. The theories involve first or second order effects on adherence.

A first mechanism proposed by Wood and Boustead was based on the idea that a "graded-seal" acts as an intermediate layer between the metal and oxide.[20] This layer contains a higher concentration of dopant which tends to increase the oxide plasticity via increased cation diffusion. The effect of increased oxide plasticity was cited by Hauntz and Delauney in their studies of iron-based Al_2O_3 formers even though no

intermediate layer was found.[21]

The effect of outward aluminum diffusion on adherence, briefly mentioned earlier, is to form new oxide within the scale interior at grain boundaries along which oxygen is diffusing inwards.[14,22] Growth of oxide within the scale causes compressive stresses resulting in buckling and spallation. However, when rare-earth dopants are added to the alloy, buckling and spallation are dramatically reduced. This is believed to occur by the "growth stress" mechanism in which the oxidized dopants block paths of outward aluminum diffusion preventing oxide formation within the scale.

In the "pegging" mechanism it is suggested that dopants induce formation of oxide stringers which mechanically key the oxide to the metal.[23] The morphology of the pegs has a great influence on the ensuing adherence properties.

Another mechanism is that of an enhanced chemical bond between the metal and oxide caused by the dopant additions.[24] The effect was noted when oxide spallation occurred at the metal oxide interface without dopants but occurred within the scale when dopants were added. Molecular orbital calculations and acoustic emmission studies have been applied to develop this mechanism.[25,26]

A final mechanism has been proposed recently. Auger studies have found traces of sulphur at the metal-oxide interface without dopant additions.[27,28] However, no sulphur was present at the

interface when Zr or Y dopants were added. The dopants are assumed to getter the sulphur, thus preventing oxide-metal decohesion.

Studies of microstructures on Al_2O_3 forming alloys have been performed to explain many of the above mentioned characterisics of a slow growing, adherent oxide scale through structure-property relationships. The major study of Al_2O_3 scale microstructure was performed by Smialek on Zr-doped and undoped NiCrAl alloys.[29] Various times and temperatures were used to encompass the different stages of oxidation. The transient phases and morphologies were studied, as well as the mature α-Al_2O_3 scales. The main features of the transient scales were porosity and oriented patches of transient oxides having specific orientation relationships with the metal.[30] The mature scales showed randomly oriented grains of α-Al_2O_3 having intergranular and intragranular porosity varying as a function of scale depth. Implications on formation, growth and adhesion mechanisms were made throughout the study.

The same detailed microstructural studies of Al_2O_3 formed on β-NiAl have not been performed. However, β-NiAl has been used as a model alloy for the study of growth rates and oxide adherence of Al_2O_3 scales.[31,32] Through these studies, observations were made of the microstructures using optical microscopy and scanning electron microscopy(SEM) methods. Many new and interesting microstructural observations were made but the lack of sufficient

crystallographic and chemical information prevented complete characterization. The present study, combined with a recent study of the transient oxidation of single-crystal β-NiAl,[33] was designed to improve the understanding of the overall oxidation of β-NiAl and characteristics of Al_2O_3 scales in general. Detailed crystallographic information is essential in order to develop mechanisms of the transient stages of Al_2O_3 formation and growth, the transformation to mature stages and ensuing morphologies and growth. Particular attention will be paid to the role of metal-oxide and oxide-oxide epitaxy necessary to control oxide microstructure.

Material and Procedures

The Ni-Al material was purchased from TRW, Inc. A master ingot of nominal composition Ni-50 at% Al plus 0.5 wt% Zr was heated in a high vacuum(10^{-7} Torr) furnace and cast into rectangular bars 25 mm X 12 mm X 120 mm and round bars 120 mm X 25 mm in diameter. The bars were intended to be single crystals obtained by selective grain growth. However, only large grained material was obtained with the largest grains being several centimeters in size. The actual composition of the cast bars was determined by wet chemistry and spectrographic methods. The results are shown in Table I. Zr was intentionally added to improve oxide adherence but Si, Fe, Cr, Ti and Y were also present as impurities. The alloy was single phase β-NiAl except for impurities. The majority of impurities were tied up as a separate Zr,Si-rich phase along grain boundaries and dispersed throughout grains. The composition of this intermetallic phase is portrayed in the electron microprobe measurements as shown in Figure 3.

Single crystal specimens were obtained by orienting the cast bars using the Laue x-ray diffraction technique followed by spark machining into slices. Transmission electron microscopy(TEM) specimens were obtained by spark machining 3 mm discs from the

TABLE I

Composition of the Ni-Al alloy used for the present study determined by spectrographic analysis. The results are given in at%.

Element	Test A*	Test B¶	average(at%)
Ni	52.132	———	52.132
Al	47.158	———	47.158
Mo	.001	———	.001
Fe	.086	.118	.102
Cr	.005	.042	.024
Co	.004	———	.004
Zr	.031	.073	.052
Cu	.003	———	.003
Ti	.007	———	.007
Si	.528	.471	.500
Mg	.002	———	.002
V	.003	———	.003
Y	———	.002	.002

* National Spectrographic Laboratories

¶ NASA Lewis Research Center

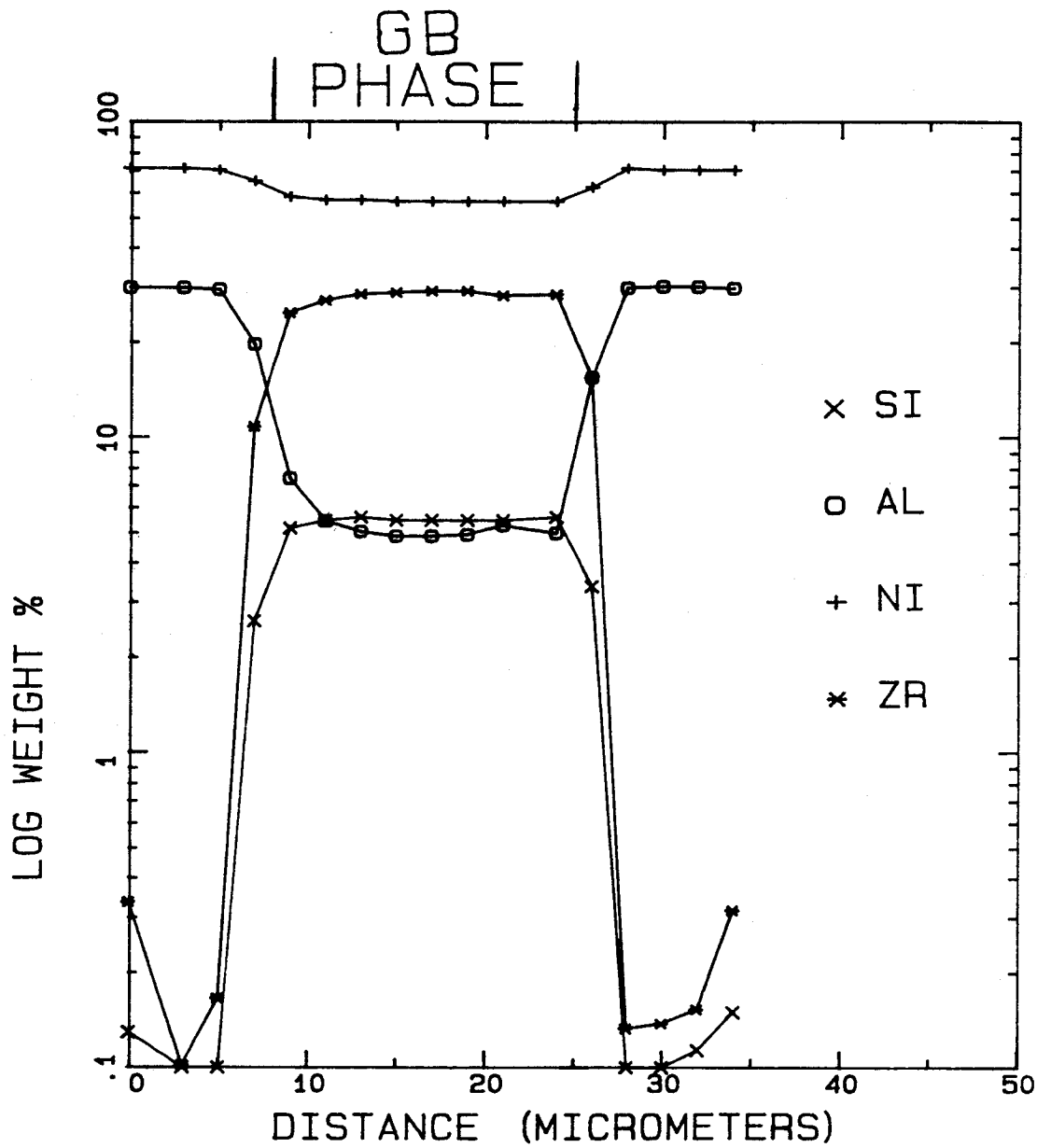

Figure 3

Electron microprobe analysis of the intermetallic phase in the cast β-NiAl alloy. The results are given by a log concentration versus distance plot. The distance indicated by "GB Phase" corresponds to the size of the intermasetallic phase traversed during the microprobe scan.
(Courtesy of Frank Terepka, NASA LRC)

slices. Polycrystalline specimens were obtained by spark machining buttons of the casting into slices. The grain size in button regions was approximately 0.5 to 1.0 mm.

All specimens were mechanically polished through 3 μm diamond. Most experiments required electropolished surfaces which were obtained by electropolishing in a 2:1 methanol: nitric acid solution at 12 V and 0°C. The final surface preparation of specimens involved ultrasonic cleaning in ethanol followed by a similar treatment in acetone.

Oxidation tests were performed in various furnaces at the NASA Lewis Research Center and at Case Western Reserve University. Specifics of isothermal weight gain experiments will be discussed in a later section.

Specimens suitable for TEM examination were prepared by backthinning the metal away to reveal the oxide scale and possibly thin metal around the hole. Backthinning was performed using a Struers Tenupol with a 2:1 methanol: nitric acid solution at 30 V and -20°C. Ion thinning of thick scales was performed as necessary using a Gatan Model 600 ion miller. Specimens were carbon coated prior to examination reduce charging effects in the microscopes.

Analytical electron microscopy was performed using a Philips EM400T analytical electron microscope at Case Western Reserve University. The microscope was equipped for scanning transmission electron microscopy(STEM), energy dispersive spectroscopy(EDS),

secondary electron microscopy(SEM), and backscattered electron microscopy(BSM); other available techniques such as electron energy loss spectroscopy(EELS) were not used for this study. Additional SEM was performed using a JEOL 7B at NASA Lewis Research Center and a JEOL 35CF at Case Western Reserve University.

Results and Discussion

I. Transient Oxidation Stage

Studies of the oxidation of β-NiAl and other alumina formers have revealed that, for ambient conditions, a transient stage of oxidation always exists.[6,7] During this stage, metastable Al_2O_3 phases comprise the majority of the oxide scale. The metastable Al_2O_3 phases are based on the spinel structure with the structural formula $(Al_{\{x/3\}}[\,]_{\{(1-x)/3\}})(Al_{\{y/3\}}[\,]_{\{(1-y)/3\}})_2O_4$, such that $(x+2y)=8$ to preserve stoichiometry. The remaining fraction of both tetrahedral and octahedral sites are occupied by vacancies, indicated by [ ]. Table II lists the known metastable Al_2O_3 phases with appropriate crystallographic information. Schematics of these structures are shown in Figure 4. Many metastable Al_2O_3 phases occur in nature as hydrated forms or can be obtained by calcination, sol-gel or other processing methods.[34] For thermal oxidation, the most common metastable polymorphs of Al_2O_3 are γ-Al_2O_3 and δ-Al_2O_3. γ-Al_2O_3 is a defective spinel with Al cations arranged randomly over 7/8 of the normally occupied octahedral and tetrahedral positions with the other sites vacant.[35] Other forms of γ-Al_2O_3 have been found involving

TABLE II

Structures of Al_2O_3 phases and transformation sequence to α-Al_2O_3.(Ref. 34).

Phase	Crystal System
γ-Al_2O_3	cubic(spinel)
↓	↓
δ-Al_2O_3	tetragonal
↓	↓
θ-Al_2O_3	monoclinic
↓	↓
α-Al_2O_3	rhombohedral

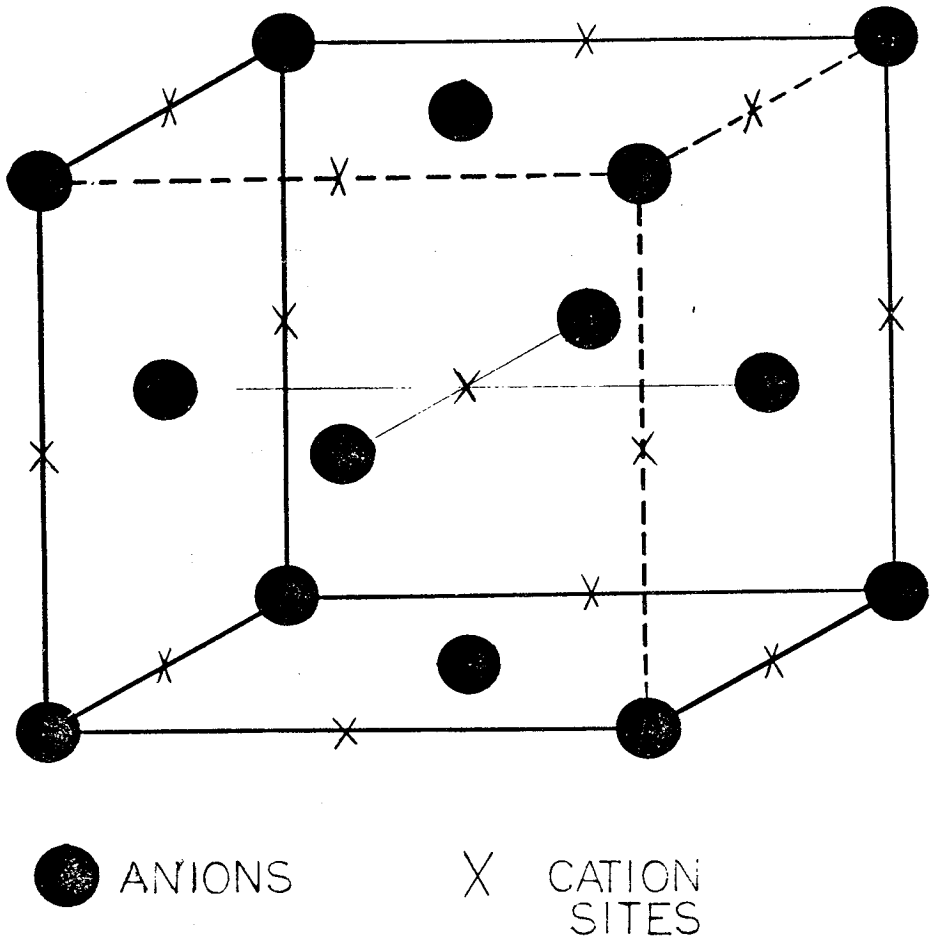

a)

Figure 4

Schematics of the structures of various Al_2O_3 phases; a) one-eighth the unit cell of γ-Al_2O_3 with tetrahedral and octahedral cation sites indicated, b) one-eighth the unit cell of δ-Al_2O_3 with possible cation sites indicated, c) θ-Al_2O_3 and d) α-Al_2O_3.

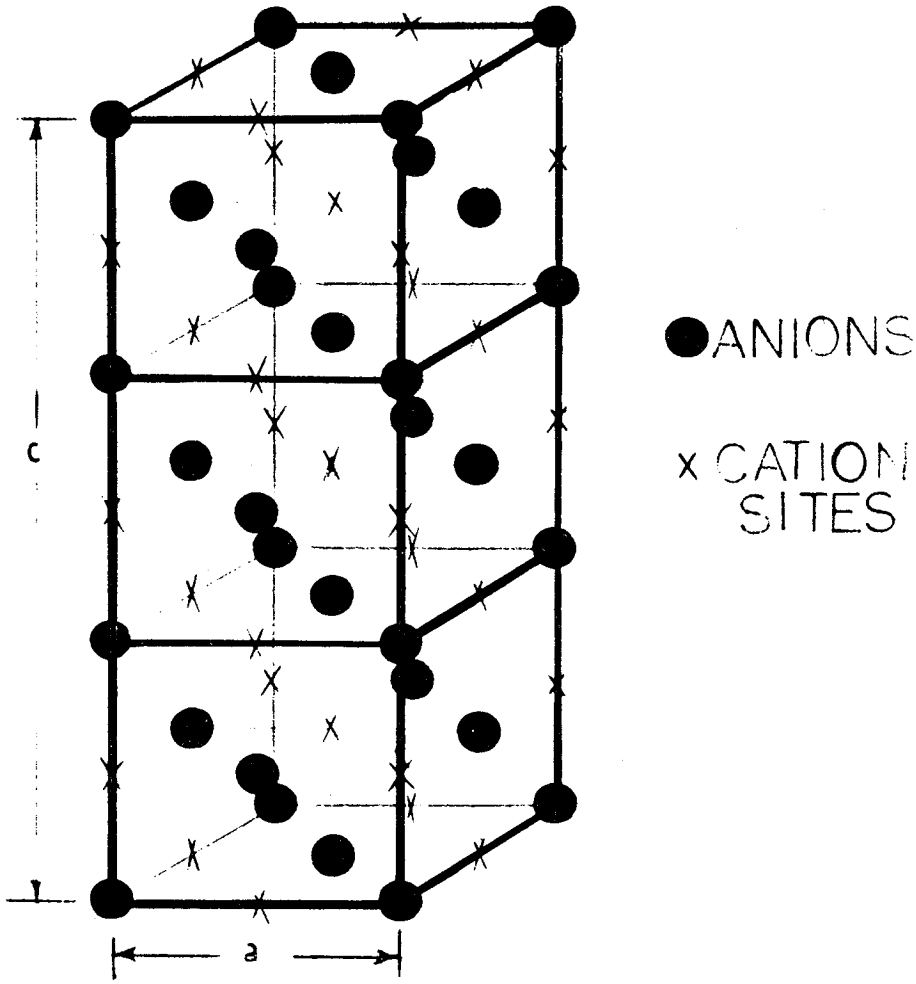

Figure 4b)

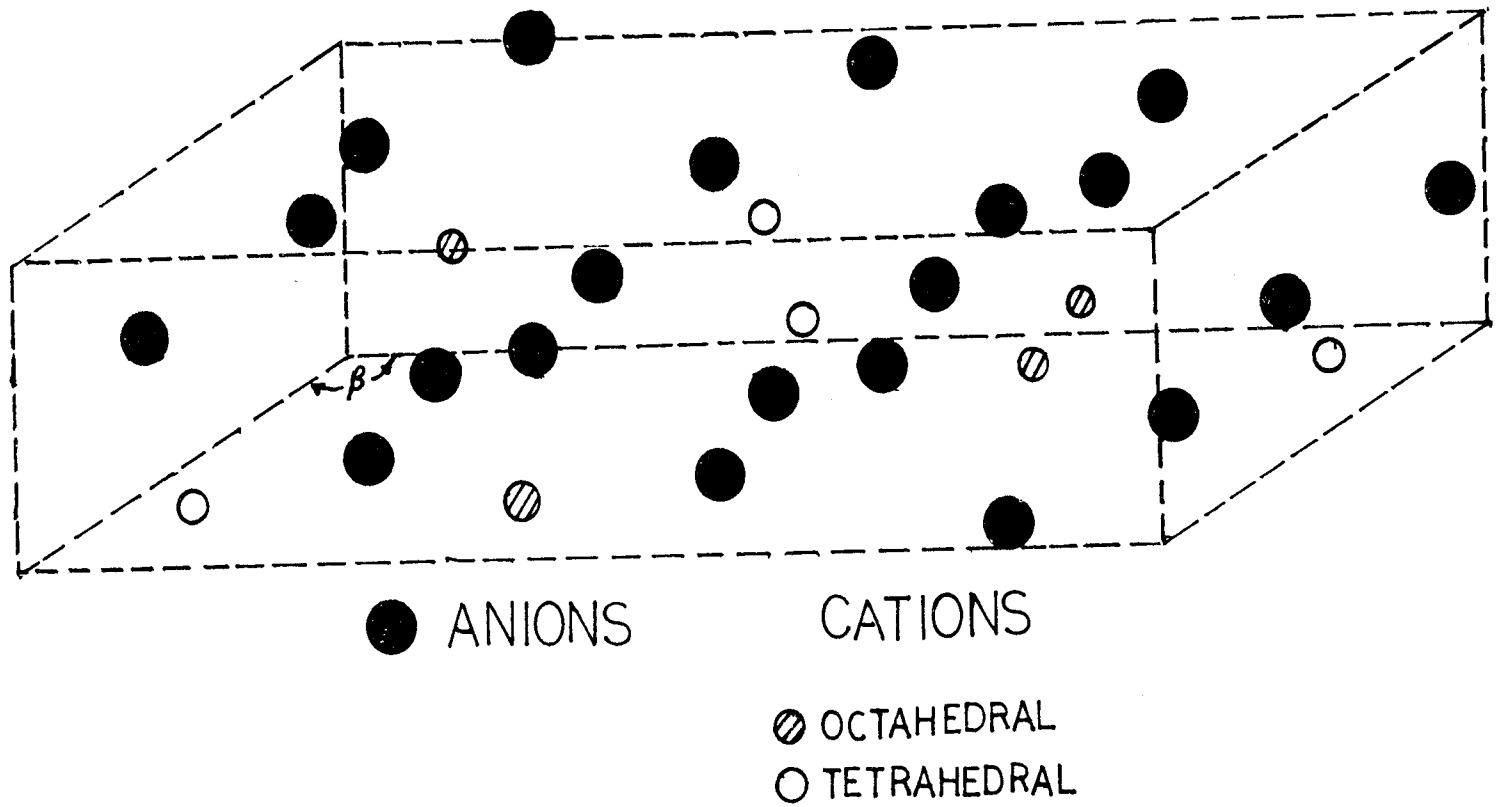

Figure 4c)

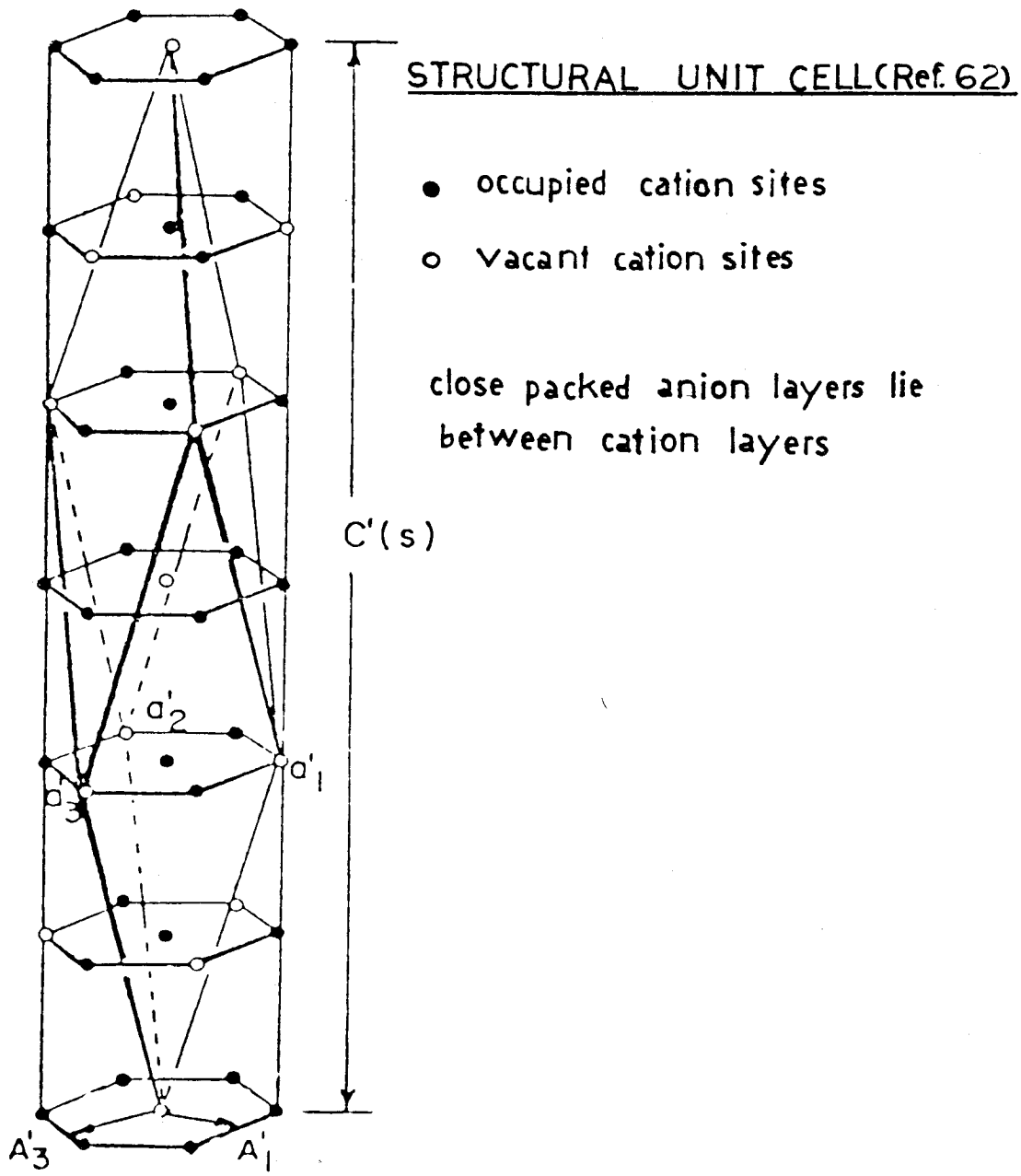
STRUCTURAL UNIT CELL(Ref. 62)
● occupied cation sites
o Vacant cation sites
close packed anion layers lie between cation layers
C'(s)
a'2
a'1
a'3
A'3
A'1

Figure 4d)

ordered arrangements of vacancies in the spinel lattice. δ-Al_2O_3 resembles γ-Al_2O_3 in the basic spinel structure but differs because of cation ordering and a tetragonal distortion with a periodicity of $3a_o$ with respect to the spinel lattice along the c-direction. Other polymorphs of Al_2O_3 occur during the sequence of transformation to α-Al_2O_3 involving further cation ordering and distortions of the anion sublattice, but have not been observed during thermal oxidation. The transformation to α-Al_2O_3 occurs at temperatures around 1000°C and involves a reconstruction of the anion sublattice from distorted FCC to HCP.[36]

A. Oxidation at 800°C

A precursor to the present work involved a study of the transient stages of oxidation using the same alloy, Zr-doped β-NiAl.[33] That study was designed to characterize the transient stages of oxidation with particular attention given to the oxide phases that form and the orientation relationships that exist between the metal substrate and the oxide. A brief summary of those results will be presented to put the present work in perspective.

All the results were obtained using oriented single crystal TEM specimens that had been electropolished, oxidized at 800°C for times less than 10 hours, backthinned and observed by TEM.

The only exception was a study on (001) single crystals that had been abraded with 600 grit paper and oxidized for 0.1 hours at 1100°C. Electron diffraction, microstructural and some qualitative EDS data were obtained.

Four orientations were chosen for the 800°C work; (001), (012), (011), and (111). $NiAl_2O_4$ was the initial oxide to form on (001) and (012) metal orientations followed by formation of metastable Al_2O_3 phases. The $NiAl_2O_4$ was identified by electron diffraction and also by higher Ni concentrations within the oxide layer. Diffuse intensity was observed in the diffraction pattern of a specimen oxidized for 0.1 hours and was ascribed to metastable Al_2O_3 formation. The metastable Al_2O_3 phase appeared to be a precursor of δ-Al_2O_3 containing some Ni in solid solution. For specimens oxidized 1.0 hours at 800°C, δ-Al_2O_3 became the predominant oxide phase although it did not appear to be completely ordered. After 10.0 hours, δ-Al_2O_3 was the main oxide phase with some remnants of $NiAl_2O_4$ still observed.

For the (001) metal orientation, the metal-oxide orientation relationship was found to be the classical Bain relationship:

$$(001)_m \;||\; (001)_{ox}$$
$$[100]_m \;||\; [110]_{ox}$$

and for the (012) metal orientation:

$$(012)_m \;||\; (112)_{ox}$$
$$[100]_m \;||\; [110]_{ox}$$

The fine grained oxides had a strong epitaxial relationship to the metal for these conditions. The existence of these orientation relationships is attributed to the small, approximately 3% mismatch along cation close-packed directions in the sublattices of the metal and oxide phases.

For (011) and (111) metal orientations, the results were not as straightforward. $NiAl_2O_4$ was again the first oxide to form, but the kinetics for metastable Al_2O_3 formation were slower. Also with increasing oxidation time, γ-Al_2O_3 rather than δ-Al_2O_3 became the primary oxide phase. This is attributed to the resistance of these particular metal orientations to accomodate the tetragonal structure of δ-Al_2O_3 in the orientation relationships that were present. For the (011) metal orientation, three orientation relationships were observed on specimens oxidized for 0.1 hours at 800°C. These are the Nishyama-Wassermann relationship:

$$(011)_m \;||\; (\bar{1}11)_{ox}$$
$$[100]_m \;||\; [110]_{ox}$$

the Kurdjumov-Sachs relationship:

$$(011)_m \;||\; (\bar{1}11)_{ox}$$

$$[11\bar{1}]_m \;||\; [011]_{ox}$$

and a third relationship:

$$(011)_m \;||\; (\bar{1}11)_{ox}$$
$$[21\bar{1}]_m \;||\; [01\bar{1}]_{ox}$$

These orientation relationships were observed when $NiAl_2O_4$ was a major part of the scale. When γ-Al_2O_3 was the major phase(after 1.0 hours of oxidation), only the Nishyama-Wassermann relationship persisted. For (111) metal orientations, three variants of the following relationship were observed:

$$(111)_m \;||\; \text{near } (021)_{ox}$$
$$[1\bar{1}0]_m \;||\; [100]_{ox}$$

Again, the fine grained oxide had a strong epitaxial relationship to the metal as in the case of the previous two metal orientations.

Simplified computer modeling was performed to qualify the orientation relationships that were observed in terms of optimum atomic matching at the metal-oxide interface. However, the method used appeared to be too simplistic to draw reliable conclusions. An attempt was made to discuss the as yet unknown detailed

structure of δ-Al_2O_3 involving unit cell dimensions and cation vacancy ordering. This discussion was based on the information available in the diffraction patterns of the polycrystalline scale. The fine structure that accompanied almost every observed diffraction pattern was considered to result from incomplete cation ordering, multiple variants and possibly microtwinning.

As mentioned, one segment of the work also involved the oxide scale that formed on a (001) single crystal abraded with 600 grit paper and oxidized for 0.1 hours at 1100°C. As in the lower temperature studies, δ-Al_2O_3 was observed to be the main oxide phase with the Bain orientation relationship existing between the metal and oxide. The oxide morphology was markedly different however. Instead of a fine, equiaxed microstructure, the scale contained plates of oxide. Also, a texture of thicker oxide was observed corresponding to scratches in the metal.

The study just summarized only dealt with a very limited region of the overall transient stage of oxidation on β-NiAl. The transient stage exists for longer times and at higher temperatures as indicated by the results on specimens oxidized at 1100°C for 0.1 hours in which the oxide still had not transformed to the thermodynamically stable α-Al_2O_3 phase. A more complete characterization of the transient regime requires a treatment of oxide phase development, growth rates,mechanisms of scale growth and scale microstructures and morphologies. The remainder of this first chapter will be devoted to filling in as many gaps as

possible related to the transient stages of oxidation.

1. Oxidation for times of 10.0 hours or less

Following completion of the previous study, additional TEM work was performed on the same specimens to resolve dilemmas involving identification and description of oxide phases that formed on β-NiAl specimens oxidized at 800°C for times up to 10.0 hours. The main questions arose from the tremendous amount of detail within each selected area electron diffraction pattern(SADP) of the oxide scale. Much of the detail in the patterns was attributed to multivariants or incompletely ordered oxide phases such as δ-Al_2O_3. Certain characteristics regarding the tetragonality and cation ordering are common, but have not been explained well enough to account for all the features obtained in the diffraction patterns. Besides superlattice reflections, streaking, extra reflections and fine structure have been observed. Additional work involved microdiffraction and more detailed analysis of the results already presented.

An SADP from a (001) specimen oxidized for 1.0 hours at 800°C is shown in Figure 5. This pattern, taken in the prior study, contains additional information not mentioned previously. Besides superlattice reflections at 1/3(400) spinel spacings(specifically, the spinel spacings of γ-Al_2O_3) indicating the presence of

ORIGINAL PAGE IS
OF POOR QUALITY

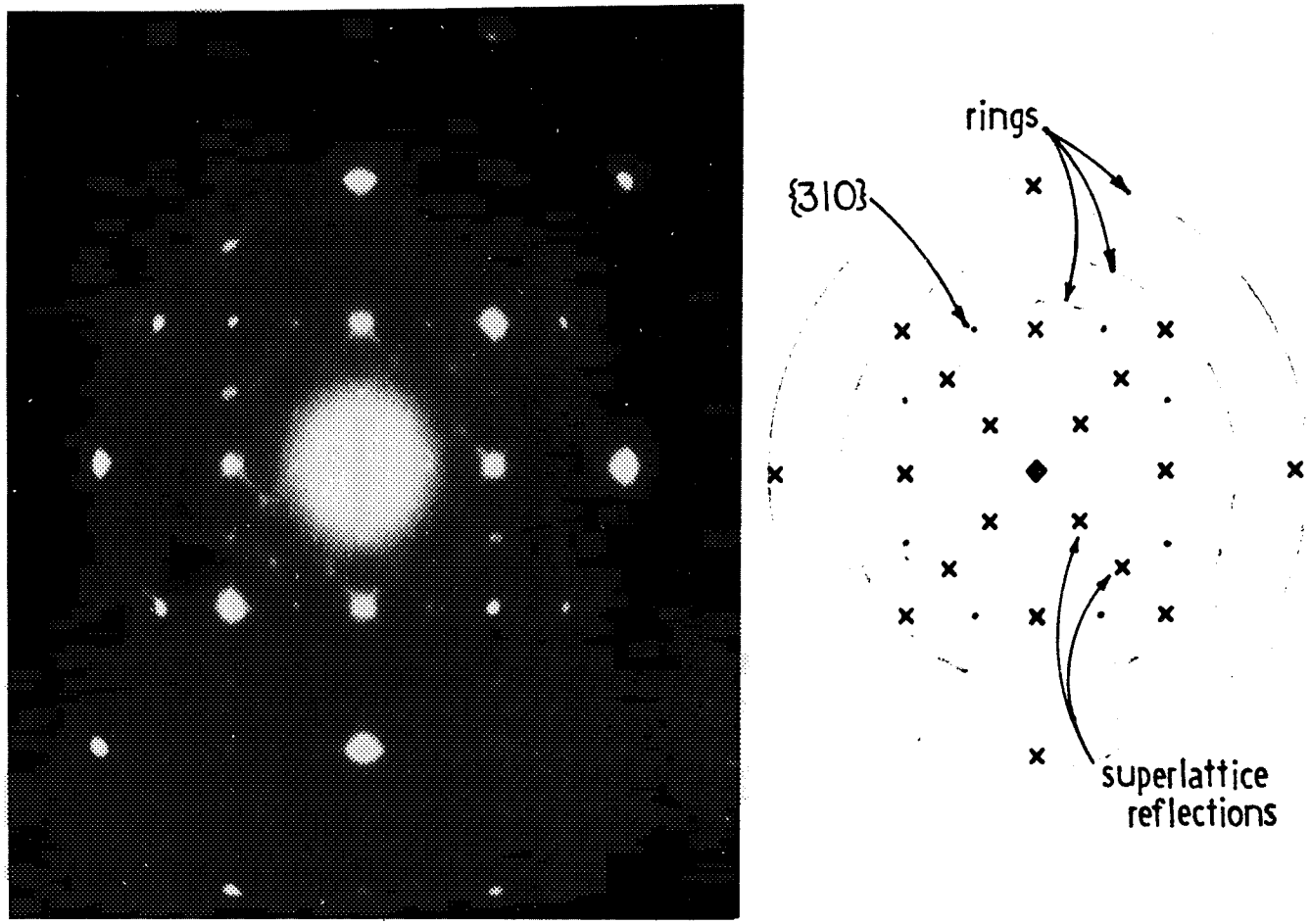

Figure 5

Selected area diffraction pattern of an oxide scale formed on an (001) β-NiAl specimen oxidized for 1.0 hours at 800°C. Superlattice reflections corresponding to δ-Al_2O_3 and faint rings are indicated.

δ-Al_2O_3, additional reflections and streaks are observed. To study the additional information, this same specimen was ion-thinned from the side in contact with the atmosphere during oxidation and observed in the microscope. A diffraction pattern of an <001> zone is shown in Figure 6.

A number of changes in the two patterns can be seen. The faint rings which for example give rise to the double reflections at (310) spinel positions in Figure 5 are no longer observable in Figure 6. This indicates that all impurity oxides that formed during initial oxidation and were present on the oxide scale must have been sputtered away during the ion-thinning process. The impurity oxides consisted of Fe and Cr containing spinels or other cubic oxides. These impurity oxides must have been present in a layer near the gas-oxide interface agreeing with what was previously assumed.

There is a great deal more streaking observable in Figure 6 than in Figure 5. Both patterns contain streaking along $\langle 100 \rangle_\gamma$ with the streaking being most intense near the $\{220\}_\gamma$ reflections. To explain this phenomenon, another SADP from an (001) specimen oxidized for 10.0 hours at 800°C is shown in Figure 7 with the analysis of the diffraction pattern being the same as in Figure 6. The streaking along $\langle 100 \rangle_\gamma$ can be attributed to relplane intersections with the Ewald sphere because streaking along $\langle 001 \rangle_\gamma$ directions is observed for all orientations. The relplanes result from streaking perpendicular to faults on $\{100\}_\gamma$ planes shown in

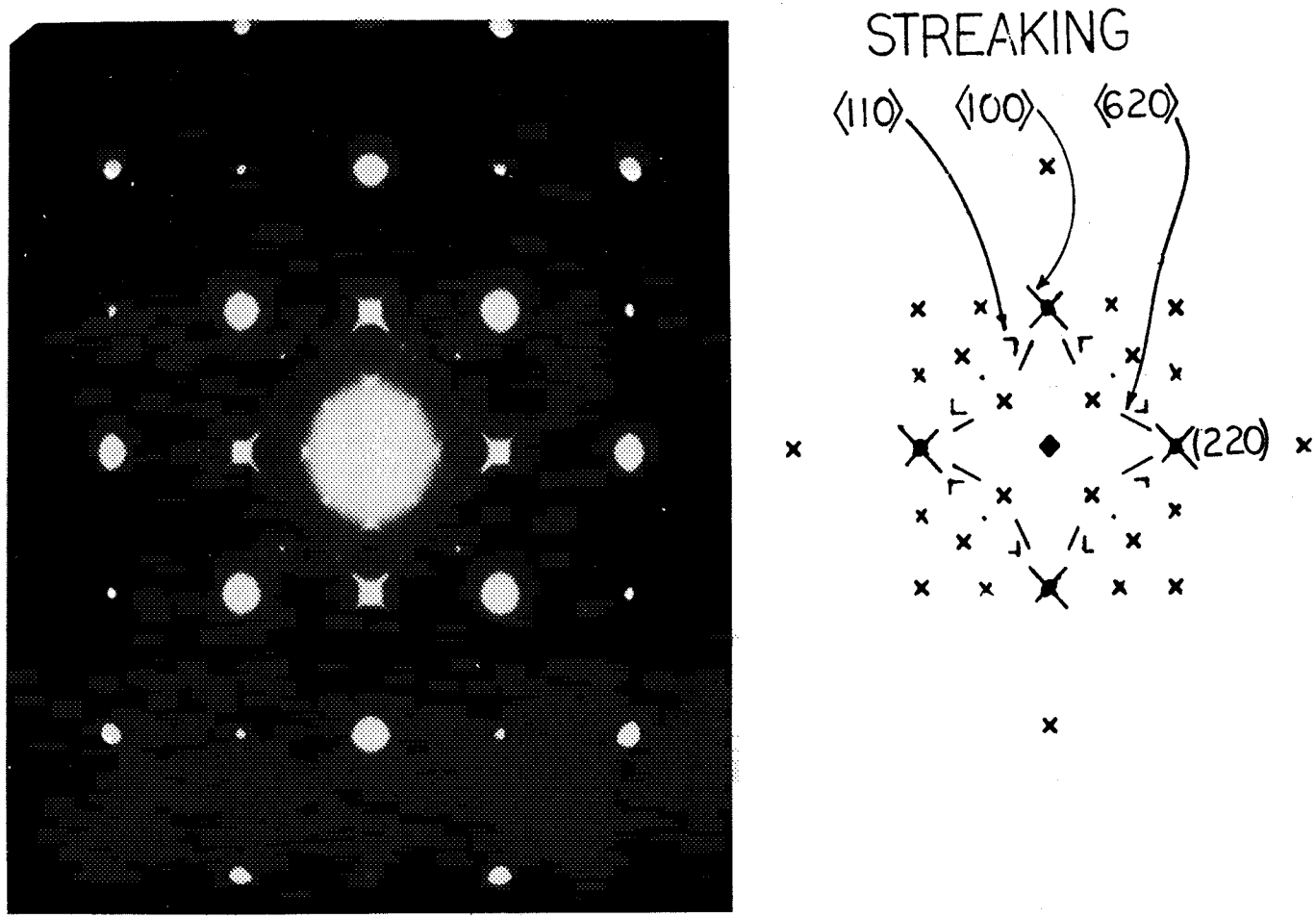

Figure 6

Selected area diffraction pattern from the same specimen as in Figure 5 after being ion-thinned from the gas-oxide surface. Intense perpendicular streaking is observed at $\{220\}_\gamma$ reflections. Streaking along $\langle 620\rangle_\gamma$ and $\langle 110\rangle_\gamma$ directions is indicated. Many variants contribute to this pattern.

ORIGINAL PAGE IS
OF POOR QUALITY

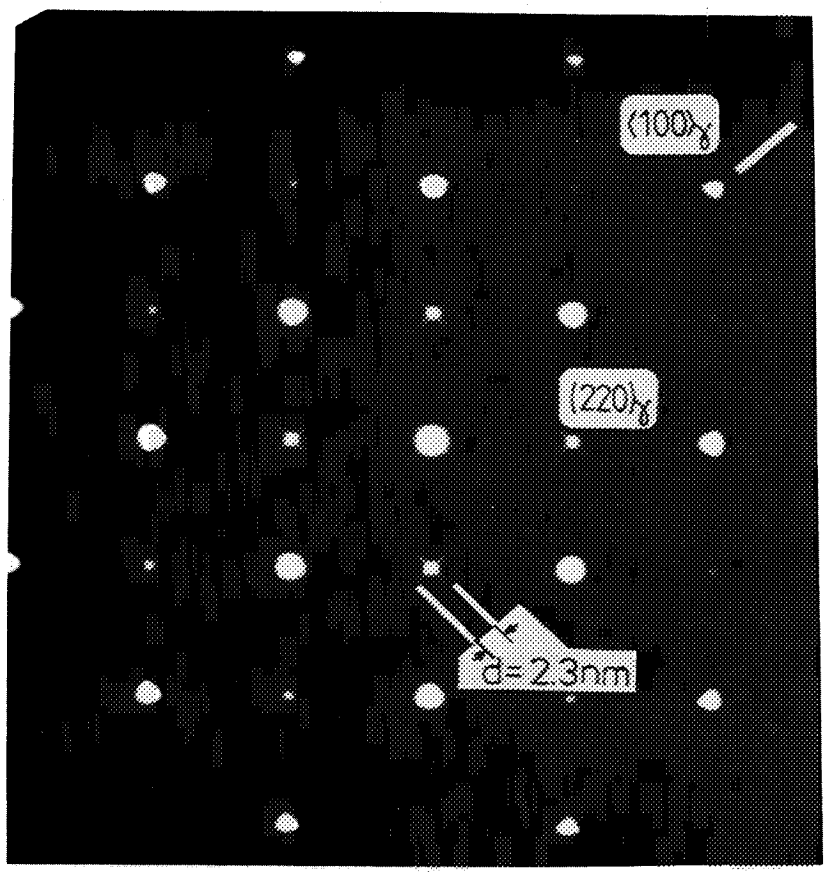

Figure 7

Selected area diffraction pattern of a δ-Al_2O_3 scale formed on an (001) β-NiAl specimen oxidized for 10.0 hours at 800°C. Maxima are observed to have formed in the <100>γ streaking at {220}γ reflections. The spacing of these maxima is approximately 2.3 nm which is the c_o spacing of δ-Al_2O_3.

the DF image of Figure 8. This image was taken using a large objective aperture surrounding the intense <100>γ streaking through the (220)γ reflection in Figure 6. The very fine fringes having a spacing less than 1 nm are possibly Moire fringes resulting from overlapping regions having slight misorientations and differences in d-spacings. The <100>γ streaking is diffuse because the spacing between faults is not constant, varying between approximately 1 and 3.5 nm. In Figure 7, the streaks near the (220)γ reflection have developed maxima to become individual reflections along <100>γ directions. The spacings of these reflections are 2.3 nm which is approximately the c_o spacing in δ-Al_2O_3. Dauger and Fargeot attribute these extra relfections to 1/4<110>{100}γ antiphase boundaries in the cation sublattice(Figure 9).[37] This vector translation does not effect the anion sublattice. Dauger and Fargeot also mention that periodic stacking of these APB's could give rise to the various structures of the metastable Al_2O_3 phases. By ordering of this nature, vacancies within the cation sublattice are arranged into one-dimensional arrays along <100>γ directions.

The increased intensity of APB reflections near {220}γ reflections corresponds with the increased contribution of scattering from cations in tetrahedral sites. The argument is confirmed by structure factor calculations.[38] The general structure factor formula is given as:

ORIGINAL PAGE IS
OF POOR QUALITY

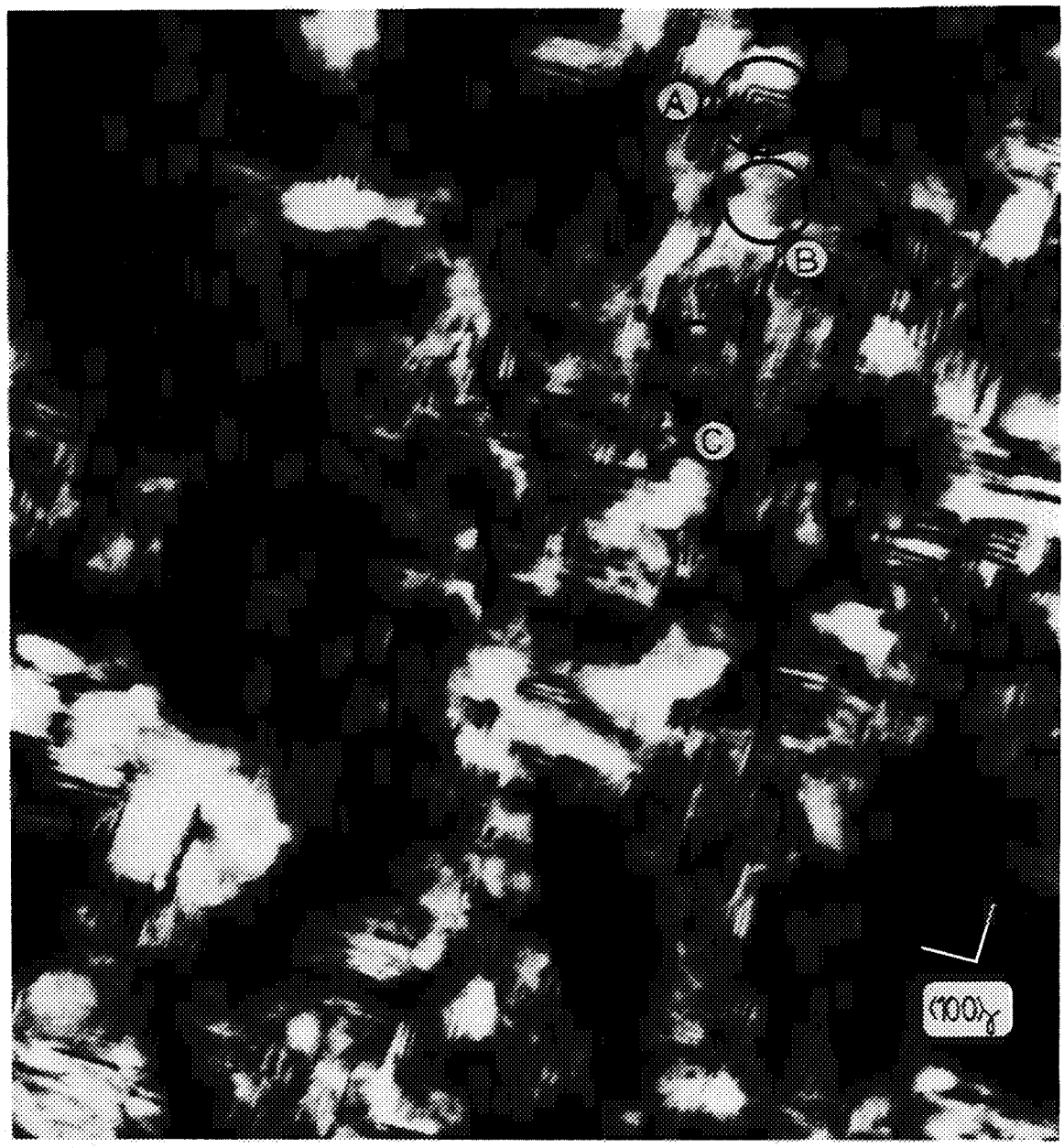

Figure 8

10 nm

Dark field image of a region of an ion-thinned δ-Al_2O_3 scale formed on an (001) β-NiAl specimen oxidized for 1.0 hours at 800°C. $\langle 100 \rangle_\gamma$ planar faults(A), fine fringes along $\langle 620 \rangle_\gamma$(B) and fringes along $\langle 110 \rangle_\gamma$(C) are indicated.

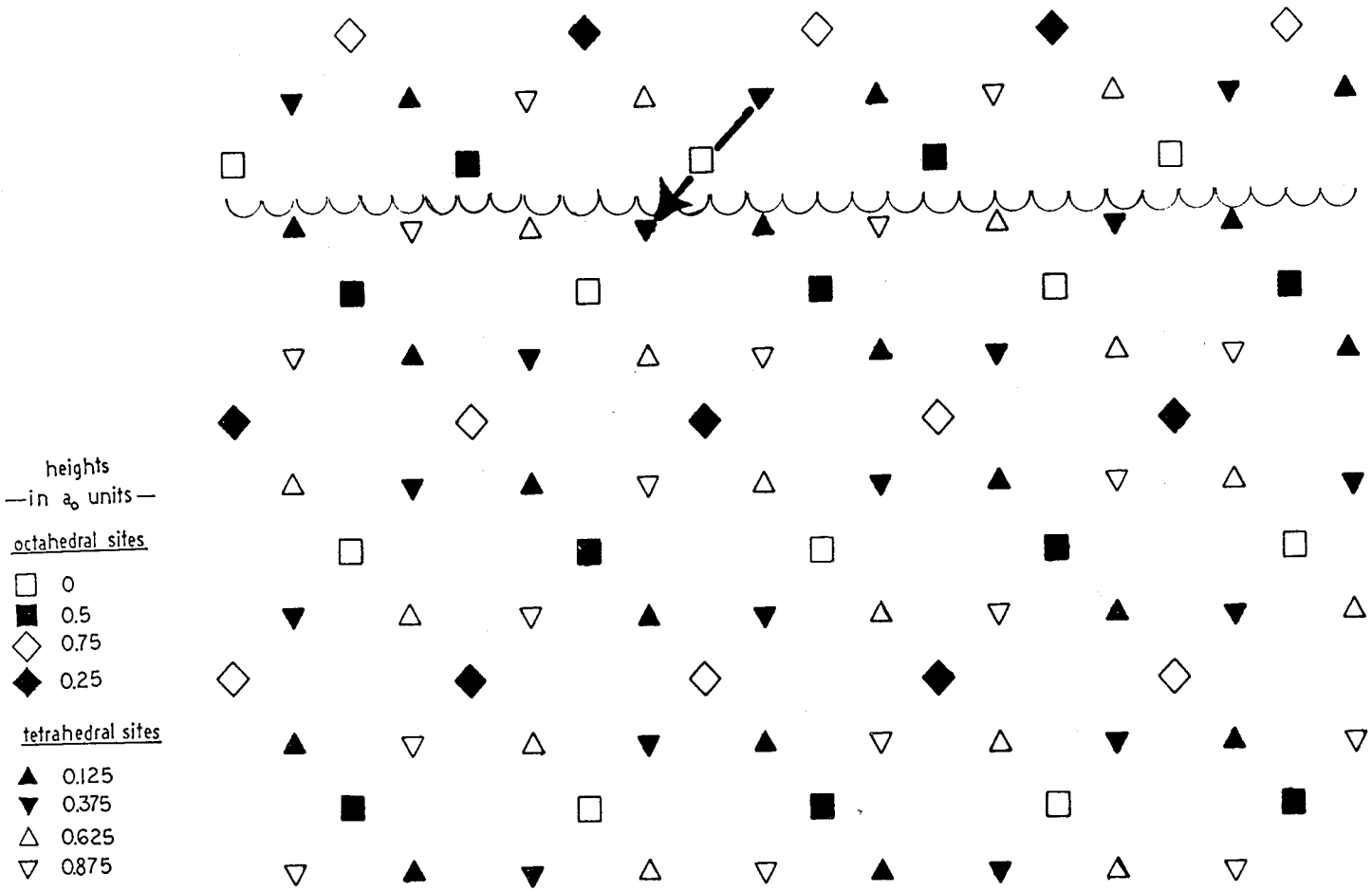

Figure 9

Schematic of 1/4{100}<110> anti-phase boundary formation in the γ-Al_2O_3 crystal structure. The various symbols represent different cation sites on {001} planes. The 1/4<110> displacement vector is indicated.(Ref. 37).

$$F_g = \Sigma_j\ f_j(\sin\theta/\lambda)\exp[2\pi i(g\cdot r_j)] \qquad [1]$$

$$= \Sigma_j\ (f_a)_j\cdot\exp[2\pi i(hx + ky + lz)]$$

where $(f_a)_j$ = atomic scattering factor for atom j

h,k,l = indices of reflecting plane

x,y,z = atomic coordinates of atom j in the unit cell.

For a spinel lattice, such as γ-Al_2O_3 phase, the structure factor for a (220) reflection simplifies to:

$$F_{(220)} = \Sigma_j\ (f_a)_j\cdot\exp[4\pi i(x + y)] \qquad [2]$$

For an ideal structure, the 32 oxygen atoms are at positions:

x	y	z
0	0	0
0.5	0	0
0.25	0.25	0
0.75	0.25	0
0	0.5	0
0.5	0.5	0
0.25	0.75	0
0.75	0.75	0
0.25	0	0.25
0.75	0	0.25
0	0.25	0.25
0.5	0.25	0.25
0.25	0.5	0.25
0.75	0.5	0.25
0	0.75	0.25
0.5	0.75	0.25

(continued)

x	y	z
0	0	0.5
0.5	0	0.5
0.25	0.25	0.5
0.75	0.25	0.5
0	0.5	0.5
0.5	0.5	0.5
0.25	0.75	0.5
0.75	0.75	0.5
0.25	0	0.75
0.75	0	0.75
0	0.25	0.75
0.5	0.25	0.75
0.25	0.5	0.75
0.75	0.5	0.75
0	0.75	0.75
0.5	0.75	0.75

The sum of the structure factors for atoms in these positions will yield a result of zero for the contribution of oxygen atoms to the $(220)_\gamma$ reflection. The occupancy of aluminum atoms in octahedral positions would also yield a zero contribution to the $(220)_\gamma$ structure factor providing all 16 positions are filled for a spinel lattice. These positions are given as:

x	y	z
0	0.75	0
0.75	0.5	0
0.5	0.25	0
0.25	0	0
0.25	0.75	0.25
0.5	0.5	0.25
0.75	0.25	0.25
0	0	0.25
0.5	0.75	0.5
0.25	0.5	0.5
0	0.25	0.5
0.75	0	0.5
0.75	0.75	0.75
0	0.5	0.75
0.25	0.25	0.75
0.5	0	0.75

An ideal spinel structure would contain 8 tetrahedral aluminum cations in positions:

x	y	z
0.625	0.875	0.125
0.125	0.375	0.125
0.875	0.625	0.375
0.375	0.125	0.375
0.125	0.875	0.625
0.625	0.375	0.625
0.375	0.625	0.875
0.875	0.125	0.875

The tetrahedral aluminum cations would contribute to the structure factor as:

$$F_{(220)} = \Sigma\ f_{Al}(\exp[4\pi i(x + y)] \qquad [3]$$

$$= 8f_{Al}$$

However, γ-Al_2O_3 is a defective spinel in which $21^2/_3$ aluminum atoms are arranged randomly over all octahedral and tetrahedral positions. Therefore, the non-zero structure factor of a $(220)_\gamma$ reflection for this system is solely due to cation scattering. Ordering of vacancies could effect the contributions from both the octahedral and tetrahedral sublattices. Smialek has observed anti-phase boundaries in transient alumina scales formed on NiCrAl alloys oxidized at 1100°C.[30] The APB's were imaged in dark field

using either a $(311)_\gamma$ or $(111)_\gamma$ reflection. When the structure factor is calculated for these reflections, similar results are obtained as for the $(220)_\gamma$ structure factor; that is, the non-zero terms arise solely from cation scattering. If the cations were absent, the unit cell of the resulting anion lattice would be 1/2 that of the spinel structure along the cube directions.

Also in Figure 6, extra reflections are observed at $1/4\{110\}_\gamma$ and $1/6\{620\}_\gamma$ positions. The reflections occur along all the $\langle 110\rangle_\gamma$ and $\langle 620\rangle_\gamma$ directions in this zone because of many variants which contribute to the selected area diffraction pattern. A microdiffraction pattern of one variant in a small region, approximately 10 nm in size, is shown in Figure 10.
The extra reflections at $1/4(110)_\gamma$ and $1/6(620)_\gamma$ are easily observed. Superlattice reflections indicative of δ-Al_2O_3 are also observed. Therefore, if this oxide phase is δ-Al_2O_3, the zone axis would be either $[100]_\delta$ or $[010]_\delta$ because the c-direction is perpendicular to the zone axis. However, the microdiffraction pattern in Figure 11 shows how an expected $[100]_\delta$ or $[010]_\delta$ zone would look. This pattern was taken from a region adjacent to the area giving rise to Figure 10. In Figure 11, the zone axis is again $[100]_\delta$ or $[010]_\delta$ but no extra reflections are observed at $1/4(110)_\gamma$ or $1/6(620)_\gamma$ spacings. The two microdiffraction patterns in Figure 10 and Figure 11 obviously do not come from the same crystal structure.

The extra reflections in Figure 10 might be indicative of a

ORIGINAL PAGE IS
OF POOR QUALITY

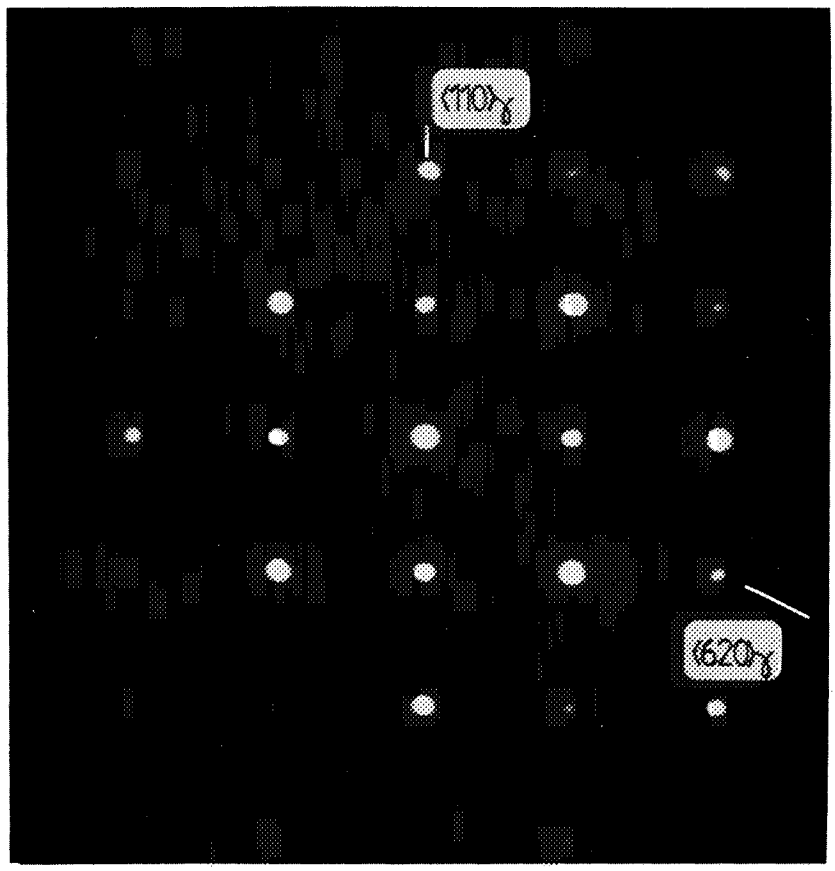

Figure 10

Microdiffraction pattern for the same specimen as in Figure 6. Extra reflections are indicated at $1/4(110)_\gamma$ and $1/6(620)_\gamma$ spacings.

ORIGINAL PAGE IS
OF POOR QUALITY

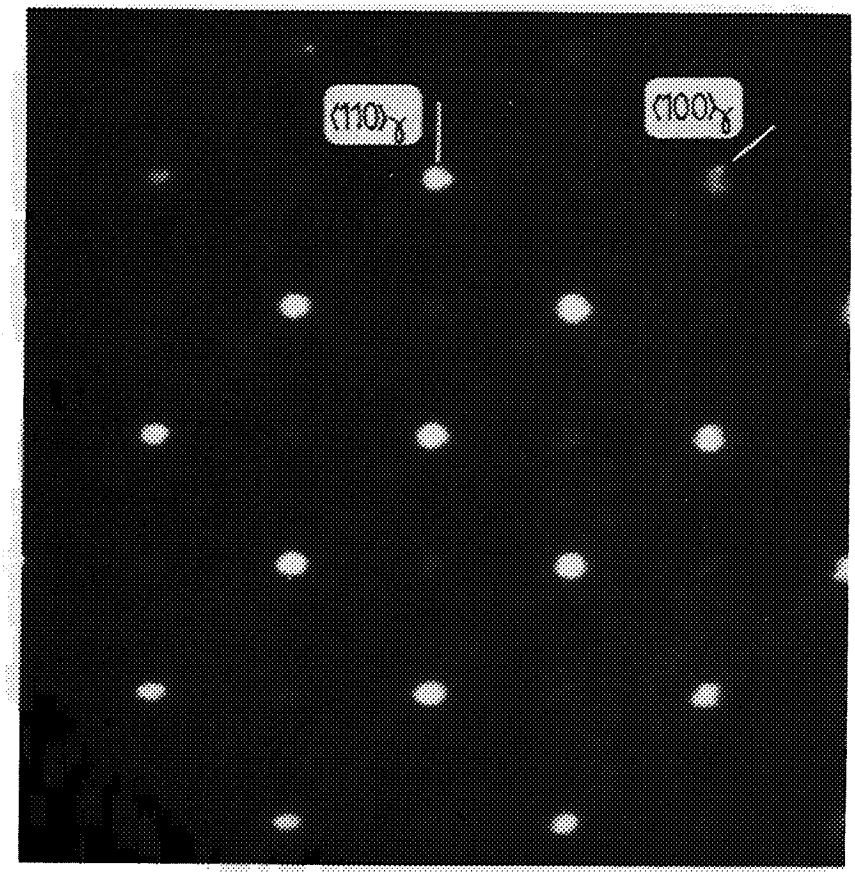

Figure 11

Microdiffraction pattern taken from a δ-Al_2O_3 region adjacent to the region of Figure 10. The extra reflections are absent in this pattern.

new and different phase. This phase would be similar to the tetragonal δ-Al_2O_3 phase but, according to the diffraction pattern, could have orthorhombic symmetry. This phase exists simultaneously with δ-Al_2O_3 and might be an intermediate phase found only at short times and lower temperatures, probably in between γ-Al_2O_3 and δ-Al_2O_3 in the transformation sequence. However, an orthorhombic structure has less symmetry than a tetragonal structure. The transformation sequence in Table II would then be violated because the symmetry of the crystallographic structures of the transition phases generally decreases with increasing time and temperature prior to formation of α-Al_2O_3.

An alternative explanation involves the argument by Dauger and Fargeot for APB formation with regard to ordering of structural vacancies in the spinel lattice giving rise to the extra reflections. APB's were described to arise from translations similar to crystallographic shears within the spinel lattice on {100} planes having a displacement vector equal to 1/4[110], (Figure 9). In a perfect spinel structure, the cations are arranged in a specific manner on the octahedral and tetrahedral sites. A translation with a displacement vector mentioned above for an ordered cation lattice would give rise to faults on {100} planes as shown in Figure 9. Periodic arrangements of these fault planes form a new superstructure giving rise to the extra reflections at $1/4\{110\}_\gamma$ and $1/6\{620\}_\gamma$

spacings. The periodicity of these faults must be equal to 4X the interplanar spacing along the $[110]_\gamma$ direction and 6X the interplanar spacing along the $[620]_\gamma$ direction. With a perfectly ordered cation sublattice, these faults become part of the δ-Al_2O_3 structure as in Figure 11. Experimental evidence needed to prove this suggestion requires that the faulted planes be observed with the given periodicity. This evidence might be provided in Figure 8 by the fine fringes mentioned earlier. The fringes were attributed to Moire effects because of the various spacings and directions. However, the majority of observable fringes are clustered and have a direction approximately 18.5° from $\langle 100 \rangle_\gamma$. These fringes would correspond to the streaking that is observed along the $\langle 620 \rangle_\gamma$ directions. Features from the streaks are included in the dark field image because the 20 micron objective aperture used to take this image encompasses the streaking, as well. However, the spacing of the fringes is consistently 0.59 nm which does not correspond to the 0.756 nm d-spacing of the extra reflections in Figure 10.

If the microdiffraction patterns of Figures 10 and 11 are compared, the {220} reflections do not have the same intensity. This corresponds to a difference in the distribution of cation occupation on tetrahedral and octahedral sites using the structure factor argument as before. The higher the occupation of tetrahedral sites by cations, the more intense would be the {220} reflections. Therefore, the structure giving rise to the

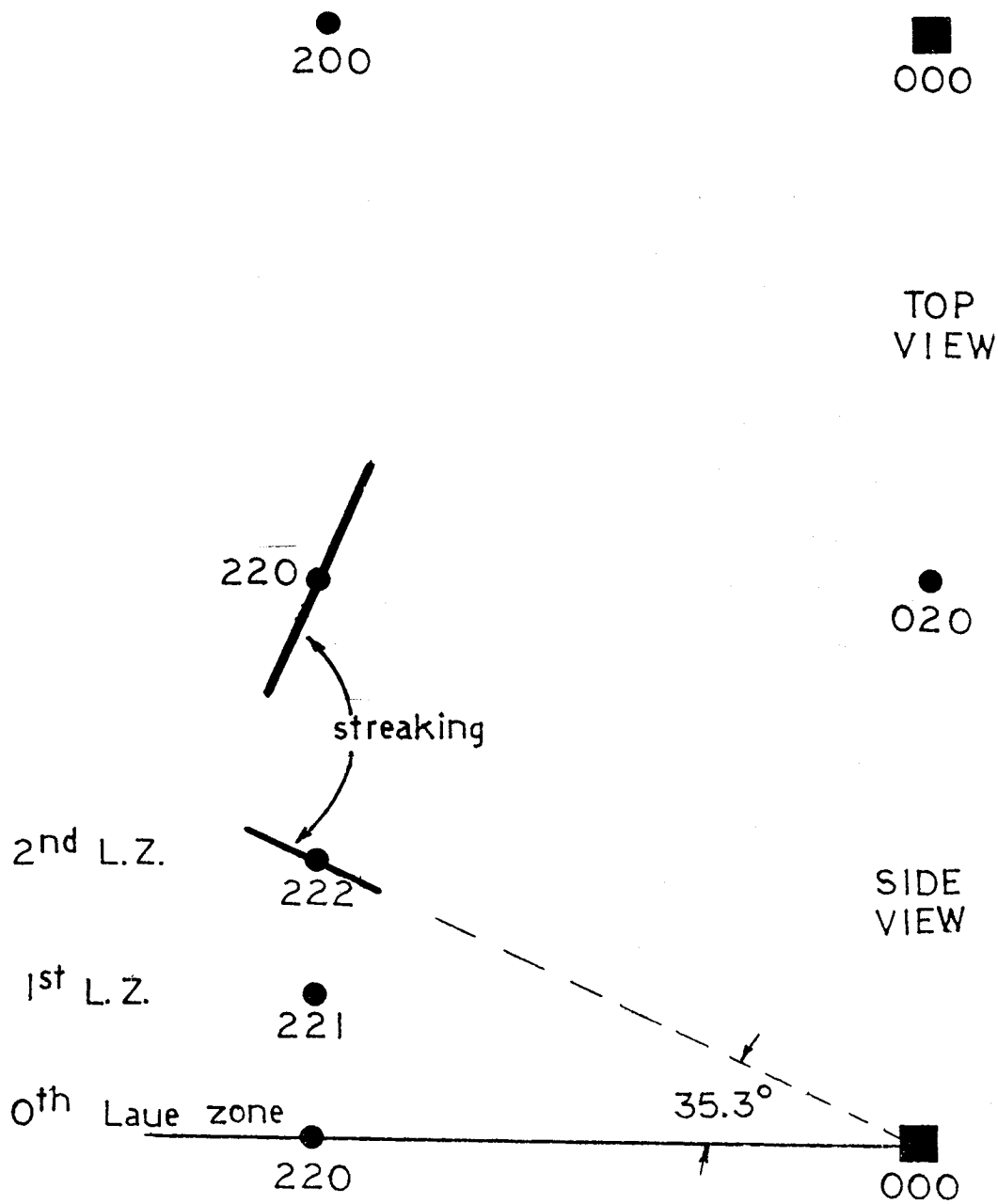

Figure 12

Schematic of a possible mechanism for streaking along $\langle 100 \rangle_\gamma$ directions observed at $\{220\}_\gamma$ reflections.

diffraction pattern in Figure 11 is less ordered than the δ-Al_2O_3 structure and has a lower cation occupancy on the tetrahedral sites. The occupation of tetrahedral sites should continue to increase until, in the θ-Al_2O_3 structure, equal numbers of cations are on both the octahedral and tetrahedral sites as mentioned by Geller.[39] Another feature in Figures 10 and 11 indicating that the phase is not the well-ordered δ-Al_2O_3 phase is the equal spacing of perpendicular $(0{\cdot}0{\cdot}12)_\gamma$ and $(400)_\gamma$ reflections in the diffraction patterns. The c-direction should be slightly longer than the a-direction in the diffraction pattern of a [010] or [100] zone if this were truly the tetragonal δ-Al_2O_3 structure. The phases present after an oxidation time of 1.0 hours are still very similar to γ-Al_2O_3 from which the later metastable Al_2O_3 phases are derived.

Additional information in Figure 6 includes streaking along both $\langle 620 \rangle\gamma$ and $\langle 110 \rangle\gamma$ directions. The streaking along $\langle 620 \rangle\gamma$ appears to emanate from $\{220\}\gamma$ reflections. However, the streaks do not intersect the Ewald sphere at $\{220\}\gamma$ reflections. Therefore, the streaking must be from reciprocal lattice points in higher or lower order Laue zones above or beneath the $\{220\}\gamma$ reflections. A schematic of this phenomenon in Figure 12 shows the streaking going through a reflection in a higher order Laue zone above the $(220)\gamma$ reflections. The difficulties in assuming the streaking occurs as shown in Figure 12 are that the streaks do not intersect the Ewald sphere at a point but rather along a line.

This indicates that the streaks are relrods at a very small angle of inclination from the {100} plane of the diffraction pattern or that the streaks are ribbons of intensity. If the streaks are relrods, they result from planar defects perpendicular to planes having reflections above or below the $\{220\}_\gamma$ reflections; i.e. $(221)_\gamma$, $(222)_\gamma$, $(223)_\gamma$, etc. However, the angle between the $(222)_\gamma$ reflection from the second order Laue zone and the $(220)_\gamma$ reflection from the zero order Laue zone is 35.3°. This angle is much too large to result in intersection of a relrod and the Ewald sphere at a point. The only other situation if the streaks are relrods would be for the relrods to intersect satellite reflections immediately above or below the $\{220\}_\gamma$ reflections. There is no physical basis for this, however. If the streaks are ribbons of intensity, they may arise from finite planar defects such as long platelets or planar boundaries. If streaking was on $\{222\}_\gamma$ planes, no meaningful crystallographic fault would produce projections of perpendicular streaks along $\langle 620\rangle_\gamma$ directions on $(001)_\gamma$ planes, as in Figure 6. If streaking was on $\{224\}_\gamma$ planes, the $\langle 620\rangle_\gamma$ projections could arise from $\langle 622\rangle_\gamma$ streaking which would seem more probable.

This section was intended to provide some insight into the crystallographic structure of the oxide phases present during the inital 10 hours of oxidation at $800^\circ C$. The main oxide phase that was observed, δ-Al_2O_3, can be described as having a spinel-like structure similar to γ-Al_2O_3. Antiphase domains of faulted

crystal occur along with non-faulted regions. The faults can be described as 1/4<110>{100} in terms of spinel dimensions, having an eventual periodicity of $3a_o$. The domains form in all crystallographic variants. Subgrains form within scales, but have strong epitaxial relationships to the underlying β-NiAl substrates.

2. Oxidation for times greater than 10.0 hours

The oxide scale had not transformed into α-Al_2O_3 even after 10.0 hours of oxidation at 800°C in agreement with the previous study. A complete characterization of the transient stage of oxidation on β-NiAl requires that conditions of longer oxidation times and higher temperatures be studied. Therefore, oxidation times up to 100 hours at 800°C were employed to further characterize the transient stage. Both thermogravimetric data to determine growth rates and electron microscopy data of diffraction and microstructures will be presented.

a. Growth rates. An essential part of understanding oxide scales is to measure quantitatively the kinetics of scale formation and growth. This information will help to determine diffusion mechanisms providing certain growth laws can be applied. The Wagner theory of oxidation (Appendix A) is utilized to

interpret parabolic growth rate constants and activation energies for diffusion. The constants can be obtained using thermogravimetric data (weight gain per unit area of exposed specimen) or scale thickness measurements.

The raw data in thermogravimetric weight gain experiments consist of actual weight measured by a highly sensitive microbalance with a sensitivity of 1 μg. The actual weight is plotted continuously on a strip chart recorder. The actual weight is also stored by a computer at chosen regular intervals. In this study, the actual weights were sampled every minute and the average of each 6 minute interval stored with a time and temperature reading. The system is described in Appendix B.

Every plot of actual weight change versus time contains not only the actual weight gain due to oxygen uptake during oxidation, but other factors as well. A correction must be made for platinum loss due to sublimation of the weighing chain. This correction can be determined apart from weight gain experiments and is applied as a constant change in weight per unit time. Another correction must be made for buoyancy of the specimen and can be determined in a number of ways. The buoyancy correction is applied as a constant measured weight between the entire specimen fixture at room temperature and at the oxidation temperature. Further explanation is provided in Appendix B.

Thermogravimetric measurements were obtained for (001) and (011) single crystals. Data were also obtained using

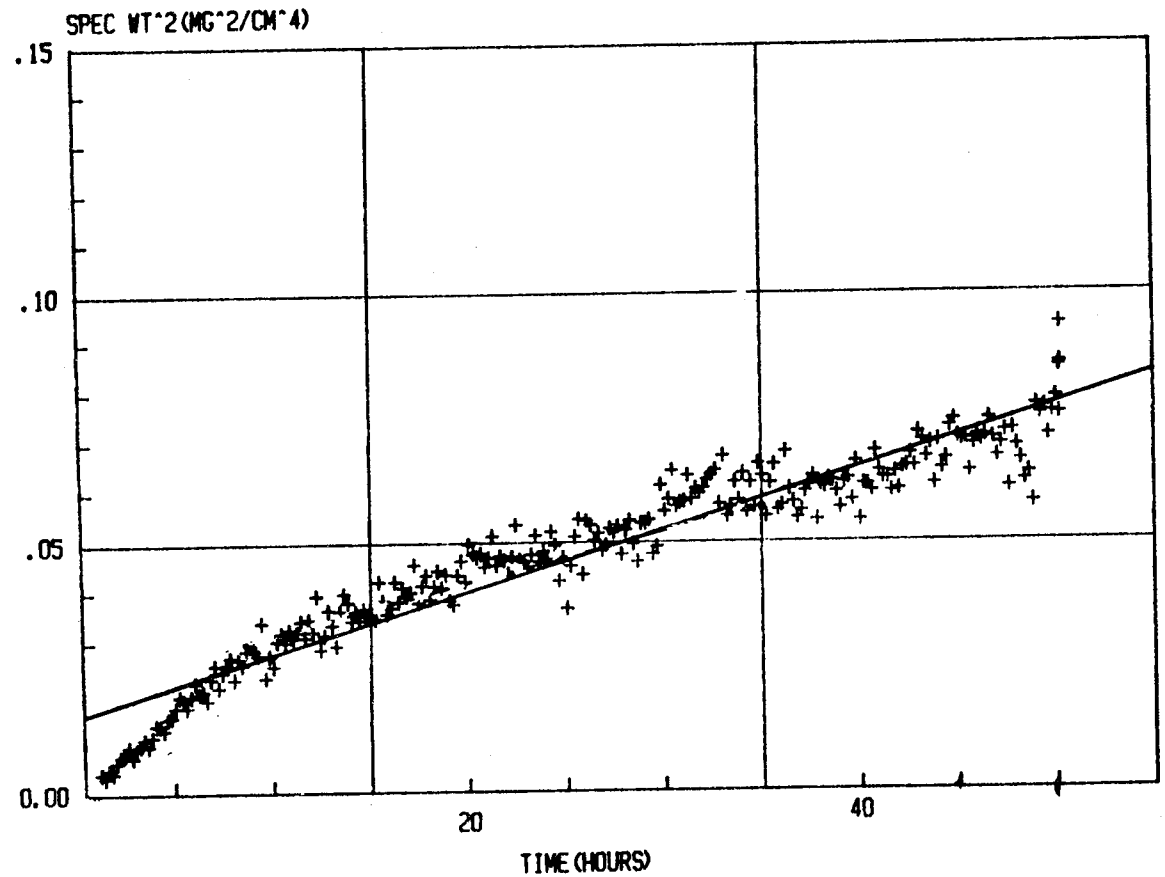

Figure 13

Parabolic weight gain versus time plot for the 800°C, isothermal oxidation of an (001) β-NiAl single crystal specimen. $k_p = 4.00 \times 10^{-4} (mg^2/cm^4 \cdot hr)$.

polycrystalline specimens having a metal grain size of approximately 0.5 mm. The results for each condition will be presented separately followed by a discussion.

i. (001) single crystal. Results of isothermal oxidation of a (001) single crystal of β-NiAl are shown in Figure 13. The curve was obtained by first correcting the raw data for buoyancy and platinum loss. The weight gain values were then divided by the surface area of the specimen, squared and plotted versus time. If the oxidation process follows ideal parabolic kinetics according to the Wagner theory, the plot of weight gain divided by surface area squared versus time should yield a straight line, i.e.,

$$d/dt(\Delta W/\text{unit area})^2 = \text{constant} = k_p \qquad [4]$$

The slope of this line is the parabolic rate constant, k_p.

The largest error involved in the measurement arises from the small specimen having an effective surface area of only 2.4 cm^2. The actual weight gain approaches the sensitivity of the system. Additional errors can be attributed to buoyancy correction miscalculation, electronic instability of the system during oxidation and improper calibration.

For this condition, the scatter among data points is small considering the small specimen surface area. The calculated value

of the slope, k_p, is 5.15 x 10^{-4}($mg^2/cm^4 \cdot hr$). Linear regression was used to fit the slope and an R value of 0.913 was obtained.

The actual k_p would be smaller if the inital fast oxidation region is omitted from the calculation. This second value of 4.0 x 10^{-4}($mg^2/cm^4 \cdot hr$) is more representative of steady state conditions. The initial steep portion of the curve would be significant to results if better control and heating procedures had been employed. Because the furnace is raised after the specimen is in position, equilibrium temperature conditions are not achieved until approximately 20 minutes after the test has begun.

ii. (011) single crystal. Two runs for this condition were conducted. Both specimens were small (3.552 cm^2 and 2.356 cm^2 in area) causing some scatter in the data. The parabolic weight gain plots are shown in Figure 14 for both runs.

A first observation is the cyclic nature of the weight change with time. After many tests were performed to determine the cause of this anomaly, it was concluded that the changing environment of the laboratory was effecting the results. In Figure 14b, the period of each cycle is approximately 24 hours. This corresponded with the daily change in heating of the laboratory building. Also, the amplitude within each cycle and the scatter of the data varied directly. Sometimes, the cyclic effect was not observed as in the case of (001) specimens oxidized at 800°C. The causes for

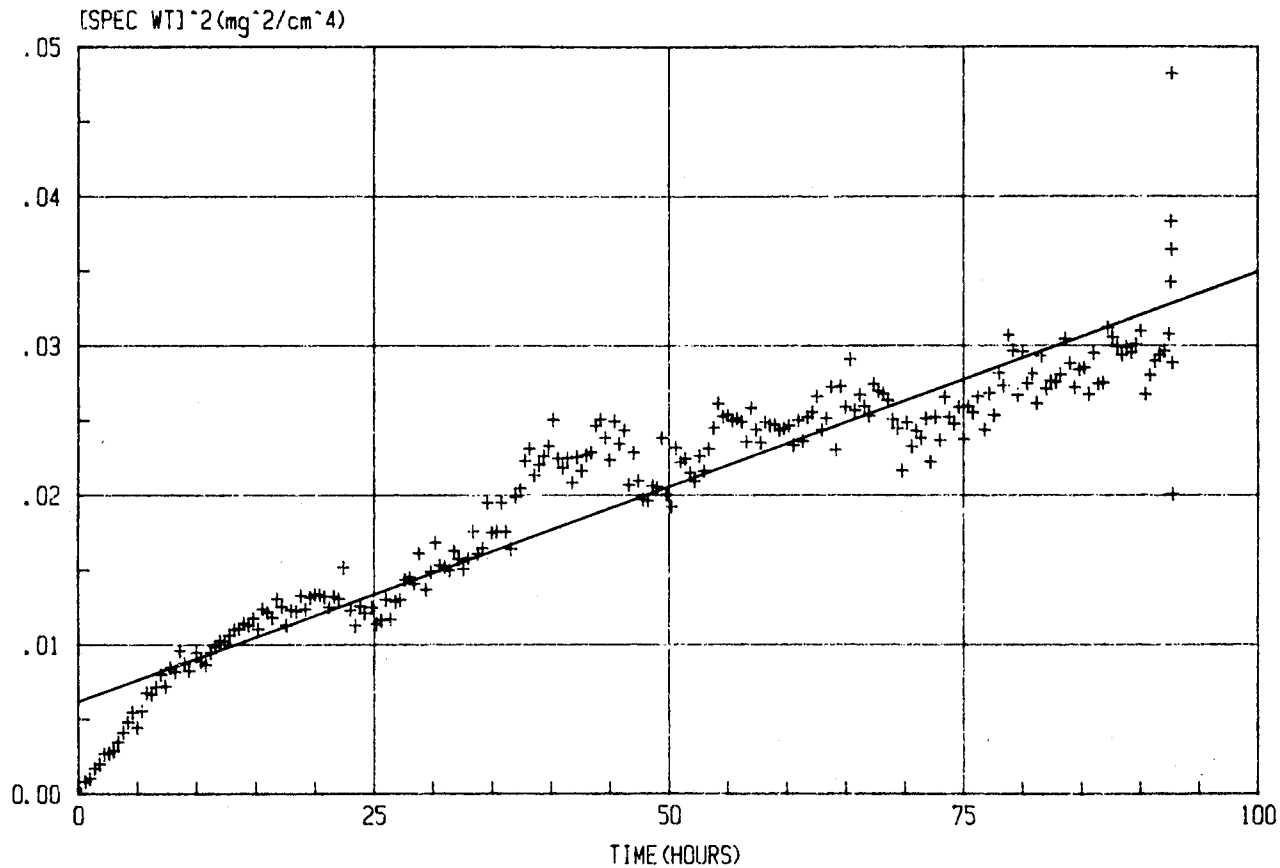

a)

Figure 14

Parabolic weight gain versus time plots for the 800°C isothermal oxidation of β-NiAl single crystal specimens. a) $k_p = 2.875 \times 10^{-4} (mg^2/cm^4 \cdot hr)$, b) $k_p = 2.42 \times 10^{-4} (mg^2/cm^4 \cdot hr)$.

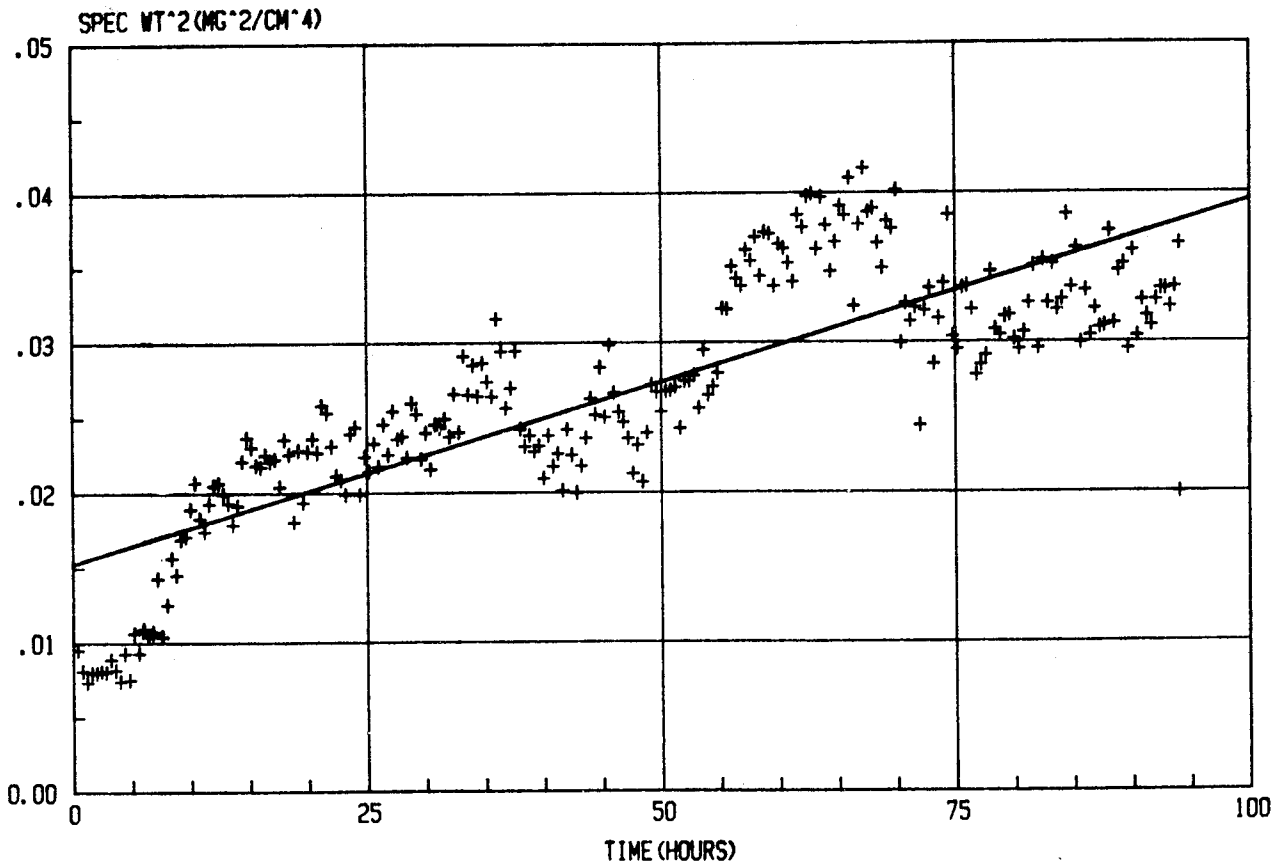

Figure 14b)

inconsistencies are still unknown. However, if observed, corrections for this effect can be used cautiously. The scatter (R = 0.676) is misleading.

The two values obtained for (011) single crystals isothermally oxidized at 800°C are 2.875 x 10^{-4}($mg^2/cm^4 \cdot hr$) and 2.42 x 10^{-4}($mg^2/cm^4 \cdot hr$). Final weight gains measured with a standard Metler balance agree within .1 mg of the weight gain at the end of the isothermal oxidation run measured by the Cahn 1000 electrobalance system. Confirmation of k_p values was achieved by performing the isothermal oxidation test a second time and thereby obtaining consistent results.

iii. Polycrystalline. Although the term "polycrystalline" implies a random orientation of grains, heavy texture was observed for specimens cut from button sections of the casting. For specimens cut perpendicular to the crystal growth direction, the grains had a [001] texture. A specimen cut parallel to the crystal growth direction had [012] texture.

The effective surface areas of the polycrystalline specimens were much larger than surface areas of single crystals. This helped to eliminate scatter in the data. Figures 15a and 15b show results for the two specimens, respectivly. For the [001] textures mentioned, the parabolic rate constant is k_p = 2.31 x 10^{-4}($mg^2/cm^4 \cdot hr$). For the [012] textured material, kp = 3.04 x 10^{-4}($mg^2/cm^4 \cdot hr$). Some longer period cyclic nature can be

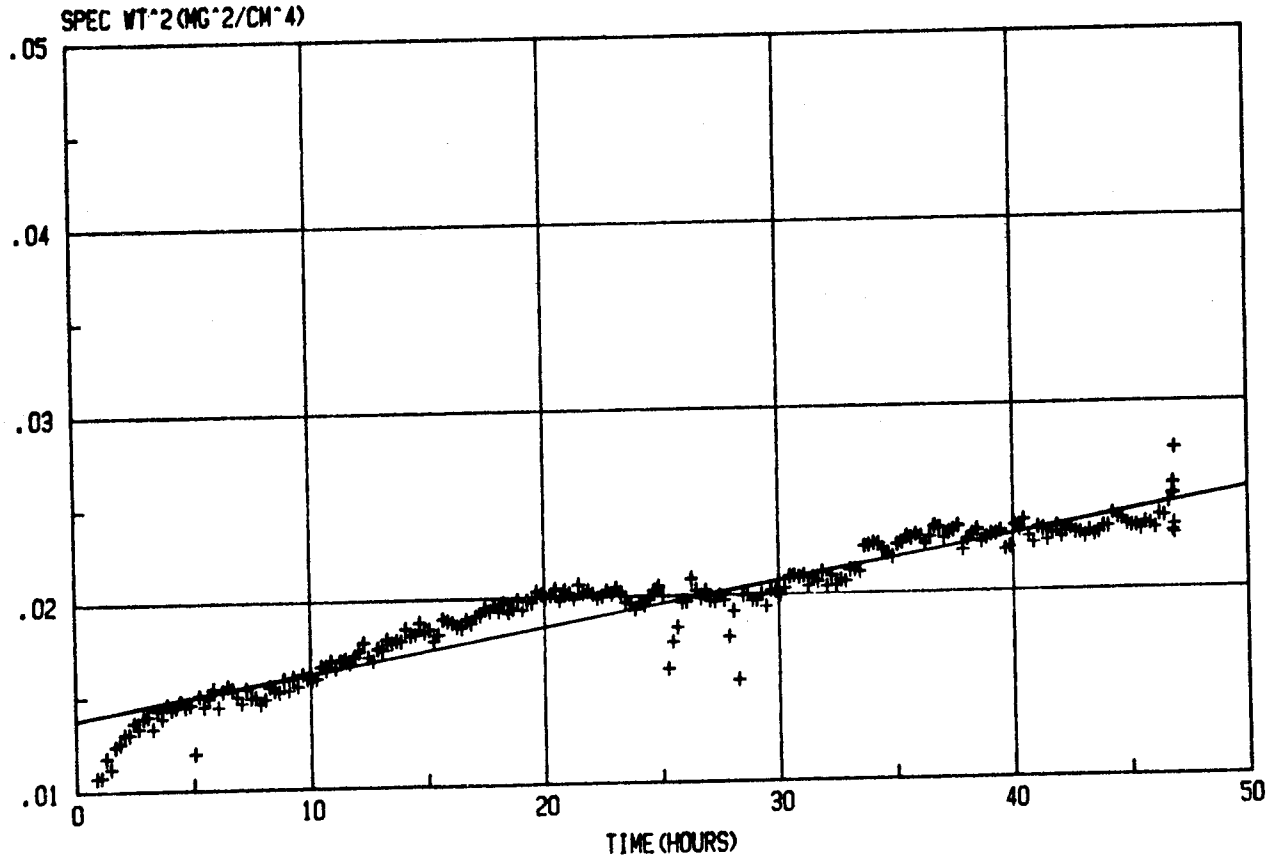

a)

Figure 15

Parabolic weight gain versus time plots for polycrystalline β-NiAl specimens oxidized at 800°C. a) [001] texture, $k_p = 2.31 \times 10^{-4}$ ($mg^2/cm^4 \cdot hr$), b) [012] texture, $k_p = 3.04 \times 10^{-4}$ ($mg^2/cm^4 \cdot hr$).

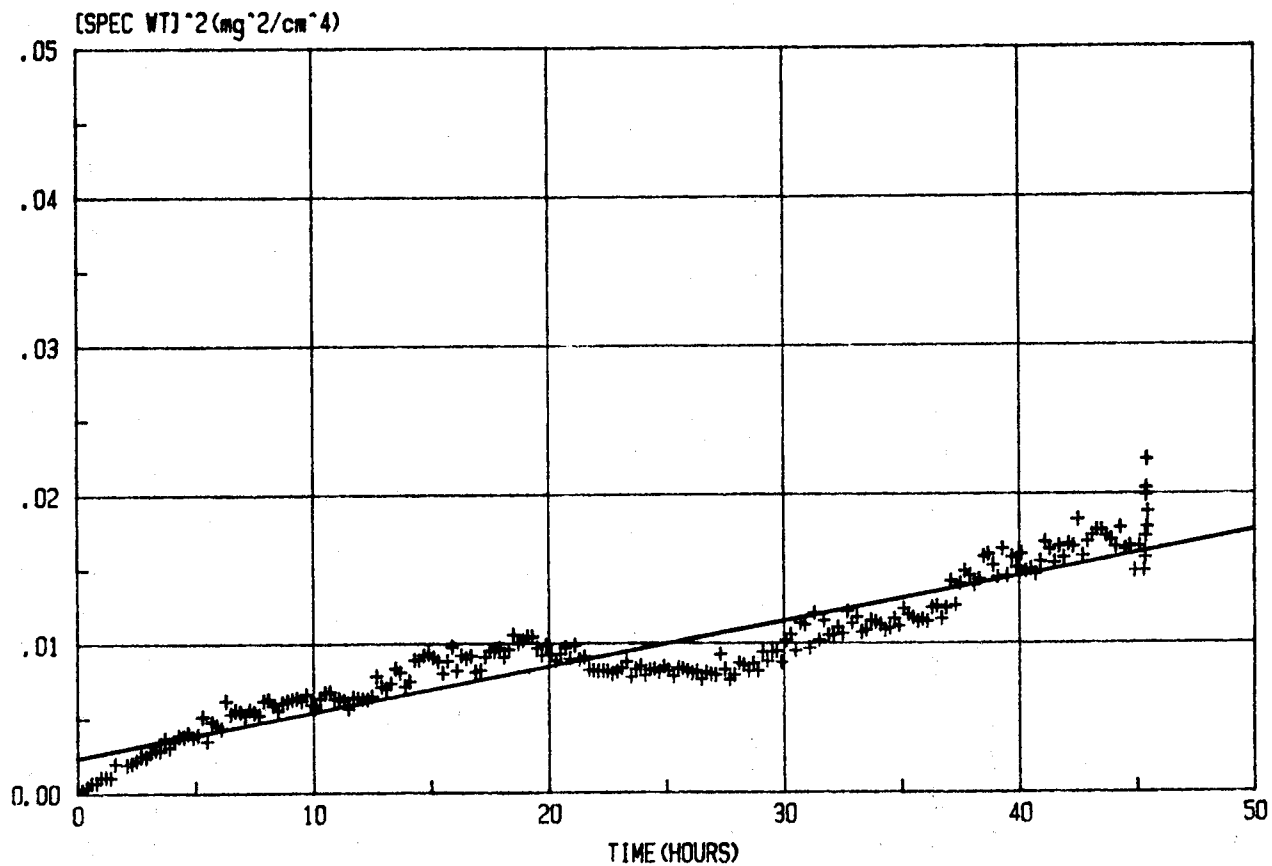

Figure 15b)

observed but it does not appear to effect the overall average slope.

iv. Discussion. Wagner's theory of parabolic oxidation, in simple form, predicts:

$$x^2 = k_p \cdot t \qquad [5]$$

where x = oxide thickness(m)

k_p = parabolic rate constant(m^2/s)

t = time(s)

The units of k_p suggest that the parabolic rate constant is also an effective diffusion coefficient. Therefore, some insight into [6~diffusion mechanism can be obtained from parabolic growth rate data.

Table III lists the results presented above. Limited results from 800°C oxidation studies of high aluminun content alloys were available for comparison. Values of 1.2×10^{-3}($mg^2/cm^4 \cdot hr$) and 2.0×10^{-4}($mg^2/cm^4 \cdot hr$) were obtained for Ni-50 at% Al and Ni-42 at% Al respectively, oxidized at 900°C.[40] Extrapolated parabolic rate constant results to 800°C were at least one order of magnitude higher than the present study. A study performed by Rybicki and Smialek on the same material as the present study revealed a k_p value of 7.3×10^{-4}($mg^2/cm^4 \cdot hr$).[41] The difference

TABLE III

Values of parabolic rate constants, k_p, for the isothermal oxidation of β-NiAl at 800°C.

Metal Orientation	k_p ($mg^2/cm^4 \cdot hr$)	Comments
(001)	4.00×10^{-4}	----------
(011)	2.88×10^{-4}	Case I
(011)	2.42×10^{-4}	Case II
polycrystal	2.31×10^{-4}	(001) texture
polycrystal	3.04×10^{-4}	(012) texture

between this value and those in the present study is small and is believed to be due to specimen preparation. The higher k_p was obtained on a 600 grit abraded surface whereas the lower k_p was obtained on an electropolished surface.

Identification of the oxide phase after 10 or 100 hours of oxidation at 800°C was not feasible by normal x-ray diffraction techniques because the oxide layers were too thin. The diffracted intensity of the oxide was overshadowed by the underlying metal intensity. Therefore, TEM was used for phase identification. The scales were found to consist of δ-Al_2O_3, the same phase observed after 10.0 hours of oxidation at 800°C. Moreover, with longer oxidation times, δ-Al_2O_3 was observed on all metal orientations.

Growth of oxide scales results from diffusion of mobile species through the scale. In the case of δ-Al_2O_3, Al ions can diffuse outward through the scale to form new oxide at the oxide-gas interface or oxygen ions can diffuse inwards forming new oxide at the metal-oxide interface. Experimental evidence for transient Al_2O_3 scale diffusion mechanisms was given by Hindam and Smeltzer.[13] In their experiment, Pd markers were placed on the β-NiAl surface prior to oxidation at 1000°C. After a 5 minute oxidation treatment, the Pd was found to be at the gas-oxide interface as determined by Auger Electron Spectroscopy, a technique for sputter-depth profiling. Therefore, scale growth was concluded to occur by inward oxygen diffusion. This result

contradicts principles of diffusion in spinels which suggests a high cation diffusivity amongst a rigid oxygen network. In defective spinels such as the metastable Al_2O_3 phases, the cation diffusivity should be greater because of the large number of vacant cation positions by which diffusion could occur. The result of Hindam and Smeltzer thus contradicts principles of diffusion through spinels and suggests questions on the validitly of inert marker experiments. However, if correct, their results might indicate that an alternate diffusion mechanism occurs for transient scale growth. Young and de Wit have studied growth mechanisms of Al_2O_3 scales formed on β-NiAl at 900°C using ^{18}O tracer techniques with Rutherford back-scattering(RBS).[42] Their results clearly indicate that the scales grow by an outward aluminum diffusion mechanism. Also, Pt markers were used to determine scale growth mechanisms. RBS measurements of specimens with Pt markers indicated Pt on the outer surface of the oxide implying an inward oxygen diffusion mechanism. However, tracer measurements on the same specimens indicated an outward aluminum diffusion mechanism. An experiment was performed in which Pt markers were placed on an Al_2O_3 scale formed at 900°C. The markers and scale were overlayed by a layer of synthetic Al_2O_3. The specimens were then oxidized at 900°C. New oxide was observed above the markers indicating that outward aluminum diffusion was responsible for further scale growth. The study by Young and de Wit shows that the results of inert marker experiments as a method

of determining Al_2O_3 scale growth mechanisms could be invalid.

Diffusion through oxide scales can occur by short-circuit diffusion, most probably along grain boundaries. For many oxide systems, diffusion along grain boundaries is the predominant mechanism especially at lower temperatures. Short circuit diffusion has been observed for scales that grow by cation diffusion(NiO, CoO, Cu_2O)[43-45] or by anion diffusion (α-Al_2O_3,α-Cr_2O_3).[9,46] Many oxide systems appear to have a preference for one type of ion mobility, either cation or anion. Counterdiffusion of both ions has been speculated, but has only been observed in a few studies dealing with α-Al_2O_3 scales of which more will be discussed later. The high grain boundary diffusion of only one ion could be attributed to the grain boundary charge induced by impurities.[47]

The effect of grain boundary diffusion on growth rates is most dramatic when scales having different grain sizes and morphologies are compared. Textured scales having few high-angle grain boundaries have been found to grow more slowly than scales having randomly oriented grains; for example, in the case of NiO growth on nickel (001), (011), and (111) single crystals.[43] This same effect was expected in this study for growth rates of oxides on (001) and (011) single crystals versus polycrystals of β-NiAl. Transient scales formed on (001) and (011) orientations of β-NiAl were epitaxially related to the metal so that only low angle grain boundaries were present. However, the changes between measured

growth rates were too small relative to scatter in the data for any quantitative conclusions to be made on orientation effects. Although no large differences were observed in thermogravimetric measurements, thickness changes of the scales existed for different orientations as evidenced by interference color changes of scales. Figure 16 shows a polycrystalline specimen oxidized for 50 hours at 800°C. Good indications of thickness changes besides color are the visibility of scratches and pits in the metal surface after oxidation.

A formula for determining film thickness on reflecting surfaces is given as:[48]

$$t = m\lambda/2n_i \qquad [6]$$

where t = film thickness(m)

m = order of interference color

λ = wavelength of relfected light(m)

n_i = index of refraction of film material

In Figure 16, most colors of the optical spectrum can be observed. The thinnest film appears to reflect gold light as indicated by the high visibility of surface deformities on the metal in Figure 16. The thickest oxide film appears goldish white. This indicates that the variation in thickness spans one order of the interference spectrum which is calculated to be about

ORIGINAL PAGE IS
OF POOR QUALITY

0.25mm

Figure 16

Optical micrograph of a polycrystalline β-NiAl specimen oxidized for 50 hours at 800°C. The different colors of grains correspond to oxide thickness changes.

170 nm. The film thickness corresponds to sample weight gain using the formula:

$$t = \Delta W/\rho A \qquad [7]$$

where t = thickness(cm)

ρ = density of oxide(g/cm^3)

A = surface area of specimen(cm^2)

Using approximate values for ρ and A of 3.348(g/cm^3) and 3(cm^2) respectively, the weight change is calculated to be 0.17 mg, a value too small to be measured accurately with the present sensitivity of the system used. This example involves the extreme case for the difference in the oxide film thickness, with the thinnest scale most likely being oriented and the thickest scale having a random orientation. The actual weight change difference between two textured films, such as those on (001) and (011) metal orientations, would be much less. Therfore, for oxidation of β-NiAl at 800°C for times less then 100 hours, more sensitive methods than those used in the present study are required to perform an exact quantitative analysis of weight gain due to oxidation. Relative oxide thickness is best compared using interference color effects. With longer times, greater changes in total weight gain per unit area will occur and should be observable using the present thermogravimetric set-up. However,

measured parabolic rate constants were consistent and can be used as approximate values.

b. Microstructure. Figures 17 and 18 are bright field images of oxide microstructures on (001) and (011) metal respectively, oxidized for 100 hours at 800°C. Corresponding SEM images of the gas-oxide interface are shown in Figures 19 and 20. As can be seen, the microstructure of the (001) scale consists of highly faceted platelets of oxide. Electron diffraction results indicated that this scale is oriented δ-Al_2O_3 having the same Bain orientation relationship with the metal as in the shorter oxidation times.

The faceted nature of the oxide formed on (001) metal faces at the gas-oxide interface indicates that the oxide grows by outward cation diffusion preferentially forming new oxide on particular crystallographic faces. The long faces are predominantly {110} oxide planes. The microstructure of the oxide on (011) metal faces is drastically different than on (001). The oxide consists of fine equiaxed grains and the oxide surface is smooth. The oxide was determined to be δ-Al_2O_3 from electron diffraction, but the degree of preferred orientation remained rather weak as shown in the diffraction pattern of Figure 21. The more random nature of the oxide could give rise to the smooth surface. However, the gas-oxide surface on (111) metal orientations oxidized for 100 hours at 800°C consisted of fine

ORIGINAL PAGE IS
OF POOR QUALITY

Figure 17 0.25μm

Bright field image of an oxide scale formed on a (001) β-NiAl specimen oxidized for 100 hours at 800°C. The microstructure consists of many oxide platelets.

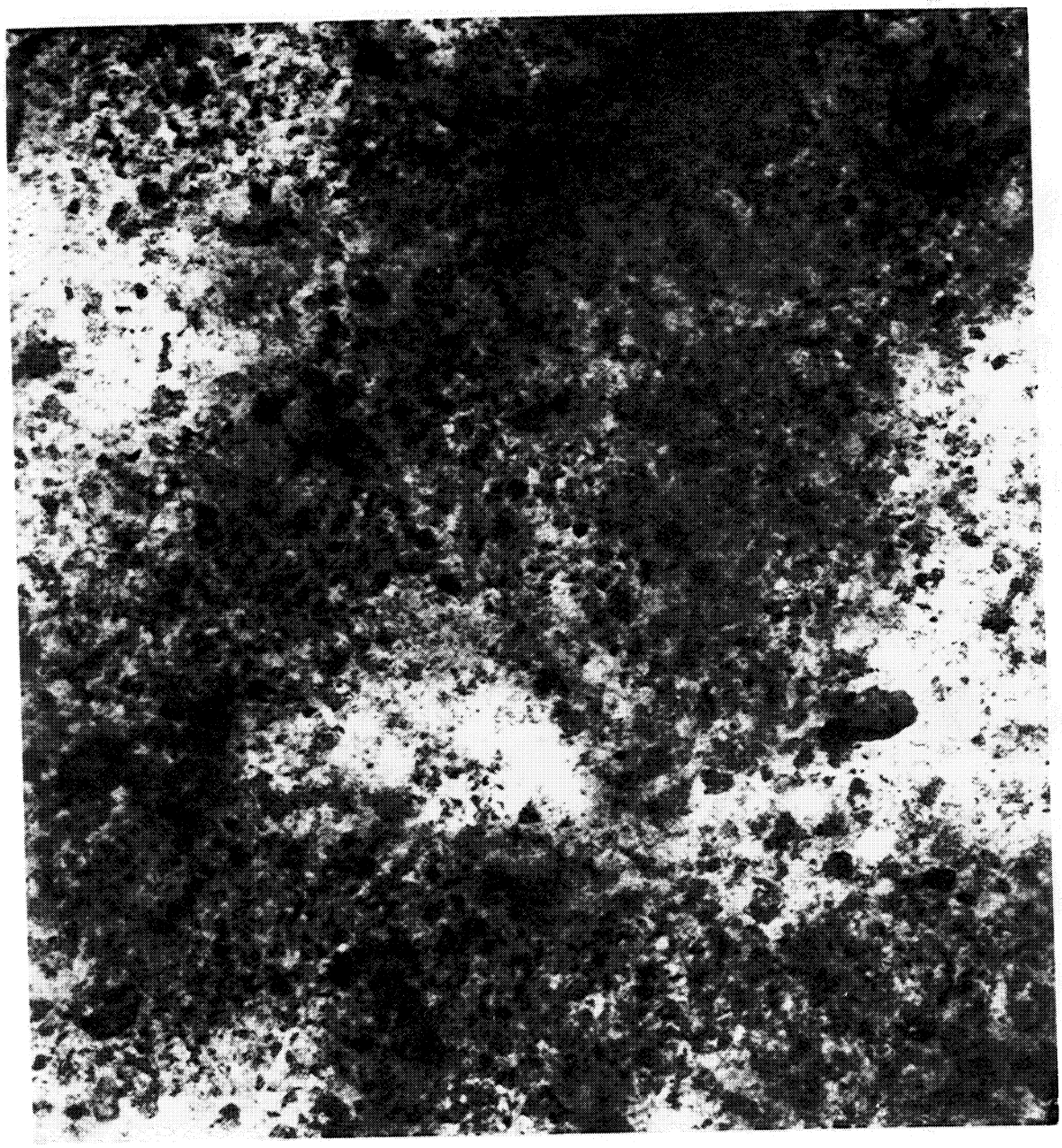

Figure 18 0.25μm

Bright field image of an oxide scale formed on a (011) β-NiAl specimen oxidized for 100 hours at 800°C. The microstructure consists of fine, equiaxed subgrains.

ORIGINAL PAGE IS
OF POOR QUALITY

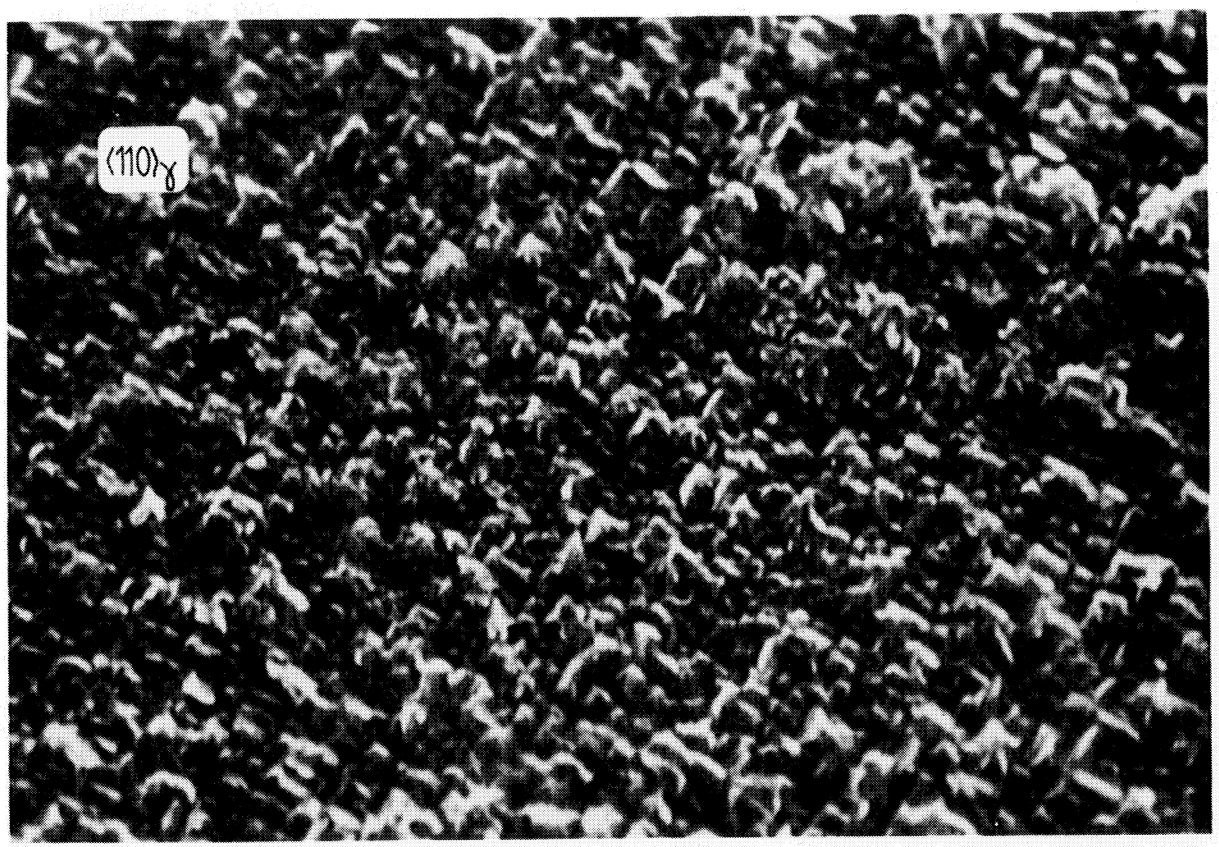

1.0μm

Figure 19

SEM image of the gas-oxide surface of an (001) β-NiAl specimen oxidized for 100 hours at 800°C.

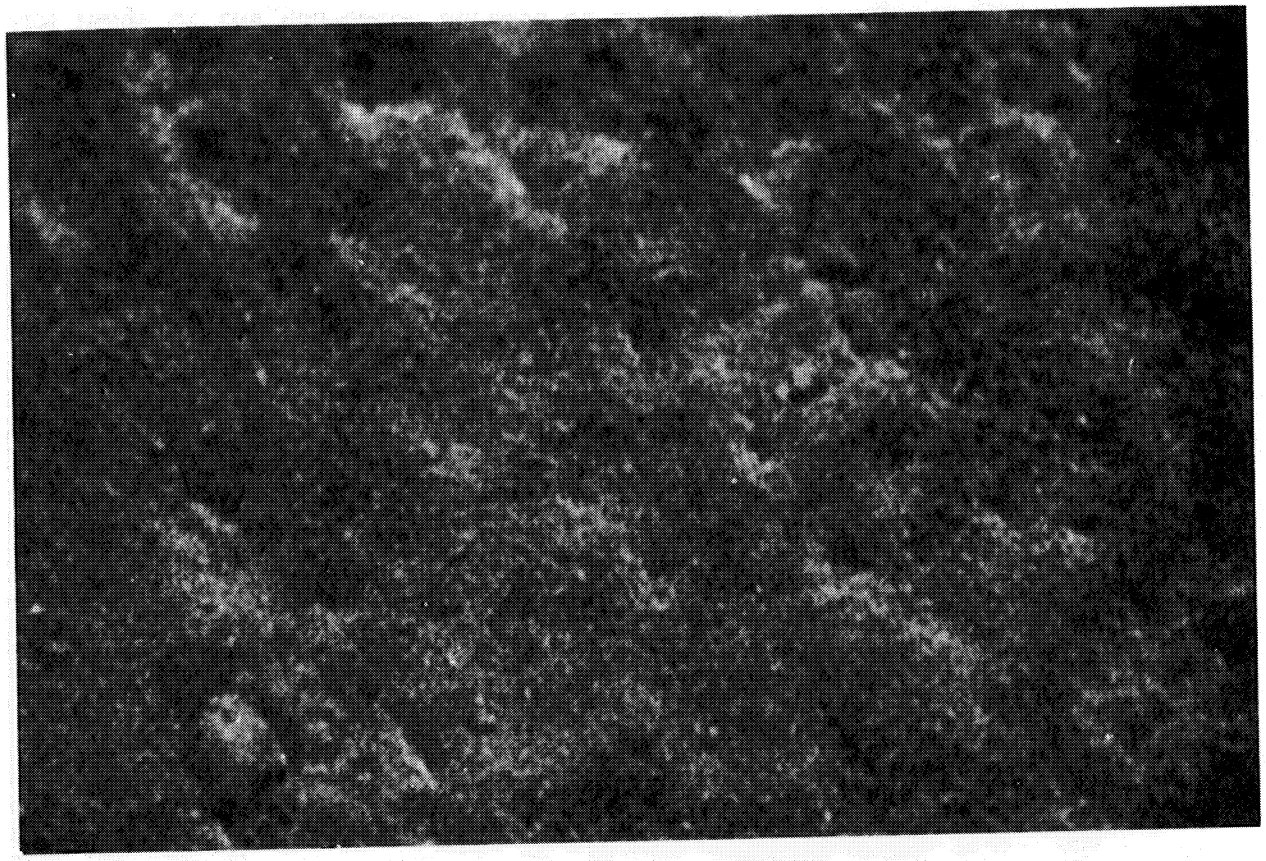

1.0 μm

Figure 20

SEM image of the gas-oxide surface of an (011) β-NiAl specimen oxidized for 100 hours at 800°C.

ORIGINAL PAGE IS
OF POOR QUALITY

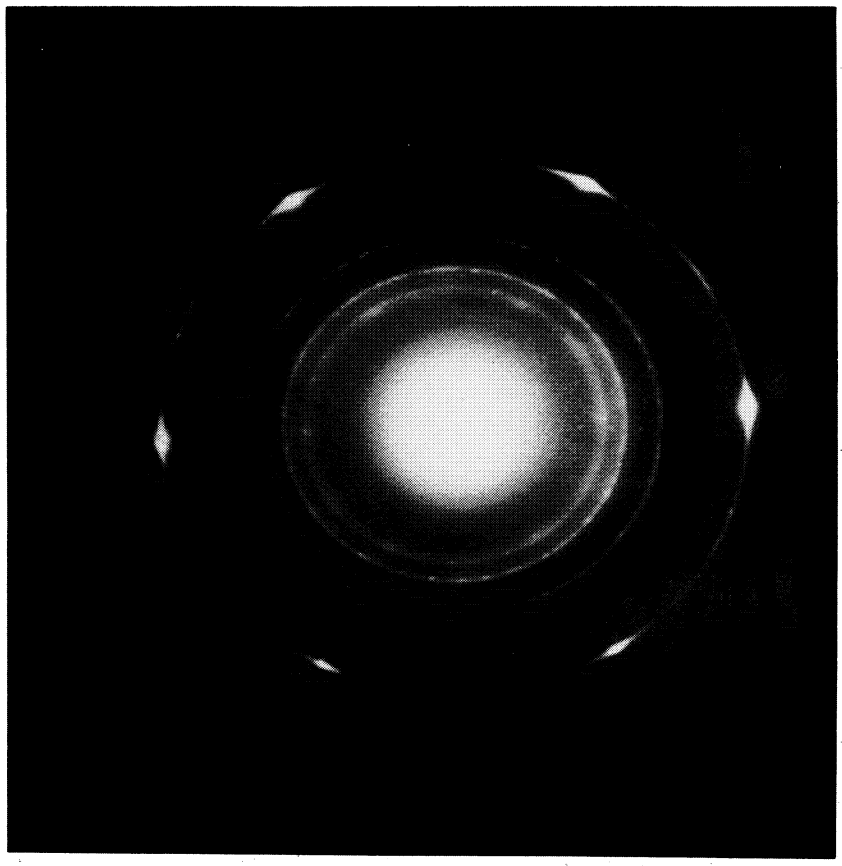

Figure 21

Selected area diffraction pattern of an oxide scale formed on a (011) β-NiAl specimen oxidized for 100 hours at 800°C. The oxide is δ-Al_2O_3 with a $\langle 111 \rangle_\gamma$ preferred orientation.

needles(Figure 22). The δ-Al_2O_3 in this case was also random, yet the needles are present in contrast to the smooth surface in Figure 20. The needle morphology is clear evidence of outward cation diffusion resulting in scale growth.

The microstructures of the 800°C scales have been shown to be a function of metal orientation inferring the importance of the degree of preferred orientation between metal and oxide. The oxide scales formed after 100 hours of oxidation at 800°C have been found to consist of δ-Al_2O_3 on all metal orientations studied by both TEM and x-ray diffraction.

B. 1100°C Oxidation

As mentioned before, after oxidation for 0.1 hours at 1100°C, the oxide scale had not transformed to α-Al_2O_3 and therfore was still in a transient stage. This section is intended to complete the study of the transient stages of oxidation by describing the oxide growth rates, microstructure and morphologies at 1100°C prior to the transformation. In doing this, more insight will be gained into the structure of metastable Al_2O_3 phases immediately before the transformation to α-Al_2O_3 and into the overall picture of the transient stages. Limited growth rate data will be presented for correlation with previous results. Detailed crystallographic and morphological data will also be presented.

ORIGINAL PAGE IS
OF POOR QUALITY

1.0μm

Figure 22

SEM image of the gas-oxide surface of an oxide scale formed on a (111) β-NiAl specimen oxidized for 100 hours at 800°C.

1. Growth rates

TEM results indicated that, within one hour of oxidation, the oxide scale began to transform to α-Al_2O_3. From that point on, the measured growth rates are that of α-Al_2O_3 and not δ-Al_2O_3, the metastable phase. Plots of parabolic weight gains versus time were plotted for the first hour of oxidation at 1100°C. Although measurements were only taken every six minutes, good correlation was obtained for parabolic growth rate calculations.

The calculated slopes, k_p, were fitted using linear regression and the results given in Table IV for the various conditions. As observed in the listing of parabolic growth rate constants, the difference between the different conditions is small. Without doing more precise experiments, it is difficult to conclude that any trends exist for different metal orientations. However, as in the case of 800°C weight gain measurements, the data are consistent enough to obtain a reasonable figure for parabolic growth rate constants at 1100°C. This value is an average of the lower five values and is calculated to be 6.17 x 10^{-3}($mg^2/cm^4 \cdot hr$). An extrapolated value from the study by Rybicki and Smialek using the same material gave a k_p value an order of magnitude larger.[41] Different specimen preparations (600 grit versus electropolishing) could be responsible for the differences

TABLE IV

Values of parabolic rate constants, k_p, for the isothermal oxidation of β-NiAl at 1100°C. Results are obtained from initial portions of parabolic growth rate curves while still in the transient stage.

Metal Orientation	$k_p (mg^2/cm^4 \cdot hr)$	Comments
(011)	1.45×10^{-2}	Case I
(011)	7.38×10^{-3}	Case II
polycrystal	4.61×10^{-3}	no preox.
polycrystal	5.84×10^{-3}	50 hrs. preox.
polycrystal	7.59×10^{-3}	100 hrs. preox.
(001)	5.41×10^{-3}	600 grit surf.

in parabolic growth rate constants.

2. Microstructure

At 1100°C, the transient stage of oxidation that exists prior to the transformation to α-Al_2O_3 involves many interesting features of the oxide scale. This section deals with the microstructures of these scales in terms of oxide phases and morphology. Detailed TEM work has been performed on a (001) single crystal specimen of β-NiAl oxidized at 1100°C for 1.0 hours. SEM images of surface oxide morphologies formed on polycrystalline β-NiAl specimens oxidized at 1100°C will be shown to further generalize the 1100°C transient condition.

a. (001) single crystal. A bright field image is shown in Figure 23 of an oxide scale formed on a (001) single crystal of β-NiAl oxidized for 1.0 hours at 1100°C. The scale consists of dark platelets within a matrix of oxide. In this image, the platelet size approaches 1 μm. The platelets do not appear to have a textured orientation in this image although a definite texture is observed in a SEM image of the surface of this same scale shown in Figure 24. Many of the platelets lie along orthogonal directions indicating a tendency to form on cubic {110} and occasionally on {100} planes.

ORIGINAL PAGE IS
OF POOR QUALITY

Figure 23

1.0 μm

Bright field image of an oxide scale formed on a (001) β-NiAl specimen oxidized for 1.0 hours at 1100°C.

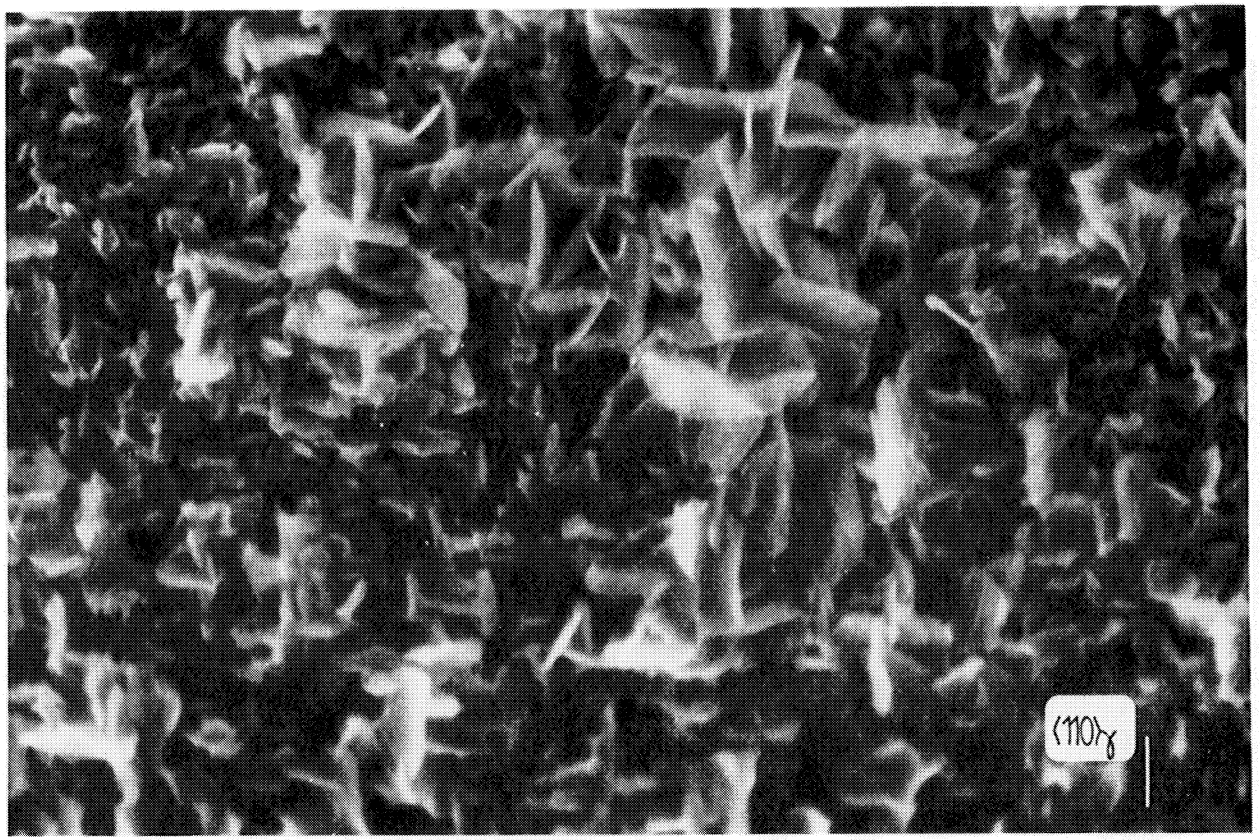

Figure 24

SEM image of the gas-oxide surface formed on a (001) β-NiAl specimen oxidized for 1.0 hours at 1100°C.

The cubic texture exhibited by the platelets corresponds with the Bain epitaxial relationship that exists between the oxide and metal. Figure 25 is a diffraction pattern of a thicker region of the oxide scale and shows a definite preferred orientation. This pattern is similar to oriented δ-Al_2O_3 observed on (001) β-NiAl single crystals oxidized at 800°C. However, the 1100°C scale is more complex in terms of oxide phases. The reflections in Figure 25 are diffuse because of the thick oxide region from which this pattern was taken. A SAD from a thinner oxide region is shown in Figure 26. This pattern shows the same oxide texture. However, the oxide phase is indexed as θ-Al_2O_3, the monoclinic form of metastable Al_2O_3 which is described below.

The results from a study by Yamaguchi et al. on θ-Al_2O_3 provide the crystallographic information necessary to characterize θ-Al_2O_3.[49] θ-Al_2O_3 is approximately isostructural with β-Ga_2O_3, but is more distorted. θ-Al_2O_3 is monoclinic and has a C2/m space group. As for all metastable Al_2O_3 phases, the structure of θ-Al_2O_3 is based on spinel. The lattice dimensions of θ-Al_2O_3 are, in nm:

$$a = 1.1813$$
$$b = 0.2906$$
$$c = 0.5625$$
$$\beta = 104.6^{\circ}$$

The transformation matrix for indices of lattice planes of spinel to monoclinic θ-Al_2O_3 is as follows:

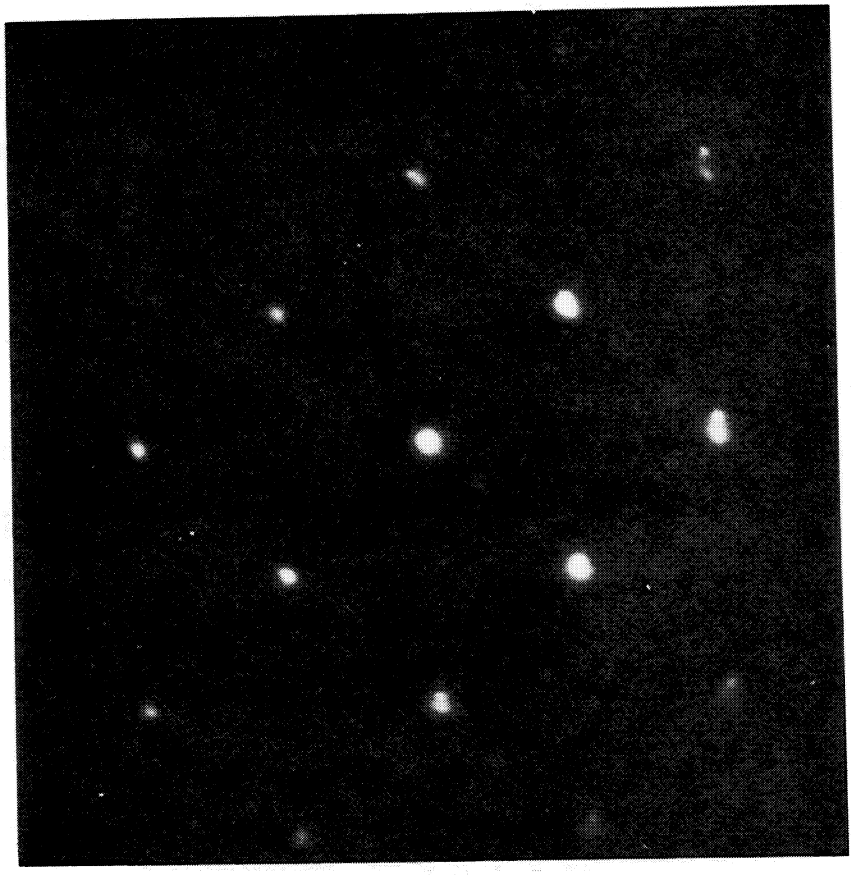

Figure 25

Selected area diffraction pattern from a thick oxide region of a (001) β-NiAl specimen oxidized for 1.0 hours at 1100°C. The orientation of the oxide reflects the Bain orientation relationship observed at a lower oxidation temperature.

ORIGINAL PAGE IS
OF POOR QUALITY

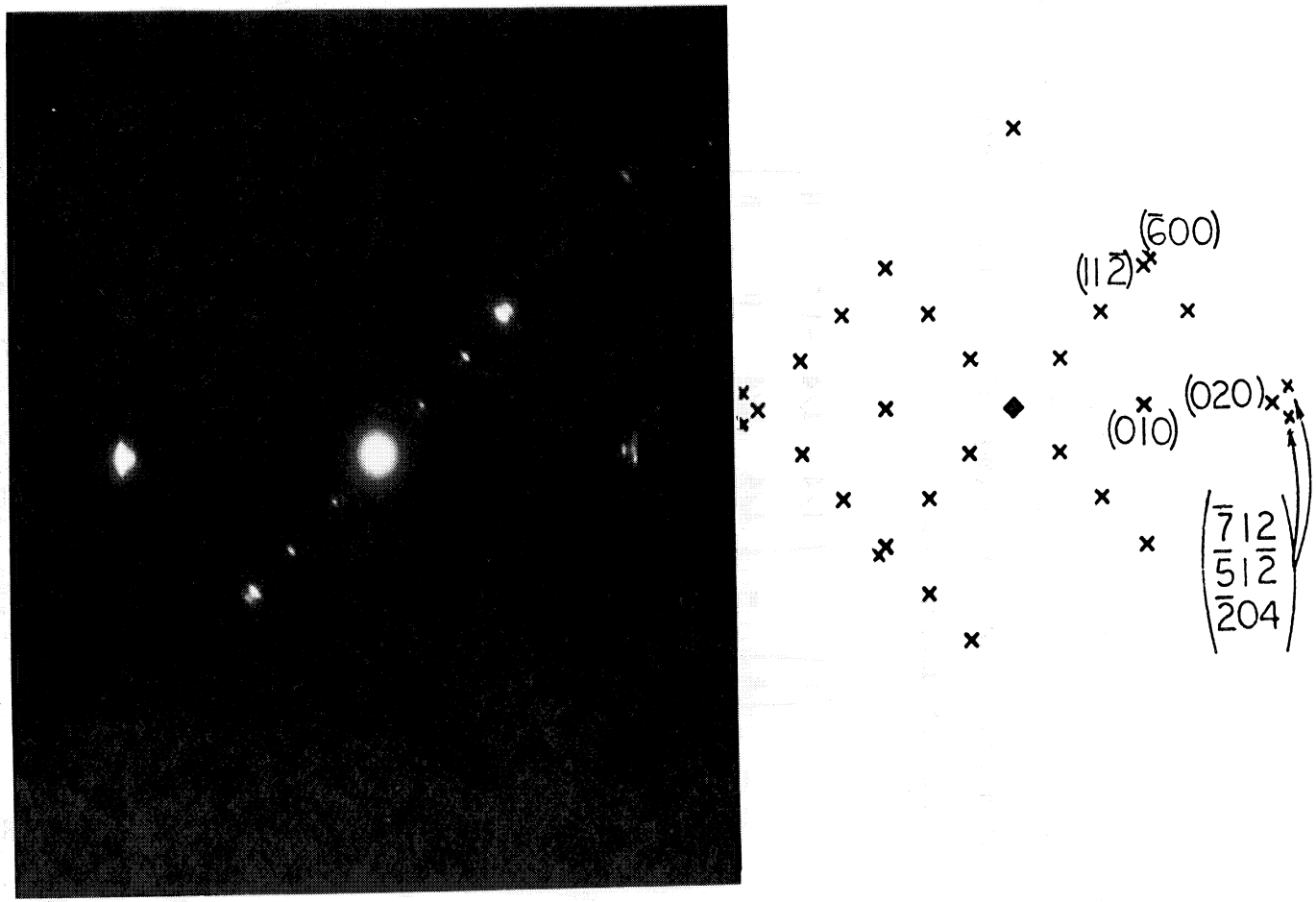

Figure 26

Selected area diffraction pattern from a thinner oxide region from the same specimen as in Figure 25. The oxide is indexed to be θ-Al_2O_3. Up to 12 variants of θ-Al_2O_3 contribute to this pattern.

$$\begin{pmatrix} h \\ k \\ l \end{pmatrix} = \begin{pmatrix} -1/4 & 1/4 & -3/2 & H \\ 1/4 & 1/4 & 0 & K \\ 1/2 & -1/2 & 0 & L \end{pmatrix} \qquad [8]$$

where (hkl) are the indices of the monoclinic lattice and (HKL) are the indices of the cubic lattice. Likewise, the same type of transformation matrix from the tetragonal δ-Al_2O_3 structure to the monoclinic θ-Al_2O_3 structure is:

$$\begin{pmatrix} h \\ k \\ l \end{pmatrix} = \begin{pmatrix} -1/4 & 1/4 & -1/2 & H \\ 1/4 & 1/4 & 0 & K \\ 1/2 & -1/2 & 0 & L \end{pmatrix} \qquad [9]$$

where (hkl) are indices for planes in the monoclinic lattice and (HKL) are indices of planes in the corresponding tetragonal lattice. The θ-Al_2O_3 monoclinic indices corresponding to both γ-Al_2O_3 and δ-Al_2O_3 have been calculated and are tabulated in Table V.

Indexing the diffraction pattern of Figure 26 requires the use of many θ-Al_2O_3 variants. Due to the similarities in structure of γ-Al_2O_3, δ-Al_2O_3 and θ-Al_2O_3, their structures are related by the original c-axis of δ-Al_2O_3. Because there is a possibility of three δ-Al_2O_3 variants, there will be a possibility of twelve θ-Al_2O_3 variants. Many of the reflections in Figure 26 are

TABLE V

Corresponding indices of planes in three metastable Al_2O_3 phases having cubic(γ), tetragonal(δ) and monoclinic(Θ) crystal structures.

γ	δ	Θ
111	113	—
$11\bar{1}$	$11\bar{3}$	—
$1\bar{1}1$	$1\bar{1}3$	$\bar{2}01$
$\bar{1}11$	$\bar{1}13$	$\bar{1}0\bar{1}$
200	200	—
020	020	—
002	006	$\bar{3}00$
220	220	010
202	206	—
022	026	—
$2\bar{2}0$	$2\bar{2}0$	$\bar{1}02$
$20\bar{2}$	$20\bar{6}$	—
$\bar{2}02$	$\bar{2}06$	—
311	313	$\bar{2}11$
131	133	$\bar{1}1\bar{1}$
113	119	—
$31\bar{1}$	$31\bar{3}$	111
$3\bar{1}1$	$3\bar{1}3$	—
$3\bar{1}\bar{1}$	$3\bar{1}\bar{3}$	—

TABLE V(cont)

γ	δ	Θ
$13\bar{1}$	$13\bar{3}$	$21\bar{1}$
$\bar{1}31$	$\bar{1}33$	---
$\bar{1}3\bar{1}$	$\bar{1}3\bar{3}$	---
$1\bar{1}3$	$1\bar{1}9$	$\bar{5}01$
$\bar{1}13$	$\bar{1}19$	$\bar{4}0\bar{1}$
$\bar{1}\bar{1}3$	$\bar{1}\bar{1}9$	---
400	400	$\bar{1}12$
040	040	$11\bar{2}$
004	$0\cdot0\cdot12$	$\bar{6}00$
440	440	020
404	$4\cdot0\cdot12$	$\bar{7}12$
044	$0\cdot4\cdot12$	$\bar{5}1\bar{2}$
$4\bar{4}0$	$4\bar{4}0$	$\bar{2}04$
$40\bar{4}$	$4\cdot0\cdot\bar{1}\bar{2}$	512
$0\bar{4}4$	$0\cdot\bar{4}\cdot12$	$7\bar{1}\bar{2}$

capable of being indexed from more than one variant.

As was observed by comparing the diffraction patterns of Figure 25 and 26, a majority of fine detail is lost due to the thick scale and the many variants of the oxide involved. By studying progressively thinner regions of the oxide scale, much more detailed information was obtainable. The thinner regions were present at the edge of the hole through the scale in the microscope specimen or at regions that were preferrentially ion-thinned away. Near the edge of the hole in the microscope specimen, the platelets that were shown in the previous bright field image of the oxide scale could be individually observed and studied. Figure 27 shows one such case in which a platelet extends outward over the hole in the specimen.

The microstructure is observed to consist of linear fringes corresponding to planar faults running along the length of the particle. The diffraction patterns in Figure 28 serve to provide some insight into the nature of the microstructure. In Figure 28a, the specimen has been tilted so that the electron beam is parallel to what appears to be a $[011]_\gamma$ zone axis. Streaking is observed along the $[\bar{1}1\bar{1}]_\gamma$ direction. This streaking in the reciprocal lattice of the platelet is due to relrods perpendicular to the fringes in the real lattice. Although the streaking is along the $[\bar{1}1\bar{1}]$ direction in Figure 28a, it is only a projection on the $[011]_\gamma$ of the streaking intersecting the Ewald sphere. This is observed by tilting to various zone axes(Figure 28b-e) of

Figure 27 50nm

Bright field image of an oxide platelet extending over the hole of the TEM specimen. Fringes corresponding to planar faults are indicated.

ORIGINAL PAGE IS
OF POOR QUALITY

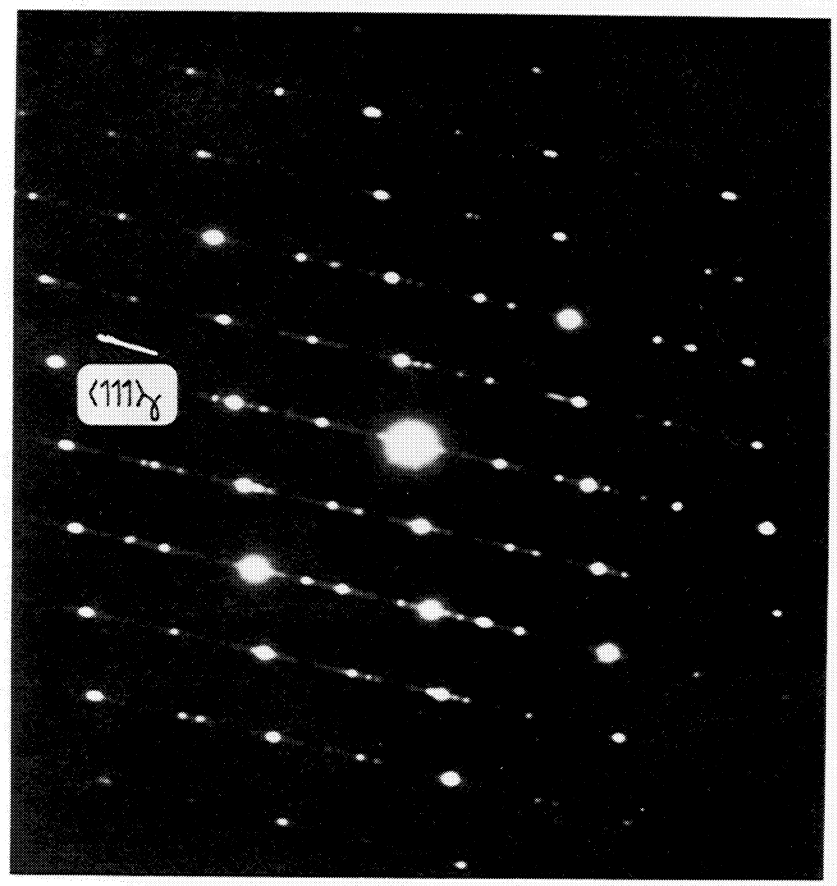

a)

Figure 28

Selected area diffraction patterns of the oxide platelet of Figure 27. a) pattern resembles a $[013]_\delta$ zone but has streaking through a $\langle 111 \rangle_\gamma$ direction and extra reflections, b) pattern resembles a $[100]_\delta$ zone, c) mirror symmetry is absent along a $[001]_\delta$ direction, d) smallest spacing between reflections corresponds to an interplanar spacing of 4.6 nm which is twice the c_o spacing of δ-Al_2O_3.

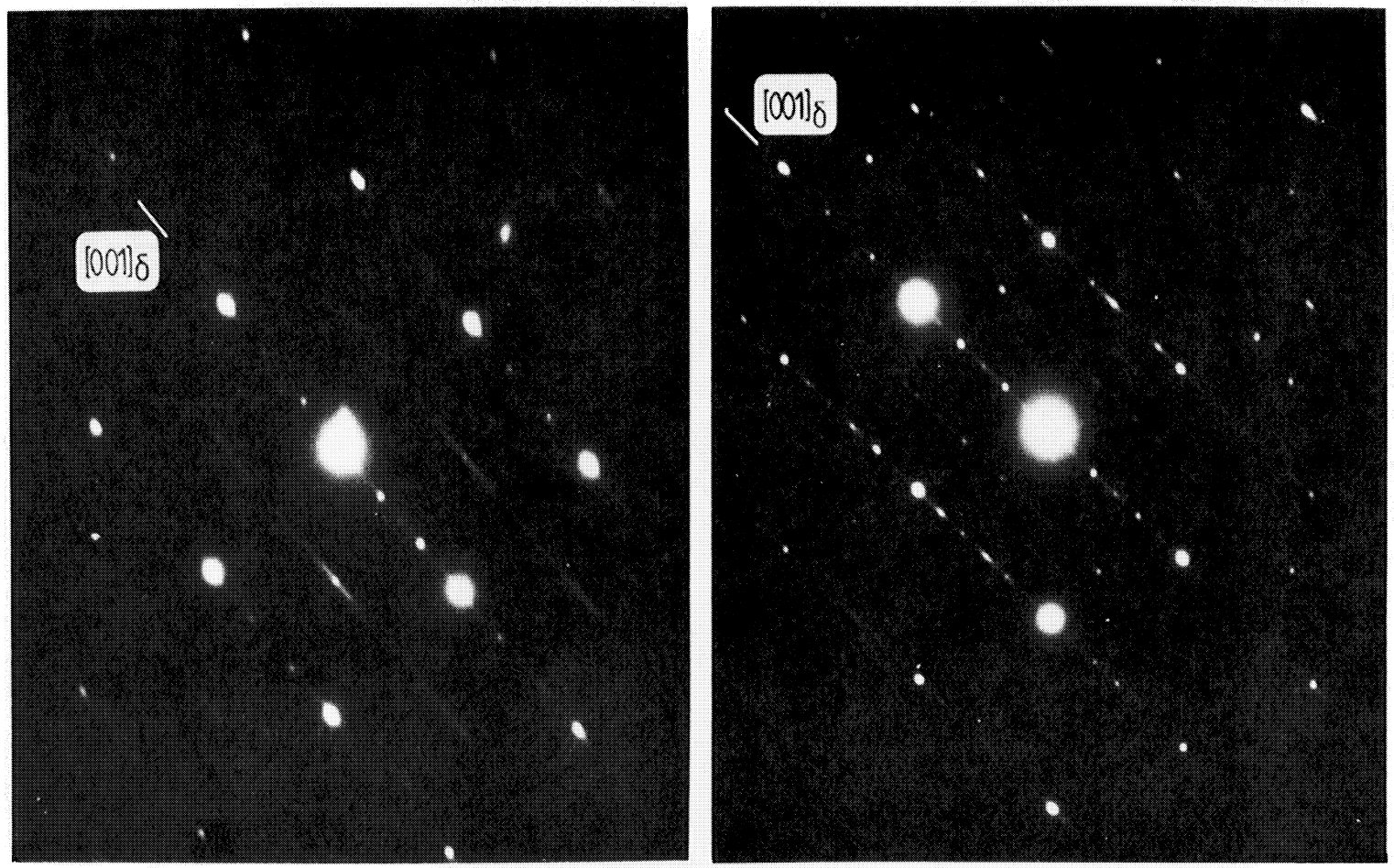

b) c)

Figure 28b) and c)

ORIGINAL PAGE IS
OF POOR QUALITY

d)

e)

Figure 28d) and e)

the crystal and observing the change in direction of the streaks. By plotting the directions of the streaking on a stereographic projection, the streaks are observed to be perpendicular to a $\{110\}_\gamma$ plane(Figure 29).

The diffraction patterns in Figure 28 serve to help identify the structure. Many of the zones correspond to spinel type zones, but are obviously not from a cubic structure. If the $1/3(400)_\gamma$ reflections in Figure 28c arise from the characteristic reflections of δ-Al_2O_3, there should be a mirror symmetry along this direction. Because a mirror symmetry is absent along the $[001]_\delta$ direction in Figure 28c, the diffraction pattern must be of a structure having a lower symmetry than tetragonal. From analysis of the diffraction patterns, the structure appears to be monoclinic, similar to θ-Al_2O_3. However, some features do not correspond to the quoted monoclinic structure. These features are the streaking and the extra reflections along the streaks. Yamaguchi et al. have observed a similar phenomenon in θ-Al_2O_3 derived from boehmite.[49] They attributed the extra reflections to twinning arising from a twin plane along one of two $\{110\}_\gamma$ mirror planes in the crystal structure of θ-Al_2O_3(Figure 30). A high resolution bright field image is shown in Figure 31 and contains regions of fringes having different spacings and periodicities. The finest fringe spacing is 0.81 nm which corresponds to the a_o spacing of δ-Al_2O_3. The fringes have various periodicities with longest periodicity being indicated by the small spacings of

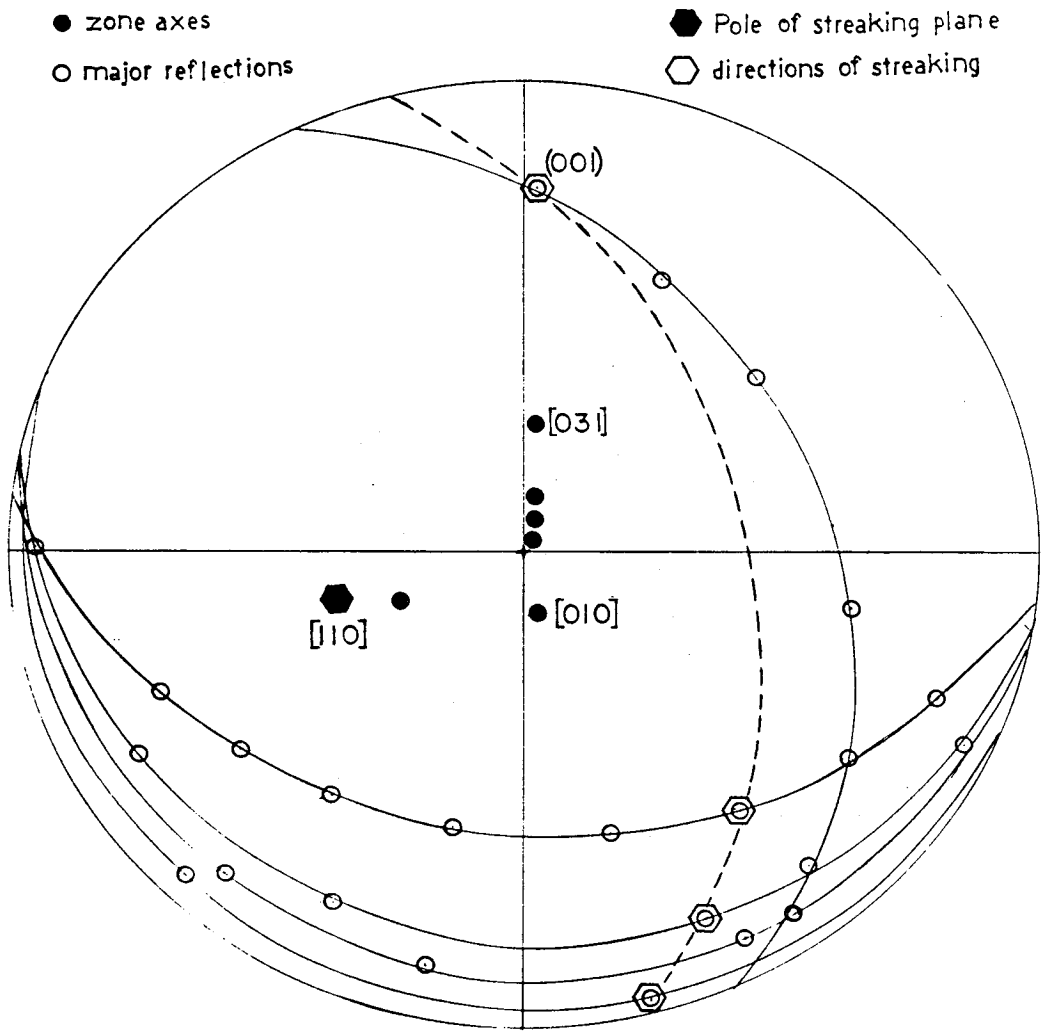

Figure 29

Stereographic projection showing that the direction of streaking in the diffraction patterns of Figure 28 is the $[110]_{\gamma}$ direction.

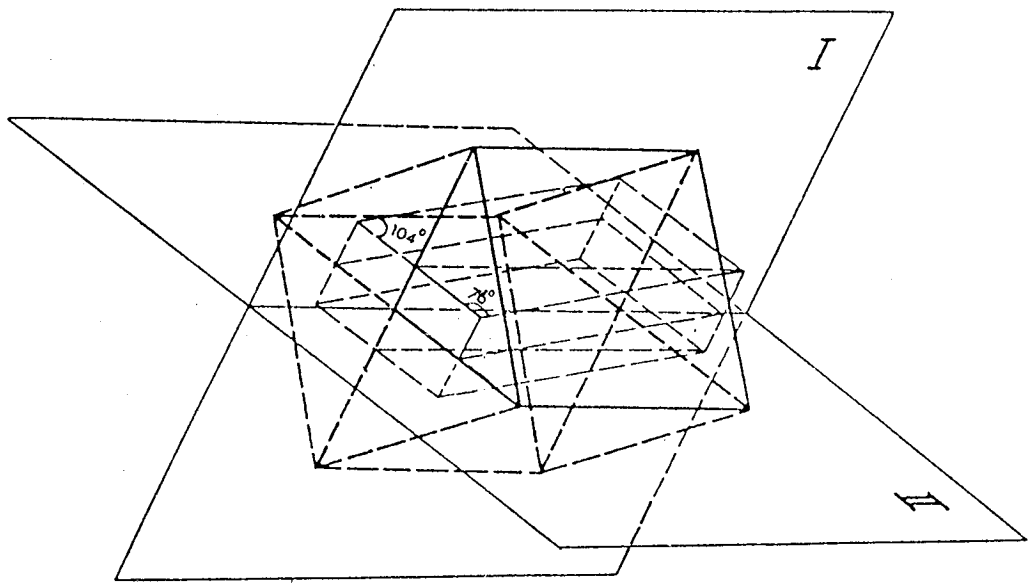

Figure 30

Perspective drawing of the structure of γ-Al_2O_3 with that of θ-Al_2O_3 showing the two $\{110\}\gamma$ mirror planes. (Ref. 49).

ORIGINAL PAGE IS
OF POOR QUALITY

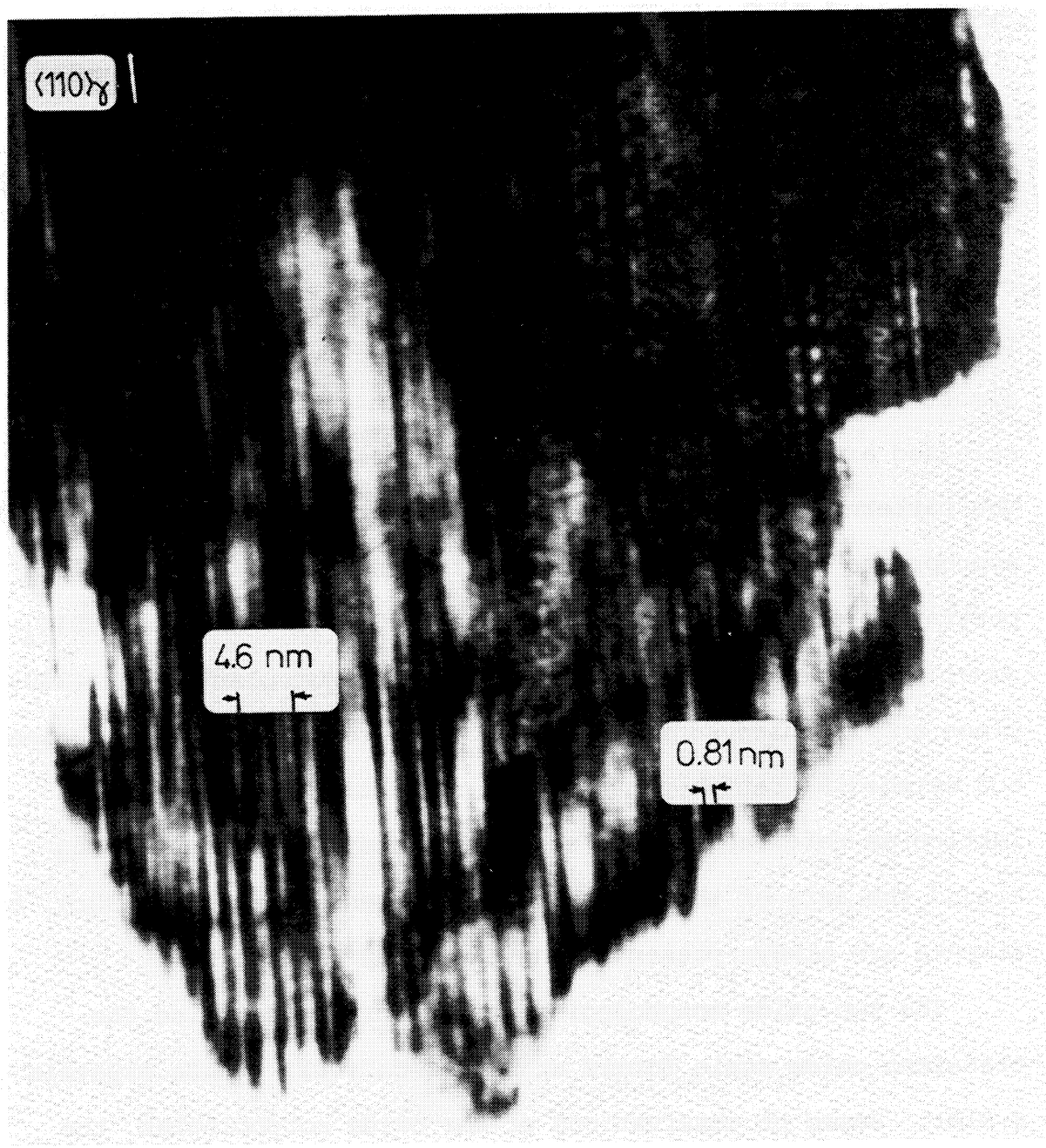

Figure 31 5.0nm

High-resolution bright field image of the platelet in Figure 27 showing various periodicities and spacings of fringes. The smallest fringe spacing(0.81 nm) and largest periodicity(4.6 nm) are indicated.

diffraction spots in Figure 28d. The smallest spacing in the diffraction pattern is 4.6 nm which corresponds to twice the c_o spacing in δ-Al_2O_3.

In an ion-thinned region of the oxide scale, the transient oxide was dramatically different in both phase and morphology. Figure 32 contains images of this interior part of the scale. The microstructure consists of regions of oxide in which many crystallographic variants are imaged separately. In regions where the diffracting conditions are not optimized, the scale appears almost uniform, showing few features. In Figure 33, three selected area diffraction patterns of these regions are shown. The patterns are clearly indexed to be tetragonal δ-Al_2O_3 with the appropriate zone axes indicated. Figures 33a and 33b are clear portrayals of the differences in the [100]δ zone and the $[001]_\delta$ zone. The streaking in Figure 33b is perpendicular to the (110)δ plane and is observed to intersect what would be the major anion and octahedral cation-contributing reflections of the spinel lattice as referred to earlier in this chapter. When tilting around the axis of the streak to a different zone(Figure 32c), the streaks are always present along the $[110]_\gamma$ direction.

The two oxide morphologies just described comprise the transient oxide scale formed at 1100°C on (001) single crystals of β-NiAl. Based on observations of the oxide morphologies, the blade-like platelets are believed to be a result of fast growth of the oxide scale. The fast growth results in monoclinic θ-Al_2O_3.

ORIGINAL PAGE IS
OF POOR QUALITY

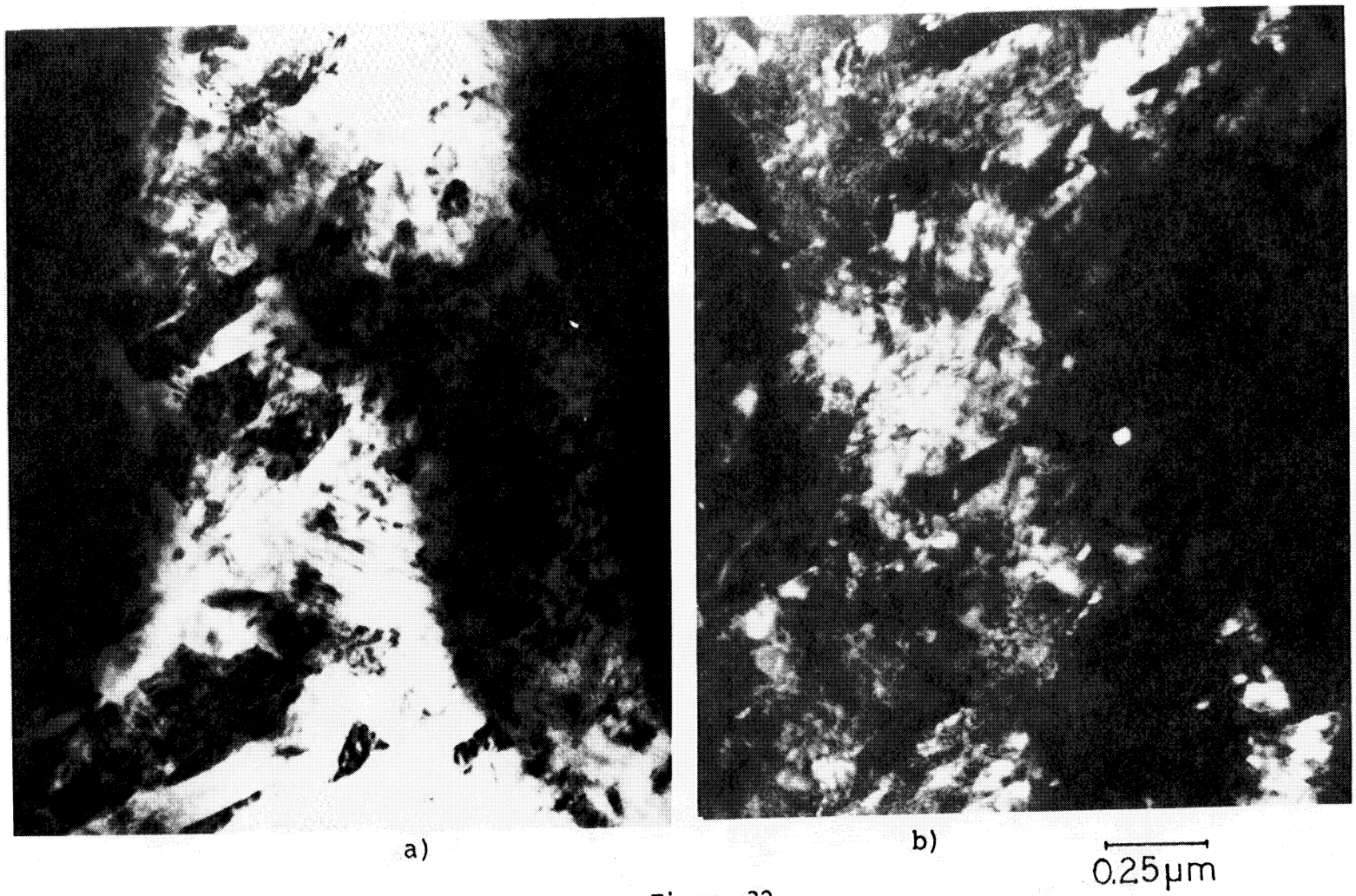

Figure 32

a) Bright field image of an interior part of the scale formed on a (001) β-NiAl specimen oxidized for 1.0 hours at 1100°C. The contrasting regions are different variants of the oxide. b) correspnding dark field image.

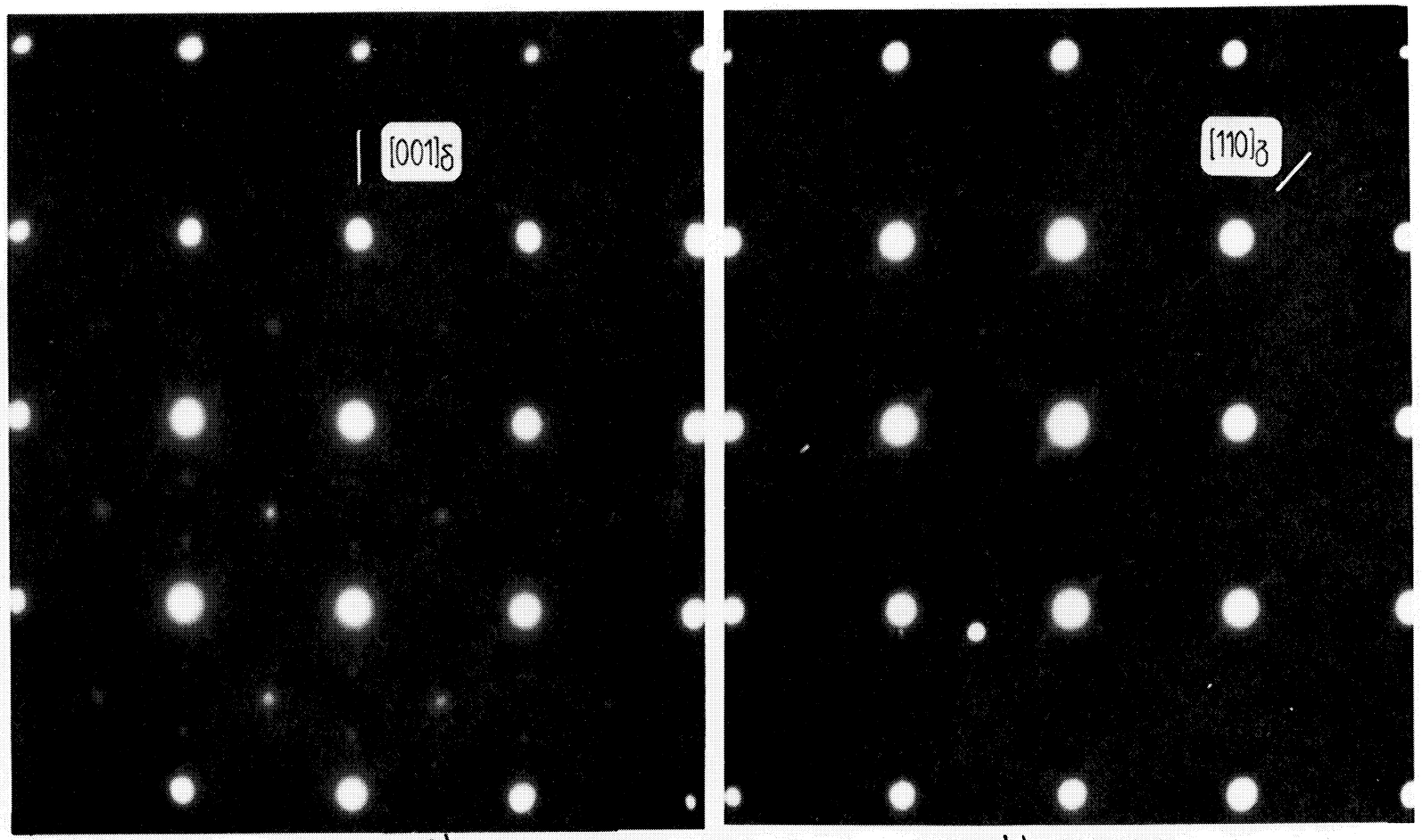

a) b)

Figure 33

Selected area diffraction pattern of an oxide scale formed on a (001) β-NiAl specimen oxidized for 1.0 hours at 1100°C. The patterns are indexed to be a) $[100]_\delta$ zone, b) $[001]_\delta$ zone in which streaking is along the $[110]_\delta$ direction, c) a $[11\bar{9}]_\delta$ zone in which streaking along $[110]_\delta$ is also evident.

ORIGINAL PAGE IS
OF POOR QUALITY

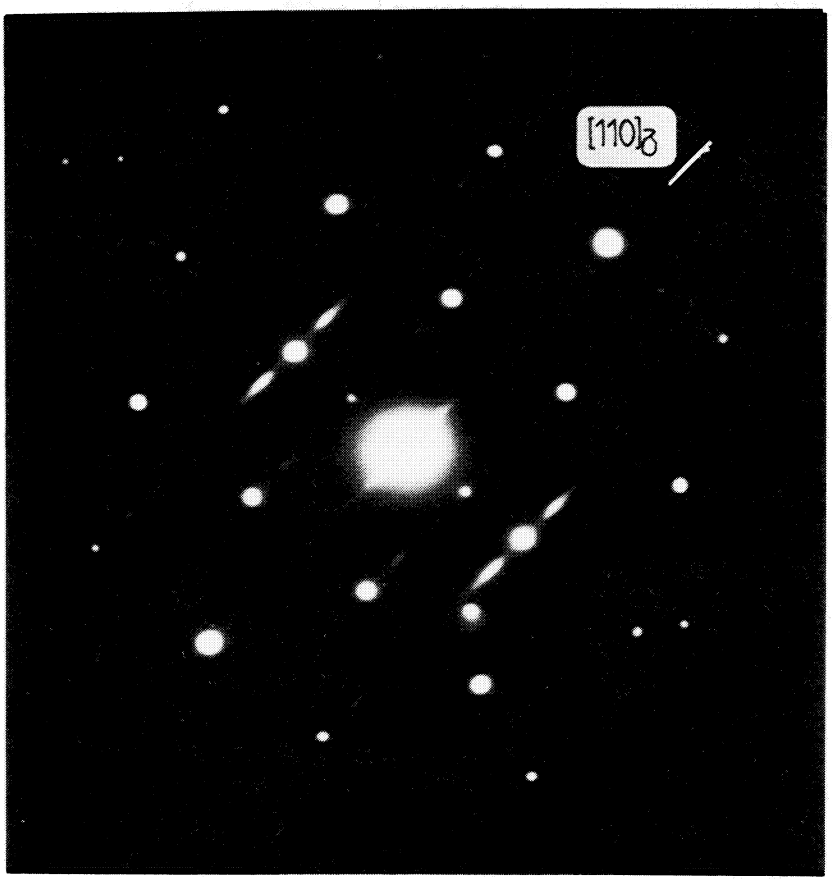

Figure 33c)

C-3

The underlying transient scale consists of the agglomeration of these platelets forming a less-faulted δ-Al_2O_3 structure. As previously mentioned, both phases have been found to exist up to the transformation to α-Al_2O_3. Although θ-Al_2O_3 is thermodynamically more stable than δ-Al_2O_3, the phases co-exist under the restrictions of an epitaxial oxide scale.

b. Polycrystal. This section contains a brief discussion of the observations of surface oxide morphologies of polycrystalline specimens oxidized at 1100°C for times greater than 1.0 hours. The experimental conditions for these specimens were different than for all other specimens. In this case, less control was maintained on surface preparation, chemical homogeneity of the alloy and oxidizing environment. However, results of these SEM studies do indicate a large effect of metal orientation on oxide morphologies.

Figure 34a is an SEM image of the gas-oxide surface of a polycrystalline specimen oxidized for 50 hours at 1100°C. Although x-ray diffraction experiments indicate the scale is completely α-Al_2O_3, meaning that the transformation has already occurred, TEM studies by imaging and electron diffraction indicate that a thin surface layer consists of the same monoclinic structure as discussed in the previous section. The surface layer must have be too thin to be detected by standard x-ray diffraction. The reason that the metastable Al_2O_3 phase is still

ORIGINAL PAGE IS
OF POOR QUALITY

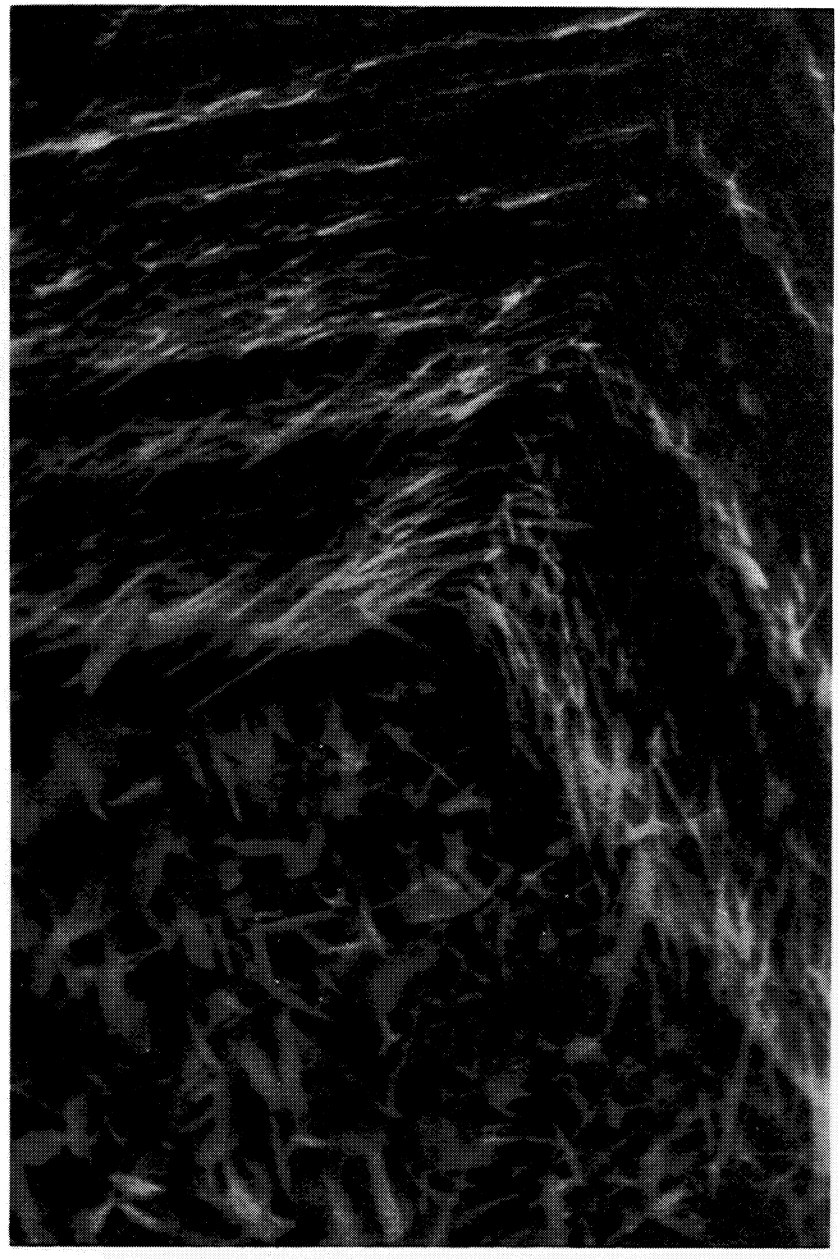

a) 1.0μm

Figure 34

SEM images of the transient morphology on the gas-oxide surface of polycrystalline β-NiAl specimen oxidized for 50 hours at 1100° showing a) a triple point in the metal showing the various morphologies formed on different grains, b) a fine, needle morphology, c) textured blades.

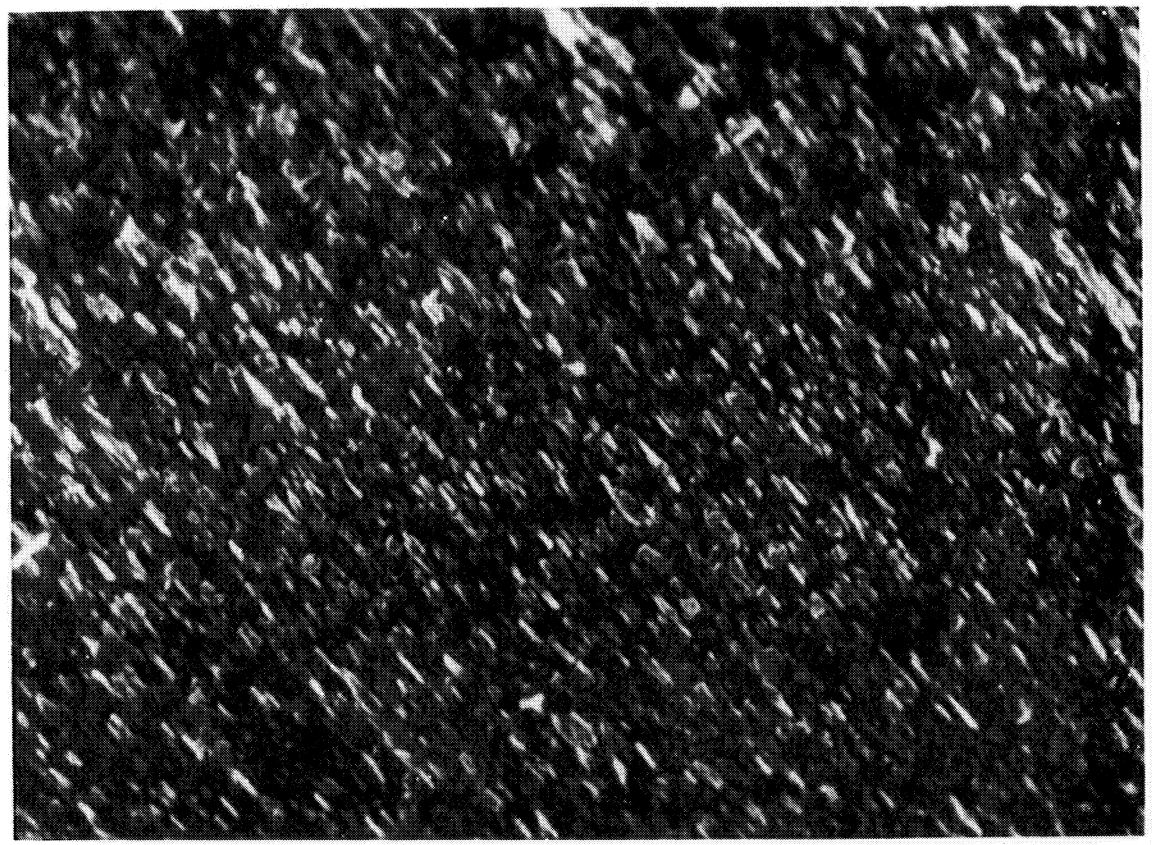

1.0 μm

Figure 34b)

ORIGINAL PAGE IS
OF POOR QUALITY

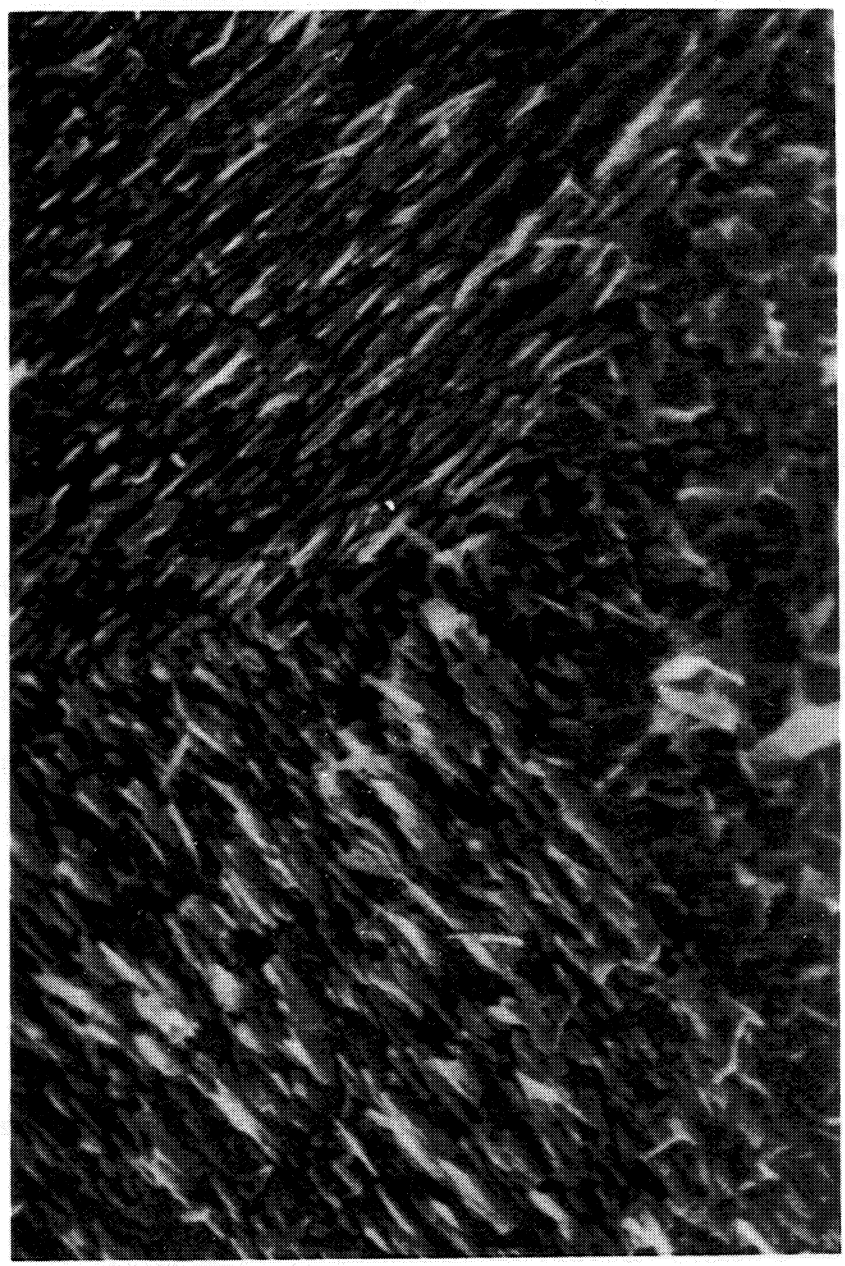

1.0 μm

Figure 34c)

present after 50 hours of oxidation at 1100°C will be dealt with later. This layer is θ-Al_2O_3 and is a remnant of the transient stage of oxidation at 1100°C. The oxide morphologies have all been developed during the transient stage.

The major SEM observation is the difference in oxide morphology on different metal orientations of the polycrystalline β-NiAl substrate. As shown in the previous section, the surface oxides formed on (001) orientations are platelets. On some metal orientations, the oxide morphology is a very fine needle-like structure(Figure 34b). Some metal orientations show oxide morphologies that are oriented blades(Figure 34c).

Although attempts at observing consistencies of metal orientation with both oxide texture and morphology were inconclusive, the effect of metal orientation has been shown to be quite drastic. With reference to the successful results for (001) metal orientations, the effect of metal orientation is believed to result from the effect of epitaxy between the oxide and metal upon scale formation.

3. Summary

The 1100°C transient oxidation of β-NiAl results in the formation of a complex scale consisting of both δ-Al_2O_3 and θ-Al_2O_3. The δ-Al_2O_3 matrix found on (001) single crystals of

β-NiAl contains planar faults parallel to {110}γ. Planar faults are also observed in the fast growth morphology of θ-Al_2O_3. The fast growth morphology of θ-Al_2O_3 results from outward diffusion of cations along high diffusivity paths, as described by Voss, for growth of hematite blades on iron.[50] On (001) substrate orientations, the morphology of θ-Al_2O_3 is blade-like and is textured to reflect the Bain orientation relationship between metal and oxide. However, on other substrate orientations, the θ-Al_2O_3 morphology varies dramatically. This dependence of morphology on metal orientation is believed to result from the preferred oxide orientation arising from the metal-oxide orientation relationships. This morphological change could also explain changes in growth rates of oxide scales on different metal orientations.

D. Concluding remarks on the transient oxidation of β-NiAl

This chapter has been devoted to the study of the transient oxidation of β-NiAl at 800°C and 1100°C. Although these two temperatures do not represent the entire transient region, this range of temperatures spans the applicable range of use for this alloy. The results have been presented in terms of microstructural development and mechanisms of scale growth.

As was mentioned in a previous study, the metastable Al_2O_3 phases comprise the majority of the oxide scales at 800°C.[33] The particular phase present within the scale has been shown to be a function of temperature, time and substrate orientation. As is expected from the transformation sequence of Al_2O_3, the initial phases to form are cubic defective spinels with the general name of γ-Al_2O_3. The scale morphology consists of a fine-grained oxide having a definite tendency to form with an epitaxial relationship to the underlying metal substrate. On (001) metal orientations, planar faults are observed which tend to have a periodicity of $3a_o$ with respect to the spinel unit cell. This periodicity is indicative of the presence of tetragonal δ-Al_2O_3. The formation of δ-Al_2O_3 from γ-Al_2O_3 occurs by formation of a distinct periodicity of these faults. Because δ-Al_2O_3 is observed as the scale matrix phase at 1100°C, it is believed that this is the most common phase for oxidation of β-NiAl. θ-Al_2O_3 is observed as a fast growth morphology when specimens are oxidized at 1100°C. Although θ-Al_2O_3 is considered to be thermodynamically more stable than δ-Al_2O_3, it does not appear to form directly on the metal in preference to δ-Al_2O_3. The strong tendency of the oxide to grow with an epitaxial relationship to the metal appears to promote formation of δ-Al_2O_3 over θ-Al_2O_3. A schematic is shown in Figure 35 which summarizes the evolution and growth of a transient scale formed on β-NiAl up until the transformation to α-Al_2O_3.

The method of producing metastable Al_2O_3 phases appears to

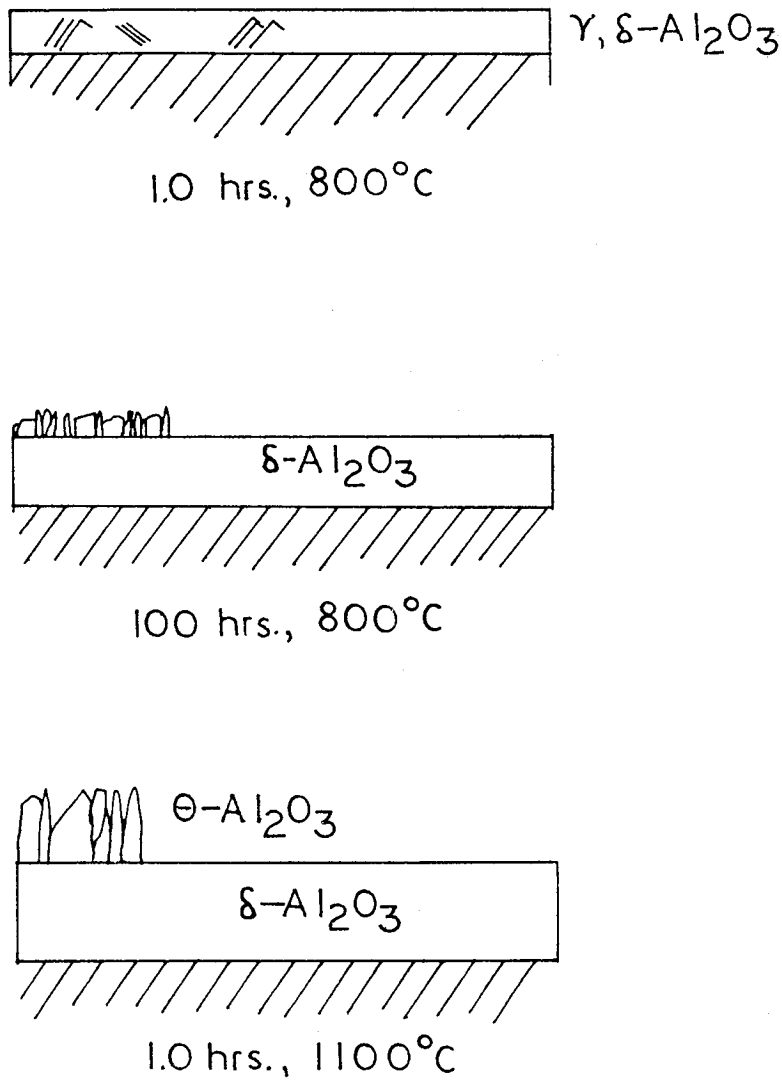

Figure 35

Schematic of the transient oxidation of β-NiAl. a) Initially, oxides of all metal constituents form with faulted γ-Al_2O_3 being the predominant phase after 1.0 hours at 800°C. b) Longer oxidation times at 800°C produce δ-Al_2O_3 scales with various surface morphologies being a function of metal orientation. c) At higher temperatures(e.g. 1100°C), a fast-growth surface layer of θ-Al_2O_3 lies above an inner δ-Al_2O_3 scale.

have a strong influence on their thermodynamic and kinetic properties. For thermal oxidation, this study has shown that δ-Al_2O_3 is the most stable transition alumina phase. However, when scales are stripped from the substrate and then heated at temperatures similar to those used for oxidation, the resulting phases and morphologies change drastically. New transition alumina phases have been discovered which appear to depend strictly on the environment. Kear et al. attributed the formation of their orthorhombic Y phase to the lowering of the oxygen partial pressure near the metal oxide interface within a scale.[6] The oxide phase resembles other transition aluminas, but had not been previously observed or reported since. Another study was performed in which TEM specimens of β-NiAl oxidized for 10.0 hours at 800°C and backthinned were heated to much high temperatures while being observed with a high voltage electron microscope. This study is described in Appendix C. The specimens were heated to temperatures above 1100°C for up to 0.5 hours in the microscope vacuum without transforming to α-Al_2O_3. Rather, new transient phases based on the spinel structure were formed.

The growth rates and growth mechanisms of scales formed on β-NiAl appear to be similar in situations where outward cation diffusion predominates. A plot of the logarithm of parabolic growth rate constants versus reciprocal temperature from previous studies is shown in Figure 36. Included within this plot are the results from the present study. The activation energy of scale

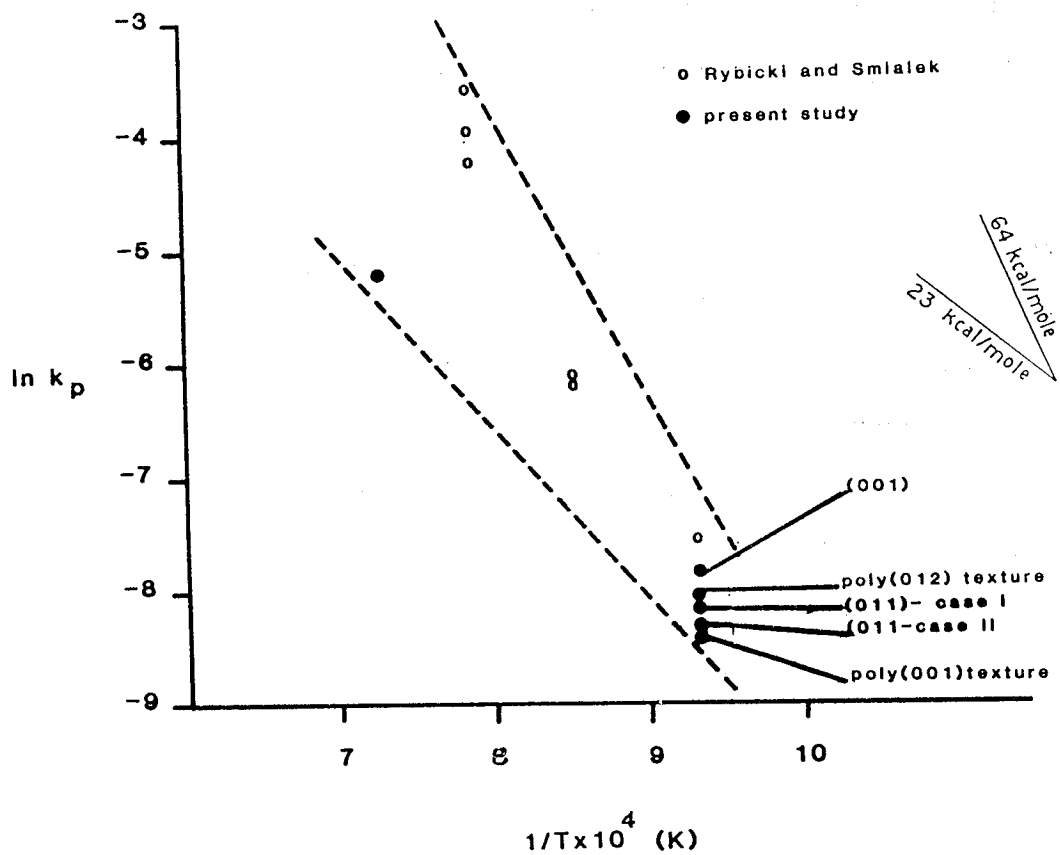

Figure 36

Logarithm of parabolic rate constant, k_p, as a function of reciprocal temperature to determine activation energies of diffusion for the transient oxidation of β-NiAl. The large scatter in data prevents accurate determination of diffusion mechanisms.

growth is represented by the slope of the line drawn through the data points. This activation energy should represent the activation energy of aluminum diffusion in the transition alumina phases. However, as shown in the polycrystalline study, the growth rate changes as a function of substrate orientation. Because of scatter in data points, it is impossible to determine the diffusion mechanism. Therefore, determination of scale growth by short circuit or bulk diffusion cannot be provided by these studies.

The importance of this study on the transient stage of oxidation of β-NiAl comes from the knowledge gained on scale growth properties as well as information on metastable Al_2O_3 formation and transformations. The effect of metal orientation has been shown to be responsible for many of the observable changes in oxide phases, morphologies and growth rates. This information will be applied to the following studies on the transformation to and growth of stable α-Al_2O_3 scales.

II. The Transformation to α-Al_2O_3

The stable form of Al_2O_3 is the alpha phase which is the mineral corundum. During oxidation, the attainment of a complete layer of α-Al_2O_3 dictates the beginning of the steady state region. The previous chapter has dealt with the transient stages of oxidation of β-NiAl to better define the starting point of the transition region in which metastable Al_2O_3 phases transform to α-Al_2O_3. This chapter deals with the mechanisms of the metastable γ-Al_2O_3 to α-Al_2O_3 (now called $\gamma \rightarrow \alpha$) transformation. Particular attention is paid to the crystallography of the transformation and the resultant microstructures of the transformed oxide.

A. Review of previous studies

Numerous authors have studied the $\gamma \rightarrow \alpha$ transformation, most of them investigating the change in catalytic and sintering properties of alumina. The starting materials include commercial alumina powder, sol-gel precipitated alumina, plasma sprayed aluminas, and thermally grown γ-Al_2O_3 layers stripped from the metal. No study has implicitly dealt with the present situation

involving the transformation of a thermally grown transient scale to an α-Al_2O_3 scale. However, the knowledge gained from the previous studies can often be applied to the present work. The current thermodynamic, kinetic and crystallographic understanding of the $\gamma \rightarrow \alpha$ transformation are therefore reviewed in the following sections.

1. Thermodynamics of the $\gamma \rightarrow \alpha$ transformation

The free energies of formation of various metastable Al_2O_3 phase have been tabulatd in a review paper by Carniglia, and are shown in Table VI for applicable phases.[51] The data have been compiled from many studies, calculated or estimated as required. The dehydrated forms of Al_2O_3 are much more stable than the hydrated forms at temperatures where appreciable oxidation occurs. Also, α-Al_2O_3 is more stable than δ-Al_2O_3 which is more stable than γ-Al_2O_3. The change in free energy of transformation to α-Al_2O_3 has been plotted in Figure 37 using the values from Table VI to show the irreversibility of the $\gamma \rightarrow \alpha$ transformation.

However, the transformation seldom proceeds according to equilibrium conditions. The observed transition temperatures usually exceed the equilibrium transition temperatures by 100°C or more. Three main points regarding the transformation series have been mentioned: 1) all transitions in these series are thermally

TABLE VI

Free energies of formation for crystalline aluminas.(Ref. 51).

	$-\Delta G_f^o$(kJ/g·mole)		
Temp.(°K)	γ-Al_2O_3	δ-Al_2O_3	α-Al_2O_3
298	1564.6	1573.7	1583.0
400	1532.7	1541.6	1550.9
500	1501.6	1510.2	1519.4
600	1470.5	1478.9	1488.0
700	1439.7	1447.8	1456.7
800	1409.1	1417.0	1425.6
900	1378.7	1386.2	1394.5
1000	1346.9	1354.0	1362.0
1100	1314.5	1321.2	1328.8
1200	1282.2	1286.5	1295.7
1300	[1250.1]*	1255.9	1262.7
1400	[1218.1]	1223.4	1229.7
1500	[1186.2]	[1191.1]	1196.9
1600	[1154.5]	[1158.9]	1164.2

*Brackets are used where a given species is not ordinarily encountered.

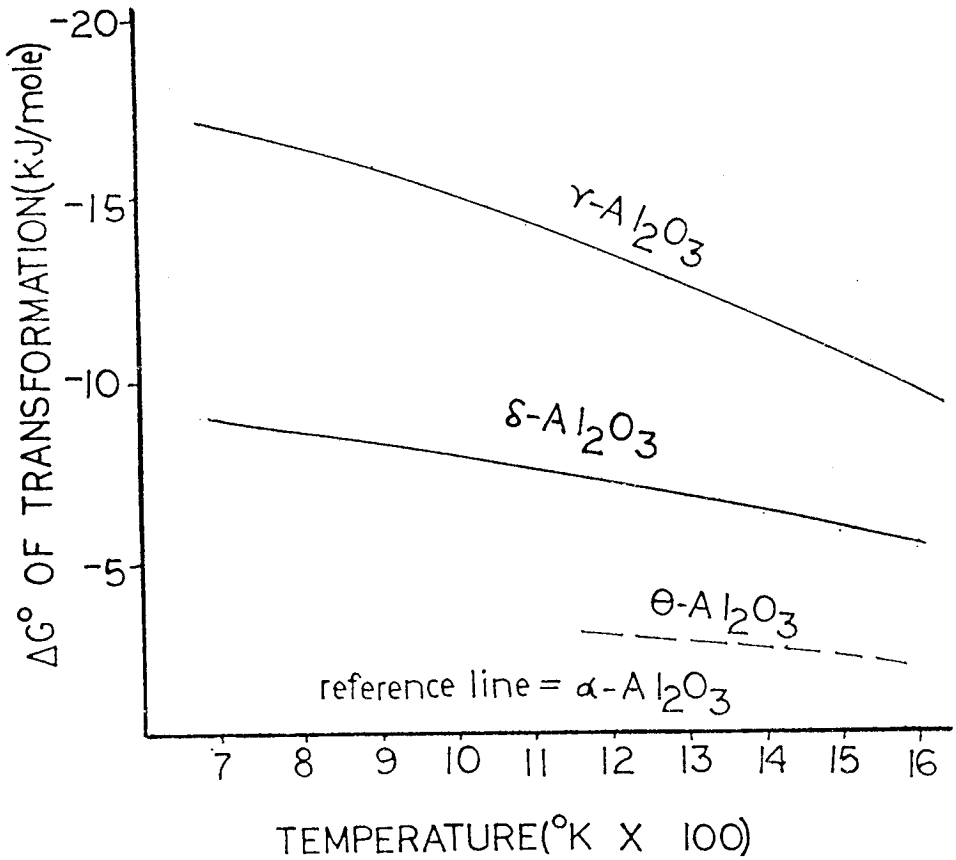

Figure 37

Change in free energy of transformation to α-Al_2O_3 as a function of temperature using values from Table VI. The values of ΔG for θ-Al_2O_3 have been estimated. (Ref. 51).

activated only at temperatures far above the thermodynamic minimum so that kinetics play the important role in transformation, 2) most transitions observed with increasing temperature cannot be retraced in reverse, 3) numerous transitions that are highly favored thermodynamically are never seen at all.

Because the transitions are irreversible, phase equilbria determination is generally impossible. Also, numerous reports of high activation energy barriers due to surface, crystallographic and other effects add to the difficulties in determining phase equilibria conditions.

Although equilibrium conditions appear to be impossible to define, some conclusions can be drawn. α-Al_2O_3 is the most stable phase of Al_2O_3 with the transformation to α-Al_2O_3 being irreversible. The thermodynamics are effected by many physical properties which are referred to later such as precursor morphology, orientation, surface condition, externally applied electric fields, impurities and stress state. These factors will also be shown to affect the kinetics of transformation as well.

2. Kinetics of the $\gamma \rightarrow \alpha$ transformation

A comparison of data from studies on the kinetics of the $\gamma \rightarrow \alpha$ transformation becomes tedious because of effects mentioned in the previous section. Therefore, a brief description of the studies

will be provided with the following summary.

A study by Clark and White revealed that first order kinetics were observed for the first 50% of γ-Al_2O_3 transformed into α-Al_2O_3.[52] Their starting material was derived from bayerite in contrast to material from a study by Steiner which was alum derived.[53] In the latter material, zero order kinetics were observed. The differences between the two results was attributed to a variation in starting material composition and crystallinity. Discrepancies in activation energies were attibuted to different forms of metastable Al_2O_3, i.e. δ-Al_2O_3 or θ-Al_2O_3 instead of γ-Al_2O_3.

Dynys and Halloran performed a kinetic study of the transformation beginning with alum-derived γ-Al_2O_3.[54] Various pre-treatments were found to effect the incubation time and rates of reaction. Mechanical treatments that would induce heterogeneities tended to hasten the overall transformation process. The morphology of the subsequent α-Al_2O_3 colonies showed remnants of the pretransformed γ-Al_2O_3 "wormy" morphology, although much more porosity was noted in the α-Al_2O_3 colonies than in the γ-Al_2O_3 matrix. The kinetics were described in terms of nucleation and growth with growth of α-Al_2O_3 being controlled by surface diffusion.

Surface effects played a major role in the study of precipitation of α-Al_2O_3 in non-stochiometric Mg-Al spinels by Donlon, Mitchell and Heuer.[55] A large nucleation barrier for

α-Al_2O_3 precipitation was concluded to result from the large strain energy involved in the transformation. Linear growth kinetics of the surface α-Al_2O_3 precipitates were observed.

Bye and Simpkin have studied the effects of Cr and Fe additions on the $\gamma \rightarrow \alpha$ transformation.[56] Their results indicate that Fe enhances α-Al_2O_3 formation and Cr deters α-Al_2O_3 formation. Little attempt was made to describe the approximate linear kinetics they observed because of the many factors mentioned earlier that affect results.

The kinetics of the $\gamma \rightarrow \alpha$ transformation were found to be effected by an external electric field.[57] The transformation was inhibited near the cathode to which an excess of spinel stabilizating protons migrated. The effect of spinel stabilization by hydroxyl ions was observed with hydrated metastable Al_2O_3 phases on oxide scales by Ramanarayanan.[58]

The results from previous studies indicate there are many unknown variables that first must be characterized before a complete description of kinetics can be given. This was found to be the case for the thermodynamics and will be shown to be correct for the mechanisms of transformation as well.

3. Crystallography and mechanisms of the $\gamma \rightarrow \alpha$ transformation

The transformation from metastable Al_2O_3 phases can be described by a reconstruction of the anion sublattice with subsequent shifting of cations.[59] The mechanisms by which this occurs has been descibed in terms of both a diffusion controlled and a diffusionless transformation. Ridge et al. have proposed that the transformation of cubic to trigonal(rhombohedral) Fe_2O_3 powder occurs by a surface diffusion process.[60] The temperature at which the transformation takes place is in between the temperature at which surface diffusion becomes effective (approximately 350°C for Fe_2O_3) and the Tammann temperature, the temperature at which defect mobility becomes substantial (approximately 650°C in Fe_2O_3). The conclusion that the transformation occurs by a diffusion process was drawn from the result that water vapor catalyzed the transformation which would not be the case if the transformation was diffusionless. The differences in surface diffusion properties of the two iron oxide phases in question were not mentioned in the results. However, the results can still be applied to a nucleation and growth mechanism such that the nuclei of α-Fe_2O_3 are constantly fed by surface diffusion. An added comment suggested that the transformation could be initiated at the surface by short-range diffusion and grow by a diffusionless transformation.

Dynys and Halloran have suggested that the growth of α-Al_2O_3 following the transformation was controlled by surface diffusion.[54] Very porous α-Al_2O_3 colonies were observed in a

γ-Al_2O_3 matrix, but no pores were observed at the interface between γ-Al_2O_3 and α-Al_2O_3. Also the particle spacings fits an empirical model in which surface diffusion is responsible for growth.

The most convincing argument for a definite transformation mechanism was provided by Kachi and co-workers in their study of the transformation in Fe_2O_3 which has been applied to the same phenomenon in Al_2O_3.[61] The transformation can be described by a dislocation model in which there are cooperative shifts of anions and cations. This mechanism, known as synchro-shear, was first described by Kronberg[62] for α-Al_2O_3 and later by Hornstra[63] for the spinel structure. Kachi et al. have applied the synchro-shear mechanism to the specific case of the $\gamma \rightarrow \alpha$ transformation in Fe_2O_3.

It is necessary to describe the structures of both the spinel and rhombohedral oxide phases before the transformation can be discussed because similar rearrangements occur in both structures. The structure of the spinel phase(γ-Fe_2O_3 and γ-Al_2O_3) can be described as an ABCABC stacking of oxygen ions on {111} planes and Fe or Al ions as interstitial arrays between them. Two different arrays comprise the cation layers between the close-packed oxygen layers. One cation layer is called the "kagome" lattice and the other, the "mixed" lattice. In the kagome lattice, all cation lattice points are surrounded by six oxygen ions forming arrays of hexagons and triangles in two dimensions(Figure 38a). In the kagome lattice, all of the cations lie in octahedral sites of the

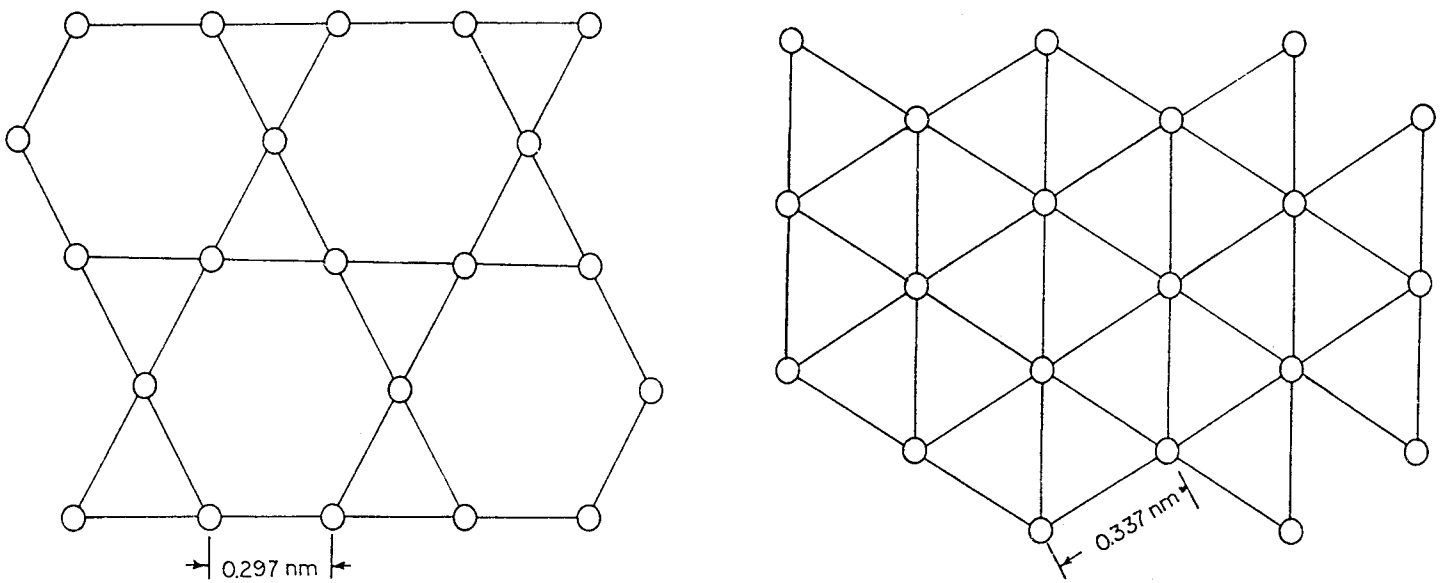

a) b)

Figure 38

Schematic of cation sublattices in the spinel structure on <111> planes.
a) the kagome lattice, b) the mixed lattice.(Ref. 61).

anion lattice. In the mixed lattice, one third of the cation sites are in octahedral positions and two thirds in tetrahedral positions(Figure 38b). The kagome and mixed cation layers alternate between the close-packed oxygen layers. The interatomic distance between atoms in the kagome and mixed layer in γ-Fe_2O_3 are 0.297 nm and 0.337 nm respectively. To preserve stoichiometry, one ninth of the cation sites must be occupied by vacancies in the defect structure of both γ-Fe_2O_3 and γ-Al_2O_3.

The structure of the α-Fe_2O_3 and α-Al_2O_3 rhombohedral phases can be described as close-packed oxygen layers on the basal planes stacked in an ACACAC sequence. The cations form a "honeycomb" lattice(Figure 39), in between the close-packed oxygen layers to form an overall ABCABC stacking sequence of cation between the anions. The interatomic spacing in the honeycomb cation lattice of α-Fe_2O_3 is 0.290 nm. The spacings and structure of the honeycomb lattice in α-Fe_2O_3 and α-Al_2O_3 are similar to the kagome cation layer in γ-Fe_2O_3 and γ-Al_2O_3.

The actual transformation is described as a shear mechanism of "sandwiched" close-packed oxygen layers of the spinel structure with a synchronous motion of cations. The "sandwich" consists of two close-packed oxygen layers with a kagome layer of cations in the middle. The magnitude of the Burgers vector and direction of the shear is $^{a}/_{\sqrt{3}}$ in the <112> directions with respect to a sandwich above or below; in much the same way the FCC→HCP transformation in cobalt has been described.[64] Simultaneously

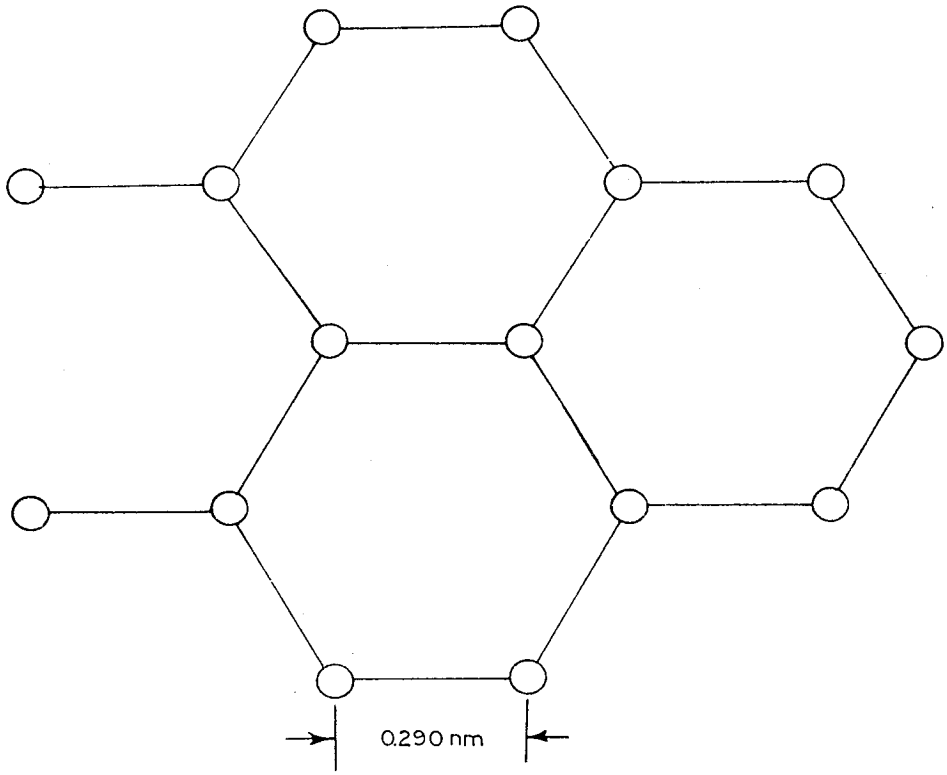

Figure 39

Schematic of the "honeycomb" sublattice of cations on basal planes of the rhombohedral oxide phases, α-Al_2O_3 and α-Fe_2O_3.(Ref. 61)

with the motion of the oxygen-kagome-oxygen sandwich, cations in the tetrahedral sites of the mixed layers are dragged along with the sandwiches. However, cations in octahedral sites of the mixed layer move across saddle points between two oxygen ions of the sheared planes with the same displacement magnitude, but in <112> directions 60° from the direction of shear of the sandwiched layers. The overall process produces an ACACAC stacking sequence of close-packed oxygen layers with all cations in octahedral sites. Finally, one fourth of the cations must undergo short-range movements along $\langle 01\bar{1}0 \rangle$ directions to develop the honeycomb cation lattice of the stable rhombohedral oxide phase. A simplified schematic of the synchro-shear process in spinels was developed by Hornstra and is shown in Figure 40. This schematic can be applied to the $\gamma \rightarrow \alpha$ transformation by assuming the shear corresponds to oxygen-kagome-oxygen sandwiches instead of <111> cation layers.

The mechanisms of synchro-shear and surface diffusion controlled nucleation and growth have been applied to many studies on transformations in Fe_2O_3 and Al_2O_3, but have not been experimentally proven for all cases. Many characteristics of the materials, such as parent and product morphologies, porosity, orientation relationships between the parent and the product phases, effects of impurities and transformation kinetics tend to support or detract from the proposed mechanisms. Kachi et al. have noted that the orientaion relationship between the parent

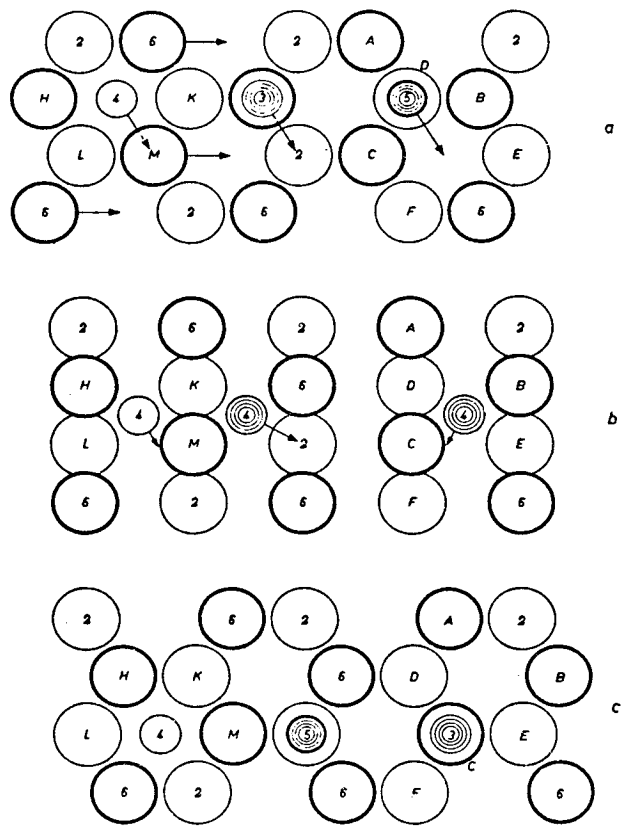

Figure 40

Schematic of the synchro-shear mechanism in spinels as described by Hornstra(Ref. 63). The same mechanism can be used to describe the $\gamma \rightarrow \alpha$ transformation assuming anion-cation-anion sandwiches instead of individual cation layers. The shear is described for one octahedral cation(left) and two tetrahedral ions projected on the (111) plane. a) initial state, b) intermediate state in which all cations occupy distorted tetrahedral interstices, c) final state. All arrows end at the final position. The unit in which height is expressed is one quarter of the distance between anion layers.

phase and product phase is given as:[61]

$$(0001)_\alpha \;||\; (111)_\gamma$$
$$[01\bar{1}0]_\alpha \;||\; [1\bar{1}0]_\gamma$$

However, Ridge et al. have suggested that this might also be the case if the product phase resulted from nucleation and growth.[60] An alternative view was provided by Bye and Simpkin suggesting that sintering and the onset of transformation were strongly correlated.[56] The transformation by synchro-shear would begin once a critical size of the metastable Al_2O_3 grains was achieved. The sintering effect is observed when poor geometric packing would be responsible for the high activation barrier to transformation. Within dense oxide scales, however, this effect would be minimal. In all studies reviewed above, the starting material was in the form of powders. The effect of surfaces cannot be overlooked in the authors' descriptions of transformation mechanisms. However, the extremely large amount of surface area in powders is absent in dense oxide scales. Therefore, the mechanism of the $\gamma \rightarrow \alpha$ transformation might be different in oxide scales.

B. <u>Results on the $\gamma \rightarrow \alpha$ transformation in oxide scales</u>

As mentioned in the previous chapter, transformed regions in the scale were observed after 1.0 hours of oxidation at 1100°C. This study on the $\gamma \rightarrow \alpha$ transformation was performed using the same (001) β-NiAl single crystal that was electropolished and oxidized at 1100°C for 1.0 hours. The discussion will involve morphological and crystallographic features of the transformed oxide. Additional discussions are included on porosity and surface diffusion phenomena which are observed with the transformation.

1. Morphology of the transformation products

The microstructure of an oxide scale region is shown in Figure 41. The microstructure consists of a δ-Al_2O_3 matrix with approximately spherical nuclei of α-Al_2O_3. The α-Al_2O_3 nuclei range from 0.2 μm to 1.0 μm and are observed to be thinner than the surrounding δ-Al_2O_3 matrix. Although the nuclei are clustered in this photomicrograph, the area surrounding this region contains randomly dispersed patches of α-Al_2O_3. However, some linear striations are observed in the δ-Al_2O_3 matrix which consist of alternating thick and thin regions of oxide. These striations most probably arise from scratches in the metal surface which were not removed by mechanical polishing or electropolishing. These scratches may be responsible for preferential nucleation of

ORIGINAL PAGE IS
OF POOR QUALITY

Figure 41

1.0 μm

Bright field image of the microstructure of a partially transformed Al_2O_3 scale formed on β-NiAl oxidized for 1.0 hours at 1100°C. The matrix is δ-Al_2O_3 with nuclei of α-Al_2O_3 being indicated by arrows.

α-Al_2O_3. The large cracks occur during specimen preparation when the underlying metal is removed prior to TEM observation.

A higher magnification BF image of one of the α-Al_2O_3 nuclei, now referred to as grains, is shown in Figure 42. The grain itself consists of coarse α-Al_2O_3 subgrains. A large amount of porosity is observed both within subgrains and at subgrain boundaries. The α-Al_2O_3 subgrains are highly dislocated indicating a large strain involved in the transformation. A discrete interface between the α-Al_2O_3 grain and the δ-Al_2O_3 matrix is difficult to observe in this image but has been observed in other regions that will be shown later. From this BF image, surface roughness is implied by the dark smudges within the α-Al_2O_3 grain. These dark regions occur because of thickness changes such as mounds on the oxide surface. The porosity and surface features will be discussed in later sections. The grain morphology and subgrain morphology within each grain will now be considered.

The general appearance of the grains is spherical. However, the actual interface normal to the oxidation plane is not uniformly curved. Some regions protrude further than others giving the edges of grains a scalloped appearance. There does not appear to be any preferred lateral growth direction of the α-Al_2O_3 grains. The α-Al_2O_3 subgrains within each grain are not equiaxed, but have long, linear boundaries. The subgrain size of the α-Al_2O_3 at this stage is approximately 1 μm. There are no

ORIGINAL PAGE IS
OF POOR QUALITY

Figure 42

0.5 μm

Higher magnification bright field image of an α-Al_2O_3 grain. Subgrains are indicated by A,B and C with subgrain boundaries arrowed. Porosity and dislocations are evident. Circled regions indicate surface roughness because thicker regions are darker.

overlapping subgrains suggesting that the α-Al_2O_3 grains consist of a two-dimensional network of columnar subgrains with the scale thickness in this region being equal to the subgrain size.

Nucleation of α-Al_2O_3 is best described as occurring in local regions. Growth of the nuclei is in the radial direction with no preferential growth direction being evident. α-Al_2O_3 grains consist of faceted grains which form during radial growth after transformation. Electron diffraction results of this process will now be presented to further describe the transformation.

2. Crystallography of the $\gamma \rightarrow \alpha$ transformation

The $\gamma \rightarrow \alpha$ transformation in oxide scales involves a change in crystal structure from the parent δ-Al_2O_3 phase to the product α-Al_2O_3 phase. Associated with the transformation are a number of other phenomena related to the morphology of the oxide scale. This section deals specifically with the crystallographic orientations and changes of the parent and product phases formed on an electropolished (001) single crystal of β-NiAl.

As mentioned in the previous chapter, the δ-Al_2O_3 that existed after 1 hour of oxidation at 1100°C was epitaxially related to the metal by the Bain orientation relationship. Therefore, since the the surface of β-NiAl was parallel to an {001} plane, the oxide scale was also parallel to {001}. The

actual oxide orientation relative to the [001] metal direction is different on the TEM specimen however because of bending and cracking of the oxide scale over the hole which occurred during specimen preparation. The stereographic projections of oxide orientations that will be presented are corrected for this misorientation.

The α-Al_2O_3 grain in Figure 42 consists of four to five subgrains of α-Al_2O_3. The orientation of three of these subgrains, marked by A, B and C, are shown in the stereographic projection in Figure 43. The orientations are shown with respect to the (100) projection of δ-Al_2O_3 which is the plane of the oxide scale. From the projection, there appears to be only slight correlation between the two crystal structures in terms of orientations. In one subgrain(C), the $(10\bar{1}0)$ pole (or direction) is nearly parallel to an (013) pole of δ-Al_2O_3. However, no further correlation exists for this orientation. The other two subgrains have no meaningful orientation relationship with the δ-Al_2O_3 matrix. Another observation is that the α-Al_2O_3 subgrains themselves are not consistent in orientation. The boundary between subgrains A and B shows an approximately 10° misorientation whereas the mismatches between subgrain C and the other two subgrains are much larger.

Two other regions of the same specimen were studied in which the interface between the two oxide phases was directly imaged and the orientations analyzed. In both cases, preferred orientations

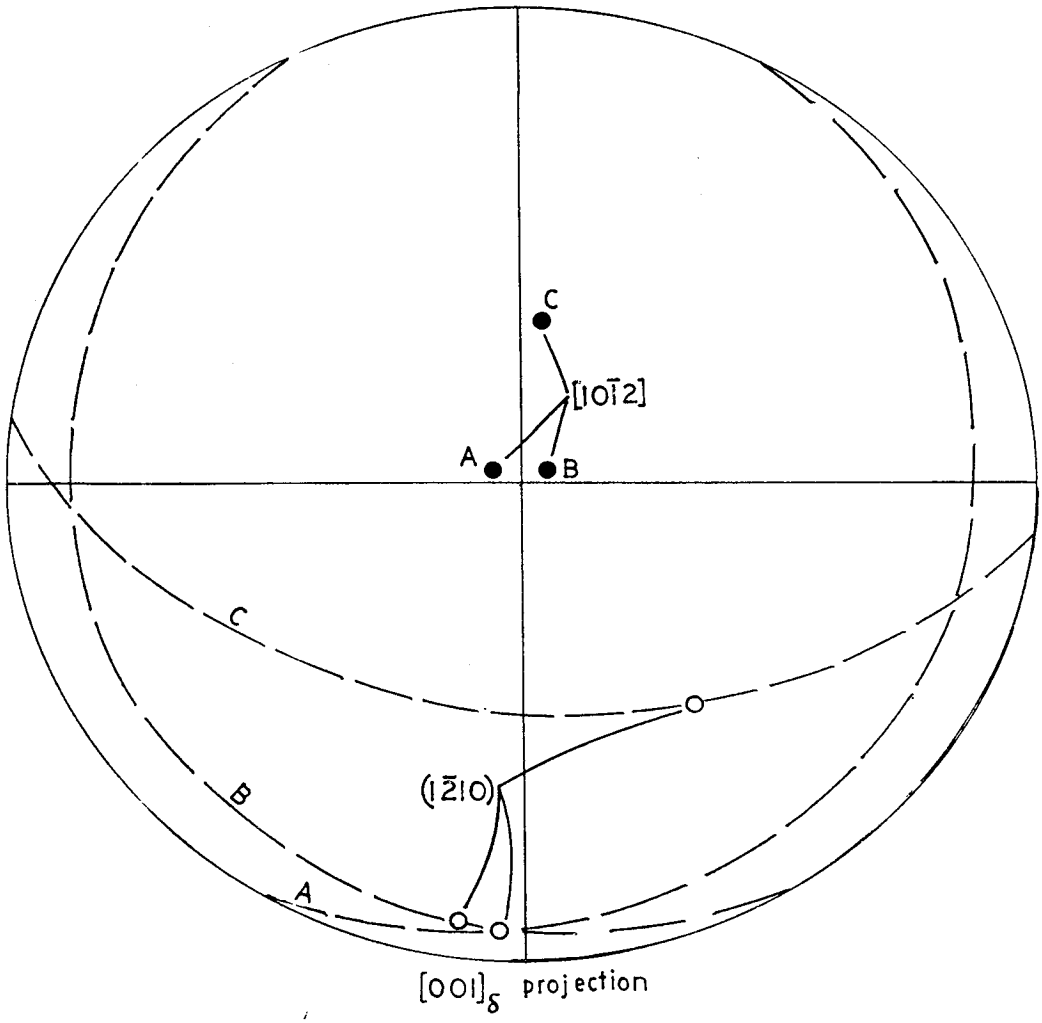

Figure 43

Stereographic projection showing the orientations of subgrains A, B and C in Figure 42. The large misorientation of subgrain C indicates the presence of a high angle boundary within the α-Al_2O_3 grain.

of the α-Al_2O_3 were observed. From one region, the preferred orientation was observed by means of parallel reflections in an SAD from the interface(Figure 44). Although neither phase has a zone axis parallel to the beam direction, analysis of the diffraction pattern shows that the δ-Al_2O_3 has an orientation near <100> and α-Al_2O_3 near [0001].[65] The main feature in this diffraction pattern is the alignment of the $(30\bar{3}0)_\alpha$ and $(440)_\delta$ reflections.

This alignment of reflections from both phases is only slightly correlated with the expected orientation relationship between the rhombohedral and spinel phases given as:[61]

$$(0001)_r \;||\; (111)_s$$
$$[01\bar{1}0]_r \;||\; [01\bar{1}]_s$$

using hexagonal coordinates for the rhombohedral phase. In this orientation relationship, the close-packed basal plane in the rhombohedral phase is parallel to the (111) close-packed plane of spinel. The planes are similar with respect to the hexagonal anion array and differ by 1.7% in their nearest neighbor distances. The parallel $(30\bar{3}0)_\alpha$ and $(440)_\delta$ reflections in Figure 44 reflect this alignment of close-packed directions. However, the planes in each phase which incorporate the close-packed directions are not the planes associated with the optimum orientation relationship mentioned above. Therefore, no epitaxial

ORIGINAL PAGE IS
OF POOR QUALITY

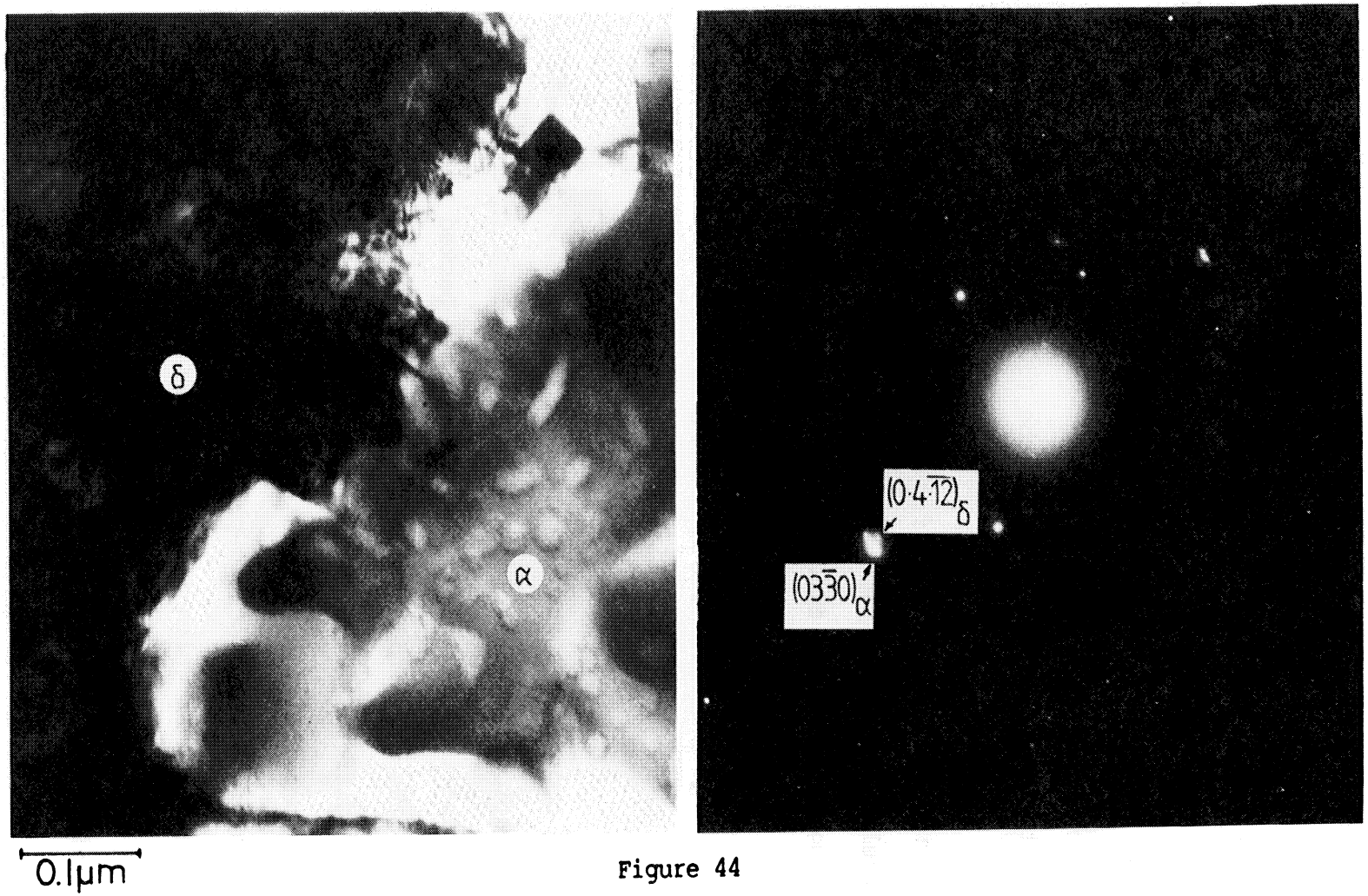

Figure 44

Bright field image and corresponding selected area diffraction pattern of a δ-Al_2O_3, α-Al_2O_3 interfacial region. The parallel reflections of each phase are indicated in the diffraction pattern.

orientation relationship exists between α-Al_2O_3 and δ-Al_2O_3.

A second interfacial region having preferred orientation of the α-Al_2O_3 is shown in Figure 45. In this case, the preferred orientation is observed as parallel zone axes. The parallel axes are:

$$[11\bar{2}0]_\alpha \,||\, [103]_\delta$$

The significance behind these preferred orientations is important in determining a transformation mechanism. The preferred orientations that are observed are easily described in terms of close-packed planes or directions. In one case, the $(30\bar{3}0)_\alpha$ and $(440)_\delta$ reflections were aligned. The symmetry of the crystal systems involved allows the alignment to be thought of as an alignment of parallel close-packed planes or parallel close-packed directions. However, the alignment in this case must be between close-packed directions because the indices of the oriented zones do not represent close-packed planes in their respective crystal structures. Because the indices represent directions, the close-packed directions in each phase are misaligned by 30°. To be considered a desirable crystallographic orientation relationship, the zone axis of α-Al_2O_3 should be $\langle 10\bar{1}0 \rangle$ which is 30° from $\langle 11\bar{2}0 \rangle$. Therefore, the alignment of crystal structures represented by the diffraction pattern in Figure 45 is not an epitaxial relationship.

ORIGINAL PAGE IS
OF POOR QUALITY

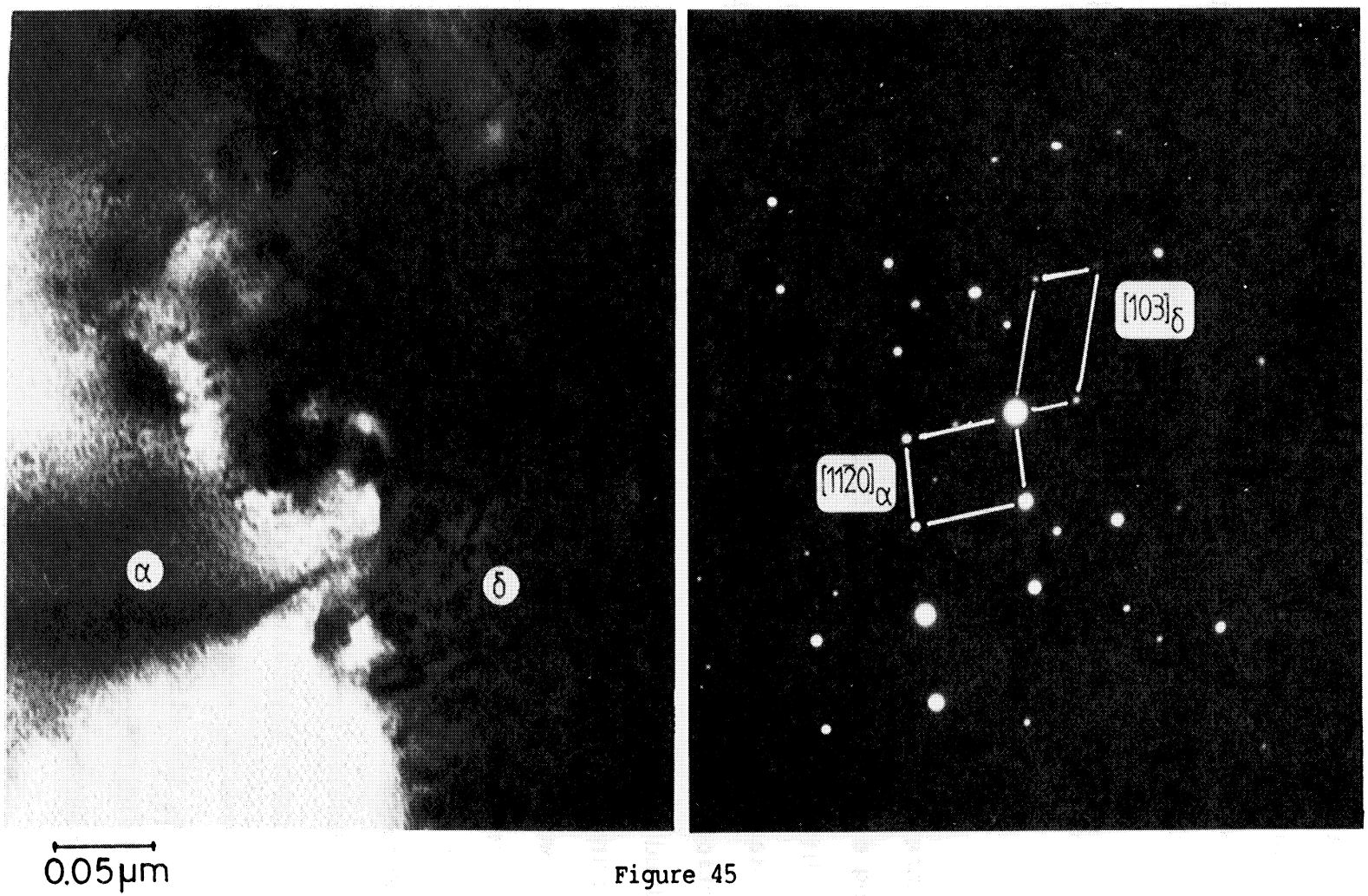

Figure 45

Bright field image and corresponding selected area diffraction pattern of a different δ-Al_2O_3, α-Al_2O_3 interfacial region than in Figure 43. The alignment of the two phases is observed by parallel zone axes which are indicated in the diffraction pattern.

Therefore, the transformation from δ-Al_2O_3 to α-Al_2O_3 within an oxide scale does not appear to transform by the synchro-shear mechanism because of the absence of the required orientation relationship. However, some local preferred orientation is observed. The transformation must be controlled by a diffusion mechanism with the possibility of local preferred orientation being dependent on the prior orientation of the phases.

3. Porosity in transformed α-Al_2O_3

The $\gamma \rightarrow \alpha$ transformation results in a volume decrease as the stable crystal structure is achieved. This change can be calculated utilizing the information known on the unit cells of the structures as in the study by Donlon et al. in which the volume per anion was determined.[55] The volume decrease in transforming from δ-Al_2O_3 to α-Al_2O_3 is calculated to be 9.6%. Using the quoted densities of the two phases from the Powder Diffraction File, the volume decrease is 8.4%.[66] The different results for volume decrease arise from the particular method used.

The volume decrease can be accomodated by morphological adaptations. Porosity within the scale would be the most obvious form of microstructural change when a decrease in volume must be accomodated. When oxidizing a metal specimen, a free surface exists at the gas-oxide interface. However in relatively thick

scales, the free surface would not have an affect on reactions occuring away from the interface because the diffusion kinetics are too slow. As mentioned in the previous section, the $\gamma \rightarrow \alpha$ transformation in oxide scales is believed to occur by a diffusion mechanism. For a diffusion mechanism to take place, the transforming species must be in intimate contact with each other; vapor transport not being applicable. Therefore, porosity is expected to occur within the transformed scale as a result of the volume decrease associated with the transformation.

Porosity has been observed in other studies involving the $\gamma \rightarrow \alpha$ transformation.[54,61] However, the porosity has always been observed behind the transformation front. Situations involving porosity within oxide scales have also been reported with the porosity being attributed mainly to the oxidation process and not the $\gamma \rightarrow \alpha$ transformation.[30] Porosity was observed both in the transient scale and in the transformed α-Al_2O_3 scale. The bright field TEM image in Figure 46 from the same specimen as in the above discussion clearly shows a large amount of porosity within the α-Al_2O_3 region of the scale. The porosity is observed throughout the entire microstructure of the α-Al_2O_3. Images of the interface between transformed and untransformed regions in Figures 44 and 45 do not show any appreciable amounts of porosity in the untransformed regions as in the transformed regions. Therefore, the assumption that porosity observed in the α-Al_2O_3 region in Figure 46 results mainly from the transformation appears

ORIGINAL PAGE IS
OF POOR QUALITY

Figure 46 0.1 μm

Bright field image of a newly transformed region showing a large amount of porosity within α-Al_2O_3.

to be correct.

The volume percent porosity in an α-Al_2O_3 region indicated in Figure 46 was calculated to be approximately 1.0% for a scale 0.5 μm thick. The scale thickness varied between 0.3 and 0.6 μm from SEM oxide cross-section measurements. The mean pore radius was 15.0 nm with the distribution of pore sizes being presented in Figure 47. The size and amount of porosity is observed to vary within the transformed region.

An additional feature of the entrapped porosity is the dark spots visible within many of the pores. Energy dispersive spectroscopy(EDS) was used to determine the chemistry of these spots. Figure 48 shows portions of EDS spectra of spots within pores and of regions directly adjacent to the pores. The results clearly indicate an enhanced zirconium concentration within the dark spots. These spots are precipitates that are present within the pores and attached to pore surfaces. The platinum peaks that are observed in the spectrum of Figure 48 result from contamination during oxidation by platinum thermocouples and hanging fixtures.

The crystallographic nature of the zirconium-rich precipitates is not known. Their presence within α-Al_2O_3 grains implies that they were present in the transient scale prior to the $\gamma \rightarrow \alpha$ transformation. However, the majority of zirconium would be expected to be swept along with the transient scale at the transformation front because the solubility of zirconium in

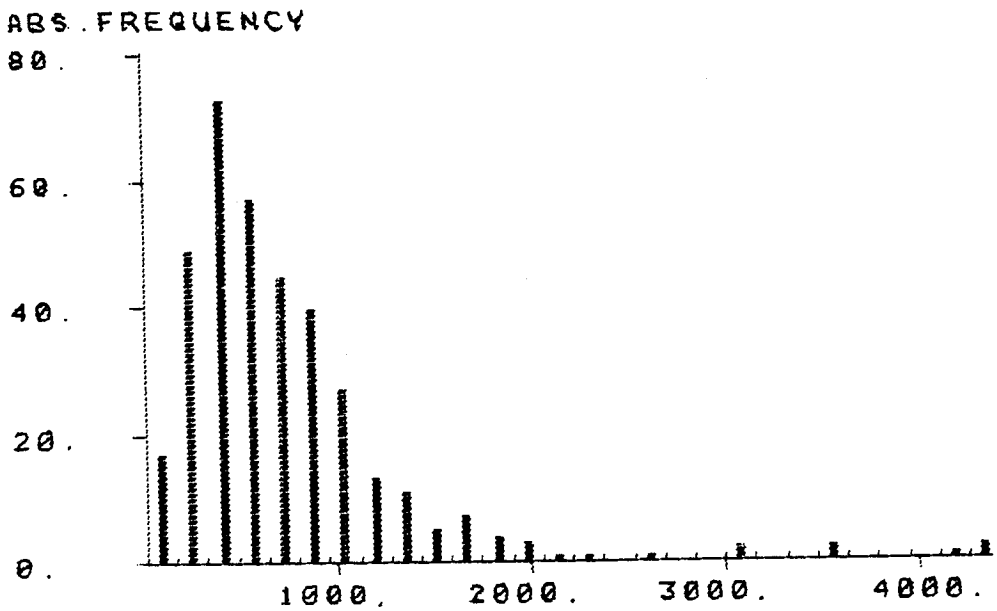

Figure 47

Histogram of number of pores from a region in Figure 46 versus pore size. The mean pore radius was determined to be 15.0 nm.

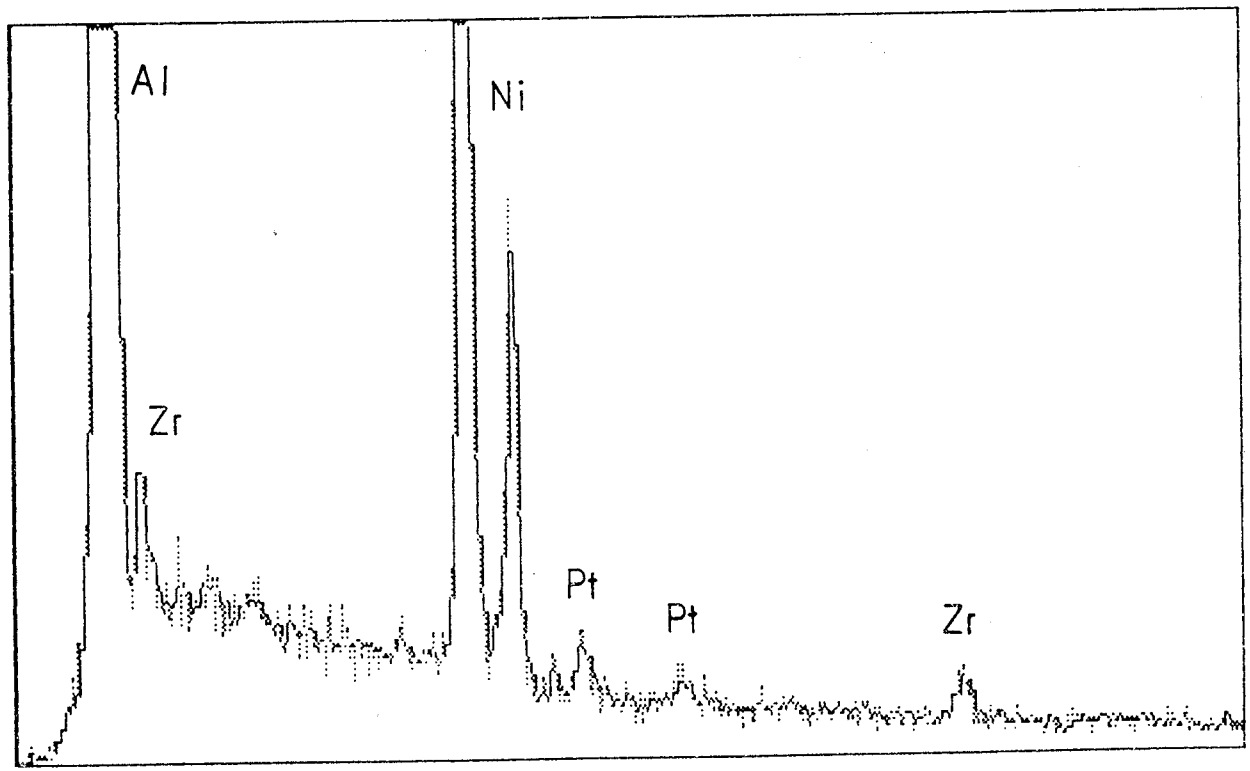

Figure 48

EDS spectra of zirconium-rich precipitates in pores within α-Al_2O_3.

α-Al_2O_3 is extremely small.[67] Therefore, the zirconium-rich precipitates can be present by one of three mechanisms: 1) the precipitates are oxides or other impurities which are not flushed out during transformation because they are stable within α-Al_2O_3, 2) the precipitates are pinned by voids or vice-versa which in turn prevent mutual mobility, trapping each other inside grains of α-Al_2O_3, 3) zirconium segregates to void surfaces where precipitates form. It is doubtful that zirconium is an effective dopant in the formation of structural vacancies resulting in voids according to the equation:

$$Zr = Zr_{Al}^{+} + V_{Al}' \qquad [10]$$

because of the low solubility of Zr in α-Al_2O_3.

4. Surface smoothing of transformed scales

An earlier discussion briefly mentioned the presence of surface protrusions or mounds of oxide within the transformed grains of α-Al_2O_3. These surface inhomogeneities are shown in the bright field image of Figure 42 as dark smudges in an otherwise uniformly intense α-Al_2O_3 grain and have been determined to be α-Al_2O_3 by electron diffraction analysis. An SEM image of the gas-oxide interface of the same α-Al_2O_3 grain is shown in Figure

ORIGINAL PAGE IS
OF POOR QUALITY

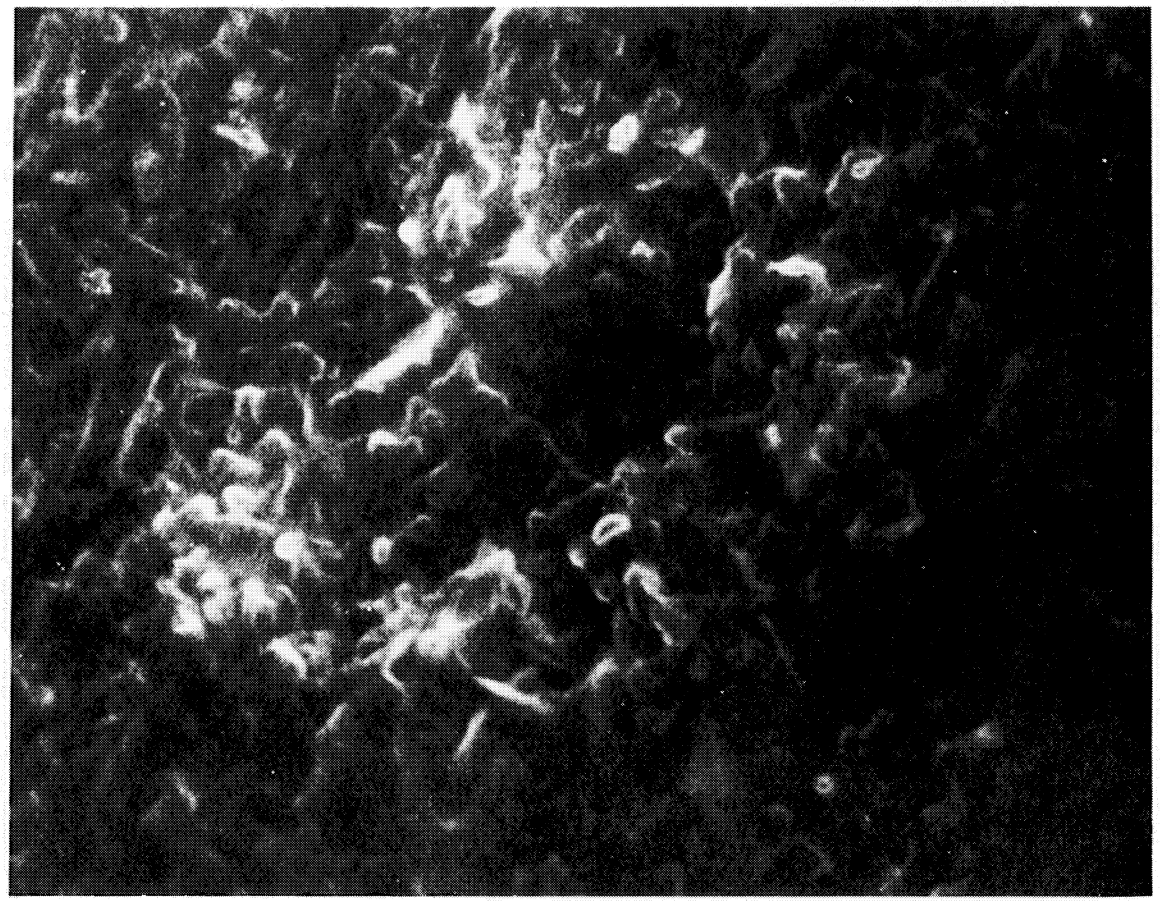

0.5μm

Figure 49

SEM image of a depression within a transient scale formed on β-NiAl oxidized for 1.0 hours at 1100°C. The depression is a result of the $\gamma \rightarrow \alpha$ volume decrease. The depression is from the same region as in the bright field image of Figure 42. The ridge within the depression corresponds to the high angle boundary within the α-Al_2O_3 grain.

49. In this image, a depression in the scale is formed where the scale had transformed to α-Al_2O_3. The same boundary between α-Al_2O_3 subgrains is observable in Figure 42.

The surface pitting is believed to result from the volume decrease associated with the $\gamma \rightarrow \alpha$ transformation as described earlier. The rough surface inside the depression appears to be a remnant of the transient scale morphology. As the center of the depression is approached within the transformed region, the scale surface becomes smoother. This phenomenon is easily observed in the TEM bright field image of Figure 50 showing constant intensities within α-Al_2O_3 grains near the center of a different patch and dark regions corresponding to surface roughness nearer the outer edges of the patch. It is quite apparent that surface smoothing of the scale is associated with the $\gamma \rightarrow \alpha$ transformation.

Surface protrusions in the transient scale have been attributed to growth by outward cation diffusion. The particular surface morphologies that have been shown in the previous chapter as well as in Figure 49 are a result of a continuous flux of aluminum ions reaching the scale surface to form new oxide along preferential directions. Once the $\gamma \rightarrow \alpha$ transformation has occured, the transient surface morphologies immediately begin to be smoothed out indicating that the outward flux of cations is no longer present. A change in scale growth mechanism upon transformation from outward growing to inward growing is therefore descriminately evident. The change in growth mechanism has been

Figure 50

1.0μm

Bright field image of an α-Al_2O_3 grain to show the effect of surface smoothing on scale thickness. Near the grain center, the grain appears to be uniformly thin. Near the grain edges, surface roughness results in non-uniform intensity due to absorption of electrons.

observed in studies by Young and de Wit using Rutherford backscattering techniques.[42]

The smoothing of surface inhomogeneities can be described as resulting from surface diffusion. Nichols and Mullins have developed a general theory which can describe the morphological change of any volume of revolution due to surface diffusion.[68] Their results have often been applied to blunting of field emission tips and sintering of spheres both to each other and onto flat planes. The surface homogeneities can be approximated to be conical mounds to which the theory has been applied. Their theory will be briefly described and applied to the phenomenon of surface smoothing of transformed α-Al_2O_3 scales. The purpose of this discussion is to ascertain the notion that surface diffusion is solely responsible for this phenomenon.

The theory is described in Appendix D. The property of interest for this study is the rate of recession of a cone having a known cone half-angle, α. This rate is given as:

$$dz/dt = (C_\alpha \cdot B^{0.25})/(t-t_o)^{0.75} \qquad [11]$$

where

$$B = (D_s \gamma \nu \Omega^2)/kT \qquad [12]$$

and t = time

D_s = surface self-diffusion coefficient

γ = surface energy

Ω = atomic volume

ν = surface concentration = $\Omega^{-0.67}$

k = Boltzmann's constant

T = temperature

The values of the constant C_α are found in the reference for various cone half-angles. This theory is tested using approximate values of surface protrusions and known constants of α-Al_2O_3. The necessary material constants are the surface self diffusion coefficient, D_s, the surface energy, γ, and the atomic volume, Ω. From the review in a study by Maruyama and Komatsu, the values or range of values for these constants at 1100°C are:[69]

$$Ds = 2 \times 10^{-8} \text{ to } 2 \times 10^{-11} \ (cm^2/s)$$
$$\gamma = 905 \ (ergs/cm^2)$$
$$\Omega = 2.11 \times 10^{-23} \ (cm^3)$$

Therefore, the values of B ranged from $4.4 \times 10^{-23}(cm^4)$ to $8.8 \times 10^{-26}(cm^4)$. From Nichols and Mullins, the values for C_α ranged from 2.14 at a cone half-angle of 3°, to a value of 0.323 for a cone half-angle of 45°.[68]

The equation for the rate of recession of a cone tip can be rearranged to be:

$$dt/_{t}0.75 = dz/(C_{\alpha} \cdot B^{0.25}) \qquad [13]$$

Integrating both sides and solving for, t, gives:

$$t = [1/4(z/C_{\alpha} \cdot B^{0.25})]^4 \qquad [14]$$

An experimental value of the height of a surface protrusion is approximately 0.5 μm. Using a calculated $B = 2.78 \times 10^{-24} (cm^4)$, (i.e. $D_s = 1 \times 10^{-9}$ cm^2/s) and a C_{α} value equal to unity, ($\alpha = 12^{o}$), the time for a protrusion 0.5 μm high to be completely smoothed is 2.4 hours. Considering that drastic surface smoothing is observed within one hour of oxidation at 1100°C, this value is quite reasonable.

The above calculation was for an ideal situation of a body of revolution. In many cases of surface oxide morphologies, the shapes of the protrusions can be blades, platelets or needles. Other factors that would effect the results are the anisotropies of both surface diffusion coefficients and surface energies.

III. Mature Oxidation Stage

The long-term oxidation of alumina forming alloys results in an α-Al_2O_3 scale. The morphologies of the oxide scales have been studied for a number of alloy systems including Ni-base, Fe-base and Co-base high temperature alloys.[29,70,23] In most cases, the alloys also contain chromium to improve both mechanical and corrosion properties of the alloys. The mature scales are generally found to consist primarily of polycrystalline α-Al_2O_3. Complications from ternary and other alloying elements make the mechanisms of scale formation and growth difficult to comprehend. Therefore, oxidation of binary alumina forming alloys have been studied to further the understanding of Al_2O_3 scale formation and growth. Aluminide intermetallics are also of interest as high-temperature materials, thereby necessitating the understanding of the oxidation characteristics of these materials.

The oxide scales formed on binary alumina forming alloys have been found to be quite unique in their morphologies. Felten and Pettit studied the oxidation of Pt-Al alloys between 1000°C and 1450°C and found that the oxide scale was dependent on the substrate phase.[71] One of their alloys consisted of two phases, Pt_2Al and Pt_5Al_3. On Pt_5Al_3, the initial scale was determined to

be textured δ-Al_2O_3 that grew by outward diffusion. With increasing time, the scale thickened and then transformed to polycrystalline α-Al_2O_3. However on Pt_2Al, the initial scale consisted of α-Al_2O_3 which was believed to thicken by inward oxygen grain boundary diffusion. The morphology of the α-Al_2O_3 scale that formed over Pt_2Al contained uniformly thin, large grains separated by thick ridges at grain boundaries. Sheasby and Jory[72] studied the electrical properties of an Al_2O_3 scale formed on Pt-50 at% Al alloy and observed the same type of oxide morphology as on the Pt_2Al phase in the work of Felten and Pettit. An additional result by Sheasby and Jory involved an early period of oxidation(times less than 1.0 hours) at 1100°C in which the scale growth rate was observed to be much faster than at later times.

Smialek observed the ridge network of α-Al_2O_3 on oxidized β-NiAl and termed it the "lacey" structure.[12] Inward oxygen grain boundary diffusion was believed to result in scale growth because of the presence of columnar grains as well as oxide ridges at grain boundaries. Rybicki and Smialek observed the lacey structure of mature Al_2O_3 scales on β-NiAl oxidized at 1000°C and at higher temperatures.[41] A SEM image from their study of the lacey structure formed at 1200°C is shown in Figure 51. Hindam and Smeltzer have performed an extensive study of the oxidation of Ni-Al alloys including the β-NiAl phase.[13] The lacey structure was also observed on their β-NiAl specimens oxidized at 1200°C. A

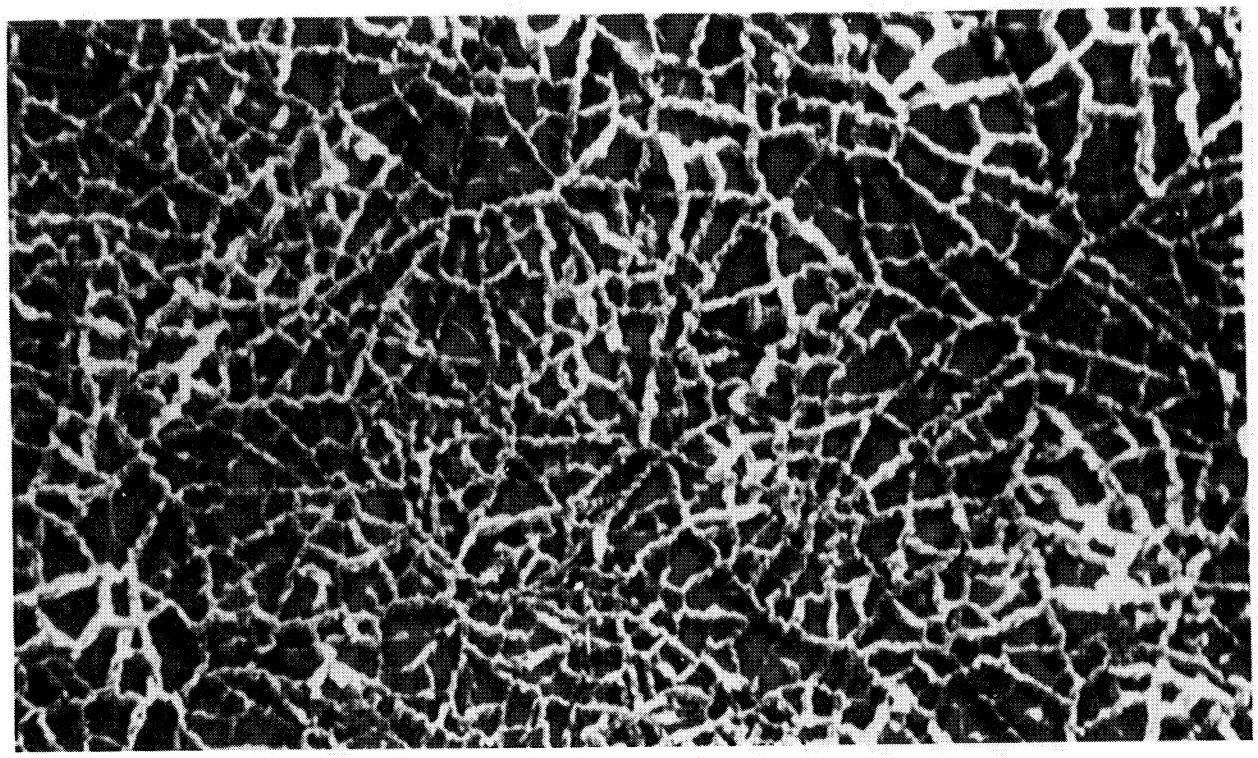

10.0μm

Figure 51

SEM image of the gas-oxide surface on a β-NiAl specimen oxidized for 100 hours at 1100°C. The oxide has the lacey morphology because of the lacey appearance resulting from thin, uniform oxide amongst oxide ridges.(Ref. 41).

model of the lacey structure was proposed with the idea that oriented α-Al_2O_3 grains were separated by misoriented oxide ridges in which the grain size was considerably finer than the oriented grain regions. The growth of these oxide scales was believed to be a result of both inward oxygen and outward cation grain boundary diffusion along the fine, polycrystalline ridges.

The present study involves a detailed examination of the growth and morphology of the lacey structure of α-Al_2O_3 that formed on β-NiAl specimens oxidized at 1100°C. The results will be discussed in light of the previous studies on the lacey structure to develop a consistent model for this particular mode of oxidation of Al_2O_3 forming alloys.

A. Growth rates

Measurement of the growth rates of mature oxide scales at 1100°C was accomplished by obtaining weight gain versus time data as described in previous sections on growth rates. A typical parabolic weight gain curve for oxidation of β-NiAl at 1100°C is shown in Figure 52. The initial steep portion of the curve is attributed to growth of the scale during the transient stage of oxidation which has been discussed earlier. The final slope is indicative of the parabolic growt of mature α-Al_2O_3 scales during the long-term region. The region of interest for mature scales

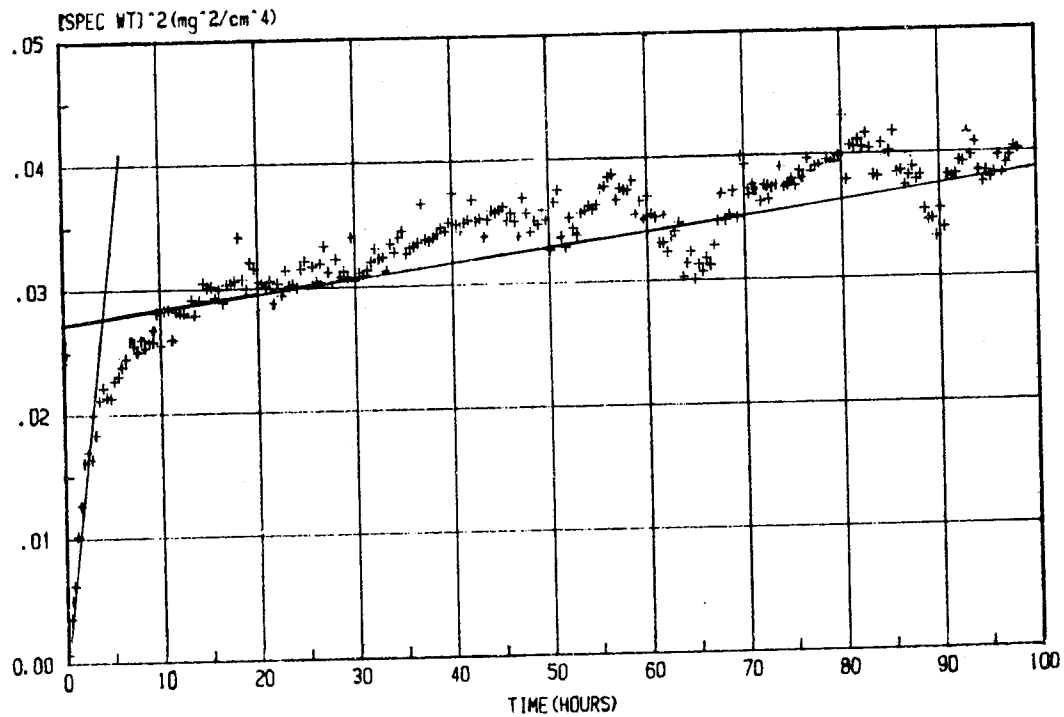

Figure 52

Parabolic weight gain versus time curve for the oxidation of a polycrystalline β-NiAl specimen oxidized at 1100°C. The inital, steep slope is due to transient oxide growth. The final slope represents growth of an α-Al_2O_3 scale.

begins after the transformation to α-Al_2O_3 has been completed and a constant slope has been achieved. In this curve, the steady state region begins after approximately 15 hours. A cyclic nature to the curve is observed and has been discussed earlier.

Parabolic rate constants were determined for (001) and (011) single crystal specimens as well as polycrystalline specimens. The results are shown in Table VII. Attempts were made to determine effects of preoxidation time at 800°C, of surface preparation and of substrate orientation. The slowest growth rate was obtained on a polycrystalline specimen having an (001) texture. The parabolic rate constant obtained on (012) textured polycrystalline material is slightly higher followed successively by rate constants on (001) and (011) specimens. No significant effect was observed for different preoxidation treatments of 100 or 50 hours at 800°C or an absence of a preoxidation treatment. However, the parabolic rate constant increased by an order of magnitude when a specimen was abraded with 600 grit paper rather than electropolished prior to oxidation. The k_p value of 2.33 X 10^{-3}($mg^2/cm^4 \cdot hr$) agrees with other studies on the growth rates of oxide scales formed on β-NiAl at 1100°C in which the final step of surface polishing was a 600 grit sanding treatment.[5,41]

B. Scale morphology

TABLE VII

Results of parabolic rate constants for the isothermal long-term oxidation of β-NiAl at 1100°C.

Metal Orientation	k_p ($mg^2/cm^4 \cdot hr$)	Comments
(001)	3.4×10^{-4}	------
(011)	4.3×10^{-4}	------
polycrystal	4.6×10^{-4}	(001)texture 45 hrs. preox.
polycrystal	1.2×10^{-4}	(001)texture 100 hrs. preox.
polycrystal	2.8×10^{-4}	(012)texture no preoxid.
(001)	2.3×10^{-3}	600 grit abr.

The lacey morphology is the predominant scale morphology that exists on oxidized β-NiAl at 1100°C after the transformation to α-Al_2O_3 has occurred. A fully developed oxide morphology is shown in the bright field scanning transmission electron microscopy (STEM) image in Figure 53 of a specimen oxidized for 100 hours at 800°C followed by oxidation at 1100°C for 100 hours and backthinned to reveal the oxide. The image contains many features which will be analyzed with the aid of additional STEM, SEM and back-scattered microscopy(BSM) images. In the STEM bright field image of Figure 53, the contrast can best be described as resulting from thickness variations. The dark regions correspond to thicker oxide whereas the light regions correspond to thin oxide or absence of material.

The most prominent feature in the STEM bright field image of the lacey morphology is thin regions of oxide surrounded by thicker regions giving a "lacey" appearance. The thin regions, referred to as grains, are observed to be non-uniform in size as well as in shape. The central grain in the micrograph is approximately circular and is observed to be thinner near its center. The overall morphology is also observed to consist of many cracks, some being radial cracks in individual grains and others cutting through and across boundaries between grains.

A higher magnification image of the central grain is shown in Figure 54. Radial cracks are observed along with branching of cracks. The central portion and one arm of the star crack is

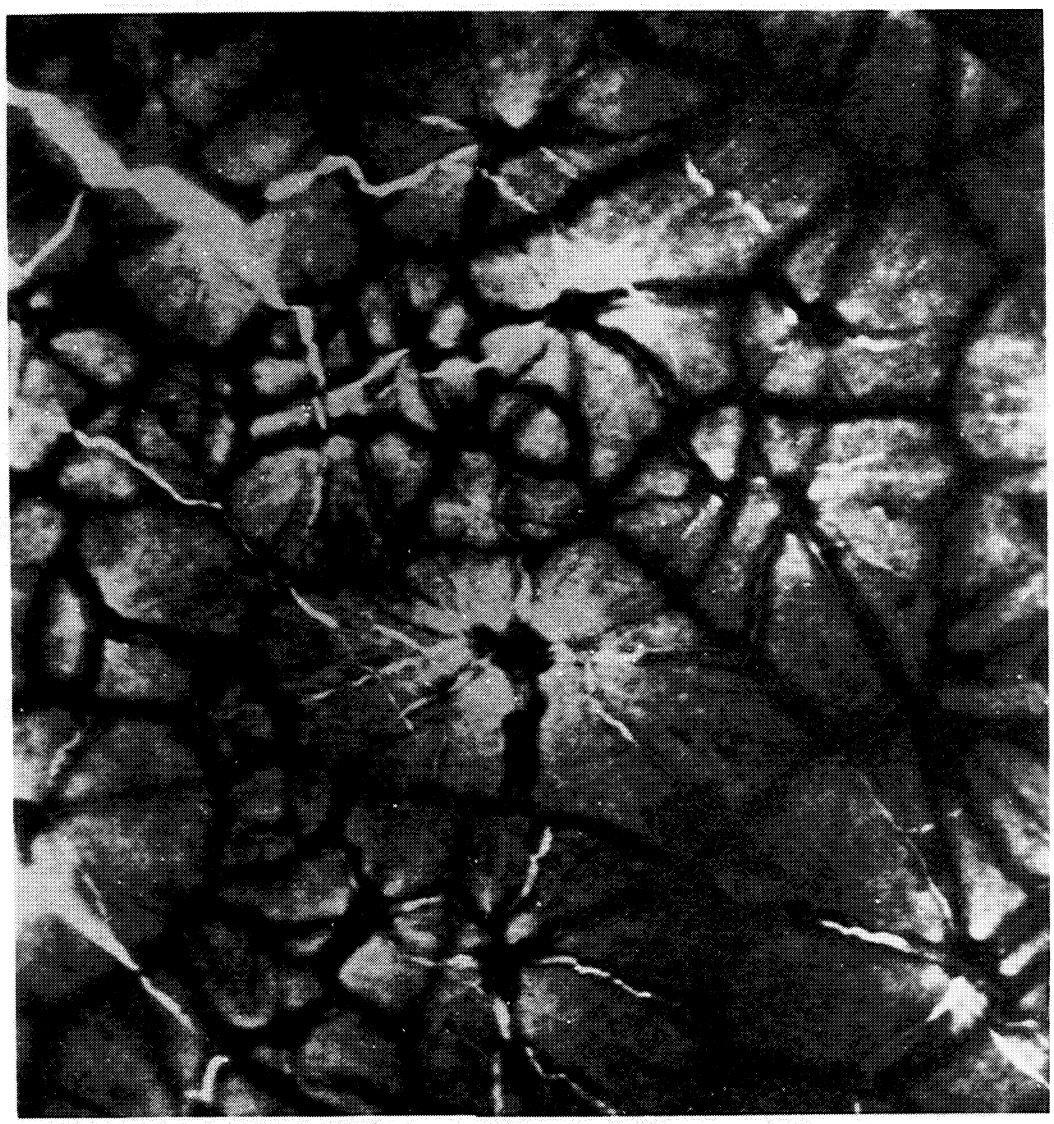

10.0μm

Figure 53

STEM bright field image of the lacey morphology of α-Al_2O_3 formed on a (001) β-NiAl specimen oxidized for 100 hours at 1100°C. Dark regions correspond to thick oxide as a result of absorption of electrons. Bright regions are thin oxide areas or cracks within the scale.

ORIGINAL PAGE IS
OF POOR QUALITY

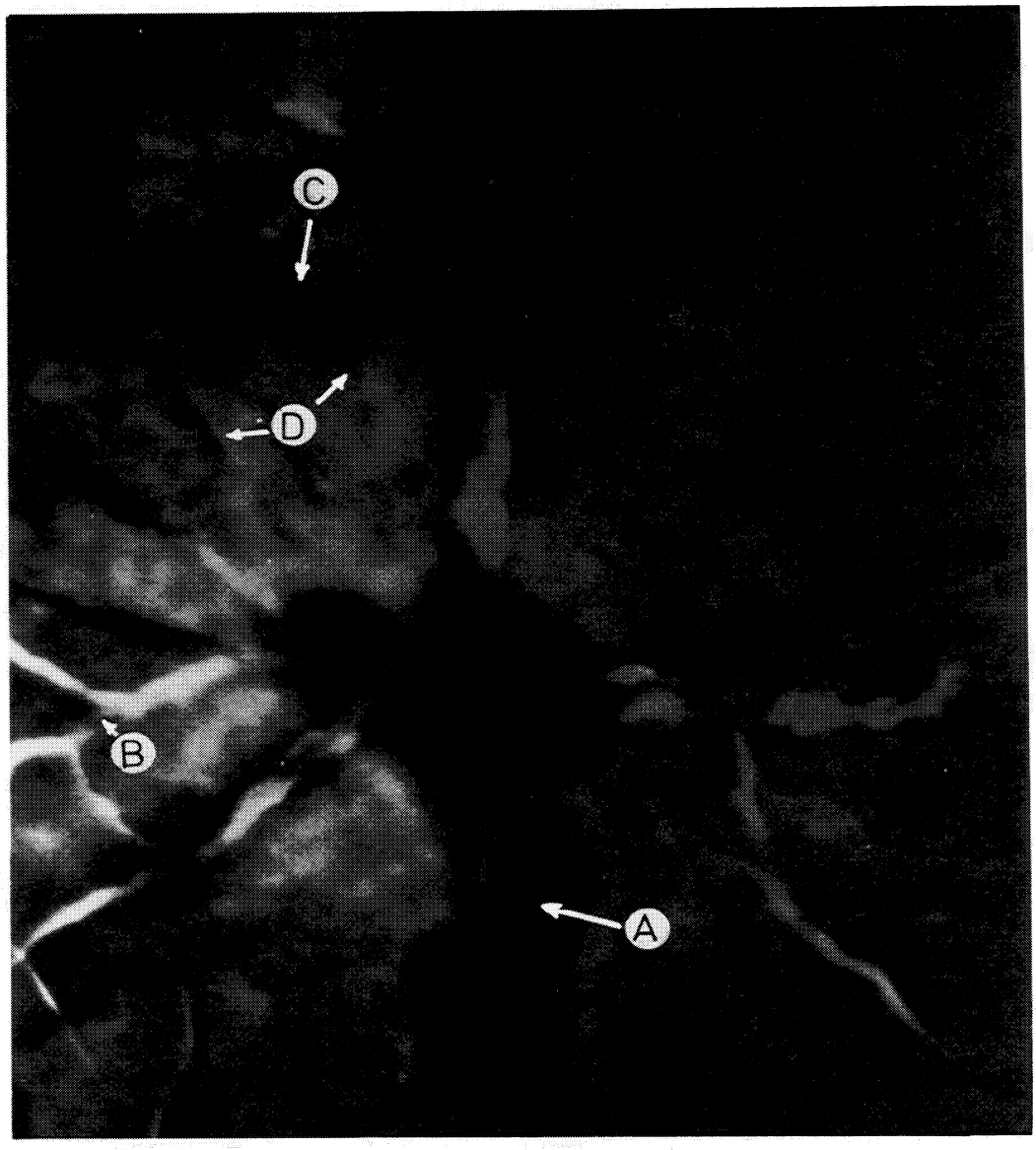

1.0μm

Figure 54

Higher magnification STEM image of the central grain in Figure 53. Two different crack morphologies exist; cracks associated with thick regions(A) and cracks not having thick regions surrounding them(B). Dark lines corresponding to thick regions are observed at grain boundaries(C) and also as hair-like lines extending radially in towards the grain center (D).

enveloped in a thick region of oxide whereas other cracks are very thin relative to the surrounding grain. The dark lines in Figure 54 are positioned at boundaries between grains and also appear to be extending radially inward in some regions of the central grain.

The SEM and BSM images in Figures 55a and 55b aid in determining the nature of the features in the STEM images. Figure 55a is a SEM image of the gas-oxide interface from the same region as in Figure 54. The thick region at the center and along one arm of the star crack is not visible at the gas-oxide surface. Therefore, this thick region in question must be underneath the scale at the metal-oxide interface. The remainder of the cracks are observed to contain material in them, although this material must be relatively thin. A fine hair-like boundary extends along the middle of each crack. The intensity along crack edges does not necessarily mean a thickness change but rather can be due to charging effects within the microscope as a result of uneven carbon coating of the specimen surface. The dark regions of the STEM image are observed to be ridges that form along grain boundaries. These ridges are associated with additional thick regions which are not visible in the SEM image. Therefore, the somewhat broad, thick regions must form at the oxide-metal interface. Fine hair-like ridges are observed to extend radially inward towards the grain center in some areas. A BSM image of the same region is shown in Figure 55b. The bright regions in this case do not come from regions of higher atomic number but rather

ORIGINAL PAGE IS
OF POOR QUALITY

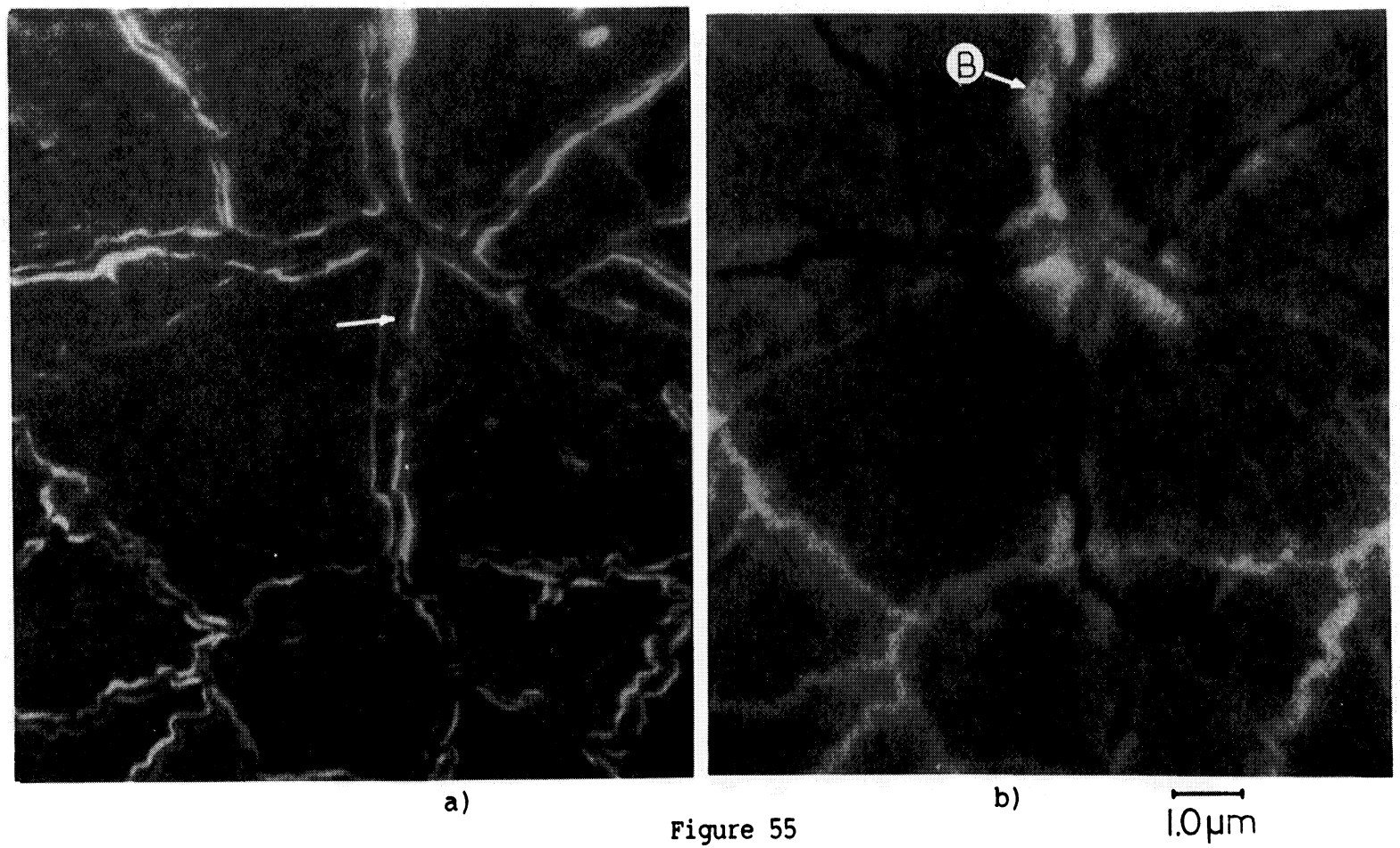

a) b)

Figure 55

a) SEM image of the gas-oxide surface from the same region as in Figure 54, and b) corresponding BSM image of the same area. In a), ridges of oxide are observed along grain boundaries and along radial lines. A boundary runs along the crack and is shown by arrows. In b), the bright regions are thicker; therefore, the thick region along the crack(B) must be on the scale underside because a thick region is not observed in a) for this same area.

from thicker regions with correspondingly more mass.

Another SEM image of the gas-oxide interface from a different region of the specimen is shown in Figure 56. This image clearly shows why the center of the grain is thinner than the outer areas near the grain boundaries. The phenomenon of surface smoothing, which was described earlier, results in a thinning of the central region of the grain. The thinning begins upon transforming to α-Al_2O_3 which is shown to begin at the center of the grain and extend radially outward. An SEM image of a scale cross-section in Figure 57 shows that the cracks are healed, but are much thinner than the surrounding grain. The material within the grain is near the bottom of the crack.

A SEM image of the oxide underside at the metal-oxide interface of a different region and the corresponding STEM bright field image are shown in Figures 58a and 58b. From the STEM image in Figure 58b, the oxide is observed to contain cracks associated with thick regions and oxide ridges which correspond to grain boundaries. The thick regions at healed cracks which were mentioned earlier are observed at the metal-oxide interface on the underside of the oxide scale. The ridges observable at the grain boundaries on the gas-oxide interface were mentioned to be associated with a thick region on the scale underside. These regions are evident in the SEM image of the oxide underside at the metal-oxide interface. The underside of grain bounaries are smoothed ridges in which grain boundary grooving is evident. The

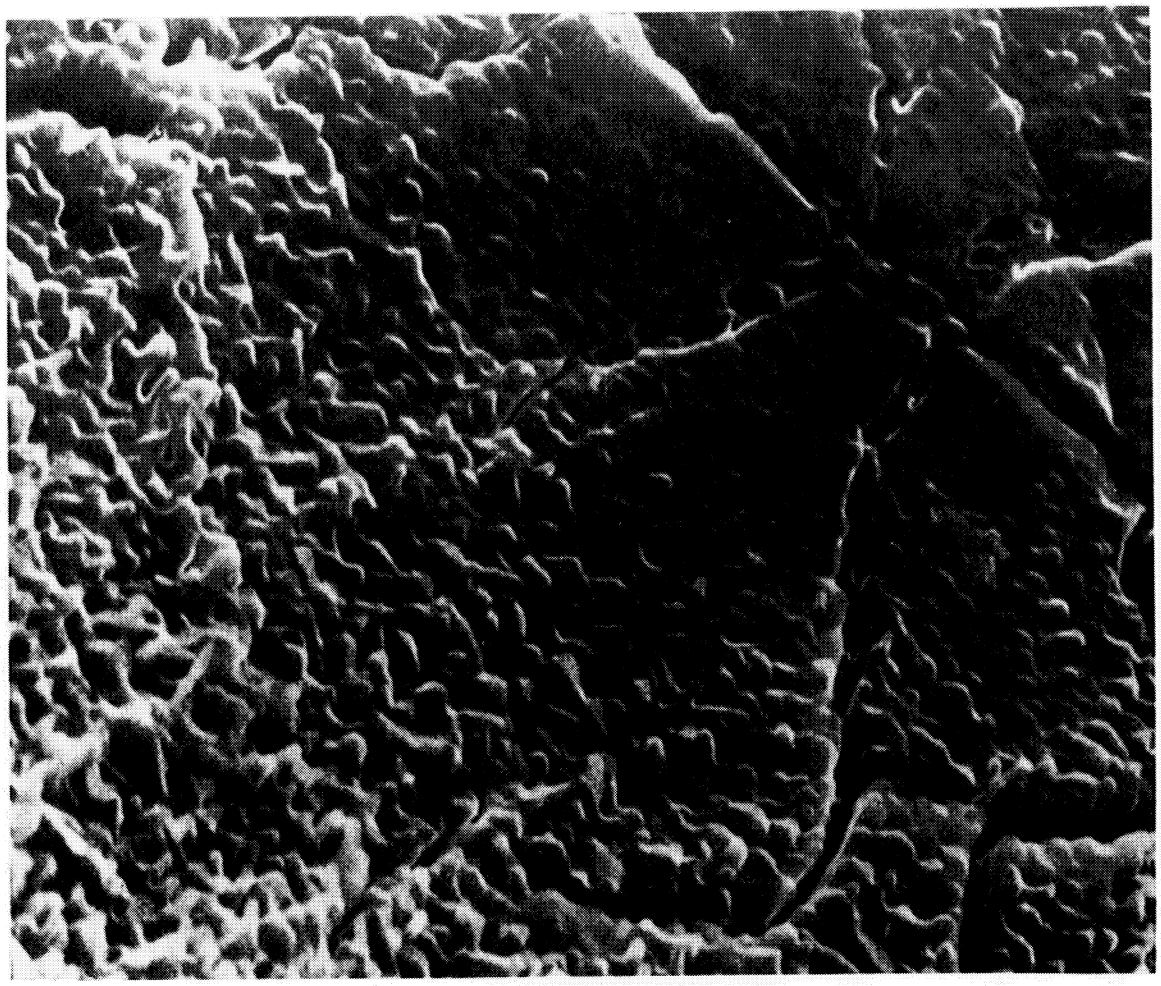

Figure 56

SEM image of the gas-oxide surface from a different region than in Figure 53. The effect of surface smoothing near the grain center is clearly evident.

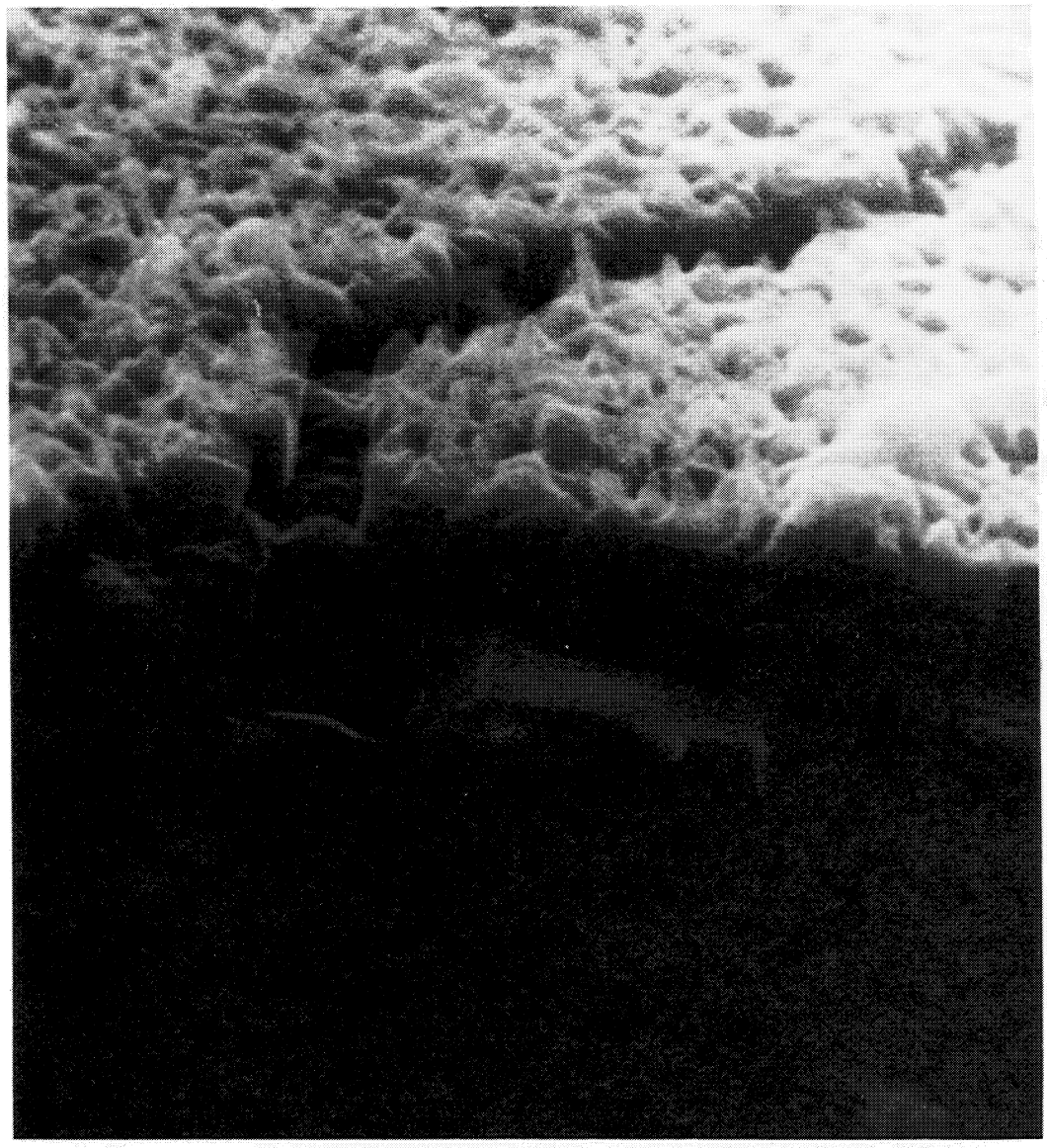

1.0 μm

Figure 57

SEM image of crack region in a lacey morphology scale cross-section obtained by freeze-fracturing an oxidized β-NiAl specimen. The healed crack appears thinner from above but may contain considerable oxide immediately underneath the healed region.

ORIGINAL PAGE IS
OF POOR QUALITY

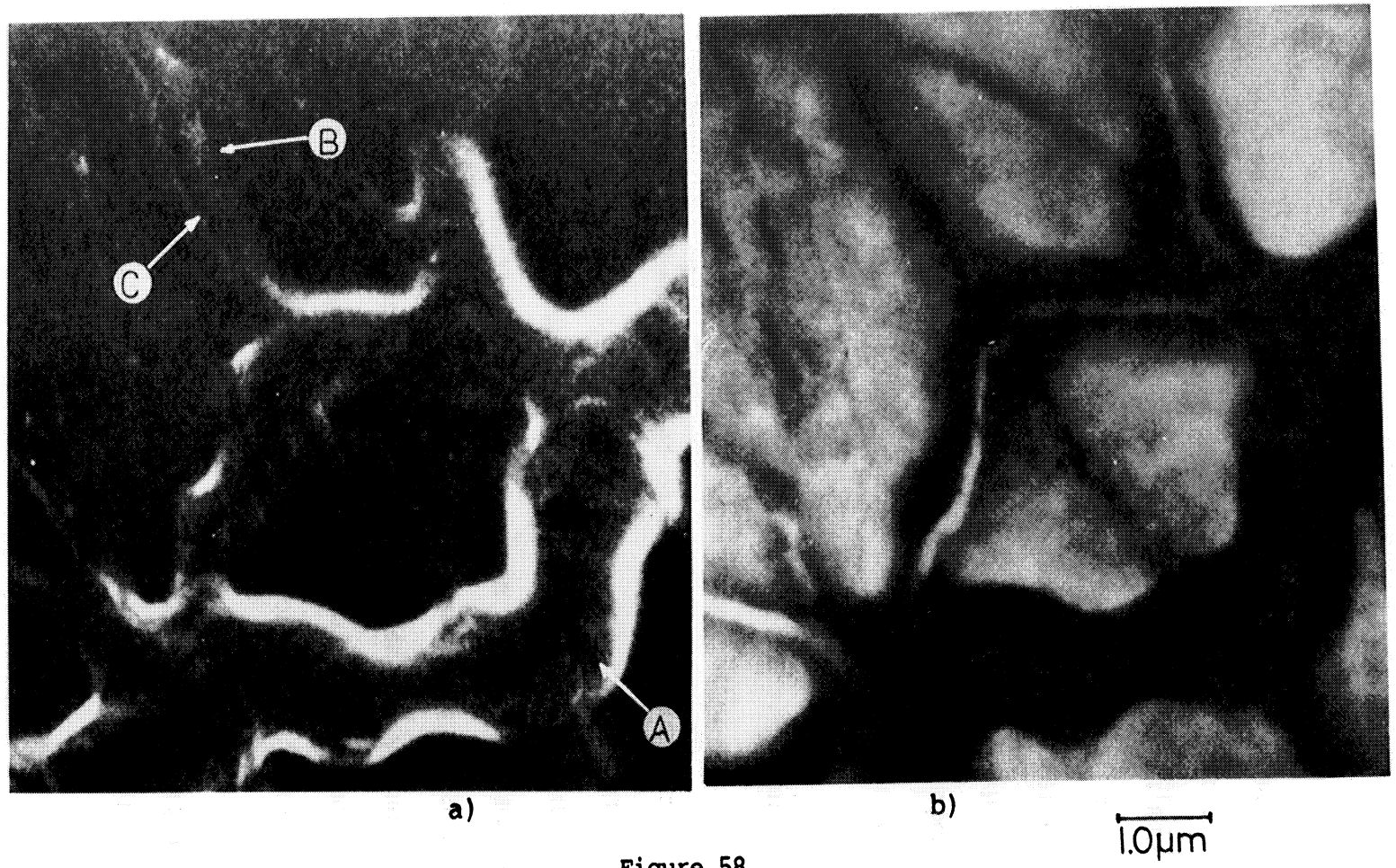

Figure 58

a) SEM image of the underside of an oxide scale having the lacey morphology, and b) corresponding STEM bright field image. Thick regions near cracks are observed on the scale underside(A). At grain boundaries, ridges are present on the scale underside(B) but are smoother and less distinct than the ridges on the scale's outer surface. Grain boundary grooving is observed to have occured at grain boundary ridges(C).

oxide underside at healed cracks is rough in comparison to ridges at grain boundaries. The remainder of the undersurface of the oxide is smooth.

The grains themselves are not single crystals as might be assumed from the the rather uniform contrast in the STEM images. A TEM image of a grain is shown in Figure 59. This image clearly shows that the "grain" consists of many subgrains of oxide. The subgrains have a radial growth texture and extend to the grain boundaries. At the grain boundaries, the oxide becomes thicker, but the lateral subgrain dimensions do not change. Electron diffraction results indicate that the entire oxide scale is α-Al_2O_3.

Additional features within the scale are large amounts of intergranular and intragranular porosity, a high density of dislocations and precipitates that tend to be segregated to grain boundaries or outer regions of the grain (Figure 60). The precipitates are rich in zirconium and impurities such as iron, chromium and titanium. Figure 61 shows an electron diffraction pattern from one of these preciptates with an approximate chemical analysis as determined by EDS measurements. This precipitate is rich in Zr and Y. The exact nature of the precipitate is unknown however an analysis of the diffraction pattern indicates that the crystal structure is cubic with a lattice parameter $\approx$ 1.153 nm. EDS measurements of precipitate free regions within the grains and at grain boundaries did not reveal any differences in chemical

ORIGINAL PAGE IS
OF POOR QUALITY

Figure 59

0.1μm

TEM bright field image of a sector of an α-Al_2O_3 grain of the lacey morphology formed on a $(01\bar{1})$ β-NiAl specimen oxidized for 100 hours at 1100°C. Radially textured subgrains, dislocations and porosity are the main features.

1.0μm

Figure 60

TEM image of a grain boundary ridge region from the same specimen as in Figure 59. Precipitates and pores are observed to be within grain boundary ridges.

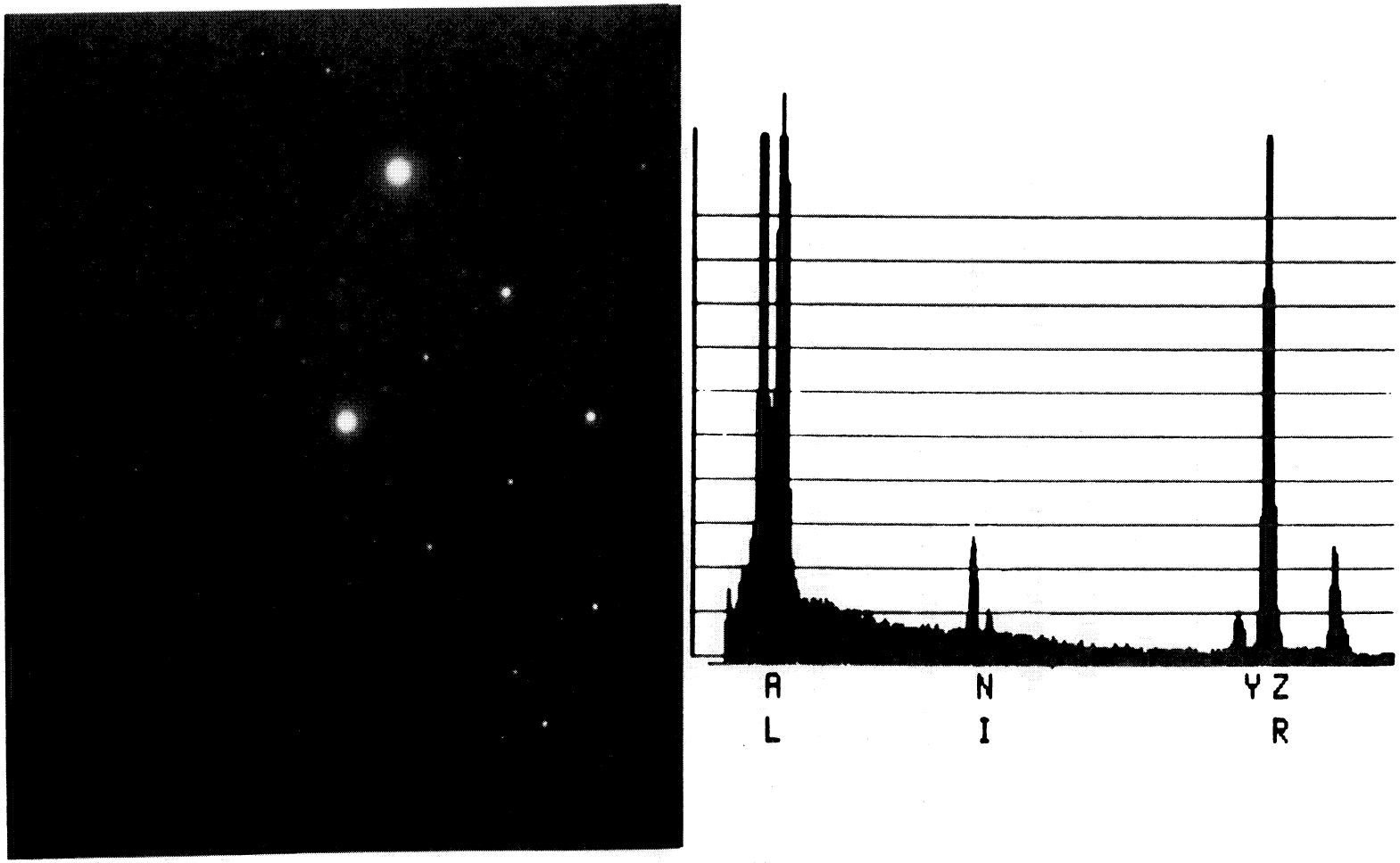

Figure 61

Selected area diffraction pattern and EDS spectrum from a precipitate within the α-Al_2O_3 scale. The precipitate contains predominantly Zr with a small amount of Y. The crystal structure appears to be cubic with a lattic parameter approximately 1.153 nm.

composition. Therefore, all the detectable impurities must be tied up within the precipitates.

The crystallographic orientations of the subgrains and relative orientations between subgrains have been determined by electron diffraction. One study was performed on a grain of α-Al_2O_3 from an oxidized (011) β-NiAl single crystal. The results are shown in the stereographic projection of Figure 62 and the TEM bright field image of Figure 63. The subgrain boundaries have a misorientation as small as 1°. As the subgrains extend further away from the grain center, the misorientations become as much as 7°. Across grain boundaries, the misorientations are 10° or greater. The orientations of the subgrains are clustered and have an plane normal approximately parallel to the $[30\bar{3}1]$ direction of α-Al_2O_3.

On an oxidized (001) single crystal of β-NiAl, the subgrain orientations within a grain are more random. The stereographic projection in Figure 64 and the TEM bright field image in Figure 65 show the results of subgrain orientations for this case. The misorienetations are much larger across cracks in the oxide scale as would be expected. Some of the misorientation may be due to scale bending upon removal of the metal. The misorientation of a subgrain from a grain 40 μm away from the one shown in Figure 65 was greater than 30°.

There are some differences in the shapes of the subgrains from the two metal orientations. On oxidized (011) metal, the

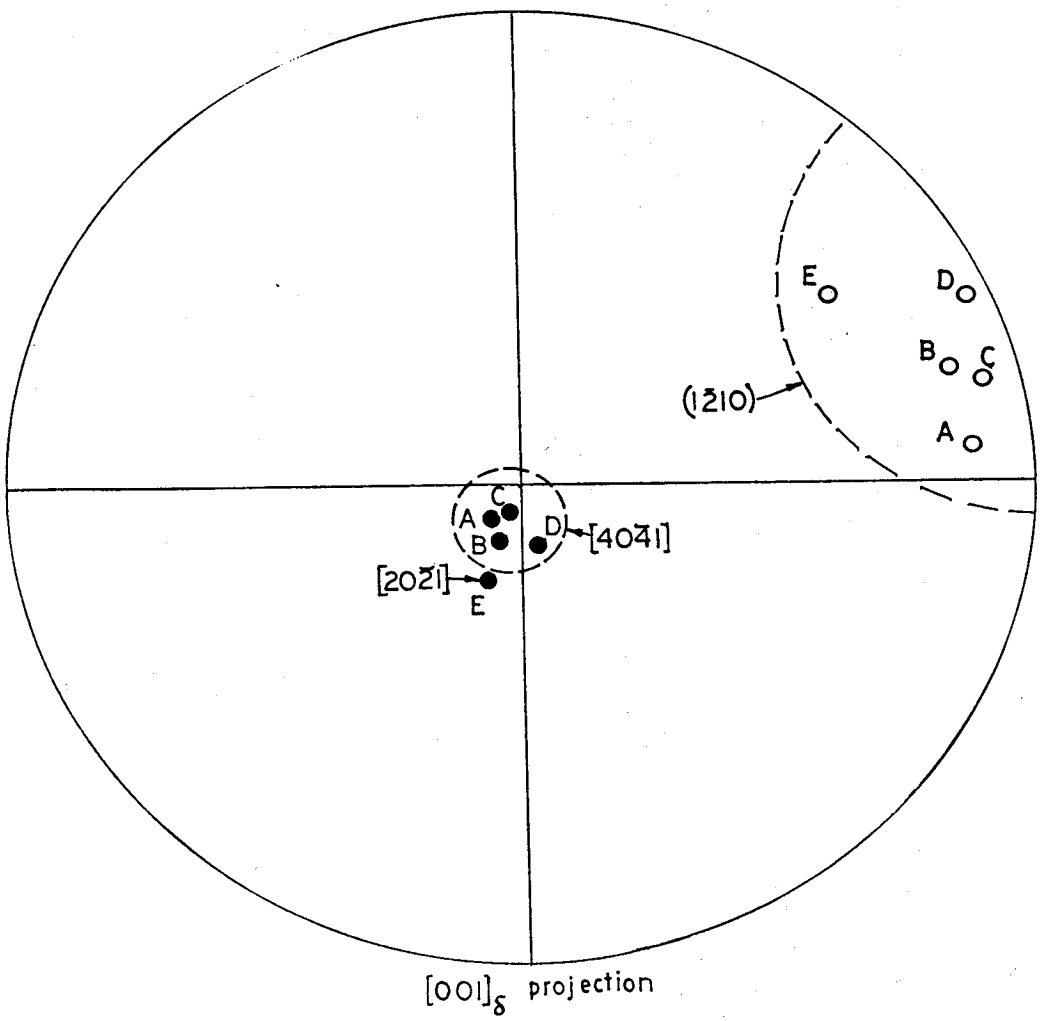

Figure 62

Stereographic projection of α-Al_2O_3 subgrain orientations from a scale formed on a (011) β-NiAl specimen oxidized for 100 hours at 1100°C. The letters correspond to individual grains in the TEM image of Figure 63.

ORIGINAL PAGE IS
OF POOR QUALITY

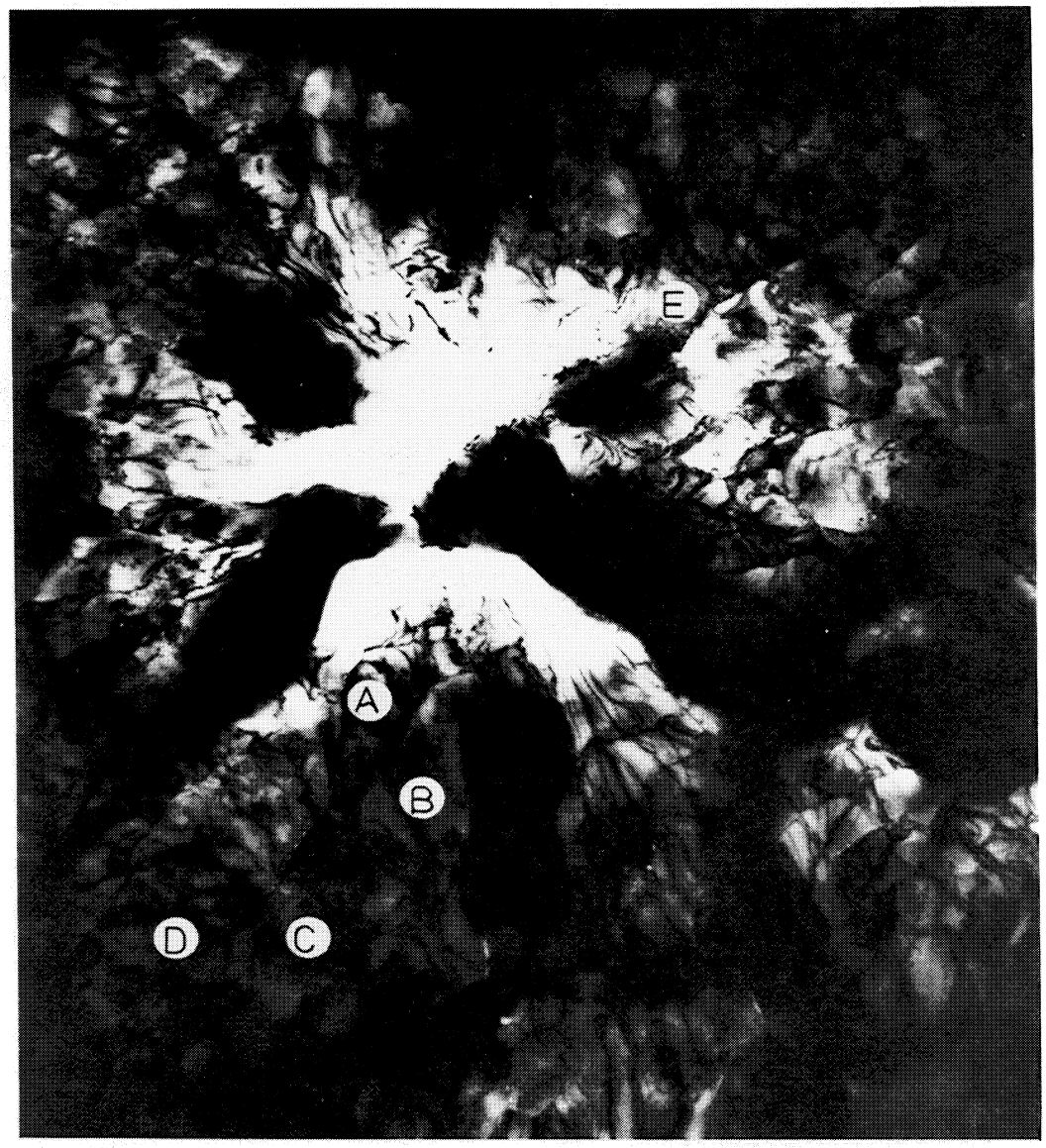

2.5μm

Figure 63

Bright field image of an α-Al_2O_3 grain from a β-NiAl specimen oxidized for 100 hours at 1100°C. The orientations of the lettered subgrains are plotted on the stereographic projection in Figure 62.

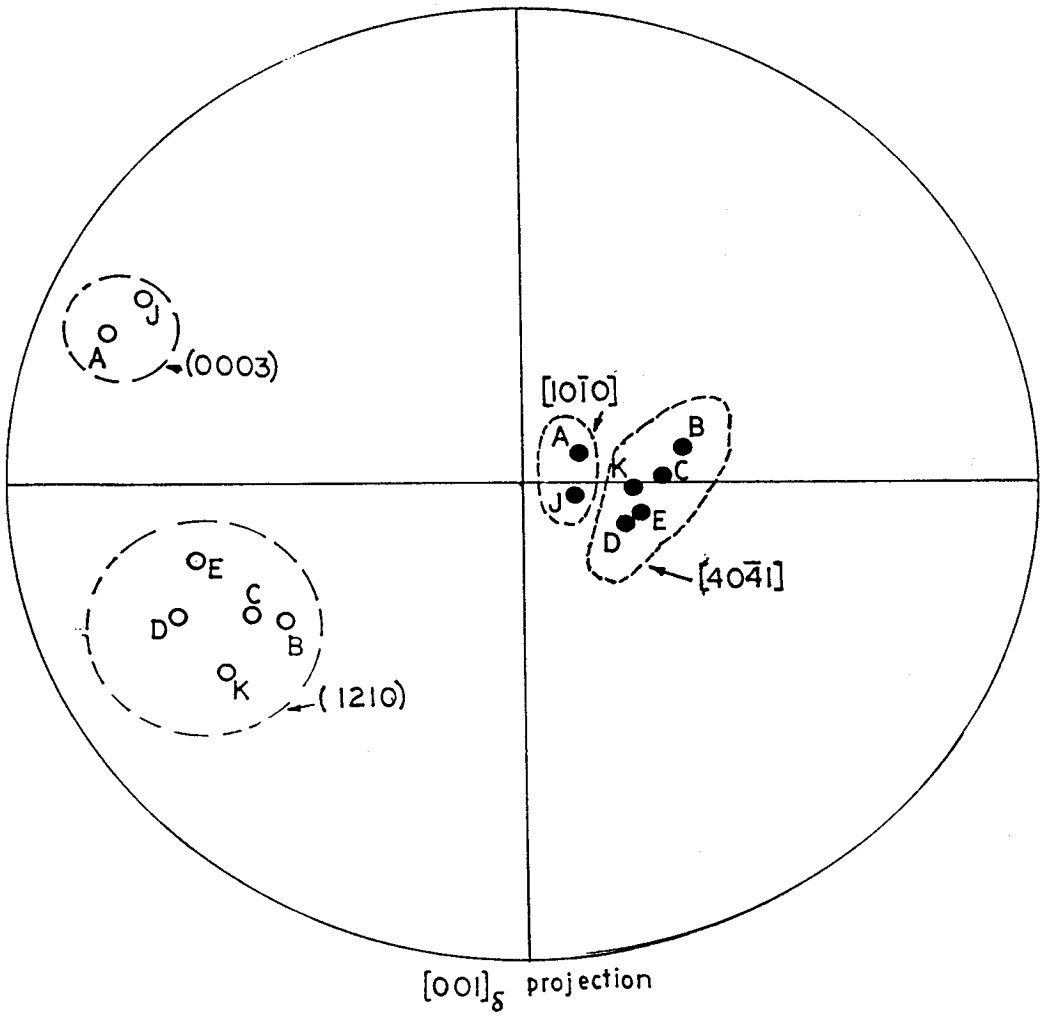

Figure 64

Stereographic projection of α-Al_2O_3 subgrain orientations from a scale formed on a (001) β-NiAl specimen oxidized for 100 hours at 1100°C. The letters correspond to individual subgrains in the bright field image of Figure 65.

2.5 μm

Figure 65

Bright field image of an α-Al_2O_3 region from a β-NiAl specimen oxidized for 100 hours at 1100°C. The orientations of the lettered subgrains are plotted on the stereographic projection in Figure 64.

subgrains are smaller, contain much more porosity, have a higher dislocation density and are more strongly clustered in relative orientation. On (001) oxidized metal, the subgrains are larger especially along radial directions and contain less porosity and fewer dislocations. The grain structure of the two orientations are also different. The (011) orientation contains more circular shaped grains whereas the grains are more blocky on (001) metal. This latter point will be discussed in the following chapter.

C. Discussion

1. Morphology

The lacey oxide morphology is unique to alumina scales. The many interesting features appear to be a result of the particular mechanism of scale formation and growth. The nucleation and growth phenomenon of the transformation to α-Al_2O_3 plays a major role in the formation of this morphology, as will now be discussed.

As mentioned in the previous chapter, α-Al_2O_3 nucleates and grows radially outward within the transient oxide scale. This process involves a large volume change which results in pores and dislocations. This volume change also results in a large stress gradient through the α-Al_2O_3 scale. This stress state can be

envisioned as that developed when a disc of smaller volume is attached to the sides and bottom of a rigid body into which a hole had been cut out for a larger disc to be placed. If the oxide is adherent to the metal, the oxide would be attached along its bottom surface to the metal. If the oxide is non-adherent to the metal, the bottom surface of the oxide would be free, setting up a biaxial stress state in the growing α-Al_2O_3 grain. The same biaxial stress state has been observed in brittle coating applications.[73] When the fracture stress of the oxide is exceeded by the magnitude of the circumferential stress component, radial cracks will form and extend outwards from a central point. These cracks are observed in the circular grains in Figure 53.

The cracks observed in the images of the α-Al_2O_3 scale having the lacey morphology can arise from three different phenomena. Transformation stresses may result in cracking as described above. The α-Al_2O_3 grains are not always ideally circular in shape so that cracks along other than radial directions can occur. The transformation cracks form at the oxidation temperatures, thus exposing metal to the oxidizing environment. Crack healing and fast oxidation in the vicinity of healed cracks results in local thick regions. Microstructural evidence for this is provided by the thick regions along some of the cracks in the oxide scale shown in Figure 54. The thickening occurs near the oxide-metal interface. Cracks can also form during cooling of the specimen due to compressive stresses created by thermal expansion mismatch

between the metal and oxide. The already present transformation cracks and grain boundaries are possible paths for this type of cracking. Because the temperature is lower when these cracks form, only slight oxidation would occur as noted by the absence of extremely thick regions along the majority of cracks. Cracks may also form upon TEM specimen preparation. However, no evidence of fast oxidation should be present for this case.

The ridges of oxide are present at grain boundaries where misorientations between adjacent grains are large and sometimes at subgrain boundaries in which misorientations might become relatively large. The ridges at grain boundaries therefore represent regions of fast oxidation relative to the grain interior. Ridges are found at both the gas-oxide and metal-oxide interfaces indicating that oxide is being formed by counterdiffusion of both aluminum and oxygen.

The radial progression of the transformation to α-Al_2O_3 implies that ridges form when two grains of transformed oxide meet. Thus, the last remaining transient oxide is present in the boundary regions between grains. Two important factors become evident. The first is that unless the radial progression rate of the transformed regions is extremely fast, the transient oxide will tend to thicken at a higher rate because of the faster rate of cation diffusion at the high oxidation temperatures where the $\gamma \rightarrow \alpha$ transformation occurs. From a study on alumina powder, the rate of transformation was found to be 2.6 X

10^{-3}(mole-fraction/minute) at 1100°C.[53] Thus, the transformation should not be complete until after 6.4 hours at 1100°C according to this transformation rate. However, only α-Al_2O_3 was observed on a β-NiAl specimen oxidized for 3 hours at 1100°C indicating that the transformation was completed within 3 hours at 1100°C.[74] The variation in scale thickness within an α-Al_2O_3 grain is dependent on both the rate of scale thickening and the rate of the $\gamma \rightarrow \alpha$ transformation. Equations for these mechanisms can be combined to calculate expected thickness contours within transformed regions of the scale. An equation for transient scale growth can be given as:

$$x^2 = k_\gamma \cdot t \qquad [15]$$

where k_γ is the parabolic rate constant for transient scale growth. The transformation front can be assumed to move radially outward according to a linear equation given as:

$$r_\alpha = V_\alpha (t - t_o) \qquad [16]$$

where r_α is the radius in the oxidation plane of an α-Al_2O_3 grain, V_α is the velocity of the transformation front and t_o is the incubation time before the $\gamma \rightarrow \alpha$ transformation begins. Solving for t in equation [16] and substituting into equation [15] yields:

$$x^2 = k_\gamma(r_\alpha/V_\alpha + t_o) \qquad [17]$$

The result of equation [17] suggests that the thickness of the transformed regions will increase parabolically with distance from the center of an α-Al_2O_3 grain to the grain boundaries where ridges form. Other factors contributing to the variation in transformed scale thickness are the volume change as the $\gamma \rightarrow \alpha$ transformation occurs, the growth of α-Al_2O_3 once the scale has transformed and surface smoothing as described in the previous chapter. Surface smoothing is the only major contributing factor.

The second factor is that the impurities or precipitates present within the transient oxide prior to the transformation will be swept outward in front of the transformation front. This occurs because the solubility of cation metal impurities(Ni, Zr, Si, etc.) is much smaller in α-Al_2O_3 than in the metastable Al_2O_3 phases. Therefore, as shown in Figure 60, a high concentration of impurities as precipitates will be present at or near the grain boundaries. This is in contrast to subgrain boundaries which do not represent the intersection of two α-Al_2O_3 growth fronts. Also, the presence of impurities is crucial in that the growth mechanisms might be drastically affected by impurities. However, both of these effects will be shown later not to be responsible for the presence of the lacey morphology.

The porosity that is present remains mostly as intergranular voids. The intragranular porosity that formed upon transformation

is seldom evident although it is not surprising because the free surface and numerous dislocations act as perfect vacancy sinks. Stereomicroscopy of the intergranular voids indicated that the voids were not interconnected. Also, the voids did not appear to segregate to either of the scale surfaces.

2. Growth mechanisms

A description of growth mechanisms for scales having the lacey morphology becomes complicated by the many effects that result in the various features. A schematic drawing of the lacey morphology including most features that have been discussed is shown in Figure 66. This perspective drawing is presented as a reference for the remaining discussion. The main observation is that boundary diffusion plays a major role in scale growth. This becomes obvious when observing the locations of thick and thin regions within the scale. Thin regions occur at grain interiors which consist of subgrains of α-Al_2O_3. Thick regions occur at grain boundaries, cracks due to the $\gamma \rightarrow \alpha$ transformation and some subgrain boundaries near the outer regions of grains. Even with large numbers of dislocations and intergranular pores between subgrains, the grain interiors remain thin relative to higher angle boundaries.

Thick regions form at cracks produced by the $\gamma \rightarrow \alpha$

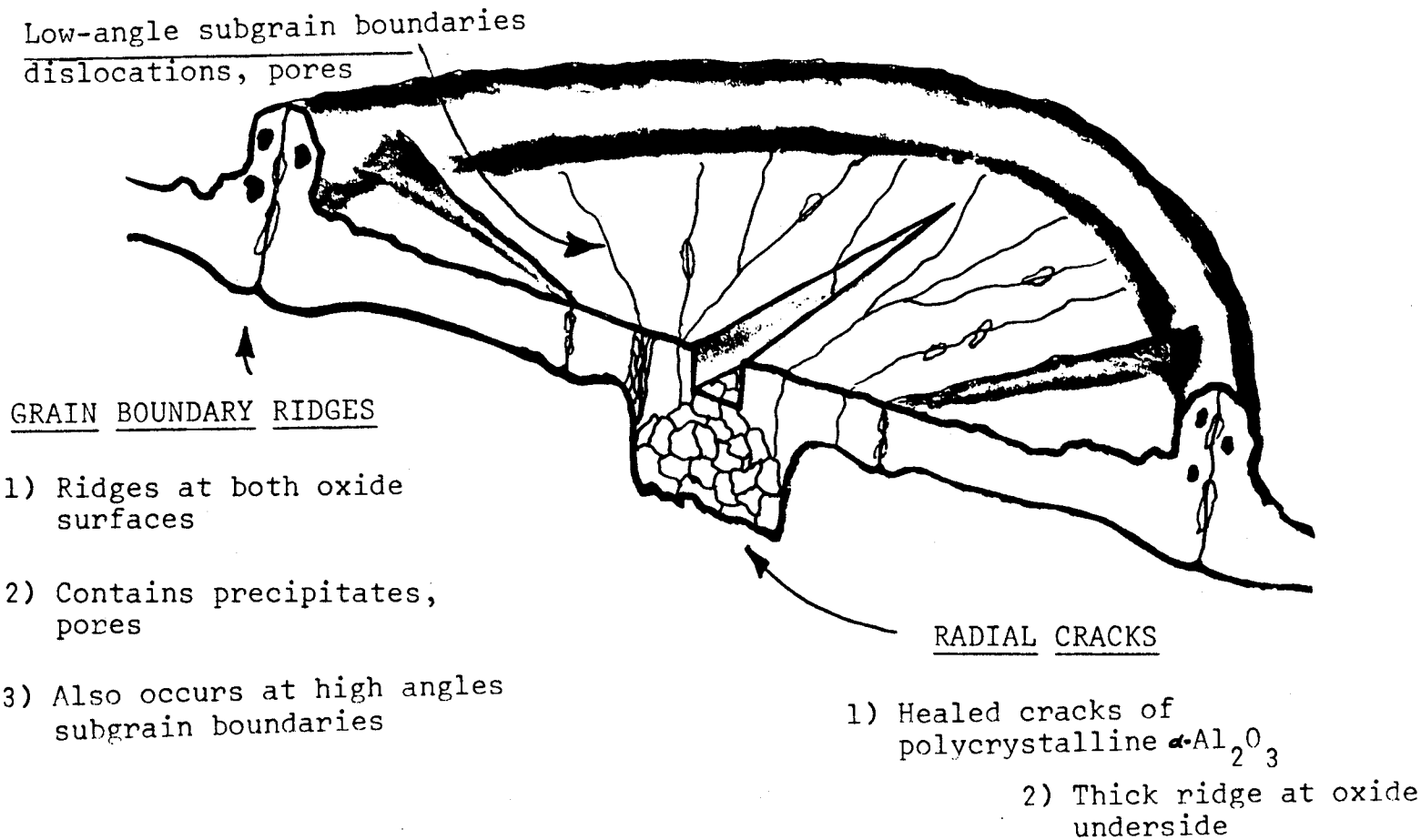

Figure 66

Schematic of the lacey morphology of α-Al_2O_3 scales.

transformation indicating that fast growth has occured to heal the crack. When cracks form in the oxide, the rate of oxidation is controlled by interface reactions resulting in a linear growth rate. Once diffusion through the scale becomes the rate limiting step, further oxidation occurs by parabolic growth. However, the presence of an extremely thick region around transformation cracks indicate that the crack healing process does not result in a uniform scale. Rather, a special type of boundary is formed by growth of oxide within cracks. This growth results in a refined grain structure as indicated by the diffraction pattern in Figure 67 showing polycrystalline α-Al_2O_3 from a region at a crack boundary. The grain size in this region is approximately an order of magnitude smaller than the adjacent subgrain. Because thick regions are only observed at the metal-oxide interface, inward diffusion of oxygen through this special boundary is responsible for fast oxide formation in healed cracks.

At grain boundaries, ridges are formed at both the gas-oxide and metal-oxide interfaces. This result implies that both inward oxygen and outward aluminum diffusion is responsible for formation of grain boundary ridges. The relative rates of both diffusion processes are complicated by the different morphologies of ridges at each interface. At the gas-oxide interface, the ridges are distinct protrusions. At the metal-oxide interface, the ridges are smoothed humps that do not extend as deep as the outer ridges extend upwards. A distinct boundary exists between subgrains from

ORIGINAL PAGE IS
OF POOR QUALITY

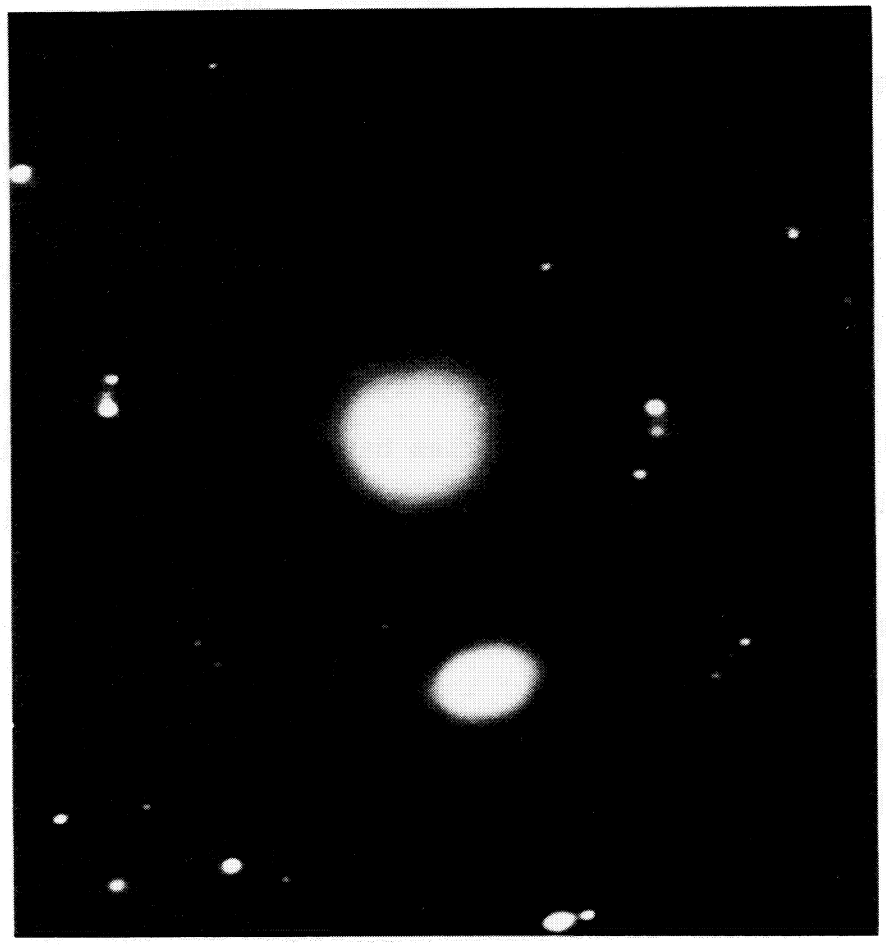

Figure 67

Selected area diffraction pattern showing polycrystalline α-Al_2O_3. The pattern was taken from a region within a healed crack.

adjacent grains and no fine grains are observed in the grain boundary regions. Grain boundary grooving is observable at grain boundary ridges in the SEM image of the metal-oxide interface in Figure 58a. The phenomenon of grain boundary grooving indicates that considerable surface diffusion occurs along the metal-oxide interface. Therefore, the relative rates of oxygen and aluminum counterdiffusion cannot be measured because ridge heights on the scale underside are reduced by surface diffusion.

The presence of ridges at radial subgrain boundaries near the outer regions of grains indicates that boundary diffusion resulting in ridge formation is highly dependent on boundary misorientation. Subgrain boundaries have a larger misorientation near grain edges than near grain centers. In fact, the ridges in question are observed to be thinner as the grain center is approached. Also, the effect of misorientation is most evident at grain boundaries in the form of the thickest ridges. At grain boundaries, the misorientations between adjacent grains are maximized.

The growth of α-Al_2O_3 scales having the lacey morphology is dominated by boundary diffusion of which there are two types. One mechanism of boundary diffusion involves inward oxygen diffusion along healed cracks resulting in scale growth at the metal-oxide interface. The healed cracks contain narrow bands of polycrystalline α-Al_2O_3 formed as a result of fast oxidation. A second boundary diffusion mechanism occurs at grain boundaries

having relatively large misorientations. In this case, counterdiffusion of aluminum and oxygen occur to form ridges. Both mechanisms of diffusion contribute to oxide formation and in fact the majority of scale growth occurs at these ridges. Diffusion through subgrains in grain interiors is considered to be a very minor contributor to total scale growth and therefore will be neglected in the following discussions. Another contributing factor in the difference between diffusion mechanism along the two distinct boundaries may be the presence of impurities. At cracks, the concentration of impurities is at a minimum because the regions are close to grain centers. At grain boundaries, the concentration of impurities is a maximum because of the the sweeping action of the transformation front on impurities. The effect of impurities may be to contribute to either, or both diffusion mechanisms depending upon the elements involved.[47]

Most studies involving growth mechanisms of α-Al_2O_3 scales in the same temperature range have resulted in the conclusion that α-Al_2O_3 scales grow by inward oxygen grain boundary diffusion. This conclusion has been obtained through ^{18}O tracer studies, inert marker experiments and Rutherford backscattering techniques. When the Al_2O_3 was not determined experimentally(α-Al_2O_3 versus metastable Al_2O_3 phases), the oxide phase was usually assumed to be α-Al_2O_3. In the present study, the same conclusion can be drawn about the growth mechanism. In polycrystalline regions (along healed cracks), inward oxygen diffusion results in scale

growth at the metal-oxide interface.

Counterdiffusion of aluminum and oxygen has been suggested in studies involving oxide adherence(growth-stress model)[22] and scales having the lacey morphology.[13] The microstructure of oxide ridges at both interfaces is enough evidence to conclude that counterdiffusion can occur within α-Al_2O_3 scales. However, the grain boundary morphology where counterdiffusion occurs is quite unique. At grain boundaries where ridges form, the boundary can be approximated by a single plane formed by two subgrains having a misorientation greater than 10°. This situation is drastically different from the case of ridges formed at healed cracks in which a band of polycrystalline oxide occurs. Hindam implied that an ultrafine grain size exists at ridges because of thick oxide formation due to fast diffusion.[75] However, no experimental evidence was provided in this and later descriptions of the work.[13,76] Felten and Pettit found polycrystalline regions in lacey scales but did not single out ridges as being polycrystalline regions.[71]

Frequent misunderstanding may have occurred in recent studies as to the nature of oxide ridges.[13,71,76] No differentiation has been made between ridges formed by cracks and ridges formed at grain boundaries. Fewer oxide ridges were observed at the metal-oxide interface by Hindam and Smeltzer who suggested that growth of the scales occured by predominately outward cation diffusion because a smaller grain size was observed at the

gas-oxide interface. However, this can be explained by fewer ridges existing at the metal-oxide interface because the frequency of cracks resulting in thick ridges at the metal-oxide interfaces is less than the frequency of grain boundaries resulting in thick ridges at the gas-oxide interface.

Because of the many complications involved with diffusion mechanisms, modelling the kinetics of lacey morphology scale growth is difficult. A model developed by Smeltzer et al. provides an expression for parabolic scale growth taking into account short-circuit(boundary) diffusion.[77] Smialek has simplified the approach for use with typical parabolic growth rate data.[29] The parabolic growth rate equation:

$$x^2 = k_p \cdot t \qquad [5]$$

can be approximated as:

$$x^2 = D_{eff} \cdot t \qquad [18]$$

where D_{eff} is the effective diffusion coefficient taking into account both lattice and short-circuit diffusion. The effective diffusion coefficient can be written as:

$$D_{eff} = D_L(1-f) + D_B f \qquad [19]$$

where D_L = lattice diffusion coefficient

D_B = short-curcuit diffusion coefficient

f = effective volume fraction of short-circuit region

The common usages of D_{eff} is for grain boundary diffusion so that, f, would be the effective volume fraction of grain boundary region. If a uniform or consistent scale morphology exists, the effective volume fraction of grain boundaries can be approximated or measured. Smialek observed columnar grains of α-Al_2O_3 on oxidized NiCrAl alloys; he approximated f to be:

$$f = 2\delta/d \qquad [20]$$

where δ = grain boundary width

d = grain size

Hindam and Smeltzer utilized grain growth laws to obtain, f, for their study of the growth kinetics of the lacey morphology scale on β-NiAl.[13] Their results relied upon grain size measurements from SEM images of scale cross sections. An increase in grain size with time was observed and compared to an empirical grain growth model for which a large error was obtained.[75] Their error in grain growth kinetics most likely was a result of invalid grain size measurements according to the following reasoning. Felten and Pettit described the growth of scales having the lacey

morphology to occur by lateral thickening of oxide ridges at the expense of grain interiors, and eventual impingement of ridges.[71] However, Hindam and Smeltzer observed an increase in lateral grain size when the grain size should stay constant. Their scale growth model must therefore be in error because of improper values of the effective volume fraction of grain boundary.

A more exact model for growth kinetics of lacey morphology scales must incorporate the various diffusion mechanisms involved. D_{eff} would be given as:

$$D_{eff} = D_L(1-f_B-f_C) + D_B f_B + D_C f_C \qquad [21]$$

where f_C = effective volume fraction of transformation crack grain boundaries

D_C = diffusion coefficient in healed crack regions

D_B = diffusion coefficient along grain boundaries

f_B = effective volume fraction of grain boundaries

Because D_L is much less than D_B, D_{eff} can be written as:

$$D_{eff} = D_B f_B + D_C f_C \qquad [22]$$

Each term in this equation requires evaluation. The term, D_C, could be approximated by the grain boundary diffusion coefficient which has often been attempted to be calculated, although it is

still unknown. The effective volume fraction of transformation crack grain boundaries could be estimated from the measured number of cracks per volume and an equiaxed grain structure within a band through each crack. However, the necessary grain boundary width is unknown as in Smialek's case. The value of the grain boundary diffusion coefficient, D_B, would have to be evaluated based on misorientation of the boundaries as this has an overriding effect on ridge formation. The effective volume fraction of grain boundary must also involve a misorientaion parameter as well as a grain boundary width. Surely, the grain boundary width would be different for the cases of boundary diffusion along equiaxed grains in cracks and along misoriented grain boundaries at ridges. Also, the effect of impurities cannot be discounted in the analysis of grain boundary properties. Therefore, because of the inability to obtain even a qualitative estimate of the unknown quantities, no attempt will be made to model the growth kinetics in terms of aforementioned approaches.

When compared to results obtained for growth rates of alumina scales from other studies, it becomes evident that those scales having a lacey morphology thicken at a reduced rate by as much as one order of magnitude less than polycrystalline scales. This occurs because the combined effective diffusion of aluminum and oxygen is less in scales having the lacey morphology due to the number and nature of higher diffusivity paths. The results of various studies are presented in Table VIII for comparison.

TABLE VIII

Approximate parabolic rate constants for the oxidation of alumina-forming alloys at 1100°C. (Ref. 76).

Material	k_p ($mg^2/cm^4 \cdot hr$)	Comments
β-NiAl	3.4×10^{-4}	this study, electro-polished
"	4.3×10^{-4}	" " "
"	4.6×10^{-4}	" " "
"	1.2×10^{-4}	" " "
"	2.8×10^{-4}	" " "
"	2.3×10^{-3}	" " ,600 grit
"	2.1×10^{-3}	(Ref. 33)
"	1.3×10^{-3}	(Ref. 41)
"	2.7 X 10-3	
"	1.3×10^{-3}	
Ni-42at%Al	2.5×10^{-3}	
"	2.2×10^{-3}	
Ni-47Al-3Cr	4.6×10^{-3}	(Ref. 33)
Ni-25Al	7.1×10^{-3}	(Ref. 80)
"	7.7×10^{-3}	(Ref. 33)
Pt-6Al	7.9×10^{-4}	(Ref. 71)
Pt-22Al	7.2×10^{-4}	(Ref. 72)

In summary, a discussion was presented in this chapter of the morphology and growth of α-Al_2O_3 scales having the lacey morphology. The lacey morphology itself is a result of localized nucleation of α-Al_2O_3 within the transient Al_2O_3 scale and radial outward growth. Cracks form due to the large stress developed upon transformation; they quickly healby oxidation, resulting in a fine equiaxed band of polycrystalline α-Al_2O_3 along the crack length. Fast oxidation by inward oxygen grain boundary diffusion results in thick oxide formation at the metal-oxide interface below healed cracks. Ridges of oxide form at both scale surfaces boundaries formed by the transformation to α-Al_2O_3; this is due to counterdiffusion along relatively high angle grain boundaries. These boundaries separate grains of α-Al_2O_3 which consist of highly textured subgrains. The extremely slow growth rates are a result of limited boundary diffusion through the highly textured α-Al_2O_3 scale.

VI. The Evolution of α-Al_2O_3 Scale Morphology on Alumina-forming Alloys

The widespread use of Al_2O_3 scales as barriers to environmental attack emphasizes the need for suitable alumina-forming coating alloys compatible with the various base alloys. Available aluminum for Al_2O_3 scale formation may come from metallic coatings or from base alloys. As a result, many different alloys have been developed that oxidize to form protective Al_2O_3 scales. The characteristics of Al_2O_3 scale formation on different alloys are dependent on the particular alloy system. In the present study, oxidation of an alumina-forming β-NiAl alloy was considered. Oxidation of Pt-Al was also mentioned as a comparison. However, the majority of alloys used in practice contain much lower concentrations of aluminum and considerable amounts of other elemental additions, especially chromium. The purpose of this chapter is to summarize the results from the present study and apply them to other alumina-forming alloy systems. Some useful insights can be gained from the generalization to other alumina-forming alloy systems.

A. Oxidation of β-NiAl

1. Single crystal studies

The majority of experiments and analysis from the present study was performed using primarily two orientations of β-NiAl, (001) and (011). The oxidation of specimens having these two orientations was similar in most respects. The mechanisms of oxidation can be broken down into three stages: 1) a transient stage, 2) a transformation stage, 3) a mature stage.

The transient stage of oxidation was observed for up to 100 hours at temperatures of 800°C and for approximately 3 hours at 1100°C until the transformation to α-Al_2O_3 was complete. The extent of the transient stage at other temperatures was not determined. However, results from the present study of two temperature extremes indicate that similar mechanisms of scale formation during the transient stage occur at both temperature extremes. The major points of emphasis for the transient oxidation of (001) and (011) β-NiAl are: 1) metastable Al_2O_3 phases comprise the scales, 2) ordering of vacant cation positions and slight distortions of the original spinel-like unit cell result in the various metastable Al_2O_3 phases of which δ-Al_2O_3 is the most prevalent, 3) the scales are strongly textured having specific orientation relationships with the metal substrate, 4) growth of the scales occurs by outward cation diffusion.

The transformation of metastable Al_2O_3 phases to α-Al_2O_3 is observed to begin within 1 hour at 1100°C. The transformation occurs by a nucleation and lateral growth process. Associated with the transformation is an approximately 9% reduction in volume resulting in porosity and a high dislocation density within the transformed regions. The mechanism of scale growth changes when α-Al_2O_3 is formed so that the outward flux of cations necessary to maintain growth of transient surface oxide morphologies no longer occurs. As a result, oxide protrusions are smoothed by surface diffusion.

The mature stage of oxidation begins when the scale has transformed to α-Al_2O_3. The presence of the lacey morphology of α-Al_2O_3 is indicative of the mature stage. Initially, a transient scale is present. The transformation to α-Al_2O_3 occurs in localized regions and spreads laterally outward. Surface diffusion becomes active, smoothing oxide protrusions present from the transient stage. The α-Al_2O_3 subgrains that are formed have a minimum misorientation near the point of nucleation and a maximum misorientation near grain boundaries where adjacent patches of α-Al_2O_3 impinge from lateral growth. At grain boundaries, ridges of oxide are formed by accelerated growth due to boundary diffusion of both oxygen and aluminum. Grain boundary ridges form at both scale interfaces but those formed at the metal-oxide interface are smoothed by surface diffusion. When tensile stresses from the $\gamma \rightarrow \alpha$ volume decrease become too large, cracks

form within the α-Al_2O_3, often initiating at regions where nucleation occurs. Fast oxide growth results in the formation of polycrystalline α-Al_2O_3 until the cracks are healed. Accelerated growth at these regions occurs by inward oxygen grain boundary diffusion.

There were no significant differences in measured growth rates of mature oxide scales formed on (001) and (011) β-NiAl specimens. However, some differences in the microstructures of mature scales were observed. These differences involved subgrains of α-Al_2O_3 within the larger grains. The subgrain size of α-Al_2O_3 on (001) β-NiAl specimens was larger and subgrains had more of a "blocky" shape than did subgrains of α-Al_2O_3 on (011) β-NiAl(Figures 63 and 65). Also, the relative misorientations between oxide subgrains were greater on (001) β-NiAl than on (011) β-NiAl. These differences could indicate that the rate of radial spreading of the $\gamma \rightarrow \alpha$ transformation front was faster on (001) β-NiAl than on (011) β-NiAl. Although the lacey morphology of α-Al_2O_3 was observed on both metal orientations, the nature of the lacey morphology on each orientation was slightly different. This indicates that there is an orientation effect of the substrate on the resulting lacey morphology.

2. Polycrystal studies

The effect of metal orientation on oxide morphologies and growth rates has been observed for the transient oxidation stage. This effect has been discussed earlier. In the previous section, only slight variations existed in the mature scale morphologies for (001) and (011) β-NiAl single crystals. However on polycrystalline β-NiAl substrates, a drastic effect of metal orientation on oxide morphology is clearly evident as shown in Figure 68 of an SEM image of the gas-oxide surface of a polycrystalline specimen oxidized for 100 hours at 1100°C. The triple point reflects the metal grains lying underneath the oxide scale. On two of the three grains, the lacey morphology is evident. On the third grain, the lacey morphology is almost non-existent. Figures 69 and 70 are optical and SEM images, respectively, of similar specimens from which the effect of metal orientation on oxide morphology is also clearly observed. Three major observations can be noted. 1) The number of α-Al_2O_3 grains is different on different metal orientations(Figure 69). 2) The shapes and sizes of α-Al_2O_3 grains are different for different metal orientations(Figures 69 and 70). 3) Oxide ridges are observed mainly where smoothing of the scale surface has occured(Figures 68-70).

The number density and size of the α-Al_2O_3 grains can all be related. Clearly, these are a function of the nucleation phenomenon as the scales transform to α-Al_2O_3. Larger but fewer grains correspond to fewer nuclei of α-Al_2O_3. Therefore, the

C-3

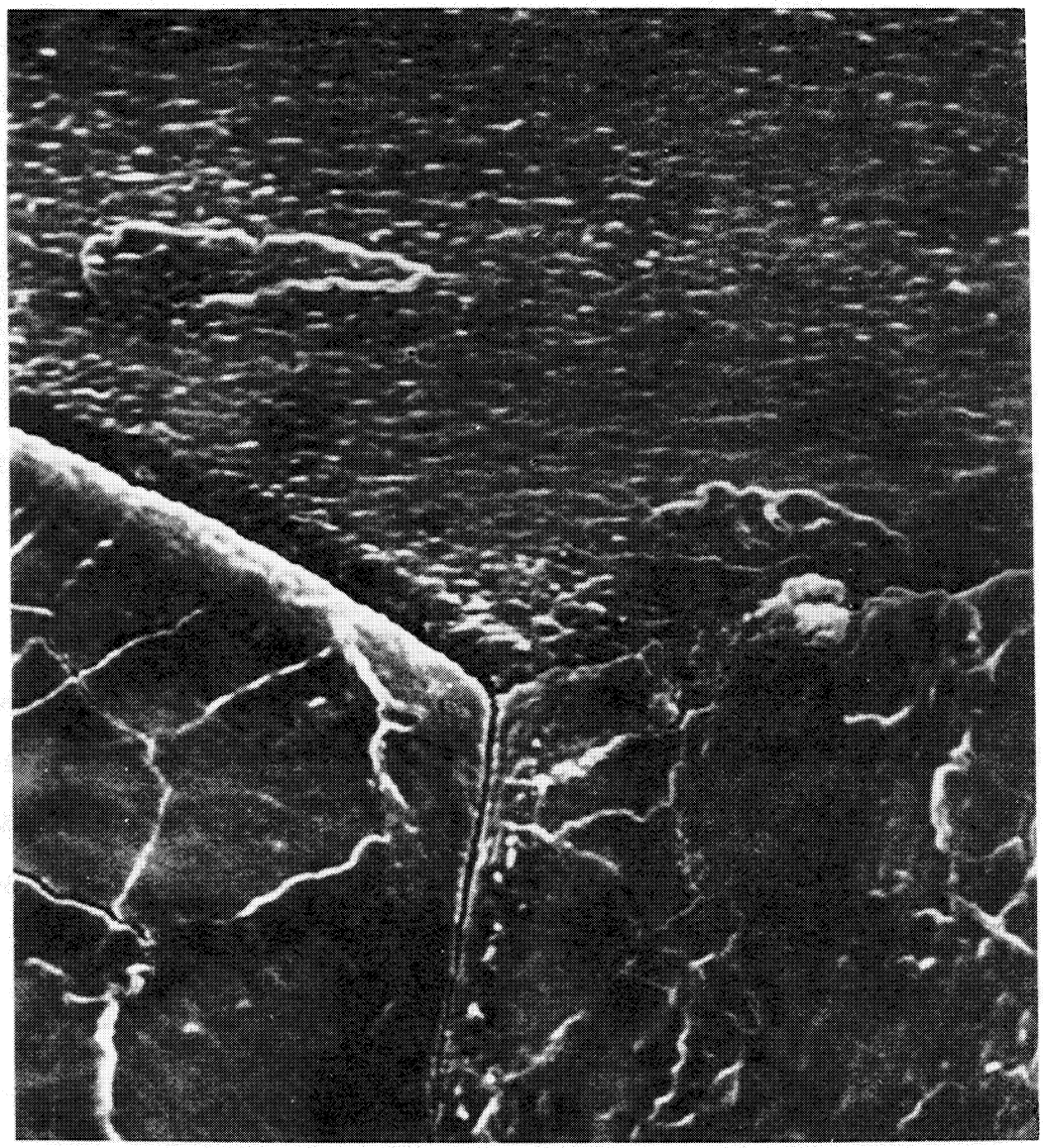

5.0μm

Figure 68

SEM image of the gas-oxide surface of a polycrystalline β-NiAl specimen oxidized for 100 hours at 1100°C. The triple point reflects the metal grain structure. Various lace morphologies are observed on the different metal orientations.

ORIGINAL PAGE IS
OF POOR QUALITY

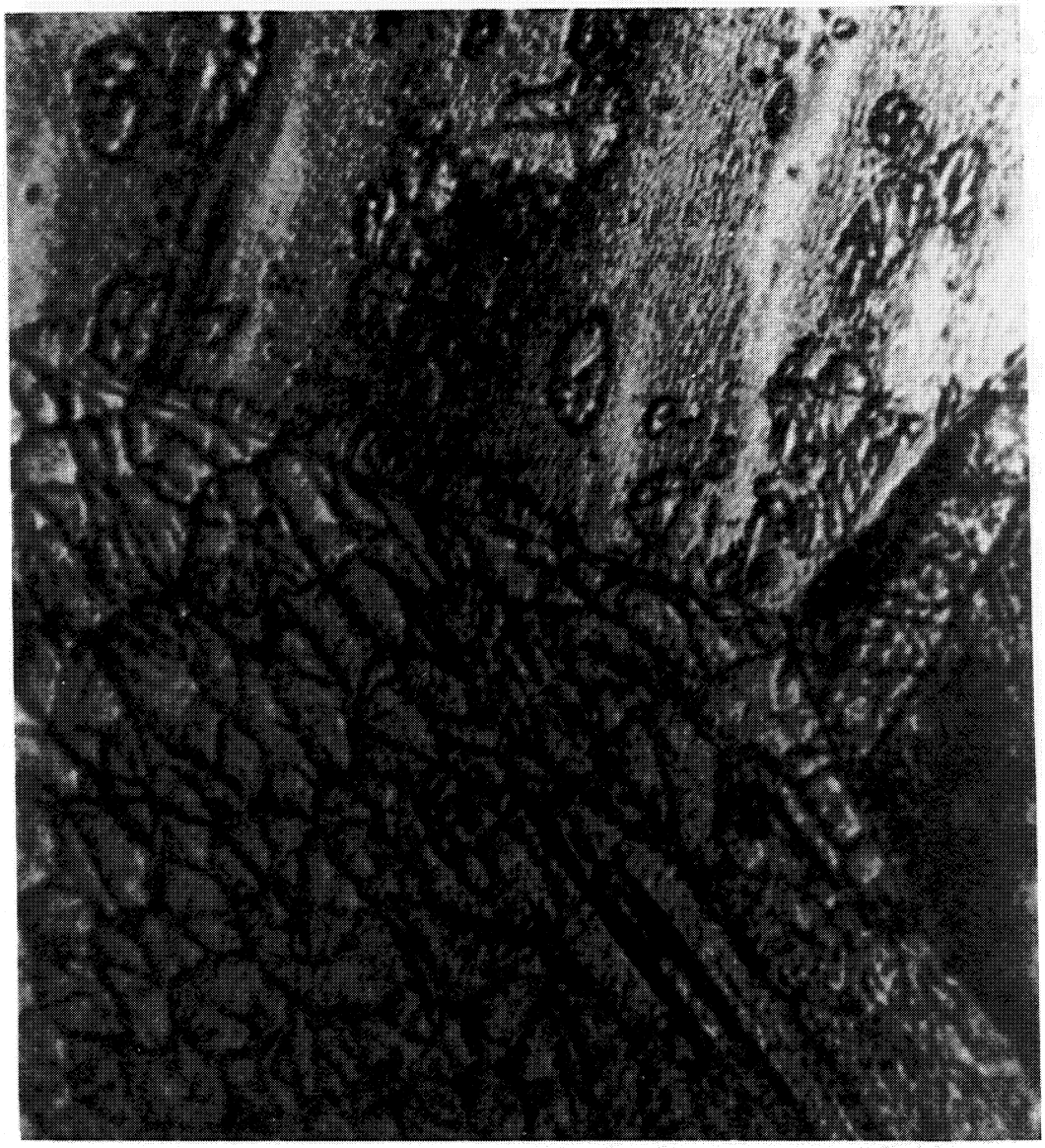

5.0 μm

Figure 69

Optical micrograph of the lacey morphology formed on a polycrystalline β-NiAl specimen.

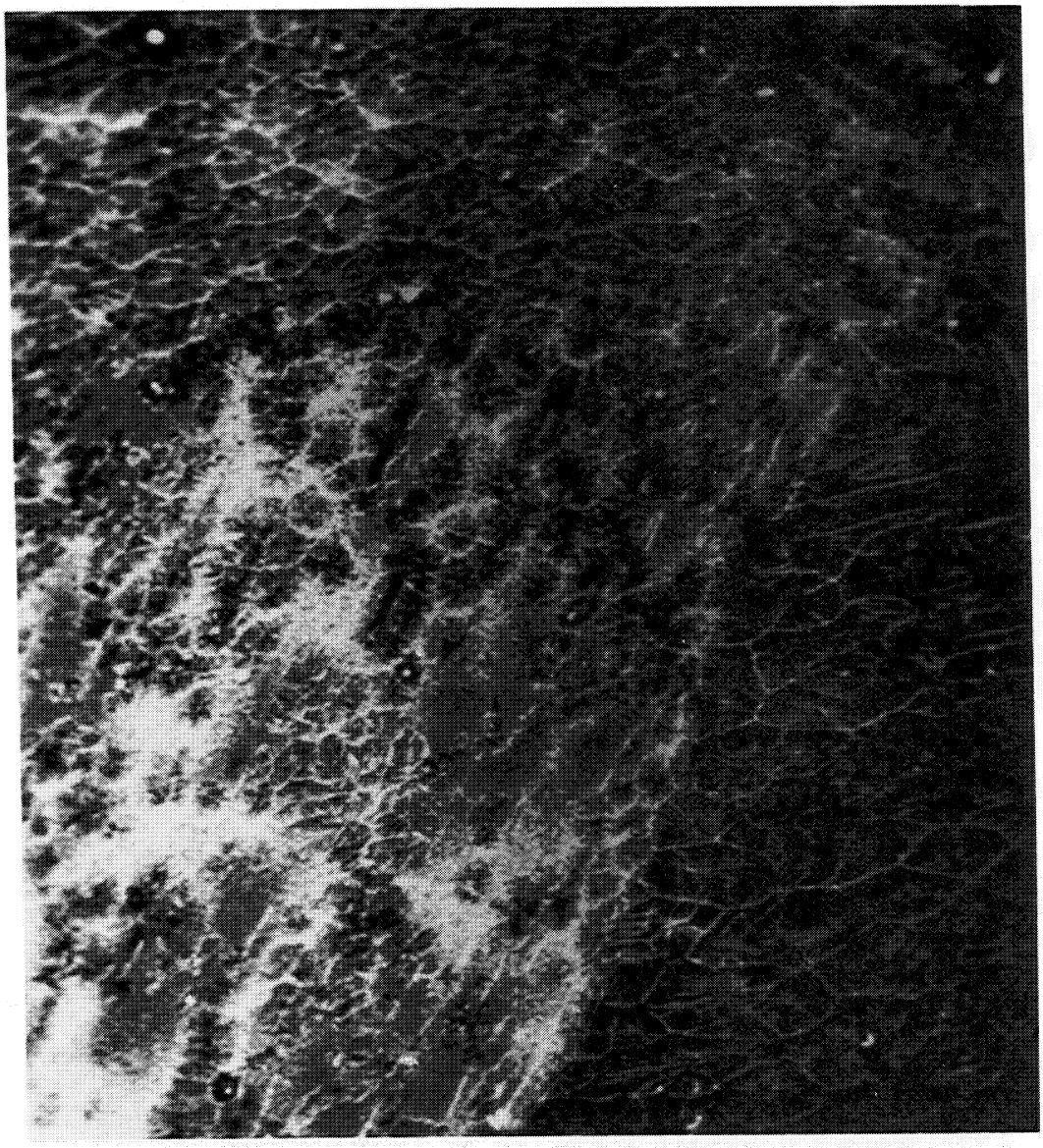

10.0μm

Figure 70

SEM image of the lacey morphology formed on a polycrystalline β-NiAl specimen.

nucleation rate of α-Al_2O_3 is different for different metal orientations. Hindam and Smeltzer observed differences in number density and size of α-Al_2O_3 grains in their studies.[13,75] They did not consider the $\gamma \rightarrow \alpha$ transformation as playing a role in the formation of the scale morphology but rather considered a "recrystallization" occuring to form large, oriented patches of α-Al_2O_3. In essence, a nucleation and growth phenomenon was implied. They suggested that the alloy substructure might play a role in the nucleation of recrystallized α-Al_2O_3. To study this effect, the X-ray Berg/Barrett technique was used. This technique is an X-ray imaging technique in which slight deviations from the Bragg condition result in contrast. Therefore, subgrains which have only slight misorientations will have a different contrast in images produced by this technique. Their results indicated that a higher number of α-Al_2O_3 grains were present on metal grains in which the metal substructure contained a higher number of subgrains. This would imply that subgrain boundaries in the metal would act as nucleation sites for recrystallization of the scale. However, the results were in no way quantitative to the extent that a correspondence between metal subgrains and oxide grains was ever observed.

No measurements of this sort or from other methods were obtained in the present study to support or reject the results of Hindam and Smeltzer. However, it is obvious that the nucleation rate of α-Al_2O_3 is different for different metal orientations.

The effect of metal orientation on the nucleation rate of α-Al_2O_3 might not be a direct effect but rather an indirect effect. Different metal orientations have been shown to result in different thicknesses and morphologies of transient scales. Depending on where the nucleation of α-Al_2O_3 takes place, i.e. within the scale or at the metal oxide interface, the change in nucleation rate of α-Al_2O_3 might be a function of the transient scale from which it forms. Nucleation sites might be within the transient scale at grain boundaries or subgrain boundaries. The oriented transient scales on (001) and (011) β-NiAl orientations would offer fewer nucleation sites than randomly oriented transient scales formed on other β-NiAl orientations in which higher angle grain boundaries exist. If nucleation sites were at the metal-oxide interface, the effect of metal orientation might be related to surface deformities acting as nucleation sites for α-Al_2O_3. Optical microscopic observations of abraded, unetched, polycrystalline, β-NiAl specimens showed an anisotropy of scratch depth and width. However, a study by Basu of oxidized FeCrAl on which the lacey morphology of α-Al_2O_3 formed showed no significant difference in grain size when specimens were polished to a 600 grit or a 1 μm diamond finish.[78] These results might not be conclusive because no control of metal orientation was maintained. Therefore, the possibility still exists that metal surface deformities affect the nucleation rate of α-Al_2O_3.

The shapes of α-Al_2O_3 grains would appear to be orientation

dependent as well. The different shapes arise from the rate of transformation being faster in some directions than in others. No orientation effect was observed for advancement of the transformation front on oxidized (001) and (011) metal orientations. However, an orientation effect is present for the rate of transformtion on some metal orientations as indicated in Figure 69.

The fact that ridges are observed only in regions where smoothing of the oxide surface has occured indicates that ridge formation and oxide surface smoothing are related. As mentioned in the previous chapter, thick oxide at ridges might initially be the remnants of the last transient oxide to transform. The SEM image in Figure 71 is a higher magnification image of Figure 70. Where the surface of the scale has been smoothed, ridges are clearly evident. In regions where surface roughness still exists, ridges are reduced in distinction or are non-existent. This same effect is shown in the SEM image of Figure 72 of a different β-NiAl specimen oxidized at 1100°C for 100 hours. The scale is completely α-Al_2O_3 as evidenced by transformation cracks, yet ridges are only faintly observed. Therefore, the various surface morphologies observed on different metal orientations might be due to relative degrees of surface smoothing. Because surface diffusion plays such an important role in this phenomenon, the effect could be due to anisotropies of surface diffusion of α-Al_2O_3 scales. This effect has been reported by Henrichsen and

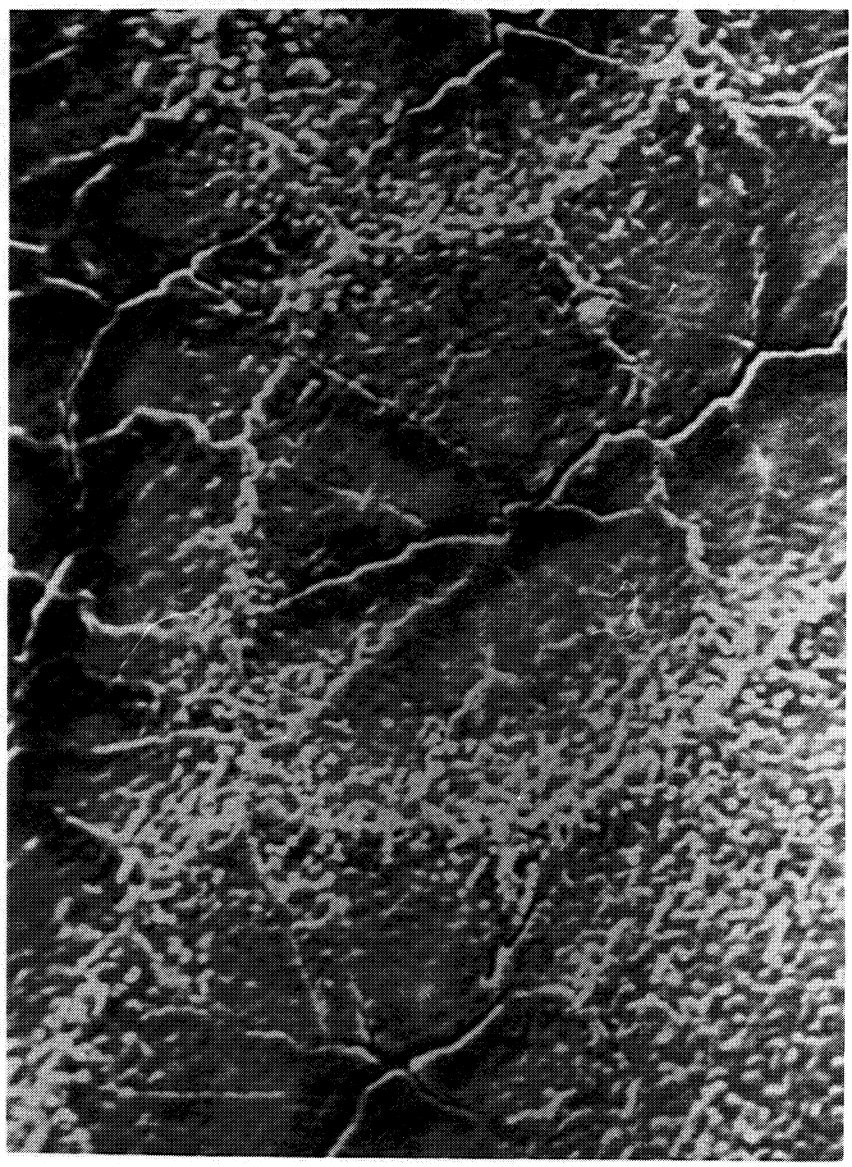

2.0μm

Figure 71

Higher magnification SEM image of a region in Figure 70. Ridges are distinct when the adjacent oxide is smooth but are difficult to observe when the adjacent regions are not smoothed.

ORIGINAL PAGE IS
OF POOR QUALITY

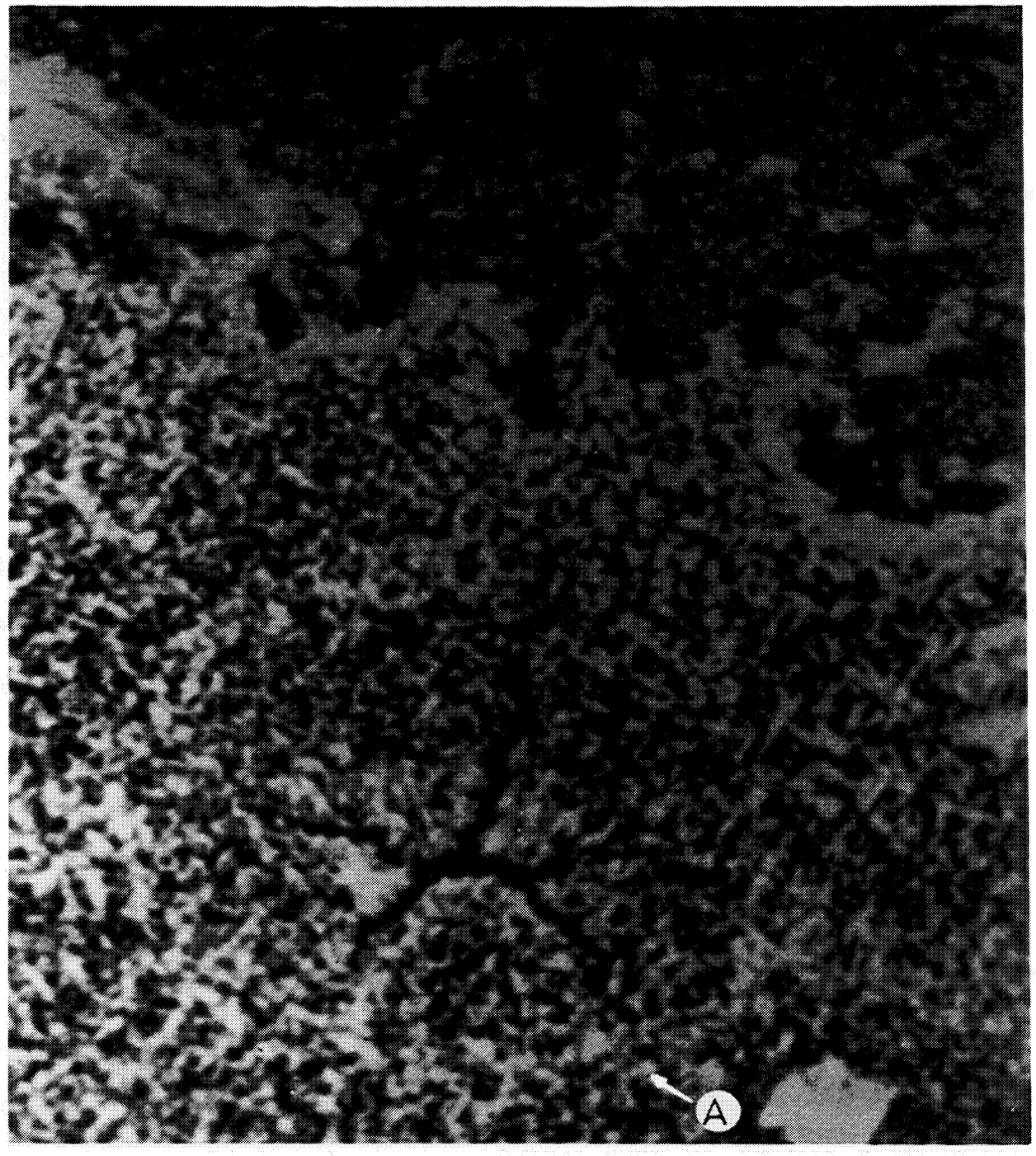

Figure 72

SEM image of an oxidized β-NiAl specimen. The presence of radial cracks indicate that the scale has transformed to α-Al_2O_3. However, the surface has not been smoothed and oxide ridges are only slightly evident(A).

Li.[79] Their studies were performed using an Al_2O_3-Ni couple in which the interface was marked with gratings. Annealing the couple at 1425°C produced faceting and various changes to the surface gratings depending upon orientation. All results for the Al_2O_3-Ni interface were consistent with Al_2O_3 surface results from other studies that were mentioned. For example, a change in orientation of Al_2O_3 by 1° away from (0001) produced a change in surface diffusion of 4X. Morphological changes were indicated to be controlled by surface diffusion for (0001) and $(11\bar{2}0)$ Al_2O_3 orientations whereas morphological changes were controlled by volume diffusion for $(11\bar{2}3)$ Al_2O_3 orientations. The change represents orders of magnitude dependencies of surface diffusion on orientation. From the section on surface smoothing in Chapter II, the time to completely smooth a surface protrusion varied as 1/B. The equation for, B, was given as:

$$B = D_s \gamma \nu \Omega^2 / kT \qquad [12]$$

B is shown to vary directly with the surface diffusion coefficient. Therefore, if only D_s changes with orientation, the time for complete smoothing varies as $1/D_s$. A decrease in surface diffusion by a factor of four would cause a fourfold increase in the time for complete smoothing. Therefore, the morphological differences of oxides formed on different metal orientations might be an effect produced mainly by anisotropies of surface diffusion

on Al_2O_3 scales.

2. Oxidation of other alumina-forming alloy sytems

Research has been performed using NiCrAl,[29] FeCrAl,[78] CoCrAl,[23] Pt-Al,[71,72] Ni_3Al,[80] dilute Ni-Al,[33,81] Co-Al[82] and other aluminum-forming alloys as materials for study. In most cases, a random, polycrystalline α-Al_2O_3 scale formed. Fine, equiaxed grains of α-Al_2O_3 are present at the gas-oxide surface or underneath transient scales which correspond to the composition of the base alloy. Because the α-Al_2O_3 scales grow by inward oxygen grain boundary diffusion, columnar grains form underneath the original layer of equiaxed grains. Except in cases where the lacey morphology forms, the mature, steady-state α-Al_2O_3 scales formed on alumina-forming alloys have the overall appearance of the schematic in shown Figure 73. Therefore, morphologies of protective Al_2O_3 scales can be classified into a lacey morphology and a polycrystalline morphology. The purpose of this section is to discuss experimental observations and the necessary requirements for the formation of the lacey morphology.

The lacey morphology has been observed most frequently on β-NiAl alloys.[12,13,41] This oxide morphology has also been observed on Pt-Al alloys as well.[71,72] For these two alloy

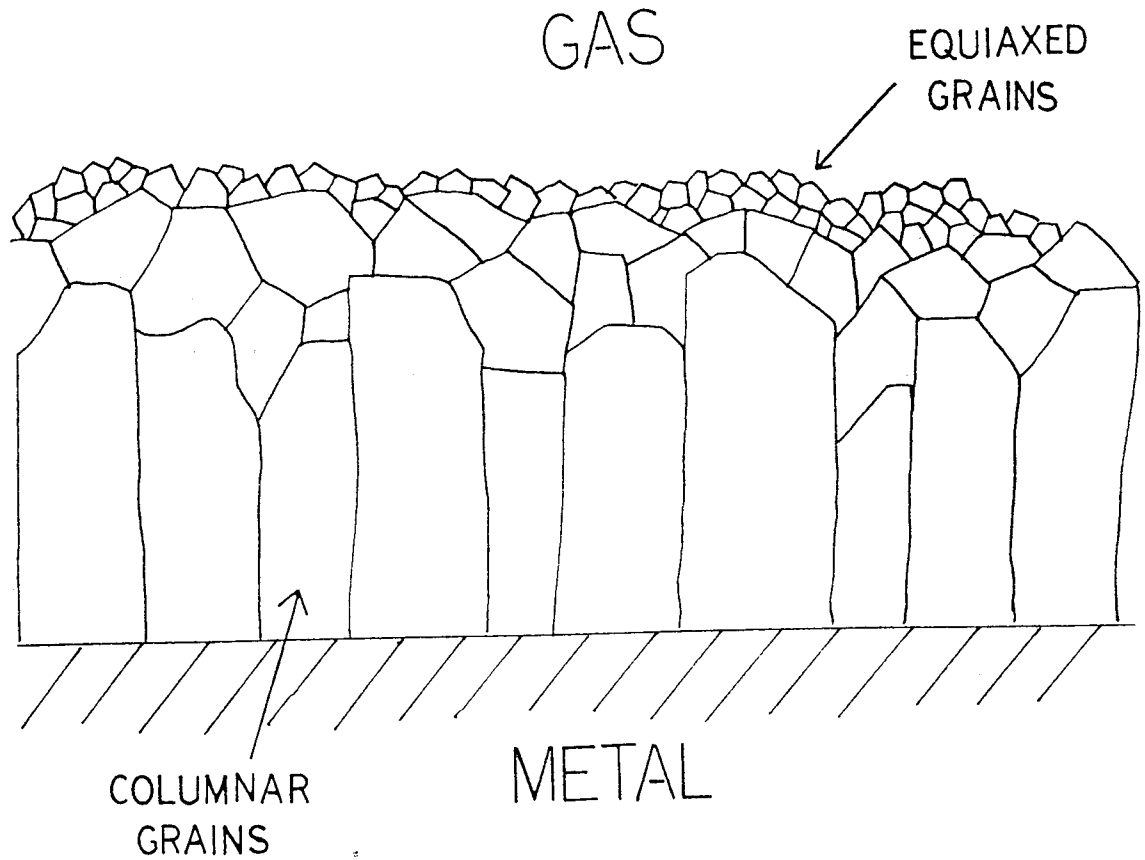

Figure 73

Schematic of a polycrystalline α-Al_2O_3 scale.

systems, formation of oxides other than Al_2O_3 is difficult at ambient pressures in the studied temperature ranges of 800°C to 1200°C. Even at 800°C, Ni-containing oxides were shown to be a very minor portion of the scale.[33] However, on most other alloys having lower concentrations of aluminum and/or additions of other more noble elements, considerable quantities of transient scales form prior to the formation of a healing layer of α-Al_2O_3. For example, scales formed on NiCrAl alloys consist of NiO, $NiCr_2O_4$, $NiAl_2O_4$, Cr_2O_3 and Al_2O_3. Thus, formation of the lacey morphology is assisted by higher aluminum concentrations in the alloy and fewer noble metal additions which grow more rapidly at typical pressures and temperatures. This conclusion was obtained by Felten and Pettit in their study of Pt-Al.[71]

Felten and Pettit also concluded that lower oxygen pressures improved lace formation. Grains of Pt_5Al_3 formed the lacey morphology at low oxygen partial pressures whereas at ambient pressures, polycrystalline α-Al_2O_3 scales were formed. Basu has observed lace formation on FeCrAl alloys when specimens were annealed in a vacuum at high temperature prior to oxidation at the same temperature.[78] Polycrystalline scales were obtained when no vacuum anneal was performed prior to oxidation. This is a case where the lacey morphology formed on a ternary alloy. However, lace formation was induced by the low oxygen pressure treatment prior to oxidation. Smialek observed the lacey morphology under spalled regions of the scale on β-NiAl.[12] This inner oxide layer

was sufficiently thin and the α-Al_2O_3 grain size sufficiently large that this layer must have formed under reduced oxygen pressure conditions prior to spalling. A low oxygen partial pressure is present in this region due to the equilibrium oxygen partial pressure at the metal-oxide interface with possible fast oxygen diffusion through cracks or boundaries allowing formation of the inner layer.

Impurities may play a role in deterring lace formation. As mentioned in the section on polycrystalline morphologies of transient scales formed at 1100°C in Chapter II, specimens oxidized for 50 hours at 1100°C still showed a transient oxide surface morphology. Analysis of the scales by X-ray diffraction indicated that only α-Al_2O_3 was present. However, TEM and EDS examination of the same specimen revealed a thin layer of the fast growth morphology of θ-Al_2O_3 above a thick α-Al_2O_3 layer separated by an amorphous SiO_2 layer. The silicon is present because specimens contained a high volume of grain boundary precipitates that were observed in the cast alloy. X-ray diffraction was not sensitive enough to detect the thin outer layer of transient oxide. The silica layer prevented the $\gamma \rightarrow \alpha$ transformation to occur as in other cases of β-NiAl oxidation causing a healing layer of α-Al_2O_3, not having a lacey morphology, to form underneath the silica layer.

According to the experimental observations mentioned above, the conditions necessary to form an α-Al_2O_3 scale having the lacey

morphology are: 1) low nucleation rates of α-Al_2O_3 by either transformation or initial formation, and 2) minimal amounts of transient scales other than metastable Al_2O_3 phases. Both these requirements can be obtained by high aluminum concentrations and/or low oxygen partial pressures. As shown in the study of FeCrAl oxidation, lace formation can occur on chromium containing ternary alloys when oxidized at low oxygen pressures which supresses formation of transient oxides of more noble metals. Therefore, it would seem probable that all alloys having enough aluminum to form and maintain a protective Al_2O_3 scale could be oxidized at low partial pressures of oxygen to form the lacey morphology of α-Al_2O_3. Because of reduced growth rates associated with the lacey morphology, these scales would offer better resistance to further oxidation.

Conclusions

The oxidation of β-NiAl can be divided into three stages: 1) a transient stage, 2) a transformation stage and 3) a mature stage. Conclusions for each stage will be discussed in sequence.

1) Transient stage

Within 1 hour at 800°C, metastable Al_2O_3 phases comprise the majority of the oxide scales. Planar faults along $\langle 100 \rangle_\gamma$ (referring to γ-Al_2O_3) directions are caused by ordering of vacancies on cation sites resulting in streaking and extra reflections in diffraction patterns of the oxide scales. The eventual periodicity of the fault planes is $3a_o$ of the γ-Al_2O_3 unit cell thereby forming δ-Al_2O_3. The strong epitaxial relationships of the δ-Al_2O_3 scales persist through 100 hours of oxidation. The surface oxide morphologies vary as a function of metal orientation as a result of preferred growth directions. Growth rates of the scales also were dependent on metal orientation indicating an effect of subgrain boundary misorientation on outward, short-circuit cation diffusion.

Oxidation for 1.0 hours at 1100°C produced transient scales consisting of layer of θ-Al_2O_3 on a δ-Al_2O_3 matrix. These scales also grew by outward cation diffusion because fast-growth morphologies of θ-Al_2O_3 were always observable.

2) Transformation stage

The transformation from metastable Al_2O_3 phases to α-Al_2O_3 occurs within 1.0 hours at 1100°C by a nucleation and radial growth process. The transformation mechanism is a diffusion process because no specific orientation relationship exists between the parent metastable Al_2O_3 phases and the product α-Al_2O_3 phase. An approximately 9% volume decrease accompanies the transformation. The decrease in volume accounts for the formation of pores within the α-Al_2O_3 regions. A change in scale growth mechanism occurs as α-Al_2O_3 is formed. An outward flux of cations is absent within the α-Al_2O_3 grains preventing continued growth of the transient surface morphologies. The transient surface morphologies become smoothed by surface diffusion. An analysis of the rate of recession of an idealized oxide protrusion was performed using the theory developed by Nichols and Mullins[68] involving morphological changes due to capillarity induced surface diffusion. The theory was able to predict the time necessary for smoothing of oxide protrusions such as those formed during

transient stages of oxidation.

3) Mature stage

The mature stage of oxidation begins when the $\gamma \rightarrow \alpha$ transformation is complete. The lacey oxide morphology forms when α-Al_2O_3 nuclei meet resulting in a ridge network due to fast diffusion along the grain boundaries. Radial cracks form at the transformation temperature due to tensile stresses resulting from the $\gamma \rightarrow \alpha$ volume decrease. The cracks quickly heal by formation of fine-grained α-Al_2O_3. Fast inward oxygen diffusion occurs along the high-angle grain boundaries in polycrystalline crack regions in contrast with counterdiffusion occurring along lower angle grain boundaries. The scale grows by the combined diffusion along high-diffusivity paths. The appearance of the lacey morphology was found to be dependent on the substrate orientation and was related to different nucleation rates of α-Al_2O_3 and surface diffusion anisotropies.

References

1. N. Birks, G. H. Meier: Introduction to High Temperature Oxidation of Metals, Edward Arnold Ltd., London, 1983.

2. C. S. Tedmon: "The Effect of Oxide Volatilization on the Oxidation Kinetics of Cr and Fe-Cr Alloys," J. Electrochem. Soc., 113, p. 766 (1966).

3. C. A. Barrett, C. E. Lowell: "Resistance of NiCr-Al Alloys to Cyclic Oxidation at 1100°C and 1200°C," Oxid. Met., 11, p. 199 (1977).

4. G. R. Wallwork, A. Z. Hed: "Some Limiting Factors in the Use of Alloys at High Temperatures," Oxid. Met., 3, p. 171 (1971).

5. F. S. Pettit: "Oxidation Mechanisms for Nickel-Aluminum Alloys at Temperatures Between 900° and 1300°C," Trans. Met. Soc. AIME, 239, p. 1296 (1967).

6. B. H. Kear, F. S. Pettit, D. E. Fornwalt, L. P. Lemaire: "On the Transient Oxidation of a Ni-15Cr-6Al Alloy," Oxid. Met., 3, p. 557 (1971).

7. G. C. Wood, B. Chattopadhyay: "Transient Oxidation of Ni-base Alloys," Corros. Sci., 10, p. 471 (1970).

8. C. Wagner: "Contributions to the Theory of Surface Colouring [of Metals]," Z. Phys. Chem., 21, p. 25 (1933).

9. K. P. R. Reddy, J. L. Smialek, A. R. Cooper: "^{18}O Tracer Studies of Al_2O_3 Scale Formation on NiCrAl Alloys," Oxid. Met., 17, p. 429 (1982).

10. Y. Oishi, W. D. Kingery: "Self-Diffusion of Oxygen in Single Crystal and Polycrystalline Aluminum Oxide," J. Chem. Phys., 33, p. 480 (1960).

11. K. P. R. Reddy: "Oxygen Diffusion in Close Packed Oxides," Ph. D. Thesis, Case Western Reserve University, Cleveland, OH, 1979.

12. J. L. Smialek: "Oxide Morphology and Spalling Model for

NiAl," Met. Trans. A, 9A, p. 309 (1978).

13. H. M. Hindam, W. W. Smeltzer: "Growth and Microstructure of α-Al_2O_3 on β-NiAl," J. Electrochem. Soc., 127, p. 1639 (1980).

14. F. A. Golightly, F. H. Stott, G. C. Wood: "The Influence of Yttrium Additions on the Oxide-Scale Adhesion to an Iron-Chromium-Aluminum Alloy," Oxid. Met., 10, p. 163 (1976).

15. D. P. Whittle, J. Stringer: "VIII. Improvement in Properties: Additives in Oxidation Resistance," Phil. Trans. R. Soc. Lond., A 295, p. 309 (1980).

16. L. B. Pfeil: U. K. Patent No. 459848, 1937.

17. J. Stringer, B. A. Wilcox, R. I. Jaffee: "The High-Temperature Oxidation of Nickel-20wt% Chromium Alloys containing Dispersed Oxide Phases," Oxid. Met., 5, p. 11 (1972).

18. J. M. Francis, W. H. Whitlow: "The Effect of Yttrium on the High Temperature Oxidation Resistance of Some Fe-Cr Base Alloys in Carbon Dioxide," Corros. Sci., 5, p. 701 (1965).

19. D. P. Whittle, M. E. El-Dahshan, J. Stringer: "The Oxidation Behaviour of Cobalt-Base Alloys Containing Dispersed Oxides Formed by Internal Oxidation," Corros. Sci., 17, p. 879 (1977).

20. G. C. Wood, J. Boustead: "The Influence of Group IIIA Metals on the Oxidation of Fe-Cr Alloys," Corros. Sci., 8, p. 719 (1968).

21. D. Delaunay, A. M. Huntz: "Mechanisms of adherence of alumina scale developed during high-temperature oxidation of Fe-Ni-Cr-Al-Y alloys," J. Mat. Sci., 17, p. 2027 (1982).

22. F. A. Golightly, F. H. Stott, G. C. Wood: "The Relationship Between Oxide Grain Morphology and Growth Mechanisms for Fe-Cr-Al and Fe-Cr-Al-Y Alloys," J. Electrochem. Soc., 126, p. 1035 (1979).

23. I. M. Allam, D. P. Whittle, J. Stringer: "The Oxidation Behavior of CoCrAl Systems Containing Active Element Additions," Oxid. Met., 12, p. 35 (1978).

24. A. S. Kahn, C. E. Lowell, C. A. Barrett: "The Effect of Zirconium on the Isothermal Oxidation of Nominal

Ni-14Cr-24Al Alloys," J. Electrochem. Soc., 127, p. 670 (1980).

25. A. B. Anderson, S. P. Mehendru, J. L. Smialek: "Dopant Effect of Yttrium and the Growth and Adherence of Alumina on Nickel Aluminum Alloys," J. Electrochem. Soc., 132, p. 1695 (1985).

26. A. Ashary, G. H. Meier, F. S. Pettit: "Acoustic Emission Study of Oxide Cracking During Alloy Oxidation," Proc. Conference on High Temperature Protective Coatings, March, 1983.

27. A. W. Funkenbusch, J. G. Smeggil, N. S. Bornstein: "Reactive Element-Sulfur Interaction and Oxide Scale Adherence," Met. Trans. A, 16A, p. 1164 (1985).

28. J. L. Smialek, R. Browning: "Current Viewpoints on Oxide Adherence Mechanisms," NASA Technical Memorandum 87168, 1985.

29. J. L. Smialek: "Microstructure of Al_2O_3 Scales Formed on NiCrAl Alloys," Ph.D. Thesis, Case Western Reserve University, Cleveland, OH, 1981.

30. J. L. Smialek, R. Gibala: "Structure of Transient Oxides Formed on NiCrAl Alloys," Met. Trans. A, 14A, p. 2143 (1983).

31. G. J. Santoro, D. L. Deadmore, C. E. Lowell: "Oxidation of Alloys in Nickel-Aluminum System with Third Element Additions of Chromium, Silicon, and Titanium at 1100°C," NASA Technical Note D-6414, 1971.

32. C. E. Lowell, G. J. Santoro: "The 1200°C Cyclic Oxidation Behavior of Two Nickel-Aluminum Alloys (Ni_3Al and NiAl) with Addititons of Chromium, Silicon, and Titatium," NASA Technical Note D-6838, 1972.

33. J. Doychak: "The Transient Oxidation of Single Crystal NiAl + Zr," MS Thesis, Case Western Reserve University, Cleveland, OH, 1984.

34. W. H. Gitzen: Alumina as a Ceramic Material, American Ceramic Society, Columbus, OH, 1970.

35. E. J. W. Verwey: "The Crystal Structure of γ-Fe_2O_3 and γ-Al_2O_3," Z. Krystallogr., 91, p. 65 (1935).

36. B. C. Lippens, J. H. de Boer: "Study of Phase

Transformations During Calcination of Aluminum Hydroxide by Selected Area Electron Diffraction," Acta Cryst., 17, p. 1312 (1964).

37. A. Dauger, D. Fargeot: "T.E.M. Study of Al_2O_3 Metastable Phases," Radiation Effects, 74, p. 279 (1983).

38. A. H. Heuer, T. E. Mitchell: "Further discussion on the space group of spinel," J. Phys. C: Solid State Phys., 8, p. L541 (1975).

39. S. Geller: "Crystal Structure of β-Ga_2O_3," J. Chem Phys., 33, p. 626 (1960).

40. K. Fueki, H. Ishibashi: "Oxidation Studies on Ni-Al Alloys," J. Electrochem. Soc., 108, p. 306 (1961).

41. G. C. Rybicki, J. L. Smialek: "High Temperature Oxidation of NiAl + Zr," to be published.

42. E. W. A. Young, J. H. W. de Wit: "The Use of a ^{18}O Tracer and Rutherford Backscattering Spectrometry to Study the Oxidation Mechanism of NiAl," to be published.

43. N. N. Khoi, W. W. Smeltzer, J. D. Embury: "Growth and Structure of Nickel Oxide on Nickel Crystal Faces," J. Electrochem. Soc., 122, p. 1495 (1975).

44. H. S. Hsu, G. J. Yurek: "Kinetics and Mechanisms of the Oxidation of Cobalt at 600 - 800°C," Oxid. Met., 17, p. 55 (1982).

45. S. Matsunaga, T. Homma: "Influence on the Oxidation Kinetics of Metals by Control of the Structure of Oxide Scales," Oxid. Met., 10, p. 361 (1976).

46. C. S. Giggins, F. S. Pettit: "The Oxidation of TDNiC(Ni-20Cr-2 vol pct ThO_2) Between 900°C and 1200°C," Met. Trans., 2, p. 1071 (1971).

47. M. F. Yan, R. M. Cannon, H. K. Bowen, R. L. Coble: "Space-Charge Contribution to Grain-Boundary Diffusion," J. Amer. Cer. Soc., 60, p. 120 (1977).

48. W. A. Pliskin: "I. Nondestructive Optical Techniques for Thin-Film Thickness Measurements," in Physical Analysis and Measurement of Thin Films, Plenum Press, New York, 1969.

49. G. Yamaguchi, I. Yasui, W. C. Chiu: "A New Method of Preparing θ-Alumina and the Interpretation of Its

X-Ray-powder Diffraction Pattern and Electron Diffraction Pattern," Bull. Chem. Soc. Jap., 43, p. 2487 (1970).

50. D. Voss: "Microstructural Aspects of the Oxidation of Iron," MS Thesis, Case Western Reserve University, Cleveland, OH, 1979.

51. S. C. Carniglia: "Thermochemistry of the Aluminas and Aluminum Trihalides," J. Amer. Cer. Soc., 66, p. 495 (1983).

52. P. W. Clark, J. White: "Some Aspects of Sintering," Trans. Brit. Cer. Soc., 49, p. 305 (1950).

53. C. J. P. Steiner, D. P. H. Hasselman, R. M. Spriggs: "Kinetics of the Gamma-to-Alpha Alumina Phase Transformation," J. Amer. Cer. Soc., 54, p. 412 (1971).

54. F. W. Dynys, J. W. Halloran: "Alpha Alumina Formation in Alum-Derived Gamma Alumina," J. Amer. Cer. Soc., 65, p. 442 (1982).

55. W. T. Donlon, T. E. MItchell, A. H. Heuer: "Precipitation in non-stoichiometric spinel," J. Mat. Sci., 17, p. 1389 (1982).

56. G. C. Bye, G. T. Simpkin: "Influence of Cr and Fe on Formation of α-Al_2O_3 from γ-Al_2O_3," J. Amer. Cer. Soc., 57, p. 367 (1974).

57. K. J. D. Mackenzie, G. Hosseini: "Effect of Electric Fields on the Transformation of Gamma to Alpha Alumina," Trans. J. Brit. Cer. Soc., 77, p. 172 (1978).

58. T. A. Ramanarayanan, M Raghavan, R. Petkovic-Luton: "The Characteristics of Alumina Scales Formed on Fe-Based Yttria-Dispersed Alloys," J. Electrochem. Soc., 131, p. 923 (1984).

59. R. McPherson: "On the formation of thermally sprayed alumina coatings," J. Mat. Sci., 15, p. 3141 (1980).

60. M. J. Ridge, B. Maloney, G. R. Boell: "Transformation of Finely Divided Cubic to Trigonal Iron(III) Oxide," J. Chem. Soc. (A), Inorganic Phys. Theor., p. 594 (1967).

61. S. Kachi, K. Momiyama, S. Shimizu: "An Electron Diffraction Study and a Theory of the Transformation from γ-Fe_2O_3 to α-Fe_2O_3," J. Phys. Soc. Jap., 18, p. 106 (1963).

62. M. L. Kronberg: "Platic Deformation of Single Crystals of

Sapphire: Basal Slip and Twinning," Acta Met., 5, p. 507 (1957).

63. J. Hornstra: "Dislocations, Stacking Faults and Twins in the Spinel Structure," in Reactivity in Solids-Proceedings of 4th Symposium, Amsterdam, 1960, Edited by J. H. de Boer, W. G. Burgers, E. W. Gorter, J. P. F. Huesse, G. C. A. Schuit, Elsevier Publishing Company, Princeton, NJ, 1961.

64. J. W. Christian: "A theory of the transformation in pure cobalt," Proc. Roy. Soc. A, 206, p. 51 (1951).

65. W. E. Lee, K. P. D. Lagerlof: "Structural and Electron Diffraction Data for Sapphire(α-Al_2O_3)," J. Elec. Microsc. Tech., 2, p. 247 (1985).

66. Powder Diffraction File, #'s 10-173 and 16-394, American Society for Testing and Materials, Philadelphia, 1969.

67. Bond and Harvey: "Decoration of Dislocations in Aluminum Oxide," J. Appl. Phys., 34, p. 440 (1963).

68. F. A. Nichols, W. W. Mullins: "Morphological Changes of a Surface of Revolution due to Capillarity-Induced Surface Diffusion," J. Appl. Phys., 36, p. 1826 (1965).

69. T. Maruyama, W. Komatsu: "Surface Diffusion of Single-Crystal Al_2O_3 by Scratch-Smoothing Method," J. Amer. Cer. Soc.-Disc. and Notes, 58, p. 338 (1975).

70. J. K. Tien, F. S. Pettit: "Mechanism of Oxide Adherence on Fe-25Cr-4Al (Y or Sc) Alloys," Met. Trans., 3, p. 1587 (1972).

71. E. J. Felten, F. S. Pettit: "Development, Growth, and Adhesion of Al_2O_3 on Platinum-Aluminum Alloys," Oxid. Met., 10, p. 189 (1976).

72. J. S. Sheasby, D. B. Jory: "Electrical Properties of Growing Alumina Scales," Oxid. Met., 12, p. 527 (1978).

73. J. S. Lynch: "The Measurement of Residual Stresses," in Residual Stress Measurements, American Society for Metals, Cleveland, 1952.

74. J. Doychak: unpublished research.

75. H. M. Hindam: "Microstructure and Growth of Al_2O_3 on Ni-Al Alloys," Ph.D. Thesis, McMaster University, Hamilton, Ontario, 1979.

76. H. Hindam, D. P. Whittle: "Microstructure, Adhesion and Growth Kinetics of Protective Scales on Metals and Alloys," Oxid. Met., 18, p. 245 (1982).

77. W. W. Smeltzer, R. R. Haering, J. S. Kirkaldy: "Oxidation of Metals by Short Circuit and Lattice Diffusion of Oxygen," Acta Met., 9, p. 880 (1961).

78. S. N. Basu: "Analysis Techniques for Tracer Studies of Oxidation," MS Thesis, Case Western Reserve University, Cleveland, OH, 1984.

79. R. A. Henrichsen, C. Y. Li: "Capillarity and Mass Transport at the Ni-Al_2O_3 Interface," J. Amer. Cer. Soc., 59, p. 65 (1976).

80. J. D. Kuenzly, D. L. Douglass: "The Oxidation Mechanism of Ni_3Al Containing Yttrium," Oxid. Met., 8, p. 139 (1974).

81. H. M. Hindam, W. W. Smeltzer: "Growth and Microstructure of α-Al_2O_3 on Ni-Al Alloys: Internal Precipitation and Transition to External Scale," J. Electrochem. Soc., 127, p. 1622 (1980).

82. R. Hutchings, M. H. Loretto: "Compositional dependence of oxidation rates of NiAl and CoAl," Metal Sci., 12, p. 503, November, 1978.

83. G. Beghi, E. Cazzaniga, G. Piatti: "Thermal Transformations of Aluminas Extracted from Al-Al_2O_3 Composites," J. Nucl. Mater., 18, p. 237 (1966).

Appendix A

Wagner Theory of Oxidation

This theory, developed by Wagner,[8] involves a description of oxidation behavior assuming idealized conditions. The complete list of assumptions are:[1]

1) The oxide layer is a compact, perfectly adherent scale.
2) Migration of ions or electrons across the scale is the rate controlling process.
3) Thermodynamic equilibrium is established at both scale interfaces.
4) The oxide scale shows only slight deviations from stoichiometry.
5) Thermodynamic equilibrium is established locally throughout the scale.
6) The scale is thick compared with the distances over which space charge effects occur.
7) Oxygen solubility in the metal may be neglected.

Since thermodynamic equilibrium is assumed to be established at both scale interfaces, activity gradients of both the anion and cation species exist across the scale. Because the species are charged, the migration induced by the activity gradient will be in

opposite directions resulting in an electric field. The electric field will be compensated by migration of electronic species because no net charge transfer across the scale is allowed to occur.

The flux of an ionic species, j_i, through the scale thickness, x, as a result of both a chemical potential gradient, $\partial\mu_i/\partial x$, and an electric potential gradient, $\partial\phi/\partial x$, is given as:

$$j_i = -\frac{c_i B_i}{N_A^2}\left(\frac{\partial\mu_i}{\partial x} + Z_i F\frac{\partial\phi}{\partial x}\right) \qquad [A.1]$$

where c_i = concentration of particle i

B_i = mobility of species i

Z_i = charge of particle i

F = Faraday's constant

An equation relating the mobility of a species with its conductivity is given as:

$$c_i B_i = \sigma_i / Z_i^2 e^2 \qquad [A.2]$$

where σ_i = partial electrical conductivity of species i

e = electronic charge

Therefore, the flux of species i can be given as:

$$j_i = -\frac{\sigma_i}{Z_i^2F^2}\left(\frac{\partial\mu_i}{\partial x} + Z_iF\frac{\partial\phi}{\partial x}\right) \qquad [A.3]$$

Electrical neutrality is maintained by a counterflux of an electronic species having an opposite charge from that of the ionic species. In the process of oxidation, usually only one ionic species has a significant mobility. Therefore, the fluxes of only one ionic species and one electronic species need be considerered at equilibrium. The condition for electrical neutrality in the case of high cation mobility is:

$$Z_cj_c + Z_ej_e = 0 \qquad [A.4]$$

Where Z_c = charge of the mobile cation

j_c = flux of cations

Z_e = charge of electron

j_e = flux of elecrons

Eliminating $\partial\phi/\partial x$ results in an equation for the flux of cations given as:

$$j_c = -\frac{\sigma_c\sigma_e}{Z_c^2F^2(\sigma_c + \sigma_e)}\left[\frac{\partial\mu_c}{\partial x} - \frac{Z_c}{Z_e}\cdot\frac{\partial\mu_e}{\partial x}\right] \qquad [A.5]$$

The ionization of a metal atom is represented as:

$$M = M^{(Z_c)} + Z_c e \qquad [A.6]$$

At equilibrium:

$$\mu_M = \mu_c + Z_c \mu_e \qquad [A.7]$$

Therefore, equation [A.5] becomes:

$$j_c = -\frac{\sigma_c \sigma_e}{Z_c^2 F^2 (\sigma_c + \sigma_e)} \cdot \frac{\partial u_M}{\partial x} \qquad [A.8]$$

Equation [A.8] is the expression for the cation flux at a position within the scale. This equation must be integrated between the chemical potential at the metal-oxide interface, μ_M', and the chemical potential at the oxide-gas interface, μ_M'', to give the cation flux through the scale thickness, x. This flux is given as:

$$j_c = \frac{1}{Z_c^2 F^2 x} \cdot \int_{\mu_M''}^{\mu_M'} \frac{\sigma_c \sigma_e}{\sigma_c + \sigma_e} d\mu_M \qquad [A.9]$$

This flux may also be represented as:

$$j_c = C_M \, {}^{dx}/_{dt} \qquad [A.10]$$

where C_M = concentration of metal in the oxide

The parabolic growth rate law is often expressed as:

$$ {}^{dx}/_{dt} = {}^{k'}/_{x} \qquad [A.11]$$

Combining previous equations results in an expression for the parabolic rate constant, k', given as:

$$k' = \frac{1}{Z_c^2 F^2 C_M} \cdot \int_{\mu''_M}^{\mu'_M} \frac{\sigma_c \sigma_e}{\sigma_c + \sigma_e} d\mu_M \qquad [A.12]$$

Combining the Nernst-Einstein equation:

$$D_i = B_i kt \qquad [A.13]$$

where D_i = diffusion coefficient of species i

k = Boltzman's constant

T = temperature

with equation [A.2] and solving for D_i gives:

$$D_i = \frac{kT\sigma_i}{Z_i^2 e^2 c_i} = \frac{RT}{Z_i^2 F^2 C_i} \qquad [A.14]$$

where c_i = concentration in particles/cm^3

C_i = concentration in moles/cm^3

R = gas constant

Substituting equation [A.14] into equation [A.12] yields for k':

$$k' = \frac{1}{RT} \cdot \int_{\mu_M''}^{\mu_M'} D_M d\mu_M \qquad [A.15]$$

Equation [A.15] provides a relationship between known or measurable quantities for the case of high cation mobility in an oxide scale. Other equations can be developed for different species.

Appendix B

Cahn 1000 Electrobalance System

The Cahn 1000 electrobalance combined with compatible electronic monitoring systems provides a very sensitive and convenient means of measuring weights and forces. This is important in measuring the continuous weight gain of a specimen during isothermal oxidation experiments. The system that was used in this study is located at the NASA Lewis Research Center.

The system consists of many components which are shown in the schematic of Figure B.1. The specimen is hung on a platinum wire which is attached to the weighing apparatus so that the specimen lies in the center of the furnace hot zone. A Pt-Pt 30%Rh thermocouple is fixed directly beneath the specimen position for temperature monitoring. The furnace is attached to a motorized hoist which allows the furnace to be raised or lowered around a stationary mullite tube. The furnace tube can be disconnected for easy specimen insertion.

The weighing mechanism for the Cahn 1000 is depicted in the schematic of Figure B.2. As shown, the sample is attached by a hangdown wire to one side of the balance beam. The beam is attached to and supported by a taut ribbon which acts as a

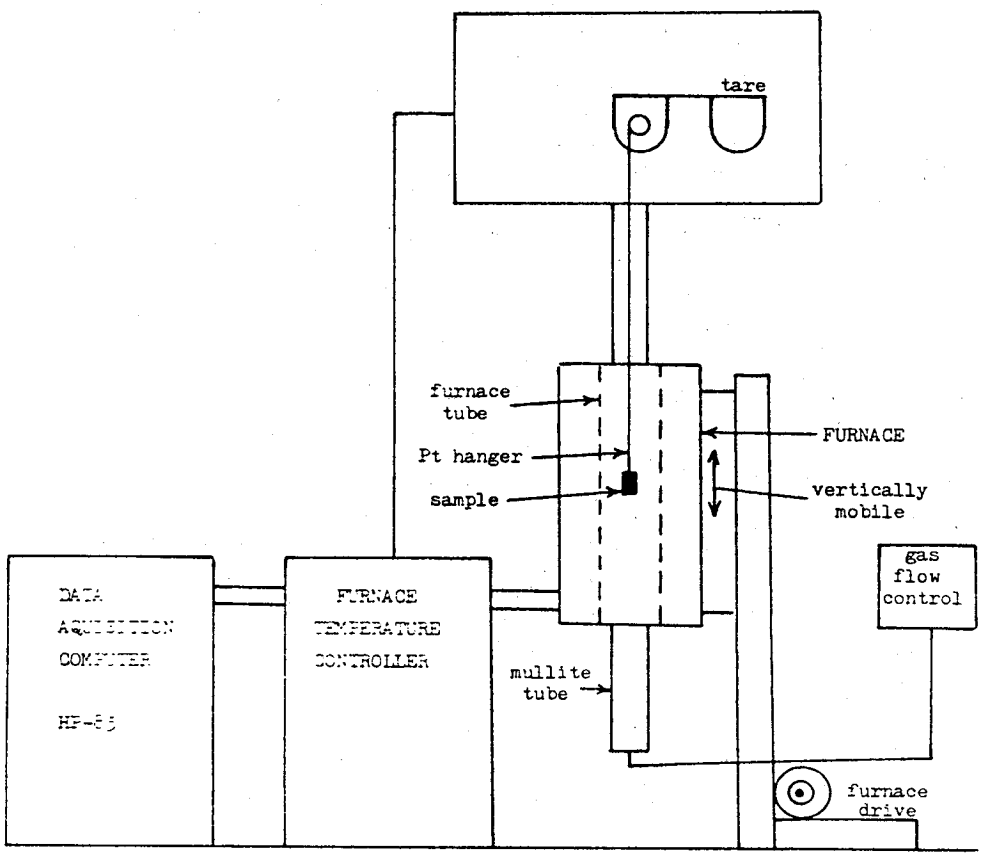

Figure B.1

The Cahn 1000 Electrobalance system.

CAHN 1000 ELECTROBALANCE, WEIGHING MECHANISM

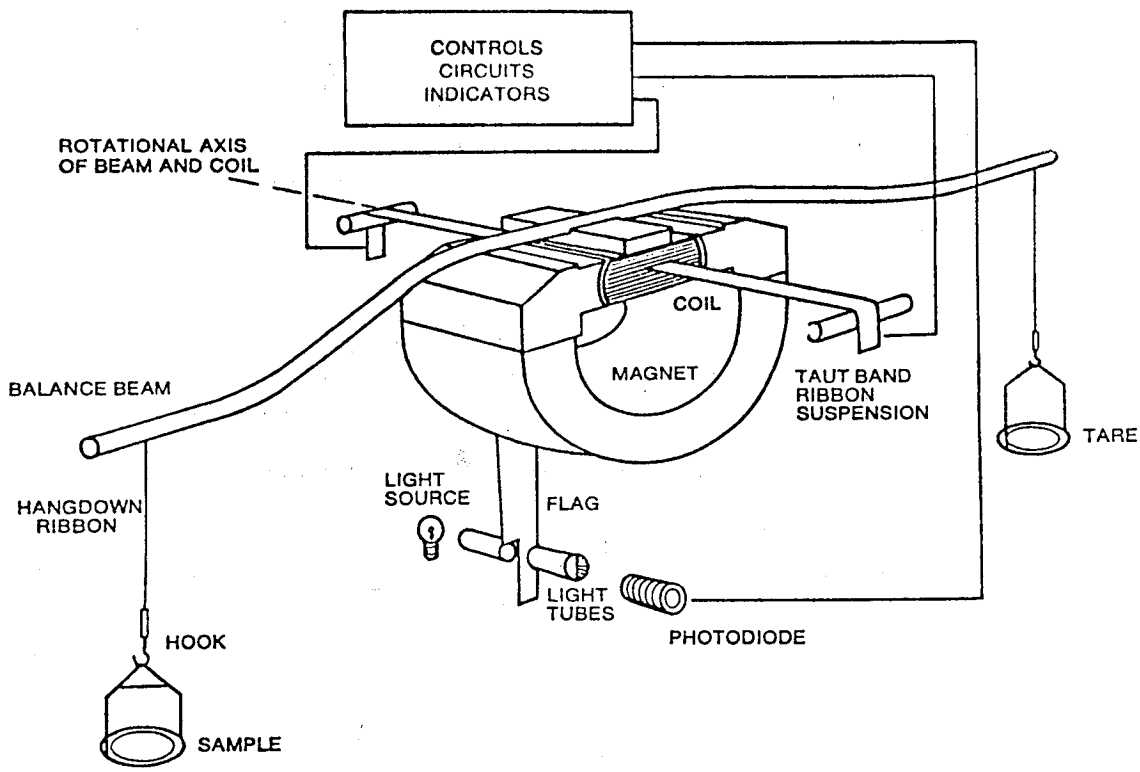

Figure B.2

Schematic of the weighing mechanism for the Cahn 1000.

fulcrum. Counterweights(tares) are attached to the opposite side of the balance beam. A torque motor coil is attached to the support ribbon and located in a permanent magnetic field. A current flows through the motor to offset the torques produced by the sample and tares so that the balance beam is always at a horizontal position. The position of the beam is measured by optical devices beneath the permanent magnet. The current flowing in the torque coil is a direct measure of the combination of forces needed to maintain the balance beam in a horizontal position. A correct calibration allows for a direct output signal corresponding to the sample weight change.

The specimen and weighing devices are maintained in a closed system during the experiment to achieve a uniform environment. The system can be evacuated or may have a flowing atmosphere pumped through from the bottom of the mullite tube.

There are two major corrections that must be accounted for in the raw data, platinum loss and buoyancy. The platinum loss correction is necessary because of volatilization of platinum fixtures at the high temperatures used. The correction is made as a constant weight gain with time to offset the constant rate of platinum volatilization. The constant can be determined by performing an isothermal weight loss test of the platinum fixtures at the same temperature and atmospheric conditions as the subsequent oxidation tests.

A buoyancy correction must be made because the density of the

atmosphere changes as the system is heated. This correction would not be necessary if the system (including the specimen) could be equilibrated at temperature prior to the oxidation test. Because the buoyancy is a function of the volume and geometry of the specimen and fixturing, the value of the correction can be obtained in a number of ways. Standards having the same volume and geometry as specimens can be tested at the oxidizing conditions and the same constant weight differences applied during calculations of oxidation weight gains.

Another method is to iterate the heatup and cooldown cycles of an actual oxidation specimen to obtain a statistical value for the buoyancy correction. However, the method used in the present study was to measure the difference in weight before and after the oxidation test at a specified temperature near ambient temperature and assume the weight difference to be strictly a result of oxidation. This can be done because no spalling of the oxide scales were ever observed. The remainder of the weight change after accounting for oxidation is due to buoyancy.

Appendix C

In-situ Observations of Transient Al_2O_3 Scale Transformations

A common method of observing thermally activated transformations utilizes hot stage electron microscopy. This is often performed using a transmission electron microscope equipped with a special specimen stage in which the specimen can be heated to desired temperatures. The microscope remains operational so that micrographs can be obtained in normal imaging and electron diffraction modes.

An in-situ heating experiment at temperatures greater than $1100^{o}C$ was performed to observe the structural and morphological changes of Al_2O_3 scales formed on β-NiAl. A Gatan platinum ribbon heating stage was used in the Kratos/AEI-EM7 high voltage electron micrscope at Argonne National Laboratory, Chicago, Illinois. The intended purpose of this experiment was to observe, in-situ, the $\gamma \rightarrow \alpha$ transformation in transient Al_2O_3 scales formed on β-NiAl. However, this transformation was never observed. Instead, unique phases formed having structures based on the metastable Al_2O_3 crystallographic structures. A description and possible explanation for the experimental observations will be provided.

A (001) β-NiAl specimen that had been oxidized for 10.0 hours at 800°C and backthinned was placed in the ribbon hot stage, inserted into the microscope vacuum and heated for 1 hour at 1250°C ± 50°C. Extreme specimen drift and other instabilities prevented detailed in-situ examination. Therefore, specimens were cooled before examining. Figure C.1 is an electron diffraction pattern of the oxide scale before and after the heating treatment within the microscope vacuum. The diffraction pattern in Figure C.1a corresponds to δ-Al_2O_3. The same basic structure is observed in Figure C.1b, but additional ordering has occurred during the heat treatment resulting in many extra reflections. A microdiffraction pattern of this scale is shown in Figure C.2. Only one variant of oxide is imaged in Figure C.2. The diffraction pattern in Figure C.1b is a combination of three orthogonal variants. The microdiffraction pattern is from a new phase having a crystal structure similar to δ-Al_2O_3 with an enlarged unit cell. Along the c-direction, the unit cell dimension is doubled as indicated by the $(004)_\delta$ reflection being halved. Along the perpendicular axis in the diffraction pattern, the smallest spacing is one-eighth of the $(400)_\delta$ spacing indicating a unit cell that is 8X larger than δ-Al_2O_3 along this direction.

Another experiment was performed using a (011) β-NiAl specimen that had been oxidized for 1.0 hours at 800°C and backthinned prior to heating. Within 10 minutes of heating at

ORIGINAL PAGE IS
OF POOR QUALITY

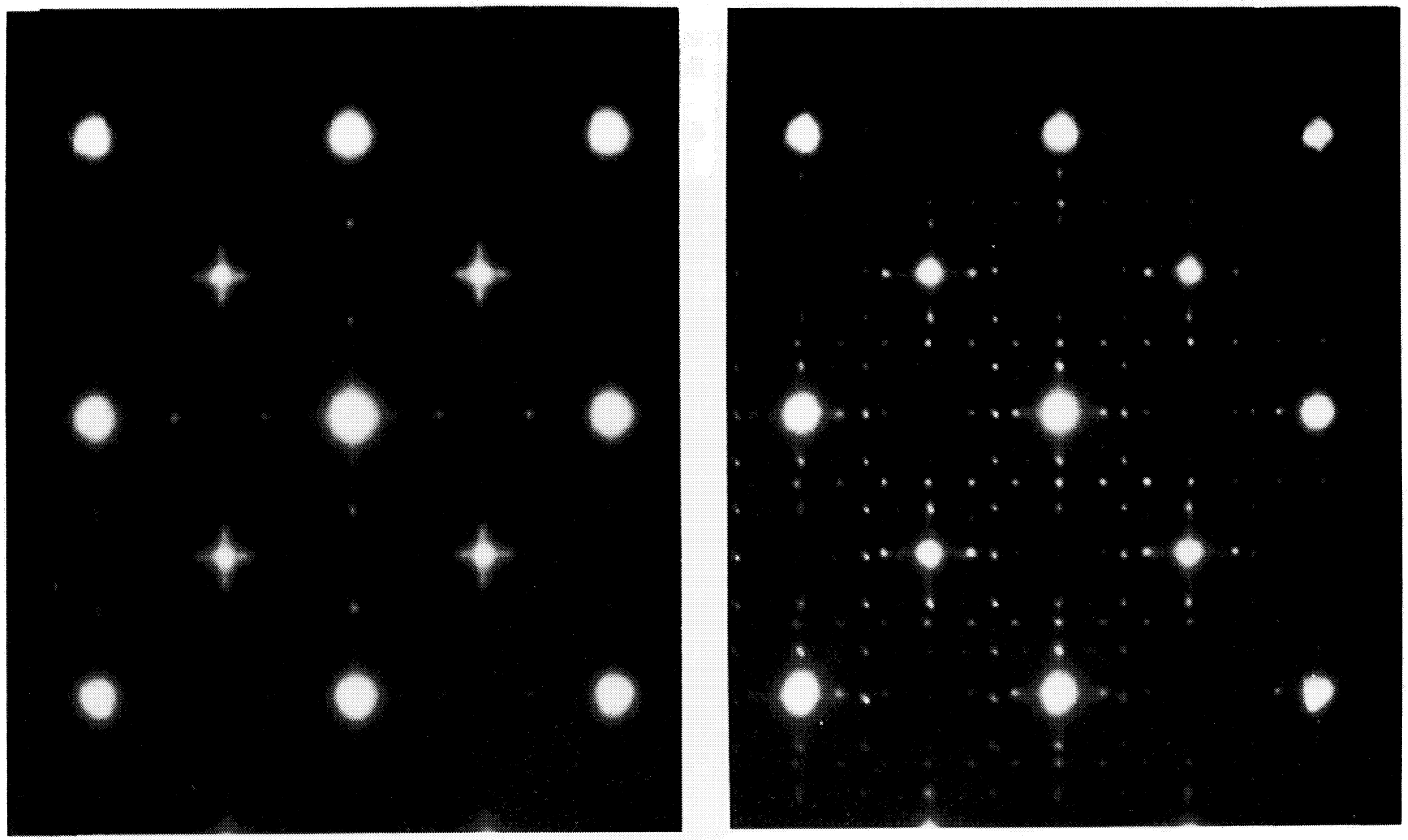

a) b)

Figure C.1

Electron diffraction patterns of oxide scales formed on a (001) β-NiAl specimen oxidized for 10.0 hours at 800°C with a) no additional heat treatment in the microscope vacuum, b) an additional heat treatment in the microscope vacuum.

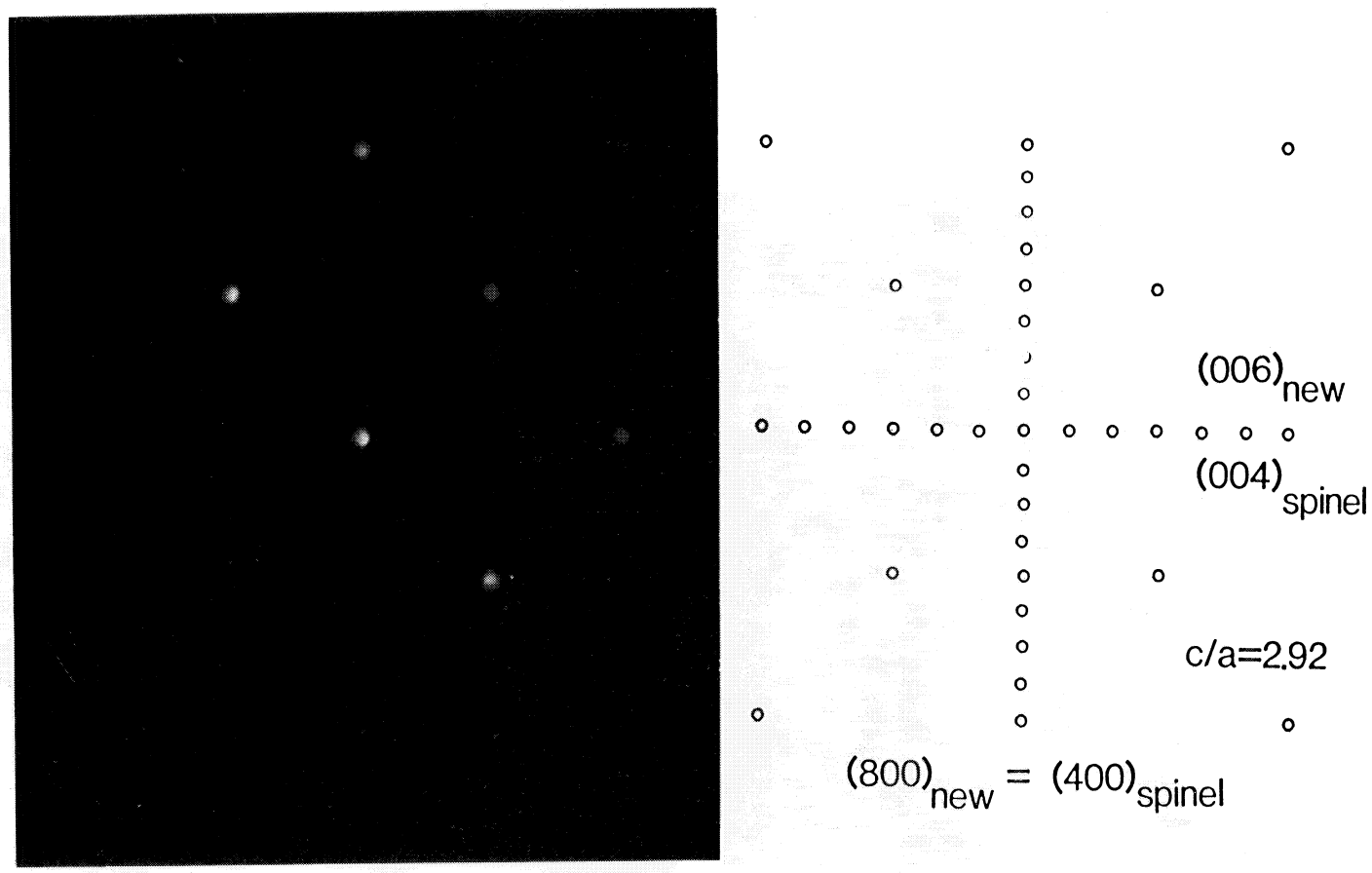

Figure C.2

Microdiffraction pattern and accompanying schematic of the new metastable Al_2O_3 phase formed as a result of the heat treatment that was described in the text. The selected area diffraction pattern in Figure C.1b) consists of many variants of the phase depicted in this microdiffraction pattern.

$1250^{o}C \pm 50^{o}C$, precipitates of a new oxide phase began to form on the scale surface. Figure C.3 is a bright field image showing the oxide precipitates. Figure C.4 contains diffraction patterns of the scale before and after heating. The extra reflections in Figure C.4b correspond to the oxide precipitates. The d-spacings of the additional reflections correspond best with the d-spacings of δ-Al_2O_3. The extra reflections do not correspond to α-Al_2O_3.

Heating of the specimens took place in the microscope vacuum. The reduced oxygen partial pressure of this environment could be responsible for the effects observed in both cases. Effects of reduced oxygen partial pressures have been observed for both phase transitions[83] in which the $\gamma \rightarrow \alpha$ transformation temperature was raised by $200^{o}C$ when specimens were heated in a vacuum and on metastable phase structure[6] in which new metastable phases based on the spinel structure were observed. The same effects are observed in this study. In addition, extensive ordering on the cation sublattice results in new, long-range periodic metastable phases of Al_2O_3.

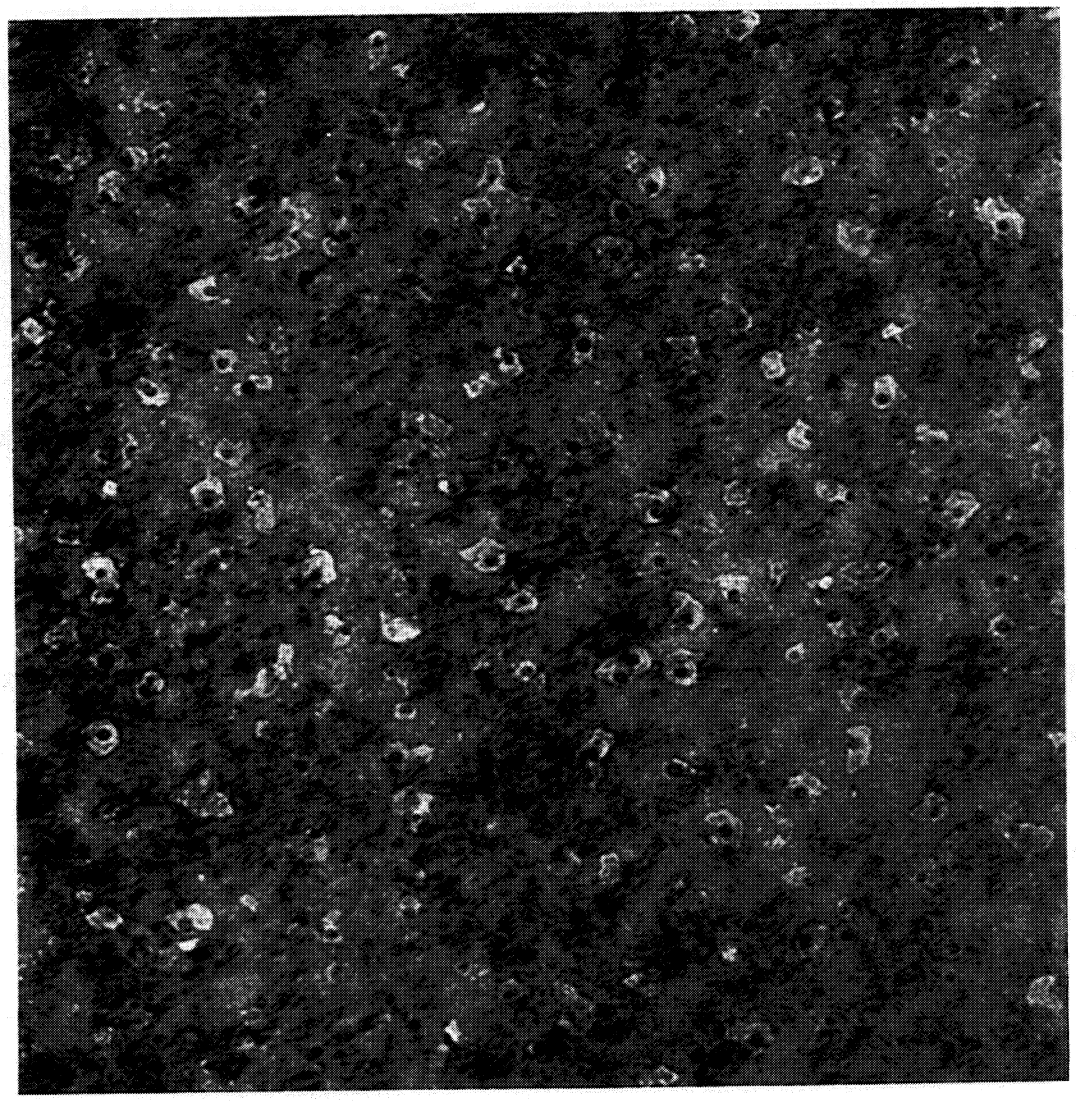

0.1 μm

Figure C.3

Bright field image of an oxide scale formed on a (011) β-NiAl specimen oxidized for 1.0 hours at 800°C followed by a heat treatment at elevated temperatures in the microscope vacuum. Precipitates of a different oxide phase form on the scale surface.

ORIGINAL PAGE IS
OF POOR QUALITY

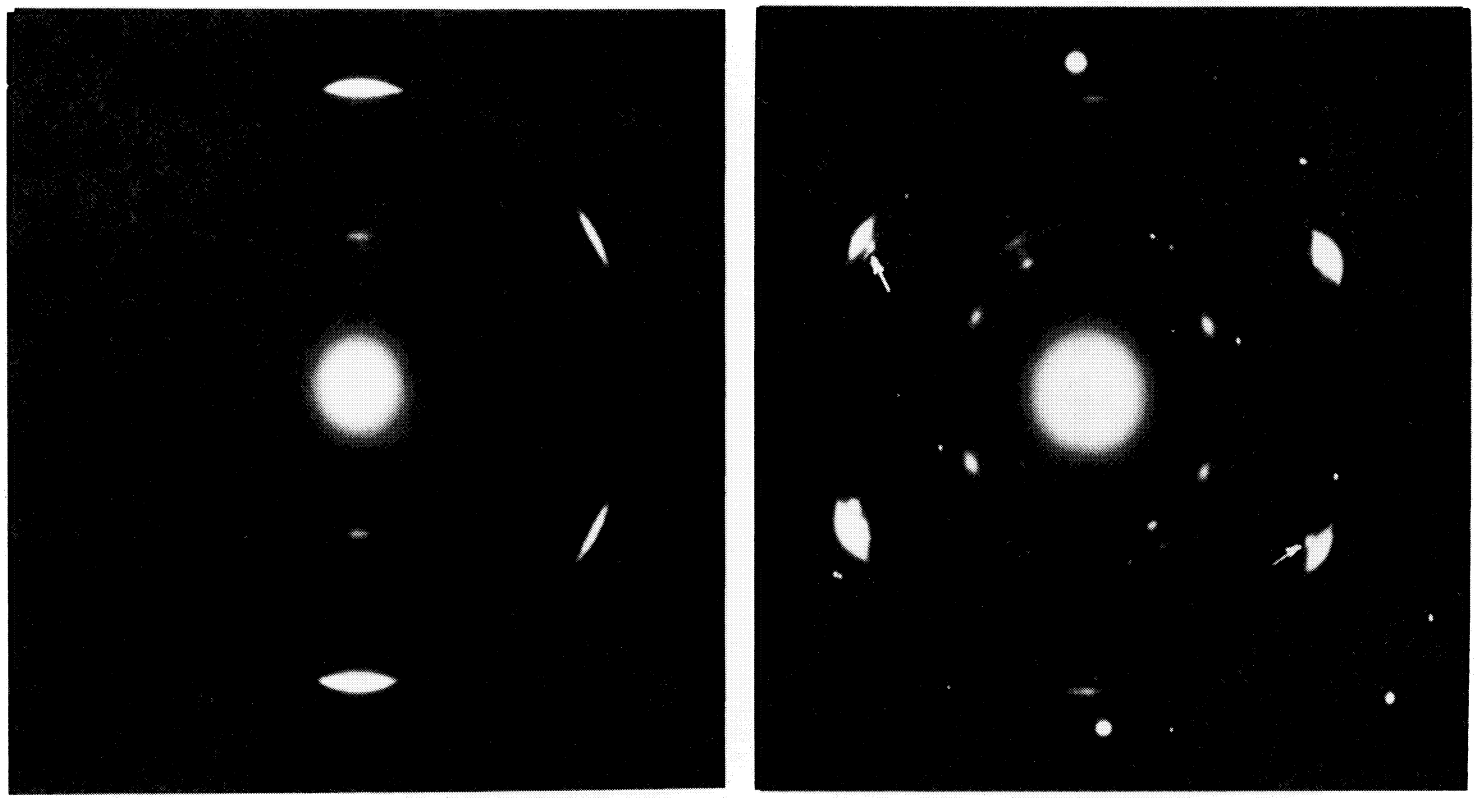

a) Figure C.4 b)

Selected area diffraction patterns of the same specimen as in Figure C.3 taken a) before the heat treatment and b) following the heat treatment. Some extra reflections corresponding to a different oxide phase are indicated in b).

Appendix D

Morphological Changes due to Surface Diffusion

The theory describes the morphological changes of a surface of revolution due to capillarity-induced surface diffusion.[68] The surface flux of atoms along an arbitrary surface is given as:

$$J_s = -(D_s \gamma \Omega \nu / kT) \nabla_s K \qquad [D.1]$$

where J_s = surface flux

D_s = surface self-diffusion coefficient(assumed isotropic)

γ = surface tension(assumed isotropic)

Ω = atomic volume

ν = number of diffusing atoms per unit area = $\Omega^{-.667}$

k = Boltzmann's constant

T = temperature

$\nabla_s K$ = surface curvature gradient given:

$$K = 1/R_1 + 1/R_2$$

R_1, R_2 = principal radii of curvature.

Figure D.1 depicts a surface element for any body of revolution. A flux J_1 crossing the edge δl_1 and a flux J_2

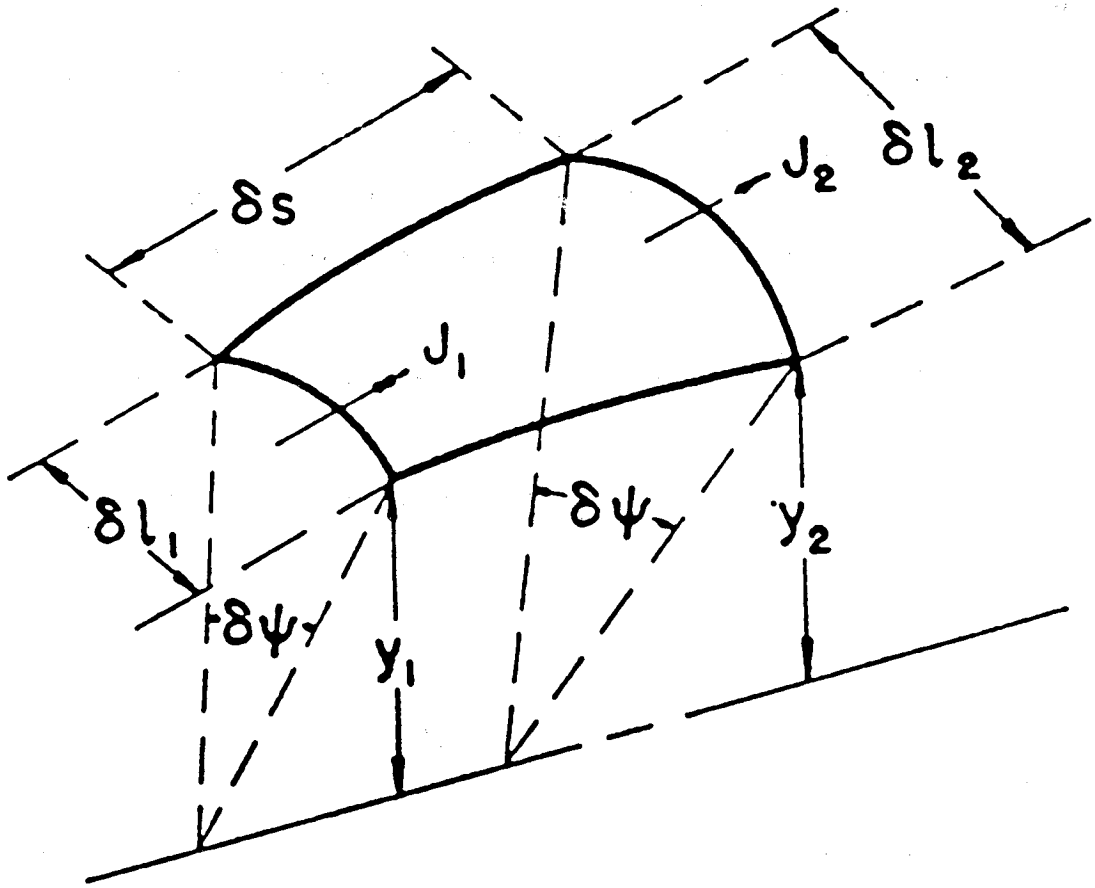

Figure D.1

Schematic of a surface element of revolution.

crossing the edge δl_2 at a height y_2 is considered. For volume to be conserved:

$$(J_1 \delta l_1 - J_2 \delta l_2)\delta t \cdot \Omega = \delta s \delta n \delta l \qquad [D.2]$$

where δl = average chord length

δn = outward distance traveled by the surface element during time increment δt

δs = incremental arc length measured along a section through the axis of revolution which is the z-axis.

Since both δl_1 and δl_2 subtend the same angle:

$$(J_1 y_1 - J_2 y_2)\delta \Psi \Omega \delta t = \delta s \delta n \delta l \qquad [D.3]$$

or

$$-\delta(J_s y)\delta \Psi \Omega \delta t = \delta s \delta n \delta l \qquad [D.4]$$

Using the relations:

$$\delta \Psi = \delta l_1 / y_1 = \delta l_2 / y_2 = \delta l / \bar{y} \qquad [D.5]$$

the flux equation becomes:

$$\delta n / \delta t = -(\Omega / \bar{y})[\delta(J_s y)/\delta s] \qquad [D.6]$$

Taking the limit of an infinitesimal surface element and employing further substitutions yields:

$$\partial n/\partial t = (B/y)(\partial/\partial s)[y(\partial K/\partial s)] \qquad [D.7]$$

where $B = D_s \gamma \Omega^2 \nu / kT$.

The equation for $\partial n/\partial t$ describes the morphological changes of an arbitrary body of revolution.

☆U.S. Government Printing Office: 1986 — 646-114/20431

1. Report No.	2. Government Accession No.	3. Recipient's Catalog No.
NASA CR-175097		

4. Title and Subtitle	5. Report Date
The Evolution and Growth of Al_2O_3 Scales on β-NiAl	May 1986
	6. Performing Organization Code
7. Author(s)	8. Performing Organization Report No.
Joseph K. Doychak	None
	10. Work Unit No.
9. Performing Organization Name and Address	11. Contract or Grant No.
Case Western Reserve University Department of Metallurgy and Materials Science Cleveland, Ohio 44106	NAG 3-498
	13. Type of Report and Period Covered
12. Sponsoring Agency Name and Address	Contractor Report
National Aeronautics and Space Administration Washington, D.C. 20546	14. Sponsoring Agency Code 505-63-01

15. Supplementary Notes

Final report. Project Manager, James L. Smialek, Materials Division, NASA Lewis Research Center, Cleveland, Ohio 44135. This report was a thesis submitted in partial fulfillment of the requirements for the degree Doctor of Philosophy in Metallurgy and Materials Science at Case Western Reserve University in May 1986.

16. Abstract

The formation and growth of Al_2O_3 scales on β-NiAl were studied using electron microscopy and other analytical techniques to gain an understanding of the oxidation properties of β-NiAl and of alumina-forming alloys, in general. The transient and mature stages of oxidation were studied as well as the transformation stage during which the oxide scale transforms from metastable Al_2O_3 phases to the thermodynamically stable α-Al_2O_3 phase. The transient oxidation stages were studied at 800°C and for short times at 1100°C. At 800°C, the scales consist predominantly of δ-Al_2O_3 which forms by cation vacancy ordering in the defective spinel lattice of γ-Al_2O_3. At 1100°C, a fast-growth morphology of θ-Al_2O_3 forms as a surface layer over δ-Al_2O_3. For both oxidation temperatures, the scales are often epitaxially oriented with respect to the metal. The transient scales grow by outward cation diffusion as evidenced by surface growth morphologies. The transformation to α-Al_2O_3 occurs within 1 hour at 1100°C by a nucleation and radial growth process. The large volume decrease associated with the transformation results in a highly strained α-Al_2O_3 microstructure. A change in scale growth mechanism from outward cation to inward anion diffusion allows transient surface morphologies to be smoothed by surface diffusion. The mature stage of oxidation involves the growth of an α-Al_2O_3 scale having the "lacey" morphology formed as a result of the $\gamma \rightarrow \alpha$ transformation. Growth of the scale occurs by counterdiffusion along grain boundaries resulting in ridges formed by impingement of α-Al_2O_3 nuclei during the transformation stage. Also scale growth occurs by inward oxygen diffusion through healed cracks; the cracks result from transformation stresses. The measured growth rates of scales having the lacey morphology are an order of magnitude less than fine-grained α-Al_2O_3 scales. Metal orientations were found to have a large effect on oxide morphologies during all stages of oxidation.

17. Key Words (Suggested by Author(s))	18. Distribution Statement
Al_2O_3 scales; β-NiAl; Oxidation; Transmission electron microscopy	Unclassified - unlimited STAR Category 26

19. Security Classif. (of this report)	20. Security Classif. (of this page)	21. No. of pages	22. Price*
Unclassified	Unclassified	242	All

*For sale by the National Technical Information Service, Springfield, Virginia 22161